A Micro Trigeneration System with Scroll-based Organic Rankine Cycle and Membrane-based Liquid Desiccant Cooling

ZIWEI CHEN

BSc. Architecture and Environmental Design
MSc. Renewable Energy and Architecture

Thesis submitted to the University of Nottingham
for the degree of Doctor of Philosophy

March 2018

Abstract

The emergence of decentralized energy resources has brought numerous novel and advanced designs of efficient power generation systems with utilisation of renewable energy for locally provided, sustainable and cost-effective energy production. The micro trigeneration system has been a highly anticipated solution to fulfil domestic energy requirements, allowing simultaneous generation of electricity, heating and cooling from one primary source. As a matter of fact, the micro trigeneration system is still under research and development stage, with limited available demonstrations around the world. Current laboratory experimental and simulation studies mainly focus on integrations of mature technologies, whereas many promising alternatives have not been widely explored, for example organic Rankine cycle (ORC) and liquid desiccant cooling technology.

The main aim of this thesis is to technically develop and evaluate a novel micro trigeneration system with a combination of scroll-based ORC and membrane-based liquid desiccant cooling (MLDC). In principle, the micro trigeneration system provides highly efficient energy conversion in a decentralized manner, as the scroll-based ORC has superior abilities in generating electricity and providing sufficient thermal output that matches the low-temperature regeneration requirement of the liquid desiccant in the MLDC. In terms of system sustainability, compact linear Fresnel reflectors (CLFR) can be one option of the primary energy source for the micro trigeneration system. A comprehensive literature review has demonstrated that no work has been conducted previously on such a system. In this thesis, the possibility of integrating CLFR to power generation systems has been firstly investigated and a detailed optical design of the CLFR-hybrid system has been conducted through geometrical modelling and experimental work. Results demonstrate that the CLFR-

hybrid system with polar orientation is feasible to efficiently convert the absorbed solar energy into thermal energy, which thereby can be utilised for powering the micro trigeneration system. The concept of the novel micro trigeneration system with scroll-based ORC and MLDC has been critically examined and energy performance of the two main components, namely scroll-based ORC and MLDC have been evaluated respectively through both theoretical modelling and experimental work. Experimental tests show that the scroll-based ORC electric output of 564.5W, scroll expander isentropic and volumetric efficiencies of 78% and 83% are achievable at a 1kW capacity. In terms of MLDC, experimental results indicate the importance of system mass balance between the membrane-based dehumidifier and regenerator for continuous operation. Under the steady operating condition of MLDC, a supply air temperature of 20.4°C with dehumidification effectiveness of 0.3 and system COP of 0.70 are attainable at calcium chloride ($CaCl_2$) solution concentration of 36%. Simulations based on a validated and comprehensive system model demonstrate the feasibility of pairing the scroll-based ORC and MLDC for the microre trigeneration system. The exhaust heat from the scroll-based ORC effectively fulfils the regeneration requirement of the MLDC. The inclusion of MLDC facilitates the micro trigeneration system overall efficiency with an increase of approximately 35.49%, compared to that of ORC-based separate power generation. Theoretical results show that the proposed micro trigeneration system has the overall system efficiencies of 38.96% in cogeneration mode and 41.23% in trigeneration mode.

The thesis makes contribution to the knowledge of micro trigeneration technology, distributed power generation, energy conversion and air conditioning. Moreover, the presented parametric studies of CLFR, ORC and MLDC can be employed for designing and optimizing the relevant individual components. Regarding the future

work, this thesis recommends more in-depth system modelling with a combination of CLFR, ORC and MLDC, logic optimisation of the micro trigeneration system and comprehensive field trial testing of the micro trigeneration system in building context.

Published Work

Journal papers

[1] J. Zhu, **Z. Chen**, Optical design of compact linear Fresnel reflector systems, Solar Energy Materials and Solar Cells 176 (2018) 239-250.

[2] H. Bai, J. Zhu, **Z. Chen**, J. Chu, Parametric analysis of a cross-flow membrane-based parallel-plate liquid desiccant dehumidification system: numerical and experimental data, Energy and Buildings 158 (2018) 494-508.

[3] H. Bai, J. Zhu, **Z. Chen**, L. Ma, R. Wang, T. Li, Performance testing of a cross-flow membrane-based liquid desiccant dehumidification system, Applied Thermal Engineering 119 (2017) 119-131.

[4] **Z. Chen**, J. Zhu, H. Bai, Performance assessment of a membrane liquid desiccant dehumidification cooling system based on experimental investigations, Energy and Buildings 139 (2017) 665-679.

[5] **Z. Chen**, J. Zhu, H. Bai, Y. Yan, L. Zhang, Experimental study of a membrane-based dehumidification cooling system, Applied Thermal Engineering 115 (2017) 1315-1321.

[6] J. Zhu, **Z. Chen**, H. Huang, Y. Yan, Effect of resistive load on the performance of an organic Rankine cycle with a scroll expander, Energy 95 (2016) 21-28.

Conference presentation (with papers)

[1] **Chen Z.**, Bai H., Ye Z., and Zhu J., 2016. Experimental study of a membrane-based dehumidification cooling system In: Proceedings of International Heat Transfer

Symposium and Heat Powered Cycles Conference 2016 (IHTS and HPC 2016), 26-29 June 2016, Nottingham, UK.

[2] Bai H., **Chen Z.**, Xu H., and Zhu J., 2016. Theoretical analysis of a membrane-based cross-flow liquid desiccant system In: Proceedings of International Heat Transfer Symposium and Heat Powered Cycles Conference 2016 (IHTS and HPC 2016), 26-29 June 2016, Nottingham, UK.

[3] **Chen Z.**, Pan Y., and Zhu J., 2015. Theoretical analysis of a membrane-based liquid desiccant system In: Proceedings of the 14th International Conference on Sustainable Energy Technologies (SET-2015), 25-27 August 2015, Nottingham, UK.

Acknowledgements

First of all, I would like to express my sincere gratitude to my main supervisor Dr. Jie Zhu for offering me this great opportunity to conduct the PhD research, for his continuous support, immense knowledge, patient guidance, valuable advice and encouragement throughout my undergraduate, postgraduate and PhD studies. I would also like to extend my appreciation to my supervisor Dr. Guohui Gan, my internal assessor Dr. Yuehong Su and head of my research group Professor Yuying Yan for their help and comments throughout my PhD study.

I truly have wonderful memories of the almost nine-year study in the Department of Architecture and Built Environment, University of Nottingham, which I believe will last forever. I really appreciate the "Dean of Engineering Research Scholarship for International Excellence" provided by the Faculty of Engineering, which have been the financial support of my PhD study. Besides, I would like to thank all the technical staffs at the Department of Architecture and Built Environment for their help, advice and tutoring with my experimental work. Special mention goes to Elaine Till, Dave Oliver, Dave Taylor, Jonathan Moss, Tony Lord, Andy Matthews, James Hazzledine and Tony Gospel. I am also thankful for my kind colleagues in the SRB office, especially Yuanlong Cui, Jiayi Jin, Hongyu Bai, Junze Chu and Xiangjie Chen for their insightful comments, help and support in the research as well as timely care in life and moral encouragement.

My sincere thank also goes to my valuable friends for always being there for me no matter what happened, especially Xiao Zhang and Jie Ding for being the treasure in my heart. Also I am thankful for the joys, inspirations and encouragements from Nan Zhou, Yiyi Liu, Ruoping Sun, Long Chen, Olivia Chen, Ning Wang, Yang Fei, Xinwen Xu, Zhe Xu, Zhiyi You, Haolin Wu and Linqi Zhang.

Lastly, but most importantly, I am of course grateful to my father and mother, for their love, for always being there and supporting me in anything I want to do. Thanks Congjing Liu, my great cousin, for accompanying me for such a long time here in the UK. I am thankful for the wonderful and supporting family that I have been blessed; all my family members are always supporting me and believing in me.

List of Contents

Abstract ..... **i**

Published Work ..... **iv**

Acknowledgements ..... **vi**

List of Contents ..... **viii**

List of Figures ..... **xiii**

List of Tables ..... **xxii**

Nomenclature ..... **xxiv**

Chapter 1: Introduction **1**

1.1 Research background **1**

1.2 Research overview **6**

1.3 Research aim and objectives **8**

1.4 Research methodology **9**

1.5 Significance of research **9**

1.6 Thesis structure **10**

Chapter 2: Literature review **12**

2.1 Introduction **12**

2.2 Micro trigeneration system **13**

2.2.1 Concept 13

2.2.2 Applications 14

2.2.3 Advantages 14

2.2.4 Limitations 15

2.3 Concentrating solar collectors **16**

2.3.1 Linear Fresnel reflector 17

2.3.2 Compact linear Fresnel reflector 20

2.4 Prime movers **23**

2.4.1 Comparisons of available prime movers 23

2.4.2 Organic Rankine cycle 36

2.4.3 Scroll expander 40

2.5 Heat recovery **45**

2.6 Thermal-activated cooling **48**

2.6.1 Comparisons of available thermal-activated cooling technologies 49
2.6.2 Liquid desiccant cooling 55
2.6.3 Membrane-based liquid desiccant cooling 61
2.7 Operating strategy 63
2.8 Recent research on micro trigeneration 65
2.8.1 Comprehensive reviews 65
2.8.2 Theoretical research 72
2.8.3 Experimental work 75
2.9 Summary 78

Chapter 3: Micro Trigeneration System Development 82
3.1 Introduction 82
3.2 System description 82
3.2.1 Overall system 83
3.2.2 Compact linear Fresnel reflector 86
3.2.3 Scroll-based organic Rankine cycle 86
3.2.4 Membrane-based liquid desiccant cooling 88
3.3 Summary 91

Chapter 4: Optical Performance Evaluation of CLFR 92
4.1 Introduction 92
4.2 Geometrical modelling of CLFR 93
4.2.1 Common tilting mirror array modelling 94
4.2.2 Alternating mirror array modelling 97
4.2.3 Optical performance evaluation metrics 100
4.2.4 Simulation approach 102
4.3 CLFR experimental set-up 104
4.3.1 Experiment description 104
4.3.2 Experimental method 106
4.4 Optical performance comparisons of LFR and CLFR 107
4.4.1 Mirror array arrangement 107
4.4.2 Concentration and ground utilisation ratios 108
4.4.3 Received solar energy 109
4.4.4 Comparison summary 110
4.5 Optical design of CLFR 111
4.5.1 With limited solar field area 111
4.5.2 With limited mirrors 116

4.5.3 At a given focal length 118
4.5.4 With variable receiver inclination angles 120
4.5.5 Optical analysis summary 121
4.6 Summary 122

Chapter 5: Performance Evaluation of Scroll-based ORC 124
5.1 Introduction 124
5.2 Scroll expander modelling 125
5.2.1 Semi-empirical model 126
5.2.2 Energy balance 131
5.2.3 Scroll expander performance evaluation metrics 132
5.3 ORC experimental description 133
5.3.1 Experimental set-up 133
5.3.2 Experimental method 138
5.4 Model validation with experimental work 144
5.4.1 Identification of input parameters 144
5.4.2 Model validation 146
5.4.3 Validation summary 148
5.5 Scroll expander parametric analysis 149
5.5.1 Effect of scroll expander pressure ratio at constant supply pressure 149
5.5.2 Effect of scroll expander pressure ratio at constant exhaust pressure 154
5.5.3 Effect of scroll expander supply pressure 159
5.5.4 Effect of scroll expander supply temperature 163
5.5.5 Effect of scroll expander rotational speed 167
5.5.6 Parametric analysis summary 171
5.6 Experimental investigations of ORC system 172
5.6.1 Variation of electric output with resistive load 173
5.6.2 Variation of electric output with pressure ratio 174
5.6.3 Variation of electric output with pressure ratio and rotational speed 176
5.6.4 Variation of electrical and scroll expander efficiencies with resistive load 178
5.6.5 Experimental investigations summary 180
5.7 Summary 181

Chapter 6: Performance Evaluation of MLDC 184
6.1 Introduction 184
6.2 Experimental set-up of MLDC 186
6.2.1 System description 186

6.2.2 Membrane-based unit 189
6.2.3 Experimental method 190
6.3 Performance evaluation metrics 194
6.4 MLDC dehumidification performance evaluation 196
6.4.1 Influence of inlet air condition 197
6.4.2 Influence of air flow rate 201
6.4.3 Influence of cold water temperature 203
6.4.4 Influence of solution concentration 205
6.4.5 Dehumidification performance evaluation summary 206
6.5 MLDC regeneration performance evaluation 207
6.5.1 Influence of air flow rate 207
6.5.2 Influence of regeneration hot water temperature 209
6.5.3 Influence of solution concentration 211
6.5.4 Regeneration performance summary 211
6.6 MLDC evaporative cooling performance evaluation 212
6.7 MLDC overall system performance evaluation 213
6.7.1 Influence of cold water temperature 214
6.7.2 Influence of regeneration temperature 215
6.7.3 System performance evaluation summary 216
6.8 Summary 217

Chapter 7: Performance Evaluation of Micro Trigeneration System 219
7.1 Introduction 219
7.2 Micro trigeneration system modelling 222
7.2.1 Scroll expander 222
7.2.2 Pump 223
7.2.3 Heat exchangers 225
7.2.4 Membrane-based unit 228
7.2.5 Performance evaluation metrics 234
7.2.6 Modelling method 236
7.3 Model validation with experimental work 239
7.4 System energy performance in different operating modes 245
7.5 Parametric study of system performance in cogeneration mode 248
7.5.1 Hot water supply temperature 249
7.5.2 Hot water supply mass flow rate 253
7.5.3 Cold water supply temperature 256

7.5.4 Cold water supply mass flow rate 260
7.5.5 Scroll expander rotational speed 263
7.5.6 Cogeneration performance summary 266
7.6 Parametric study of system performance in trigeneration mode 268
7.6.1 Hot water supply temperature 268
7.6.2 Cold water supply temperature 272
7.6.3 Scroll expander rotational speed 276
7.6.4 Trigeneration performance summary 279
7.7 Summary 280

Chapter 8: Conclusions and Recommendations for Future Work 284
8.1 Introduction 284
8.2 Major findings 284
8.3 Limitations and recommendations for future work 290
8.3.1 Limitations of the study 290
8.3.2 Recommendations for future work 292

References 294

Appendix A: Excerpt of CLFR Model Script 329

Appendix B: Excerpt of Micro Trigeneration System Model Script 332

Appendix C: Experimental Instrument Manufacture Datasheets 336

List of Figures

Figure 1-1 World total primary energy consumption and production from 1990 to 2015 1

Figure 1-2 Global total primary energy consumption by fuel types 2

Figure 1-3 Map of installed CHP systems in the UK [6] 4

Figure 1-4 Design concept of the proposed micro trigeneration system 7

Figure 2-1 Concept diagram of trigeneration system 14

Figure 2-2 Schematic diagram of LFR system 18

Figure 2-3 Cosine, end, shading and blocking effect in LFR system 19

Figure 2-4 Schematic diagram of CLFR system 20

Figure 2-5 Schematic diagrams of CLFR configurations (a) complete (b) hybrid 21

Figure 2-6 Schematic diagram of scroll expander 40

Figure 2-7 Working process of scroll expander 41

Figure 2-8 Schematic diagram of desiccant cooling 52

Figure 3-1 Schematic diagram of the proposed micro trigeneration system 83

Figure 3-2 Illustration of the micro trigeneration system 85

Figure 3-3 Schematic diagram of ORC sub-system 87

Figure 3-4 Temperature-entropy diagram of ORC sub-system 88

Figure 3-5 Schematic diagram of MLDC sub-system 89

Figure 3-6 Psychrometric process of air in the MLDC sub-system 90

Figure 3-7 Psychrometric process of solution in the MLDC sub-system 91

Figure 4-1 Schematic diagram of common tilting mirror array of CLFR system 95

Figure 4-2 Schematic diagram of CLFR-hybrid system 98

Figure 4-3 Flow chart of CLFR simulation process with MATLAB and TracePro 103

Figure 4-4 Photo of CLFR test rig 105

Figure 4-5 Concentration and ground utilisation ratios of LFR, CLFR-hybrid and CLFR-complete systems 109

Figure 4-6 Simulation and experimental results of received solar energy for LFR, CLFR-hybrid and CLFR-complete systems..... 110

Figure 4-7 Mirror width variations for CLFR-hybrid A system at different focal lengths 112

Figure 4-8 Variations of concentration and ground utilisation ratios with focal length for CLFR-hybrid A system 113

Figure 4-9 Variations of concentration and ground utilisation ratios for CLFR-hybrid A system with a focal length of 1500mm and solar field width of 2100mm..... 114

Figure 4-10 Simulation and experimental results of received solar energy for CLFR-hybrid A system 114

Figure 4-11 Ray tracing simulation result of CLFR-hybrid A..... 115

Figure 4-12 Illuminance maps of receiver surface for CLFR-hybrid A system (a) experimental (b) ray tracing simulation results..... 116

Figure 4-13 Variations of concentration and ground utilisation ratios with focal length for CLFR-hybrid system with 50 mirrors 118

Figure 4-14 Variations of concentration and ground utilisation ratios with solar field width for CLFR-hybrid system at a focal length of 1500mm..... 119

Figure 4-15 Variations of concentration and ground utilisation ratios with receiver inclination angle for CLFR-hybrid A system..... 121

Figure 5-1 Schematic diagram of semi-empirical scroll expander model 126

Figure 5-2 Internal leakages of scroll expander (a) radial and (b) flank..... 129

Figure 5-3 *P*-*V* diagrams of (a) ideal isentropic expansion (b) under-expansion and (c) over-expansion 131

Figure 5-4 Schematic graph of scroll-based ORC system 135

Figure 5-5 Photos of scroll-based ORC test rig 136

Figure 5-6 *P-h* diagram of scroll-based ORC system 141

Figure 5-7 Flow chart of overall simulation process 145

Figure 5-8 Comparisons of between calculated and measured results for: (a) working fluid mass flow rate, (b) working fluid exhaust temperature and (c) electric output power 148

Figure 5-9 Variations of (a) working fluid mass flow rate and (b) scroll expander electric output with pressure ratio 151

Figure 5-10 Variations of scroll expander (a) exhaust temperature and (b) ambient heat losses with pressure ratio 152

Figure 5-11 Variations of scroll expander (a) isentropic, (b) volumetric and (c) net efficiencies with pressure ratio 154

Figure 5-12 Variations of (a) working fluid mass flow rate and (b) scroll expander electric output with pressure ratio 155

Figure 5-13 Variations of scroll expander (a) exhaust temperature and (b) ambient heat losses with pressure ratio 156

Figure 5-14 Variations of scroll expander (a) isentropic, (b) volumetric and (c) net efficiencies with pressure ratio 158

Figure 5-15 Variations of (a) working fluid mass flow rate and (b) scroll expander electric output with supply pressure 160

Figure 5-16 Variations of scroll expander (a) exhaust temperature and (b) ambient heat losses with supply pressure 161

Figure 5-17 Variations of scroll expander (a) isentropic, (b) volumetric and (c) net efficiencies with supply pressure 163

Figure 5-18 Variations of (a) working fluid mass flow rate and (b) scroll expander electric output with supply temperature 164
Figure 5-19 Variations of scroll expander (a) exhaust temperature and (b) ambient heat losses with supply temperature 165
Figure 5-20 Variations of scroll expander (a) isentropic, (b) volumetric and (c) net efficiencies with supply temperature 167
Figure 5-21 Variations of (a) working fluid mass flow rate and (b) scroll expander electric output with rotational speed 168
Figure 5-22 Variations of scroll expander (a) exhaust temperature and (b) ambient heat losses with rotational speed 169
Figure 5-23 Variations of scroll expander (a) isentropic, (b) volumetric and (c) net efficiencies with rotational speed 171
Figure 5-24 Variations of electric output power with resistive load 174
Figure 5-25 Variations of (a) electric output power with pressure ratio and (b) optimal pressure ratio with resistive load 176
Figure 5-26 Variations of electric output power with pressure ratio and rotational speed 177
Figure 5-27 Variations of (a) ORC electrical efficiency and (b) isentropic and volumetric efficiencies of scroll expander with resistive load 179
Figure 6-1 Block diagram of MLDC system 187
Figure 6-2 Schematic graph of MLDC system 188
Figure 6-3 Illustration of membrane-based unit 190
Figure 6-4 Photos of MLDC test rig 191
Figure 6-5 $CaCl_2$ solution equilibrium humidity ratio with concentration and temperature 195

Figure 6-6 Dehumidifier inlet air condition range 198

Figure 6-7 Influence of inlet air condition on dehumidifier (a) moisture removal rate, (b) dehumidification effectiveness and (c) cooling output 200

Figure 6-8 Influence of air flow rate on dehumidifier (a) moisture removal rate, (b) dehumidification effectiveness and (c) cooling output 202

Figure 6-9 Variations of dehumidifier solution spray temperature and outlet air temperature with cold water temperature 203

Figure 6-10 Influence of cold water temperature on dehumidifier (a) moisture removal rate, (b) dehumidification effectiveness and (c) cooling output 205

Figure 6-11 Influence of air flow rate on regenerator moisture addition rate 208

Figure 6-12 Influence of air flow rate on regenerator thermal input power 209

Figure 6-13 Influence of hot water temperature on regenerator moisture addition rate 210

Figure 6-14 Influence of hot water temperature on regenerator thermal input power 210

Figure 6-15 Variations in evaporative cooler outlet air temperature and evaporative effectiveness with cold water temperature 213

Figure 6-16 Influence of cold water temperature on system cooling output and COP 215

Figure 6-17 Influence of hot water temperature on regenerator thermal input power and system COP 216

Figure 7-1 Schematic diagram of micro trigeneration system with scroll-based ORC and MLDC 221

Figure 7-2 Schematic diagram of a cross-flow single-layer membrane unit 228

Figure 7-3 Control volumes for (a) heat balance, (b) mass balance in solution channel, (c) heat balance and (d) mass balance in air channel 230

Figure 7-4 Normalization process with dimensionless parameters for governing equations 233

Figure 7-5 Modelling flow chart 238

Figure 7-6 Comparison of the calculated and measured results for: (a) scroll expander supply pressure (b) scroll expander exhaust pressure (c) working fluid mass flow rate and (d) electric output power 242

Figure 7-7 Comparison of the calculated and measured results for working fluid temperature at: (a) scroll expander inlet (b) scroll expander outlet (c) condenser outlet 243

Figure 7-8 Influence of hot water supply temperature on scroll expander supply and exhaust temperatures 249

Figure 7-9 Influence of hot water supply temperature on scroll expander pressure ratio and isentropic efficiency 250

Figure 7-10 Influence of hot water supply temperature on heat input power, electric output power and recovered thermal power 251

Figure 7-11 Influence of hot water supply temperature on system electrical, thermal and CHP efficiencies 252

Figure 7-12 Influence of hot water mass flow rate on scroll expander pressure ratio and isentropic efficiency 254

Figure 7-13 Influence of hot water mass flow rate on heat input power, recovered thermal power and electric output 255

Figure 7-14 Influence of hot water mass flow rate on system electrical, thermal and CHP efficiencies 256

Figure 7-15 Influence of cold water supply temperature on pump supply temperature and scroll expander supply and exhaust pressures 257
Figure 7-16 Influence of cold water supply temperature on scroll expander pressure ratio and isentropic efficiency 258
Figure 7-17 Influence of cold water supply temperature on heat input power, electric output power and recovered thermal power 259
Figure 7-18 Influence of cold water supply temperature on system electrical, thermal and CHP efficiencies 260
Figure 7-19 Influence of cold water mass flow rate on scroll expander pressure ratio and isentropic efficiency 261
Figure 7-20 Influence of cold water mass flow rate on heat input power, recovered thermal power and electric output 262
Figure 7-21 Influence of cold water mass flow rate on system electrical, thermal and CHP efficiencies 263
Figure 7-22 Influence of scroll expander rotational speed on scroll expander pressure ratio and isentropic efficiency 264
Figure 7-23 Influence of scroll expander rotational speed on heat input power, electric output power and recovered thermal power 265
Figure 7-24 Influence of scroll expander rotational speed on system electrical, thermal and CHP efficiencies 266
Figure 7-25 Influence of hot water supply temperature on scroll expander supply and exhaust temperatures 269
Figure 7-26 Influence of hot water supply temperature on scroll expander pressure ratio and isentropic efficiency 270

Figure 7-27 Influence of hot water supply temperature on heat input power, electric output power and total recovered thermal power 271
Figure 7-28 Influence of hot water supply temperature on system COP, electrical and CCHP efficiencies 272
Figure 7-29 Influence of cold water supply temperature on pump supply temperature and scroll expander supply and exhaust pressures 273
Figure 7-30 Influence of cold water supply temperature on scroll expander pressure ratio and isentropic efficiency 274
Figure 7-31 Influence of cold water supply temperature on heat input power, electric output power and total recovered thermal power 275
Figure 7-32 Influence of cold water supply temperature on system COP, electrical and CCHP efficiencies 276
Figure 7-33 Influence of scroll expander rotational speed on scroll expander pressure ratio and isentropic efficiency 277
Figure 7-34 Influence of scroll expander rotational speed on heat input power, electric output power and total recovered thermal power 277
Figure 7-35 Influence of scroll expander rotational speed on system COP, electrical and CCHP efficiencies 278
Figure A-1 Photo and manufacture datasheet of scroll expander 337
Figure A-2 Photo and manufacture datasheet of electric boiler 338
Figure A-3 Manufacture datasheet of refrigerant pump 339
Figure A-4 Manufacture datasheet of heat exchanger 340
Figure A-5 Manufacture datasheet of AC axial fan 341
Figure A-6 Manufacture datasheet of magnetic liquid pump 343
Figure A-7 Manufacture datasheet of power quality analyser 345

Figure A-8 Manufacture datasheet of humidity Sensor 346

List of Tables

Table 2-1 Characteristics of available prime movers for trigeneration system [4, 5, 8, 15, 20, 24, 47, 85, 87, 91-93] 25

Table 2-2 Advantages and disadvantages of available primary movers for trigeneration system [4, 5, 8, 15, 20, 24, 47, 85, 87, 91-93] 29

Table 2-3 Characteristics of available heat recovery equipment [4, 22, 161-164] 46

Table 2-4 Characteristics of thermal-activated cooling technologies [4, 8, 15, 27, 162, 165, 166] 48

Table 2-5 Operative concentration levels for different liquid desiccants [199] 56

Table 2-6 Characteristics of available liquid desiccant dehumidification systems [195, 199, 204-210] 57

Table 2-7 Review perspectives of review papers on trigeneration system 67

Table 3-1 Components of the proposed micro trigeneration system 83

Table 4-1 Specifications of CLFR experimental set-up 104

Table 4-2 Total number of mirrors for LFR, CLFR-hybrid and CLFR-complete systems 108

Table 4-3 Solar field widths for CLFR-hybrid system with the same total number of mirror elements 117

Table 4-4 Mirror arrangements of the CLFR-hybrid system at a fixed focal length of 1500mm 119

Table 5-1 Specifications of main components in scroll-based ORC system 136

Table 5-2 Measuring instruments with associated accuracies 139

Table 5-3 Identified input parameters of the scroll expander model 146

Table 6-1 Specifications of main equipment in MLDC system 189

Table 6-2 Specifications of membrane-based unit 189

Table 6-3 Measurement devices with associated accuracies 192

Table 6-4 Operating condition for MLDC dehumidification performance evaluation 197

Table 7-1 Parameters of scroll expander model 222

Table 7-2 Parameters of pump model 223

Table 7-3 Parameters of heat exchanger model 225

Table 7-4 Parameters for MLDC modelling 230

Table 7-5 Normalized equations for heat and mass balances 233

Table 7-6 Outputs of the micro trigeneration system model 239

Table 7-7 Operating variables for validation 240

Table 7-8 Energy performance of micro trigeneration system in different operating modes 246

Table 7-9 Operating variables for simulation 248

Nomenclature

Symbols

A	Surface area (m^2)
b_n	Half-width of a mirror element (mm)
B	Half-length of a receiver (mm)
C	Heat capacity (J/K)
C_p	Specific heat capacity(J/kg K)
C_{sol}	Solution concentration (%)
d	Gap (mm)
d_h	Hydraulic diameter (m)
D	Gap between the last mirror in common tilting array and the first adjacent alternating mirror (mm)
f	Focal length (mm)
h	Specific enthalpy (kJ/kg)
h_{air}	Air side convective heat transfer coefficient (W/m^2K)
h_{fg}	Water condensation heat (J/kg)
$h_{m,air}$	Air side mass transfer coefficient (kg/m^2s)
$h_{m,sol}$	Solution side mass transfer coefficient (kg/m^2s)
h_{sol}	Solution side convective heat transfer coefficient (W/m^2K)
H	Height (m)
L	Length (m)
k	Thermal conductivity (W/m K)
K	Utilisation ratio
K_{pp_loss}	Pump proportional loss factor
m	Mass (kg)

$\dot{m}$	Mass flow rate (kg/s)
m_{float}	Flow meter float weight (kg)
$\dot{m}$ / $\dot{M}$	Mass flow rate (kg/s)
$\dot{M}_{\text{i}}$	Working fluid internal mass flow rate (kg/s)
$\dot{M}_{\text{leak}}$	Leakage mass flow (kg/s)
$\dot{M}_{\text{n}}$	Working fluid nominal mass flow rate (kg/s)
$\dot{M}_{\text{r}}$	Mass removal rate (g/s)
N	Rotational speed (rpm)
N_{m}	Total number of mirror elements
Nu	Nusselt number
n	Total number of experimental tests
P	Pressure (bar)
P_{a}	Atmospheric pressure (Pa)
P_{v}	Vapour pressure (Pa)
PR	Scroll expander pressure ratio
q	Heat transfer (W)
$\dot{Q}$	Heat transfer rate (W)
$\dot{Q}_{\text{amb}}$	Scroll expander ambient heat losses (W)
$\dot{Q}_{\text{cooling}}$	Cooling output (W)
$\dot{Q}_{\text{ev}}$	Heat input to the evaporator (W)
Q_{HR}	Thermal output of heat recovery unit (W)
$\dot{Q}_{\text{in}}$	Input heat (W)
Q_{th}	Thermal output (W)
$\dot{Q}_{\text{RE}}$	Regenerator thermal input power (W)

R_{in}	Scroll expander built-in volume ratio
Sh	Sherwood number
T	Temperature (K)
T_{loss}	Mechanical loss torque (N m)
T_{wb}	Wet bulb temperature (°C)
T_{w_f}	Hot water supply temperature (°C)
T_{w_r}	Hot water return temperature (°C)
U	Heat transfer coefficient (W/m^{2}K)
U_m	Mass transfer coefficient (kg/m^{2}s)
U_X	Measured variable uncertainty
U_Y	Calculated variable uncertainty
v	Specific volume (m^3/kg)
v_f	Working fluid velocity (m/s)
V	Volume (m^3)
$\overline{V}_{air}$	Average air velocity (m/s)
V_{float}	Flow meter float volume (m^3)
$\dot{V}_{i,ideal}$	Ideal volumetric flow rate at expander inlet state (m^3/s)
$\dot{V}_i$	Actual volumetric flow rate at expander inlet state (m^3/s)
W	Total solar field width of a CLFR system (mm)
W_{el}	Electric output (W)
$\dot{W}_i$	Internal shaft power (W)
$\dot{W}_{loss}$	Mechanical losses (W)
W_n	Width of a mirror element (mm)
W_p	Input power of liquid pump (W)

W_{sh}	Shaft power (W)
$\dot{W}_{shaft}$	Shaft power (W)
x_n	Centre reference position of a mirror element (mm)
X_i	Measured variable
X_{sol}	Solution mass fraction
Y	Calculated variable

Greek letters

α	Tilt angle of a mirror element (°)
β	Inclination angle of a receiver (°)
γ	Isentropic exponent
δ	Membrane thickness (m)
ε	Transfer effectiveness
ε_{DH}	Dehumidification effectiveness
ε_{EV}	Evaporative cooling effectiveness
η_{el}	Scroll expander electrical efficiency
η_{ex}	Scroll expander net efficiency
η_g	Generator efficiency
η_{is}	Scroll expander isentropic efficiency
η_m	Scroll expander mechanical efficiency
η_p	Pump efficiency
η_v	Scroll expander volumetric efficiency
ρ	Density (kg/m^3)
ω	Humidity ratio of air flow (kg/kg_{dryair})

Subscripts

ad	Adiabatic
air	Air
amb	Ambient
c	Central alternating mirror array of a CLFR-hybrid system
cd	Condenser
cf	Cold fluid
co	Mirror array of a CLFR-complete system
cooling	Cooling
crit	Critical
cw	Cold water
de	Liquid desiccant
e	Experimental
el	Electric
eq	Equilibrium condition
ev	Evaporator
ex	Exhaust
exp	Scroll expander
f	Working fluid
g	Generator
h	Hot fluid
heating	Heating
hw	Hot water

i	Internal
in	Inlet
is	Isentropic
l	Common tilting mirror array on the left side of a CLFR-hybrid system
leak	Leakage
loss	Loss
m	mass
max	Maximum
mem	Membrane
Min	Minimum
n	Nominal
net	Net
power	Power
pp	Pump
out	Outlet
overall	Overall
r	Common tilting mirror array on the right side of a CLFR-hybrid system
re	Recovered
s	Simulated
S	Saturation
sh	Shaft power
sol	Solution
su	Supply

sw	Swept
th	Thermal
tot	Total
v	Vapour
vo	Volumetric
w	Envelope
wf	water

Abbreviations

$CaCl_2$	Calcium chloride
CCHP	Combined cooling, heating and power
CHP	Combined heating and power
CLFR	Compact linear Fresnel reflector
COP	Coefficient of performance
CR	Geometrical concentration
DH	Dehumidifier
EV	Evaporative cooler
FS	Full scale
ICE	Internal combustion engine
LFR	Linear Fresnel reflector
LiBr	Lithium bromide
LiCl	Lithium chloride
MLDC	Membrane-based liquid desiccant cooling

NTU	Number of transfer units
ORC	Organic Rankine cycle
PTC	Parabolic trough collector
RD	Reading
RE	Regenerator
RH	Relative humidity
SOFC	Solid oxide fuel cell
STC	Solar tower concentrator

Chapter 1: Introduction

1.1 Research background

The expanding economies, increasing population and higher living standard are key drivers to the rising global energy demand, which lead to the progressive increasing energy shortage gap [1]. The past decades witnessed a remarkable rise in the global total primary energy consumption, as observed in Figure 1-1. Compared to the increase in the global total primary energy production, the total primary energy consumption has been growing much faster (e.g. rose by 60.83% from 1990 to 2015). It has been projected that the rate of increase in the world energy consumption between 2014 and 2035 would be approximately 34% [2].

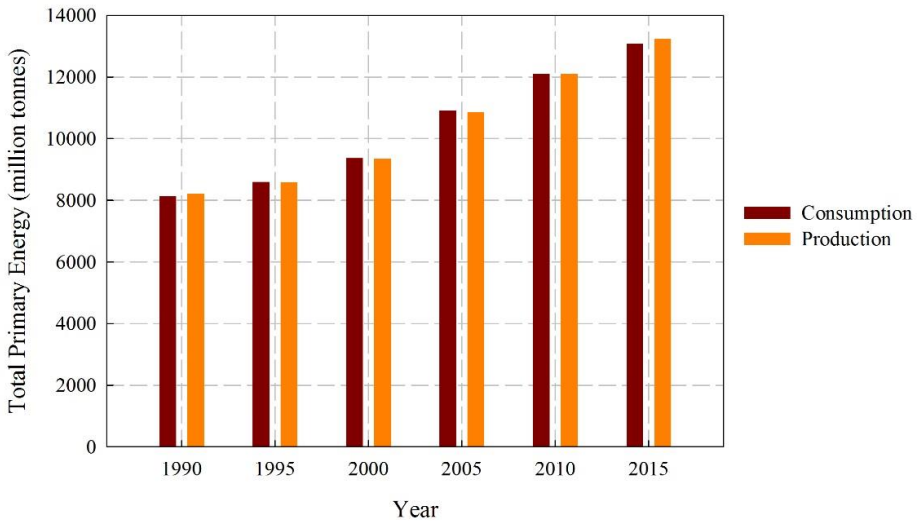


Figure 1-1 World total primary energy consumption and production from 1990 to 2015

In the current global situation, the global energy supply has heavy reliance on the finite fossil fuels [3], which has been dwindling significantly. Oil has been the dominant fuel representing 32.57% of the global energy consumption in 2015, and followed by coal (30.02%) and natural gas (23.71%) as indicated in Figure 1-2. Conversely, renewable sources only shared around 9.25% with main contributor hydroelectric accounting for

6.85%. In order to conserve conventional resources and avoid climate catastrophes, renewable energy resources such as solar, biomass, wind, geothermal and hydropower have proved to be more and more attractive for power generation with substantial reduction in the greenhouse gas emissions.

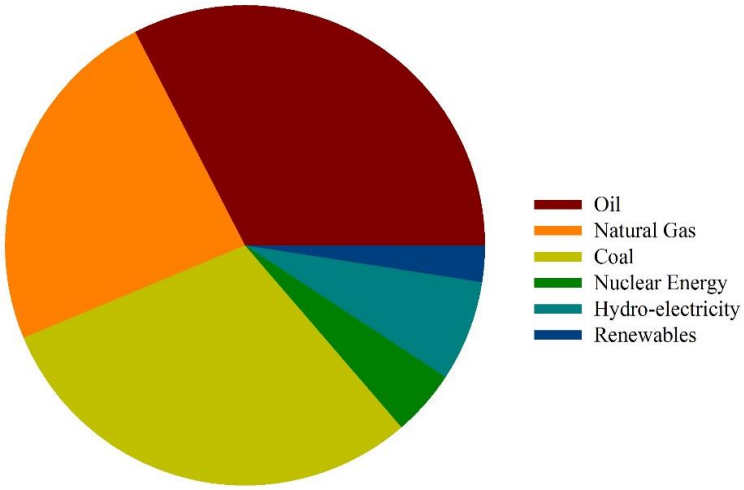


Figure 1-2 Global total primary energy consumption by fuel types

In terms of the energy consumption by sectors in the UK, approximately 40% of the total energy consumption are associated with buildings for electricity appliances, space conditioning, hot water supply etc. [4, 5]. Nevertheless, the energy demand of the building sector will continue to rise in the future [6]. Generally, the majority of households depend greatly on conventional centralized power stations or plants for electricity, heating and cooling. At present, the electricity and heating demands are usually met by the national power grid and burning fuels respectively in the UK. About 68% of the domestic energy consumption is represented by natural gas and the electricity consumption including renewable electricity accounts for the rest of 22%. Typically, the conventional power plant relies heavily on the fossil fuels and its overall system efficiency is less than 39% [7]. In other words, more than 60% of the energy is lost in the form of waste heat, together with considerable greenhouse gas emissions.

Even a minor improvement in power generation technologies, can bring out profound effect on the building energy performance and thereby the global energy consumption.

A cogeneration or combined heat and power (CHP) system is a critical solution to improve system energy efficiency and decrease greenhouse gas emissions [8], which allows productions of both heat and power from a single fuel source [9]. In recent years, extensive supportive mechanisms and policies have been introduced and implemented around the world to promote the CHP development. For instance, the European Commission has issued Directive 2004/8/EC to facilitate installations and operations of highly efficient cogeneration plants in European countries for energy conservation and combating global climate changes [10]. A number of European countries have consolidated the existing cogeneration installations and launched supportive mechanisms for new cogeneration schemes. For instance, the UK government has introduced Good Quality CHP schemes, which is certified to be highly efficient in line with Energy Efficiency Directive (2012/27/EU). Besides, the government has applied a practical method named CHP Quality Assurance (CHPQA) programme to monitor and assess CHP schemes throughout the UK. Figure 1-3 presents a map of the installed CHP systems in the UK and the vast majority have capacities ranging from 100kW_e to 1MW_e serving for the domestic sector. Nevertheless, only approximately 10.5% of the CHP systems run on the renewable fuels such as biomass, sewage gas, biogases, municipal waste and refuse derived fuel [6]. Under the circumstances spurred by government policies, there is still great potential in the development of renewable energy-driven CHP systems. On the other hand, the onsite effective micro power generation system has become a highly-anticipated alternative to the conventional centralised power generation system [11], owing to benefits in technical, environmental and economic aspects. For instance, a marked reduction of around £176

million in annual cost for energy production and mitigation of 2.1 million tons of CO_2 emissions have been achieved with installations of 1 million micro-CHP systems across the UK.

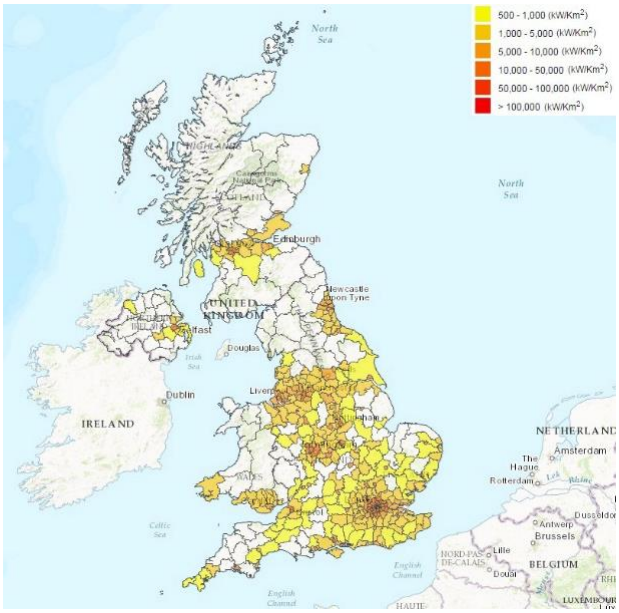


Figure 1-3 Map of installed CHP systems in the UK [6]

To address drawbacks of the CHP system in the hot and humid climate where cooling and air conditioning are demanded for the sake of indoor thermal comfort, the concept of trigeneration takes one step further by integrating thermally-activated cooling into a cogeneration system, which is also known as a combined cooling, heating and power (CCHP) system [12]. As the name implies, the trigeneration system has simultaneous production of three energies: electricity, heat and cooling. In operation, the thermal-activated equipment utilises waste heat from the prime mover for further air conditioning, refrigeration and other cooling purposes [13]. Compared with a cogeneration power plant, an increase of up to 50% in the system efficiency is attainable by a trigeneration system of the same size [14]. In particular, the micro-scale trigeneration system with a capacity less than $50kW_e$ has been emerging and more favourable in decentralized applications around the world, such as for residential

buildings, hotels, hospitals, university campus and automobiles [15]. The micro trigeneration system is capable of running on a variety of fuels, like diesel, natural gas, solar energy, hydrogen and biomass. Concentrated solar collectors can be a viable candidate of the primary energy source for the micro trigeneration system, for example Compact Linear Fresnel Reflectors (CLFR) efficiently convert the absorbed solar energy into useful thermal energy that can drive the prime mover for power generation. By integrating different fuel sources, prime movers, heat recovery and thermal-activated technologies, numerous types of the micro trigeneration system can be formed accordingly. One of the most promising prime movers of the micro trigeneration system is scroll-based organic Rankine cycle (ORC), which can be driven by low-grade heat sources to generate electricity effectively. It has been demonstrated in the existing literature that an inclusion of liquid desiccant cooling in a trigeneration system leads to a significant improvement to the total system efficiency [16]. Further, the membrane-based liquid desiccant cooling (MLDC) is attractive for an effective integration of the micro trigeneration system, which enables independent temperature and humidity controls to address both cooling and dehumidification demands and at the same time successfully eliminates the carryover problem of liquid desiccant droplets. In this thesis, a novel micro trigeneration system integrating scroll-based ORC and MLDC is developed and evaluated, which will be the first of its kind for building applications to deal with energy demands of electricity, heating, cooling and dehumidification.

On the whole, Chapter 1 is structured in the following sections: Section 1.1 briefly introduces the contextual research background; Section 1.2 presents the current research gap and rationale; Section 1.3 discusses the research aims and objectives in

detail; Section 1.4 emphases the research significance; Section 1.5 describes the research methodology and Section 1.6 provides the summary of the thesis structure.

1.2 Research overview

A distributed energy system is an energy-efficient solution for small scale and decentralized system close to energy consumers, which is available in diverse types offering end-users the potential for low-cost, reliable and high quality power [17]. The micro trigeneration system has been one of the most promising distributed energy systems, which can encompass a wide range of technologies. However, many researchers of the trigeneration system have focused on large and medium scale applications and limited demonstrations have been found regarding micro scale applications. The majority of available micro trigeneration systems are fuelled by natural gas; whereas renewable sources, like solar energy can be useful alternatives. Moreover, attention has been mostly devoted to combinations of mature technologies for the micro trigeneration system, such as diesel engine, micro gas engine, absorption and adsorption chillers, while the extensive literature searches have demonstrated that no research has been reported on such a micro trigeneration system integrating scroll-based ORC and MLDC. The main aim of this thesis is to design and evaluate the concept of micro trigeneration system combining scroll-based ORC and MLDC. In addition, for the sake of system sustainability, an idea of adopting CLFR as the primary energy source for the micro trigeneration system is considered.

Figure 1-4 depicts the design concept of the micro trigeneration system. Compared to the conventional separate power generation, the proposed multifunctional micro trigeneration system offers efficient onsite energy utilisation and meets electricity, heating and cooling/dehumidification demands. In the proposed micro trigeneration

system, the scroll-based ORC is the core of the system, providing electricity and heat. A commercially available micro-scale scroll expander is adopted instead of modifying from an existing compressor. Existing literature and demonstrations show that low-grade heat sources can be used to power the scroll-based ORC system, which thus indicates the feasibility of concentrated solar collectors (i.e. CLFR) for the energy supply. The thermal output from the scroll-based ORC will be utilised for hot water supply and driving the MLDC to meet dehumidification and cooling demands. In the MLDC, semi-permeable micro porous membranes are adopted in order to avoid liquid desiccant entrainment in the supply air stream and low cost calcium chloride desiccant solution is chosen for dehumidification. The desired supply air temperature can be attainable, as the dehumidified air exiting from the membrane-based dehumidifier will be further cooled by the cooler air stream from the evaporative cooler in the MLDC.

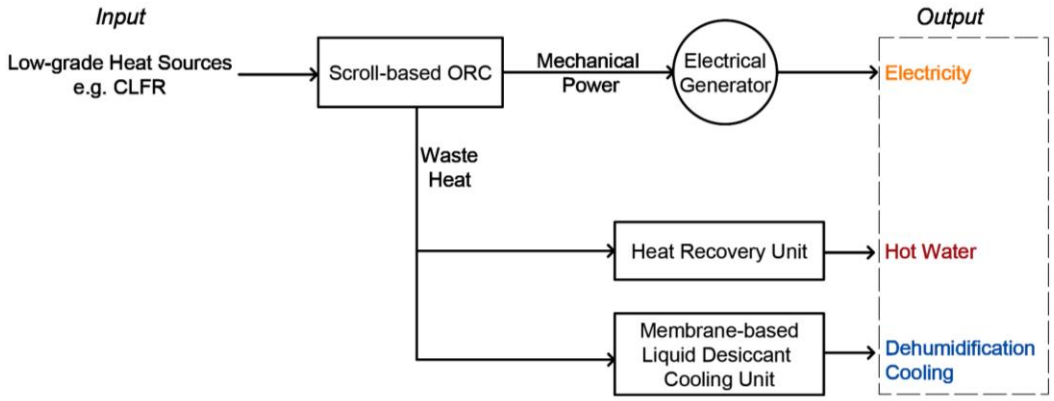


Figure 1-4 Design concept of the proposed micro trigeneration system

Furthermore, the technological foundations of scroll-based ORC and MLDC could be scalable; therefore the established system concept would be feasible for various building applications that demand simultaneous electricity, heating/hot water and dehumidification/cooling.

1.3 Research aim and objectives

The main aim of this thesis is to develop and evaluate a novel micro trigeneration system with integration of scroll-based ORC and MLDC. The research scope mainly covers system concept design, theoretical modelling, simulation program development, experimental testing, feasibility analysis and performance evaluation. Consequently, six objectives have been established to achieve the thesis aim:

1) Literature review and highlight the current gap in the existing literature of the micro trigeneration system, particularly for the combination of concentrating solar collectors, ORC and liquid desiccant cooling;
2) Numerical and experimental evaluation of CLFR under the local weather conditions and investigate the feasibility of integrating into the micro trigeneration system;
3) Performance evaluation based on simulation and experimental investigations of the scroll-based ORC system for an effective integration of the micro trigeneration system;
4) Performance evaluation based on experimental data of the MLDC system for effectively integrating into the micro trigeneration system;
5) Development of a comprehensive system model to demonstrate the feasibility of integrating scroll-based ORC and MLDC into the micro trigeneration system and to investigate effect of a wide range of operating variables on the system performance;
6) Recommendations for future work.

1.4 Research methodology

This thesis relies on numerical data obtained through both simulation and experimental testing to prove the feasibility of the proposed micro trigeneration system and conduct system performance assessment, thus the quantitative method is adopted. Generally, data sources are broadly classified into primary and secondary data [18]. Underpinned by positivism [19], this thesis analyses primary scientific data collected from theoretical modelling, computer simulation and experimental work. In terms of the validity and reliability, this thesis focuses on both theoretical and practical ways to analyse statistical data in depth. Moreover, the data produced from simulation and experiment is cross-validated.

Modelling is an efficient and cost-effective approach to represent a real-world system before building it physically. Through model simulation, the micro trigeneration system feasibility can be proved, how various components communicate with each other can be reflected, and the system performance under various operating conditions can be simulated correspondingly. In this thesis, the commercial simulation package MATLAB is selected as the main simulation program for the proposed micro trigeneration system. MATLAB has been regarded and proven as a valuable platform for programming, model development and simulation, with advantages of accessibility and flexibility. For simulation, sub-models of scroll-based ORC and MLDC will be developed and coded individually in MATLAB and a comprehensive trigeneration system model will be constructed by integrating sub-models.

1.5 Significance of research

Based on the findings of this thesis, benefits of the micro trigeneration system are demonstrated. The proposed integration of scroll-based ORC and MLDC for the

micro-scale trigeneration system will be the first of its kind, so that it would serve to progress the field of micro trigeneration for building applications and distributed energy systems. The thesis provides valuable information on the design and evaluation of the micro trigeneration system and the parametric studies presented in this thesis for CLFR, scroll-based ORC and MLDC can be employed for proposing and optimizing relevant individual systems. Therefore, this thesis not only contributes to new knowledge of the micro trigeneration system but also solar energy conversion, distributed power generation and air conditioning.

1.6 Thesis structure

The thesis is mainly organized to eight chapters to address the thesis aim and six objectives.

Chapter 1 provides the introduction to the thesis, by presenting the research background, rationale, current gap, aim and objectives as well as thesis structure. Chapter 2 is the in-depth systematic review of the existing literature in particular for the technologies of micro trigeneration, compact linear Fresnel reflector, organic Rankine cycle and membrane-based liquid desiccant cooling. In Chapter 2, the current research gap in the literature regarding the micro trigeneration system is highlighted.

Chapter 3 presents the detailed description of the designed micro trigeneration system. Chapter 4 provides theoretical and experimental analyses regarding the optical performance of CLFR and the feasibility of the CLFR system with flat mirrors and polar orientation acting as the energy supply source for the micro trigeneration system. Chapter 4 serves to progress the optical design of CLFR-hybrid system by producing a generalized methodology to optically design the CLFR system.

Chapter 5 presents the performance evaluation of scroll-based ORC based on both simulation and experimental results. The investigations prove the feasibility of the scroll-based ORC for efficient generation of electricity and heat, and provide contributions to the knowledge of simulating and testing the scroll-based ORC system. Chapter 6 presents a detailed performance evaluation of the MLDC system on a basis of experimental work, which contributes to knowledge of the comprehensive testing of a liquid desiccant cooling system under a wide range of operating conditions. Both Chapter 5 and Chapter 6 provide a benchmark of performance and facilitate an effective integration of scroll-based ORC and MLDC into the micro trigeneration system in Chapter 7.

In Chapter 7, a detailed performance assessment of the micro trigeneration system with scroll-based ORC and MLDC is conducted through simulation. Finally, Chapter 8 concludes the thesis with major findings as well as recommendations for future work.

Chapter 2: Literature review

2.1 Introduction

This chapter presents a comprehensive literature review on technologies relating to the proposed micro trigeneration system. As the proposed micro trigeneration system involves diverse technologies, extensive literature is reviewed critically covering the following key topics:

1) Micro trigeneration in Section 2.2;
2) Concentrating solar collectors in Section 2.3, in particular CLFR;
3) Heat recovery in Section 2.4;
4) Prime mover in Section 2.5, in particular scroll-based ORC;
5) Thermal-activated cooling in Section 2.6, in particular liquid desiccant air conditioning and MLDC;
6) Operating strategy in Section 2.7;
7) Current researches on micro trigeneration in Section 2.8

The aims of the literature review are: (a) to identify the current research gap regarding the micro trigeneration system integrated with scroll-based ORC and MLDC; (b) to demonstrate the feasibility of such a system and combining CLFR; and (c) to provide a detailed and comprehensive background research on the state of the art of the related technologies. To implement the aims, considerable literature from a variety of disciplines are selected rigorously and existing micro trigeneration systems are reviewed from various perspectives, for example the system design, operation, performance and assessment method. A brief summary of the literature review is presented in Section 2.9 together with specific considerations on the proposed micro trigeneration system.

2.2 Micro trigeneration system

Firstly, the literature review begins with an introduction to the micro trigeneration system concept and applications. The advantages and limitations of the micro trigeneration system are discussed as well in this section.

2.2.1 Concept

The emergence of decentralized energy resources has brought numerous novel and advanced designs of efficient power generation systems with utilisation of renewable energy for locally provided, sustainable and cost-effective energy production, for instance cogeneration, trigeneration and on-site renewable energy systems [20]. By coupling a thermally-activated equipment to utilise seasonal excess heat for cooling purpose, the trigeneration system has become a more economical and environmental alternative to the conventional refrigeration and cogeneration-only systems, especially in the hot and humid climate [21]. In general, trigeneration systems can be classified to a topping or a bottoming cycle in terms of the energy sequence [22]. In the topping cycle, the supplied fuel is firstly utilised for power generation and then thermal energy, while in the bottoming cycle, heat production is the priority and the rejected heat is recovered for power generation. Commonly, the topping cycle is widely adopted for the trigeneration system, while the bottoming cycle is selected for applications like cement, steel and ceramic industries [23]. Depending on the capacity of power generation, the trigeneration system can be categorized into: large-scale (i.e. from $10MW_e$ up to hundreds of MW_e), medium-scale (i.e. 1-$10MW_e$), small-scale (i.e. $60kW_e$ to $1MW_e$) and micro-scale (i.e. less than $50kW_e$) [4, 8].

Generally, a micro trigeneration system consists of a prime mover with a coupled generator, a heat recovery unit and a thermal-activated component [20], as illustrated

in Figure 2-1. In principle, waste heat from the prime mover, in forms of exhaust gases, lubrication oil or jacket water will be exploited partially or fully to meet heating demand by a heat recovery unit and cooling demand by a thermal-activated cooling unit [24]. Diverse micro trigeneration configurations can be proposed by combining different supply energy sources, prime movers, heat recovery and thermal-activated components, and the system efficiency is largely dependent on the component performance and the integration method in the trigeneration system.

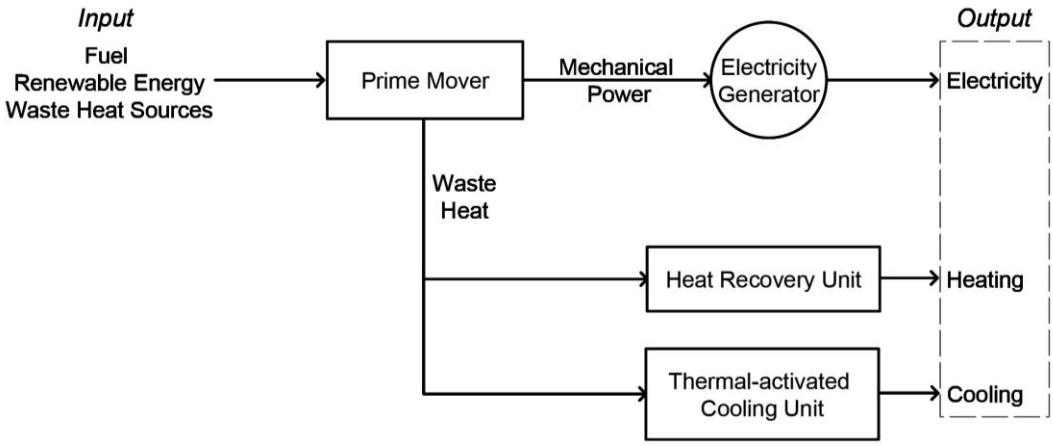


Figure 2-1 Concept diagram of trigeneration system

2.2.2 Applications

With promotions and developments of the trigeneration system around the world, a wide variety of trigeneration systems have been adopted for industrial, commercial and residential applications [25-34]. More precisely, the micro trigeneration system has been emerging for applications such as domestic and office buildings [35-40], restaurant [41], hotel [42], supermarket [43], hospital [44] and university campus [45].

2.2.3 Advantages

Advantages of the micro trigeneration system are summarised as follows from technical, environmental and economic aspects [4, 5, 8, 20, 25, 45-47]:

- Flexibility in integration of various technologies for power generation, heating and cooling purposes;
- Capability of running on diverse fuels, especially renewable energy sources;
- Summer operational hours for regions with requirements of both cooling and dehumidification;
- Significant reduction in the primary energy consumption, thermal loss and greenhouse gas emission;
- High reliability and efficiency in productions of onsite electricity and thermal energy;
- Energy reliability for power backup wherever or whenever grid power is cut;
- Reduction in overload and blackout of the electrical system;
- Greater flexibility in transmission and distribution planning;
- Economic benefits with reduction in fuel, operation and lifecycle costs and investment in infrastructure with a short payback period;
- Potential revenue stream by selling excess electricity.

2.2.4 Limitations

Compared to the traditional separate power generation and cogeneration systems, there are some limitations of the micro trigeneration system in tandem with merits. Firstly, highly variable and unpredictable energy demands of the building sector lead to technological limits in system sizing and complicated operating strategy [48, 49], and thus a detailed evaluation of the energy demand profile over a long time period is essential [21]. For instance, Chung, et al. [50] estimated the building energy demands of electricity, heating, cooling and hot water using developed load models based on direct measurements and statistical surveys in order to size the trigeneration-based

community energy system for a residential building in Korea. Secondly, the prime mover may require extensive maintenance with costs that are up to about 30% of the profits earned from the system electricity production [36]. Moreover, regarding to the associated regulation and policy framework, either the cogeneration or trigeneration system has not been acknowledged in many countries and the grid connected energy exchange is not yet allowed or regulated [15].

Section 2.2 has provided a review-based introduction of the micro trigeneration system regarding its concept, working principle, applications, advantages and limitations. Next the technologies of the micro trigeneration system are reviewed and in the Section 2.3, the concentrating solar collector technology that can be the primary energy source in the micro trigeneration system is reviewed on the basis of the existing literature.

2.3 Concentrating solar collectors

The literature review presented in this section focuses on the concentrating solar collector technology, in particular linear Fresnel reflector (LFR) and CLFR. Solar energy is regarded as the largest available carbon-neutral energy on the planet, offering great potentials for utilisation by various technologies [51] and the micro trigeneration system can be one of the options. The solar-assisted micro trigeneration system has attracted rising interest with lower environmental impact and costs. The solar-assisted micro trigeneration system is suitable for locations with good solar radiation level and demands for electricity, cooling and/or heating. Immovilli, et al. [36] stated that solar collectors are better candidates for the solar-assisted trigeneration system than photovoltaic panels in terms of electrical, cooling conversion and costs effectiveness. Generally, solar collectors are categorized into non-concentrating and concentrating

types. Non-concentrating solar collectors are commonly used in domestic hot water heating systems, whereas concentrating solar collectors have been proved to be reliable with higher efficiency at medium to high operational temperatures [52], which are feasible for the primary energy source in the micro trigeneration system. Concentrating solar collectors have been investigated for several decades with numerous published studies and successful demonstrations producing significant annual amounts of electricity under real operating conditions, especially for locations receiving high beam solar radiation. However, to date limited studies have been documented on the utilisation of the concentrating solar collectors as the primary energy source in the micro trigeneration system.

2.3.1 Linear Fresnel reflector

On the basis of the focus geometry, concentrating solar collectors are classified into parabolic tough concentrator (PTC), solar tower concentrator (STC), parabolic dish and linear Fresnel reflector (LFR). Though PTC is a more mature and widely applied technology, its higher initial cost, complex manufacturing process and serious challenge of wind resistance are noted [53]. Alternatively, the LFR system in a simple design is capable of harnessing the solar radiation efficiently with less land usage [54]. It has been proved to be a better choice for energy production where land availability is limited [55]. Figure 2-2 presents a schematic diagram illustrating the LFR system with a single centred receiver. Each mirror element is suitably placed at a proposed tilt angle to ensure the incident solar radiation converges onto the receiver after reflection.

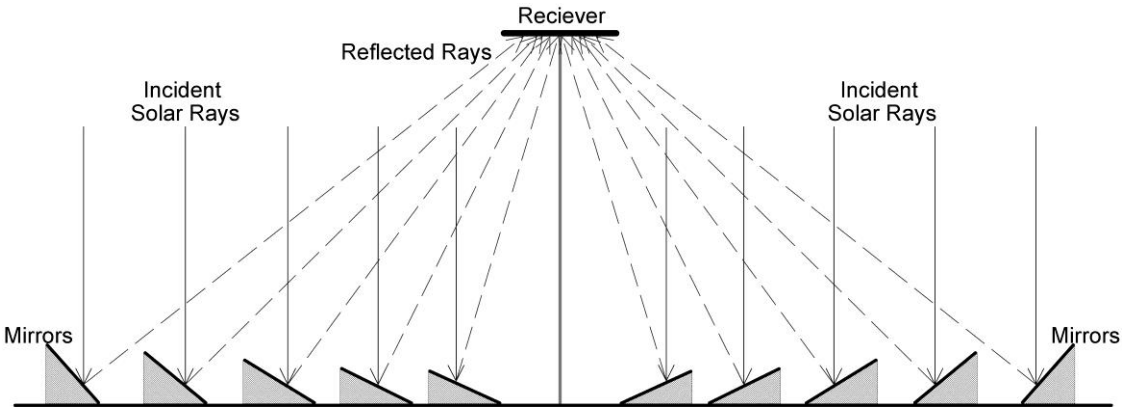


Figure 2-2 Schematic diagram of LFR system

Optical designs of the LFR system have been investigated from different perspectives, such as solar field layout and orientation, tracking algorithm and aiming strategy, reflector curvature and receiver configuration [56]. Comparatively, the solar field orientation plays a predominant role. For instance, the complexity of a tracking mechanism varies with the orientation. In general, three orientations are commonly adopted, namely north-south, east-west and polar. Both north-south and east-west orientations are mostly preferred for applications, with which tracking schemes are based on the flat ground. In operation, reflectors follow the sun movement by varying their tilt angles under the control of a tracking system [57]. However, end or lateral losses occur when the reflected solar rays do not impinge on the receiver due to the longitudinal component of the solar radiation [58, 59]. On the other hand, mirrors involved in the LFR system are commonly predefined with constant widths and shifts for the sake of simplicity. Such a simple optical design results in shading of the incoming solar radiation and blocking of the reflected solar radiation by adjacent mirror elements [60]. Graphs in Figure 2-3 depict cosine, end, shading and blocking effect of LFR system, which have been redrawn with reference to the literature [58, 61, 62] . As a consequence, numerous studies have been conducted to minimize energy losses owing to the end, inter-row shading and blocking effect. For example, optical

variables such as the width and position of each mirror element, gap between consecutive mirrors and receiver height have been considered in the literature [58, 59, 63, 64]. Abbas and Martínez-Val [64] observed an evident increase in the annual energy efficiency for a LFR system with mirrors of variable widths and shifts, but more complicated optical modelling and additional installation cost are required accordingly. In addition, the receiver also has a remarkable impact on optical and thermal performance of the LFR system, which can be assembled horizontally, vertically or in triangular configuration [65]. To address the drawbacks of shading and blocking of the LFR system, Barlev, et al. [51] suggested increasing the receiver height, but the spacing between two adjacent mirror elements causes more ground usage and investment on the receiver tower.

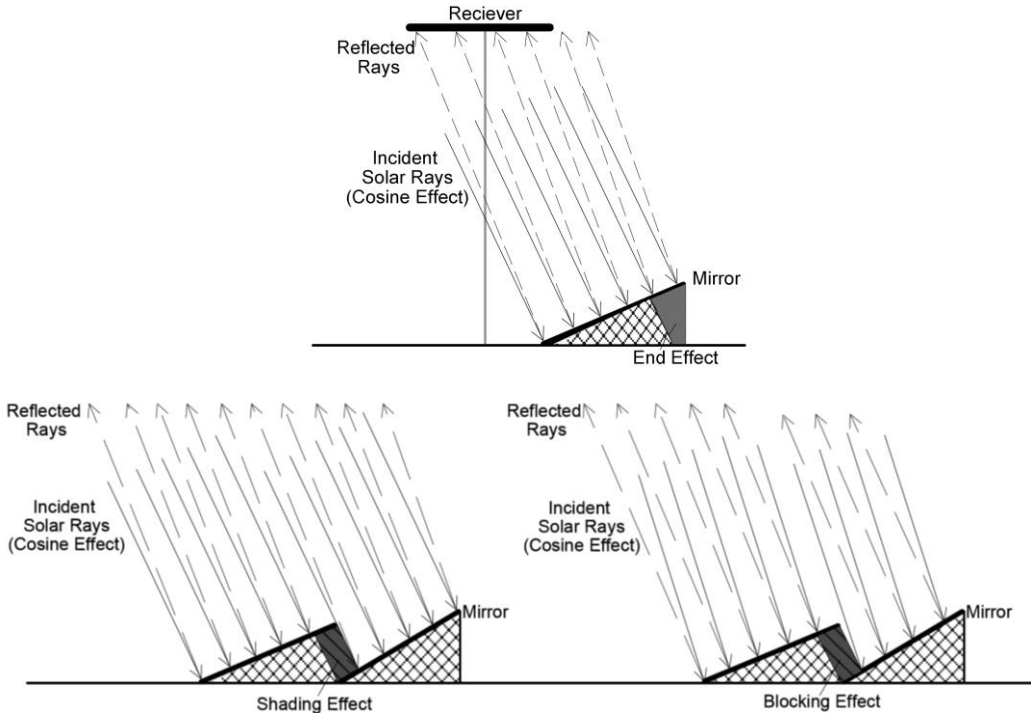


Figure 2-3 Cosine, end, shading and blocking effect in LFR system

The LFR system with polar orientation is more efficient with the simplest tracking system and the absorbed solar energy can be maximized while energy losses are minimized [66]. To ensure the solar field perpendicular to the solar rays throughout

the day, various designs of the solar tracker has been proposed to follow the sun movement in both elevation and azimuth directions, while reflectors and receiver are fixed at predefined tilt angles and positions [67, 68]. In such a way, more structural considerations should be taken into account, especially for large scale applications due to variable inclination angles of the entire solar field.

2.3.2 Compact linear Fresnel reflector

Alternatively, an innovative concept of CLFR system with multiple receivers is developed to minimize energy losses as shown in Figure 2-4. Different from the LFR system, one receiver is installed at each side of the solar field, allowing consecutive mirrors to reflect the sunlight onto the two respective receivers. The CLFR system has better system cost effectiveness [69] and is promising for applications with limited ground availability [51].

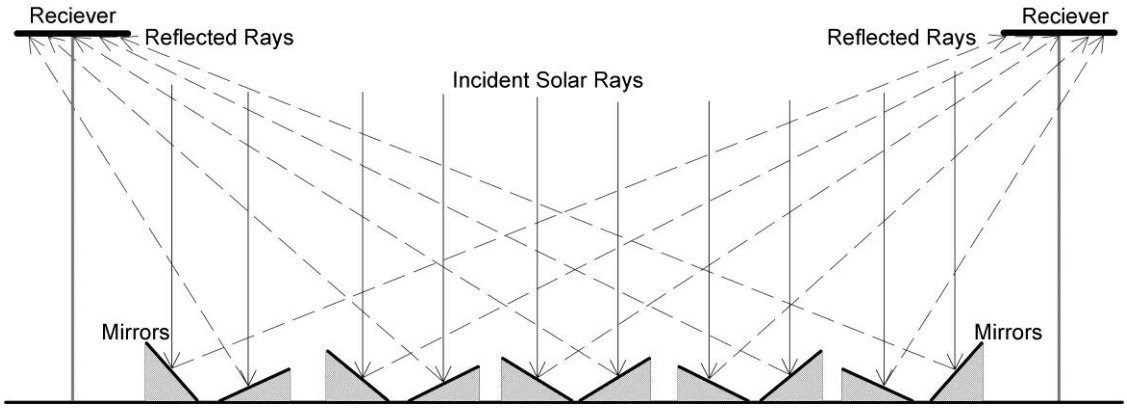
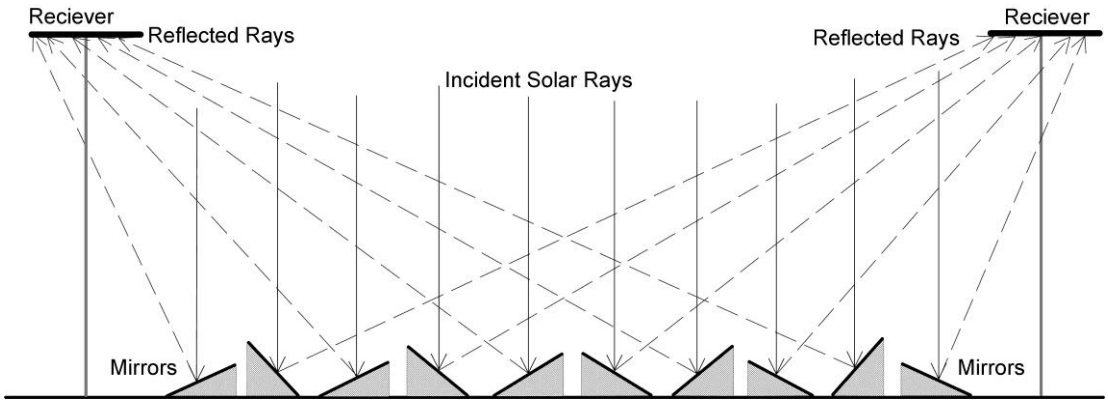


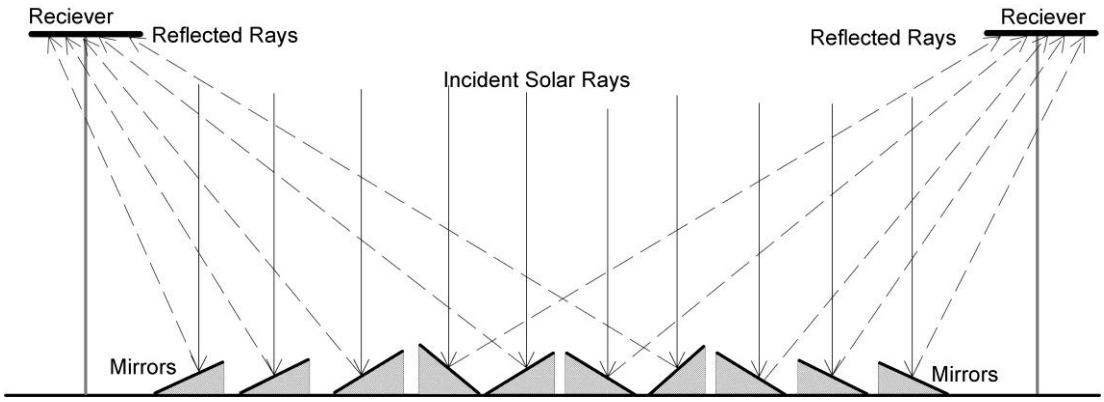
Figure 2-4 Schematic diagram of CLFR system

Nonetheless, the CLFR system has not been widely investigated with a few available demonstrations. Mills and Morrison [70] evaluated the CLFR concept applied for a large-scale solar thermal electricity generation plant from various aspects, including the receiver orientation and structure, mirror field configuration and packing density. Chaves and Collares-Pereira [71] assessed variable mirror sizes and shapes for the

CLFR system. Additionally, Montes, et al. [69] proposed two different CLFR configurations and Figure 2-5 presents graphs of the two CLFR configurations which have been reproduced based on their classification. Mirrors are arranged with alternating tilts for pointing to one or the other receiver in the CLFR-complete configuration, while only mirrors located in the central solar field alternate their tilts in the CLFR-hybrid configuration. They observed that both CLFR configurations successfully minimize the blocking and shading losses, whereas lateral losses decrease the optical efficiency due to the great dispersion of reflected rays from mirrors located far from the receivers. The majority of investigations in the existing literature have been conducted for the CLFR system with north-south and east-west orientations, while the polar orientated CLFR system has not received attention much.



(a)



(b)

Figure 2-5 Schematic diagrams of CLFR configurations (a) complete (b) hybrid

In terms of the optical performance evaluation for the LFR and CLFR systems, studies have been mainly conducted through numerical modelling [57, 58, 72-75], ray tracing simulation [59, 64, 76-78] and experimental data [79-82]. For instance, Barale, et al. [56] adopted a generalized methodology to optimise the geometry for a LFR prototype built in Sicily, including optical modelling with ray tracing techniques and analyses of mirror and receiver geometries. Pino, et al. [80] simulated a LFR solar plant using optical and thermodynamic modelling, which was validated with operating data gathered from a supervisor system. Nevertheless, studies in the optical design and performance evaluation of the CLFR system through simulation and experiments are still limited. Furthermore, few studies have been reported in terms of the applications of LFR and CLFR in power generation systems. Xu, et al. [75] theoretically evaluated a direct vapour generation supercritical ORC system driven by LFR. Based on the simulation results, the proposed hybrid system has better performance compared with conventional subcritical ORC system. Mokheimer, et al. [83] proved the technical and economic feasibility of integrating LFR with a cogeneration gas turbine system of 50MW in Saudi Arabia.

Section 2.3 has presented a detailed literature review of the LFR and CLFR systems. Until now, limited demonstrations of the LFR and CLFR systems are available for power generation systems and the feasibility of CLFR applied to the small and micro trigeneration systems has rarely been investigated. Next, a technical review based on the existing literature is presented regarding prime mover of the micro trigeneration system in Section 2.4.

2.4 Prime movers

In the micro trigeneration system, a prime mover functions as the core power generation component to produce mechanical power to drive an electrical generator for electricity output. A review of the literature on available prime movers for the micro trigeneration system is presented in this section, and the scroll-based ORC technology is discussed specifically for the micro trigeneration system.

2.4.1 Comparisons of available prime movers

Generally, there are two main categories of the prime mover, namely combustion-based (e.g. Stirling engine, reciprocating engine, gas turbine and Rankine cycle) and electrochemical-based (e.g. fuel cells) [84]. Table 2-1 lists all available prime movers with their characteristics and Table 2-2 provides a summary of their advantages and drawbacks based on a comprehensive literature review. Compared to the mature and proven technologies such as internal combustion engine (ICE), steam and gas engines, fuel cells, Rankine cycle and Stirling engines are still in the phase of research and development due to their high costs and limited adaptabilities [5]. In terms of applications, combustion and steam turbines are the most common prime movers for large-scale power plants, while micro turbine, Stirling engine and Rankine cycle are promising for medium, small and micro-scale power generation systems [85]. More specifically, interests in the micro trigeneration system employing the micro turbine, fuel cells, Stirling engine and Rankine cycle become more and more attractive recently, especially for domestic applications [86]. Comparatively, the Stirling engine requires more investment and high-quality heat input; fuel cells with a more complex design have shorter lifetime and the micro turbine with low electrical efficiency is not economically feasible; the Rankine cycle is more favourable for the micro trigeneration system owing to its simplicity, durability, technical flexibility, cost

effectiveness, low emission and acceptable electrical efficiency [8, 87]. In particular, by employing an organic type of working fluid (e.g. refrigerant) in the Rankine cycle, organic Rankine cycle (ORC) has been considered as a promising solution to harness low-grade energy sources for small and micro scale power generation.

The prime mover of the micro trigeneration system is required to be compact, cost effective and easy to install [88]. Basically, the selection of a prime mover depends on a variety of factors, for example climate, energy resource, end-user's energy and thermal demands, availability, cost, capability for electricity or thermal storage, operating strategy and excess electricity sellback [23, 37, 89, 90]. As a result, various selection methods have been proposed depending on different criteria. For instance, Khorasaninejad, et al. [91] summarised four main criteria in the decision-making process of prime mover selection, which are technological, economic, environmental and social aspects. Ebrahimi and Keshavarz [37] developed a multi-criteria function to obtain the optimum size and operating strategy for the prime mover applied to a residential micro trigeneration system in different climate regions. Roman and Alvey [89] introduced a selection method considering economic, energy consumption and emissions criteria, while Sanaye, et al. [90] adopted a different approach by taking into account the end user's electrical and heating loads.

Table 2-1 Characteristics of available prime movers for trigeneration system [4, 5, 8, 15, 20, 24, 47, 85, 87, 91-93]

	Internal combustion engine	**Steam turbine**	**Gas turbine**	**Micro turbine**	**Stirling engine**	**Fuel cell**	**Rankine cycle**	**Photovoltaic thermal system**
Availability	92-98%	Near 100%	90-98%	90-98%	82-90%	>95%	-	-
Fuel type	Natural gas, biogas, biodiesel, propane, landfill gas	All	Natural gas, biogas, propane, distillate oil	Natural gas, biogas, hydrogen, propane, distillate oil	All (e.g. gasoline, alcohol, natural gas, butane and renewable sources)	Hydrogen, natural gas, propane, methanol	Any fuel including natural gas and biofuels	Solar energy
Fuel pressure	7-310 kPa	-	689-3447 kPa	345-689 kPa	>14 kPa	3.4-310 kPa	-	-
Capacity	0.01-75 MW	0.05-500 MW	0.05-300 MW	0.025-1 MW	0.001-1.5 MW	0.005-2 MW	0.001-250 MW	-
Heat input/ combustion	External	External	External	External	External	Electrochemical	External	Solar
Start up	>=10 sec	1 hr-1 day	10 min-1 hr	60 sec	Easy	3 hrs-2 days	>1 hr	-
Hours between overhauls	25000-60000	>50000	30000-50000	5000-40000	-	10000-40000	-	-
Electrical efficiency	25-45%	5-40+%	18-40%	15-30%	58	30-70%	10-38%	0.6-11%
Thermal efficiency	60-80%	75-77%	50-70%	50-70%	75%	55-80%	-	-
Overall efficiency	50-80%	Near 80%	65-75%	55-80%	60-95%	55-90%	65-85%	90%

	Internal combustion engine	**Steam turbine**	**Gas turbine**	**Micro turbine**	**Stirling engine**	**Fuel cell**	**Rankine cycle**	**Photovoltaic thermal system**
Power density	35-50 kW/m^2	>100 kW/m^2	20-500 kW/m^2	5-70 kW/m^2	-	5-20 kW/m^2	-	-
Power to heat ratio	0.4-1	0.1-0.3	0.5-2	0.3-0.7	0.2-1.7	1-2	0.15-4	-
Partial load	OK	OK	Poor	OK	OK	Good	OK	OK
Respond to load changes	Fast	Fast	Fast	Fast	Low	Fast	Fast	
Thermal output	3376-5908 kJ/kWh	1055-52753 kJ/kWh	3376-7174 kJ/kWh	4748-6858 kJ/kWh	-	1900-4431 kJ/kWh	1065-52753 kJ/kWh	-
Exhaust heat temperature	38-200°C	<540°C	120-482°C	<320°C	<280°C	<1000°C	<100°C	<60°C
Uses for heat recovery	Hot water, LP steam	LP-HP steam, district heating	Direct heat, hot water, LP-HP steam, district heating	Direct heat, hot water, LP steam	Direct heat, hot water, LP steam	Hot water, LP-HP steam	Hot water, LP steam	Hot water
Noise level	High	Moderate to high	Moderate	Moderate	Moderate	Low	Moderate	Low
Noise protection	Building enclosure	Building enclosure	Enclosure supplied with unit	Enclosure supplied with unit	Enclosure supplied with unit	None	Enclosure supplied with unit	None

	Internal combustion engine	Steam turbine	Gas turbine	Micro turbine	Stirling engine	Fuel cell	Rankine cycle	Photovoltaic thermal system
CO_2 emissions	504-651 kg/MWh	-	580-720 kg/MWh	725 kg/MWh	673 kg/MWh	430-490 kg/MWh	Fuel-dependent	-
NO_x emissions	0.23-9.9 kg/MWh	0.18-0.91 kg/MWh	0.1-0.5 kg/MWh	0.18 kg/MWh	0.23 kg/MWh	<0.02 kg/MWh	Fuel-dependent	-
Footprint	0.062-0.47 sqft/kW_e	<0.1 sqft/kW_e	0.02-0.61 sqft/kW_e	0.15-1.5 sqft/kW_e	3-6.5 sqft/kW_e	0.6-4 sqft/kW_e	<0.1 sqft/kW_e	-
Investment	340-1600 \$/kW_e	-	450-1500 \$/kW_e	900-1400 \$/kW_e	1300-2000 \$/kW_e	2500-3500 \$/kW_e	1000-2000\$/kW_e	6000 \$/kW_e
Installation cost	1100-2200 \$/kW_e	800-1000 \$/kW_e	700-900 \$/kW_e	500-1300 \$/kW_e	1300 \$/kW_e	>3000 \$/kW_e	-	-
Operation & maintenance costs	0.009-0.022 \$/kWh	0.004 \$/kWh	0.002-0.008 \$/kWh	0.002-0.01 \$/kWh	-	0.003-0.015 \$/kWh	-	-
Turnkey costs	350-1000 \$/kW	-	650-900 \$/kW	600-1100 \$/kW	-	1900-3500 \$/kW	-	-
Lifetime	175200 hrs	>219000 hrs	5000-40000 hrs	87600 hrs	10000-30000 hrs	10000-65000 hrs	30000-5000 hrs	-

	Internal combustion engine	**Steam turbine**	**Gas turbine**	**Micro turbine**	**Stirling engine**	**Fuel cell**	**Rankine cycle**	**Photovoltaic thermal system**
Sub-categories	- Spark ignition engines with natural gas, biogas or landfill gas - Compression ignition engines with diesel fuel or other petroleum products	- Backpressure turbines (i.e. exhaust pressure at least equal to at atmospheric pressure) - Condensing turbines (i.e. exhaust pressure lower than atmospheric pressure)	-Open cycle and closed cycle - For example: micro turbines, jet engines, turboprop engines, industrial gas turbines for power generation, turboshaft engines, radial gas turbines	- Unrecuperated (or simple cycle) micro-turbines - Recuperated micro-turbines	- Kinematic Stirling - Free-piston Stirling	- Proton exchange membrane fuel cell (PEMFC) - Alkaline fuel cell (AFC) - Phosphoric acid fuel cell (PAFC) - Molten carbonate fuel cell (MCFC) - Solid oxide fuel cell (SOFC)	- Steam Rankine systems with water as working fluid - Organic Rankine system using organic working fluid	-PVT/air, PVT/ water and PVT concentrated collector

Table 2-2 Advantages and disadvantages of available primary movers for trigeneration system [4, 5, 8, 15, 20, 24, 47, 85, 87, 91-93]

Type	Features
Internal combustion engine	Mature and proven technology Most commonly installation for power generation under 1MW High efficiency at partial load operation High reliability with utilisations of flexible power sources and different energy applications Easy incorporation with different cooling technologies Lower initial capital costs Good operating reliability with fast start-up capability Good response to load fluctuations
	Relatively high vibration requiring shock absorption High noise level requiring shielding measures A large number of moving parts High nitrogen oxides emissions requiring emission control option Insufficient available waste heat temperature for higher capacity cooling purpose Necessity of engine cooling and regular maintenance High maintenance cost Complex design

Type	Features
Steam turbine	Mature applications for large central plant utilities or industrial cogenerations Equipped with a suitable boiler can be run on any kind of fuel Reliable for long lifetime Steam extraction at desired pressure and temperature High overall efficiency Flexibility in heat and power ratios
	Low electrical efficiency Slow start-up time Poor partial load performance Bulky construction High initial investment Required for high enthalpy steam for operation Inapposite for small-scale power plant

Type	Features
Gas turbine	Commercially mature technology with wide availability in the market Light, compact and flexible design requiring low maintenance level Fast manufacture and installation Moderate heat output temperature with no cooling water requirement Fast response with load variation Low nitrogen oxides emission Low initial cost and investment
	Requirement of high quality fuel input Inefficient part load performance Low electrical efficiency and inflexibility to load profile change Sensitivity of efficiency to changes in ambient conditions Unsuitable for intermittent use and frequent start/stop applications High operation and maintenance costs High noise level Short lifetime

Type	Features
Micro turbine	Only one moving part Low maintenance and operating costs Low combustion temperature with lower nitrogen oxides emissions Low noise level High thermal/ electrical load ratio High exhaust heat temperature for further heat recovery High rotational speed Suitable for distributed energy systems
	Requirement of high pressure gas Unable to operate under large load Low flexibility to load variation Short track record High capital cost with relatively short lifetime Relative low electrical efficiency Sensitivity of efficiency to changes in ambient condition (e.g. temperature and pressure)

Type	Features
Stirling engine	Low emission, noise and vibration levels Efficient with few moving parts Suitable for small scale applications, such as residential or portable applications (1-25kW). Utilisation of low grade waste heat and renewable energy sources Easily controllable combustion Independency of electricity and heat productions Low maintenance and long lifetime
	New technology still in development High investment cost Limited availability Low electrical efficiency at high cost Long start-up time Short durability of certain parts Limited adaptability for variable output

Type	Features
Fuel cell	Quiet, reliable, compact power generator without moving parts High electrical efficiency under variable load condition Low emission Suitable for transport sector High heat exhaust temperature A good match with residential thermal to power ratio Constant power production Flexibility in fuel selection
	High initial cost with short lifetime Still in research and development stage Complex design with few available commercial applications Requirement of efficient hydrogen storage Limited availability Corrosion of liquid electrolytes Sensitivity to contaminant in fuel (e.g. sulphur and chlorides)

Type	Features
Rankine cycle	High flexibility and simple design Durability and cost effectiveness Low operational pressure and temperature with high levels of safety and simplicity Flexibility in fuels utilisation Possibility to run on renewable energy sources Utilisation of low-grade waste heat and renewable energy sources
	Relative lower electrical efficiency Less expensive Still in research and development stage Limited availability
Photovoltaic thermal system	No emissions Simultaneously production of heat and power
	High capital cost

Instead of involving a single prime mover in the micro trigeneration system, more than one prime movers are feasible for incorporation in the trigeneration system [94, 95]. For example, Tse, et al. [96] proved the feasibility of a micro trigeneration system combining both solid oxide fuel cells (SOFC) and a gas turbine for marine applications, while Ozcan and Dincer [97] observed the overall energy efficiency of a trigeneration system increases by 52.5% as a solar-driven ORC unit is combined with the original single prime mover of SOFC.

2.4.2 Organic Rankine cycle

Unlike traditional power cycles, ORC is adequate for applications of small and micro scale power generation systems with high flexibility and low maintenance requirements [98]. Organic working fluids are typically characterized by low saturation temperature and pressure, which contribute to extracting low-temperature heat [99]. In general, possible low-grade energy sources utilised by the ORC system include geothermal resource, ocean thermal, solar energy, biomass combustion, exhaust gases of gas turbines and waste heat from power plants, industrial and agricultural processes [100, 101]. For instance, Li, et al. [102] designed a low-temperature power generation system involving ORC and compound parabolic concentrators, which is capable of producing around 87.1kWh/m^2 electricity per year in China and Masheiti, et al. [103] demonstrated the feasibility of harnessing the low-temperature geothermal source for an ORC system in Libya. In terms of applications, most of the ORC demonstrations are designed to efficiently recover industrial waste heat for power generation, which has been investigated in studies [104-109]. Besides, researchers have also proposed solar-powered ORC for desalination purposes as examples presented in the literature [110, 111].

An organic working fluid is typically characterized by a saturated vapour line with positive slope in the Temperature-Entropy (*T*-*s*) diagram, which guarantees the working fluid at the superheated vapour state in the expansion process [112]. Generally, working fluids can be classified into: dry fluids with high molecular number (e.g. n-pentane, benzene, toluene and R113), wet fluids with low molecular number (e.g. water and ammonia) and isentropic fluids (e.g. trichlorofluoromethane, dichlorodifluoromethane, R11 and R12) [104, 113]. The working fluid plays a vital role in the ORC system, as its thermodynamic properties greatly influence the system capital cost, efficiency, irreversibility and operating conditions as well as environment [104]. However, the selection of working fluid is quite complicated because: (a) the working condition and heat source vary widely from low-temperature (e.g. geothermal and solar collectors) to high-temperature heat sources (e.g. biomass) and (b) numerous working fluid candidates are available (e.g. hydrocarbon, aromatic hydrocarbon, ether, perfluorocarbon, CFC, alcohol and siloxane) [114]. An ideal working fluid of the ORC system should be featured with: high molecular weight, low specific volume, heat latency and enthalpy, high critical pressure and temperature, moderate pressure in the heat exchanger to avoid negative impact on the system reliability, high efficiency, low cost, non-flammable, non-corrosive, non-toxic, low Ozone Depletion Potential (ODP) and low Global Warming Potential (GWP) [103]. Declaye, et al. [115] concluded that R134a is a good choice for the small-scale ORC system. Similarly, Tchanche, et al. [116] considered R134a as the most suitable working fluid for small-scale power generation applications in terms of thermodynamic and environmental properties.

To improve the ORC system performance, different regenerative configurations have been developed by researchers. The concept of turbine bleeding to the ORC system allows a small portion of the working fluid extracted from the turbine to mix with the

working fluid before entering the evaporator [113]. In this way, the thermodynamic efficiency of the ORC system can be improved as the mean temperature of heat addition increases. By employing the First and Second Laws of Thermodynamics, Mago, et al. [117] noted that a regenerative ORC system incorporating turbine bleeding operates at high efficiency with less heat input requirement and lower irreversibility. However, a reduction in the net shaft-work is associated with turbine bleeding due to the extraction of the working fluid from turbine. To deal with the drawback of turbine bleeding, Desai and Bandyopadhyay [113] demonstrated that the ORC system can be enhanced by incorporating both regeneration and turbine bleeding for a higher thermal efficiency. As the state point of a dry fluid after expansion process lies in the superheated vapour region, the regeneration process is enabled, which contributes to the improvement in thermal efficiency of the ORC system. Usually, a regenerator or a recuperator is employed to reclaim exhaust vapour to improve the cycle efficiency; however, it would lead to higher capital costs and complexity of the ORC system design [114]. The regeneration employing an internal heat exchanger enhances the thermal efficiency of ORC system, which has been proved by Saleh, et al. [118]. Xu, et al. [119] found 1.21% of cycle efficiency of the ORC system is improved as the internal heat regeneration was adopted. Wang, et al. [120] also suggested an additional internal heat exchanger in the ORC system to reduce the cooling load of the condenser and increase the system thermal efficiency. Song, et al. [121] modified the basic ORC system to a regenerative cycle, the system efficiency of the system rises by 6.07% based on the experimental results. It is worth noting that the size of the regenerator/recuperator should be designed with considerations of the total size and cost of the ORC system. Additionally, a recuperator is not necessarily required if there is no lower limitation of the heat source outlet temperature [122].

The ORC system has become more popular for micro-scale power generation systems owing to its great flexibility, high safety, economical benefit, low energy consumption, emission and maintenance requirement [98]. However, research and development on the ORC-based micro trigeneration system are still limited, especially for those driven by renewable energy sources as the majority runs with solar thermal, fuel cell and biomass [123]. Boyaghchi and Heidarnejad [124] evaluated a solar-powered micro trigeneration system integrated with evacuated solar collectors and ORC for domestic application. Based on their simulation results, the system thermal and exergy efficiencies reach 28% and 27% respectively during summer period, Al-Sulaiman, et al. [125] proved feasibility of the ORC-based trigeneration system powered by SOFC, combined with biomass combustor and solar collectors respectively.

The key element in the ORC system is an expansion device, which can be categorized into dynamic and displacement types. Compared to the dynamic (turbo) type, the displacement (volumetric) type is more preferred for the ORC system with lower flow rate and rotational speed but at higher pressure ratio [126]. Practically, the expander selection for the ORC system depends on the overall system size and operating condition. Qiu, et al. [127] evaluated several expansion devices for an ORC-based micro CHP system including turbine, scroll, screw and vane expanders and concluded that both scroll and vane expanders are suitable for the micro-scale ORC system with capacity ranging from 1kW to 10kW. Ali Tarique, et al. [99] noted that a scroll expander is the best choice for applications of small capacity due to the more flexible operation characteristic.

2.4.3 Scroll expander

A scroll expander is a positive displacement machine with a fixed built-in volume ratio and high isentropic efficiency for operation at a large pressure ratio [128]. As illustrated in Figure 2-6, a scroll expander consists of two identical scroll wraps, namely a fixed scroll and an orbiting scroll, which are assembled at relative angle of 180°. By coupling a crankshaft to the orbiting scroll, it enables the scroll orbit eccentrically at a fixed path relative to the fixed scroll [129]. Consequently, a series of crescent-shaped pockets are formed.

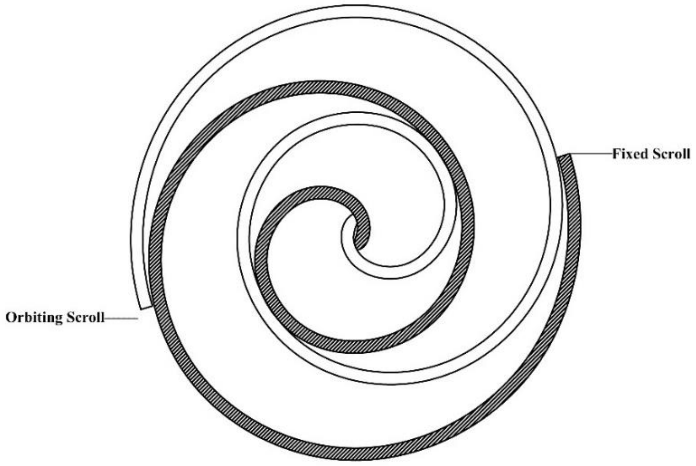


Figure 2-6 Schematic diagram of scroll expander

The three main working processes of a scroll expander are depicted in Figure 2-7, which are charging, expansion and discharging processes. The charging phase starts with the working fluid entering into the charging chamber. During the charging phase, the charging chamber traps a pocket of the working fluid and evolutes into two expansion chambers after one shaft revolution. Then the expansion phase takes place as the working fluid started to be expanded. Finally, the expansion chambers become discharge chambers once they come into contact with the discharge line of the machine [130]. Referring to experimental investigations presented in the literature [131-136], the volume ratio of the scroll expander is typically in the range of 1.5 to 5 and the

measured isentropic efficiency ranges from 48% to 84% depending on the specific operation condition.

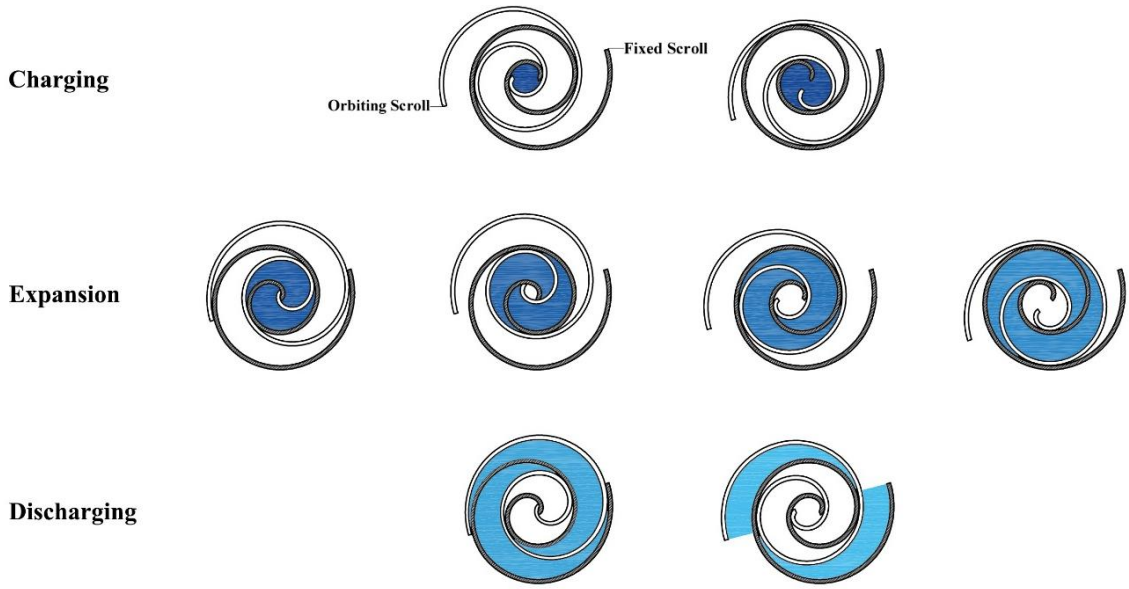


Figure 2-7 Working process of scroll expander

Currently, the scroll expander has not been widely commercially available and prototypes have been mostly modified from compressors for laboratory experiment [137]. For example, Chang, et al. [138] modified a commercial oil-free scroll compressor to a scroll expander; Brasz and Holdmann [139] developed an ORC system with a scroll expander derived from an existing centrifugal compressor and Lemort, et al. [130] built a prototype derived from an existing heat pump compressor. In such cases, limitations of the modified scroll expander should be considered in performance evaluation, which is manly attributed to the compressor built-in volume ratio, lubricating oil and motor.

To evaluate the scroll expander performance, approaches of theoretical modelling and simulation are commonly adopted. Liu, et al. [140] established a mathematical model to simulate the working process of the scroll expander by considering the suction, leakage, heat transfer and discharge losses. Liu, et al. [141] introduced an idealised

dynamic model of the scroll expander to calculate geometric characteristics for optimum geometry design. Ma, et al. [142] presented a generic dynamic model of the scroll expander with combinations of the valve model, internal leakage model, motion equation, heat transfer and energy balance equations. Nevertheless, deterministic models require an accurate knowledge of the scroll expander geometry, which may be difficult or impractical to acquire. On the other hand, computational fluid dynamic (CFD) approach is also popular to evaluate the thermal-hydraulic behaviour of the scroll expander, as examples presented in the literature [141, 143, 144]. For example, CFD based 3D numerical simulations have been performed on the scroll expander by Liu, et al. [141] to estimate transient features of the aerodynamic parameters with different suction port locations. However, the interaction of the working fluid and scroll expander structure and multiphase flow are limited for the CFD method [145]. Besides, empirical and semi-empirical models of the scroll expander are developed on a basis of experimental data, which can be regarded as direct and simple generic ways for computing the scroll expander performance. In principle, the process of working fluid flowing through the scroll expander is simulated with a lumped method in the empirical and semi-empirical models, and essential input parameters should be determined by reliable experimental results [130]. For example, Lemort, et al. [126] developed a semi-empirical model of the scroll expander, which has been validated by experimental tests with HCFC-123 as the working fluid. The maximum deviation between the model prediction and experimental measurement is 2% for the working fluid mass flow rate, 5% for the shaft power and 3K for the scroll expander exhaust temperature. A fairly good agreement between the semi-empirical steady-state model of a hermetic scroll expander and experimental data has been obtained by Ayachi, et al. [146] and the validated model can be used for predictions at further untested

operations and system optimisation design. Dickes, et al. [147] provided an open-source library of steady-state modelling and simulation for the ORC system with a scroll expander, with validity and good accuracy.

The scroll expander performance is influenced by a variety of parameters, such as the working fluid type, scroll geometry, inlet condition, imposed pressure ratio, rotational speed and coupled electrical load. Zhang, et al. [145] noted significant impact of the scroll expander clearance and vane height to pitch ratio on the scroll expander performance. Giuffrida [148] observed a linear relationship between the scroll expander rotational speed and output power through theoretical simulation, while the change in the scroll expander inlet temperature has no evident effect on the power generation. Declaye, et al. [149] experimentally observed that the isentropic efficiency of the scroll expander degrades at a high angular speed and the faster rate is achieved at a lower pressure ratio. Clemente, et al. [136] developed a one-dimensional model of scroll expander in the ORC-based cogeneration system and stated that there is an optimum expansion ratio that maximizes the ORC efficiency, but the influences of the electrical load and angular speed of the scroll expander on cycle efficiency have been not considered. Regarding to the electric output characteristics of the ORC system, there are limited studies on the effect of electrical load coupled to the scroll expander. The experimental data obtained by Pan, et al. [150] demonstrate that the electrical load significantly affects rotational speed, isentropic and mechanical efficiencies of scroll expander as well as the output power from the generator. Wu, et al. [151] found the isentropic efficiency of the scroll expander increases with the electrical resistive load. In addition, Tang, et al. [152] pointed out that the load characteristics should be matched with the scroll expander-generator unit for the best generation performance.

When adopting a scroll expander to the ORC system, consideration should be given to maximize the performance of the scroll-based ORC system. The scroll expander built-in volume ratio should match the working fluid volume ratio across the expansion process, so that more power output can be generated [153], while significant losses are associated with either with under or over expansion. Zheng, et al. [107] stated the evaporator parameters should fit the waste heat source to minimise the effect of internal and external entropy generation within the evaporator. They also recommended the ORC system operates with high evaporating pressure and low superheating temperature. Xu, et al. [119] also concluded that the electric output of ORC system increases rapidly with the rising evaporating temperature. Based on the performance optimisation of the ORC system, Wei, et al. [106] noted that the system efficiency and net output power increase with the increasing flow rate or supply temperature of heat source. Moreover, the ambient temperature also greatly influences the condenser performance of the ORC system, the cycle exergy efficiency and irreversibility [154].

In terms of the application of the scroll-based ORC system, the feasibility for the micro cogeneration system has been confirmed with the power capacity ranging from 0.1 to 12kW [127, 155-158], while little attention has been devoted to the micro trigeneration system. Karellas and Braimakis [159] thermodynamically and economically investigated a micro trigeneration system with scroll-based ORC and vapour compression cycle. They indicated that the generated profits owing to the reduction of fuel oil and electricity consumption can lead to remarkable savings, accounting for an internal rate of return about 12% and a payback period of 7 years. On the other hand, Jradi and Riffat [160] experimentally proved the feasibility of a biomass-fuelled micro

trigeneration system with scroll-based ORC and the proposed system is capable of providing about 500W electric power, 9.6kW heating power and 6.5kW cooling power.

The review of the literature presented in Section 2.4 has focussed on the prime mover as the key element of the micro trigeneration system. The literature review has demonstrated the increasing interest in the micro power generation system by employing the micro turbine, fuel cells, Stirling engine and Rankine cycle for domestic applications. Comparatively, the ORC technology becomes more favourable for the micro trigeneration system owing to its technical, economic and environmental benefits. Currently, demonstrations of the ORC-based micro trigeneration system are still limited, and little attention has been paid to the scroll-based ORC for application of the micro trigeneration system although numerous studies have proved that the scroll expander is the most preferred engine in the micro scale ORC system. The review indicates the potential to develop and test an ORC-based micro trigeneration system with a scroll expander. Next, the literature review on the heat recovery technology is presented in Section 2.5.

2.5 Heat recovery

This section presents a review of the literature on the heat recovery technology employed in the micro trigeneration system. A heat recovery unit captures the waste heat rejected from the prime mover. Typically, heat exchangers are adopted for heat recovery in the micro trigeneration system, which are categorized into: simple unfired type without any additional generation and fired type with fuel combustion to produce complementary thermal energy [4]. Either fired or unfired types can be utilised separately or together in the micro trigeneration system depending on the system

requirements. All available unfired and fired heat recovery equipment with their features are listed in Table 2-3.

Table 2-3 Characteristics of available heat recovery equipment [4, 22, 161-164]

Types	Characteristics
Unfired Types	
Heat exchanger	Availability in a variety of types (e.g. shell, tube, plate, fins and micro-channelled heat exchangers)
Unfired steam generator (waste heat recovery boiler)	Fuelled by exhaust gases Preferable with gas turbine Production of steam and hot water Availability in water-tube and fire-tube configurations
Muffler	Suitable with reciprocating engine Low noise level Generation of hot water or pressurized steam in the temperature range of 370°C to 540°C Potential risk of excessive back-pressure on the engine Requirements for regular maintenance and cleaning
Regenerator	Gas-to-gas heat exchanger Capability of harnessing hot exhaust gases to preheat combustion air in a gas turbine through indirect heat transfer Potential air leakage during operation Several constraints limit wide application, for example design challenge, cost and high temperature environment

	Characteristics
Recuperator	Gas-to-gas heat exchanger Avoid mixing between hot exhaust gas and cold incoming combustion air Preferable with gas turbine and micro turbine Reduction in fuel consumption to heat compressed air at the turbine inlet High energy efficiency Requirement of proper material selection for fabrication to avoid problems (e.g. corrosion, erosion, high temperature exposure, thermal stresses and fatigue)
Fired Types	
Supplementary fired steam generator	Incorporation with gas turbines Ability to capture exhaust heat from temperature less than 540 ℃ up to 980 ℃ Control in amount of steam production Low NO_x emission
Boiler	Production of more steam with less fuel Availability in water-tube and fire-tube types A variety of design configurations

This section has mainly reviewed characteristics of different heat recovery equipment, which are available for application in the micro trigeneration system. Next, Section 2.6 presents a detailed review of the literature regarding the thermal-activated cooling technology for the micro trigeneration system.

2.6 Thermal-activated cooling

This section firstly discusses the features of different thermal-activated cooling technologies and then highlights the liquid desiccant cooling through a detailed literature review. In terms of various configurations of the liquid desiccant cooling, the membrane-based liquid desiccant cooling is particularly reviewed regarding its principle, features, feasibility and application in the micro trigeneration system.

Depending on the prime mover type and system operation condition, exhaust heat from the prime mover can be in the form of steam, hot water and exhaust gas at various temperatures [5]. As a consequence, a suitable thermal-activated cooling technology should be selected in view of the exhaust heat characteristic. Generally, the current favoured thermal-activated cooling technologies are absorption and adsorption chillers, desiccant cooling and ejector chiller [24]. Table 2-4 presents the three most common thermal-activated cooling technologies with their respective features.

Table 2-4 Characteristics of thermal-activated cooling technologies [4, 8, 15, 27, 162, 165, 166]

Types	Characteristics
Adsorption chiller	Environment-friendly with significant energy saving potential Efficient utilisation of low-grade heat sources Simple design with low noise level and maintenance need No internal mechanical moving parts and lubrication No corrosion and crystallization risks Large chiller volume High initial cost Low COP and adsorption capacity Requirements of cooling tower and hot water tank Adsorbent with low thermal conductivity

Types	Characteristics
Absorption chiller	Mature and popular for commercial application Availability in direct and indirect-fired types Various designs of indirect-fired type (i.e. single, double and triple-effect) Viability with a wide range of prime movers Flexibility in operation on steam, hot water and high temperature exhaust gas Good partial load performance No internal mechanical moving parts Low noise, vibration and maintenance requirement High initial cost Slow transient response Corrosion and toxicity of working fluids
Desiccant cooling	Availability in solid and liquid desiccant configurations A variety of types depending on packed material Efficient with utilisations of low-grade heat sources Good supply air quality Independent temperature and humidity controls Eliminations of reheating and overcooling Low operation cost Requirement of addition chiller or cooler to handle sensible load Requirement for regular maintenance

2.6.1 Comparisons of available thermal-activated cooling technologies

Both absorption and adsorption chillers provide thermal compression instead of mechanical compression in a cooling cycle. The absorption chiller is the most commercially available cooling technology for the micro trigeneration system, especially the indirect-fired type is capable of utilising steam, hot water and high temperature exhaust gas [4]. Depending on the heat source condition (i.e. steam/hot

water pressure and temperature), various configurations have been developed to utilise heat different multiple times within the system varies, such as single, double and triple-effect absorption chillers [4, 165]. On the basis of absorption, the absorption chiller operates with a pair of working fluids, namely an absorbent and a refrigerant. Working fluids of the absorption chiller should be chemically stable, non-toxic and non-explosive [167]. For example, the lithium-bromide (LiBr)/water absorption chiller is suitable for air conditioning with an evaporation temperature ranging from 5°C to 10°C, whereas the ammonia/water one is preferred in small-scale air conditioning and large industrial applications with evaporation temperature below 0°C [165] and silica-gel/water is mostly adopted for the small-scale trigeneration system. The absorption chiller is widely used for large-scale industrial and commercial trigeneration systems, and its high initial costs limits applications for the small and micro trigeneration systems [168]. Consequently, developments on the low cost and small capacity effective absorption chiller are desired. For example, Moya, et al. [169] tested the performance of a micro trigeneration system with a micro gas turbine and an indirect-fired ammonia/water absorption chiller under different operation conditions. Chen, et al. [170] proposed a novel residential micro trigeneration system incorporating fuel cells and a single effect lithium-bromide/water absorption chiller, which is able to provide maximum cooling capacity of 4.8kW with heat source temperature of 90°C. Wang and Wu [171] proved the feasibility of integrating a mixed effect absorption chiller to recover the jacket water and exhaust waste from an internal combustion engine in a micro trigeneration system, which provides cooling output of 34.4kW and COP of 0.96.

On the other hand, the adsorption chiller runs with relatively lower temperature heat sources but with lower system efficiency [172]. Different from the absorption chiller,

two or more adsorbent beds are employed in the adsorption chiller to adsorb and desorb a refrigerant for continuous operation. Working pairs of the adsorption chiller can be divided into: physical and chemical types and adsorbents can be pure, composites or compounds with diverse properties. In particular, the working pair of silica gel/water is of mature commercialization for adoption. Compared to the absorption chiller, the adsorption chiller without corrosion and crystallization problems is more promising for small and micro trigeneration systems to handle cooling demand [165, 173]. For example, Li and Wu [174] demonstrated the feasibility of a silica-gel/water adsorption chiller for a micro trigeneration system through theoretical modelling. Kong, et al. [175] investigated a micro trigeneration system combining a gas engine and a silica-gel/water adsorption chiller. Based on their experimental results, the refrigeration COP of the adsorption chiller above 0.3 at an evaporation temperature of 13°C and cooling load of 9kW are achieved accordingly. In addition, Wu, et al. [176] conducted both experiment and simulation for a micro trigeneration comprising of an internal combustion engine and an adsorption chiller and they observed the chiller realises cooling output of 6.5kW and system COP of 0.56.

The process of removing water vapour from moist air is determined as dehumidification, which can be implemented by cooling, increasing process air pressure or absorption/adsorption of moisture with a desiccant. Conventionally, mechanical vapour compression is used to meet both cooling and dehumidification demands, in which dehumidification is accomplished by cooling air to its dew point temperature and extra energy is consumed to reheat air to the desired supply temperature [177]. However, a number of associated risks have been noted, for example leakage, bacterial breeding and fungi due to water condensation on the cooling coil surface of the mechanical vapour compression system. Alternatively, the

environmental-friendly desiccant dehumidification technology successfully eliminates the shortcomings of overcooling and reheating [178]. By coupling a desiccant dehumidification unit to other cooling technologies, a desiccant cooling system is formed to handle both latent and sensible heating loads [179]. The desiccant cooling technology has been raising great concerns for domestic applications especially in the hot and humid region, which provides high-quality supply air through independent temperature and humidity controls [20]. The desiccant cooling is of great flexibility in incorporating with various prime movers, like the internal combustion engine, Stirling engine, ORC, fuel cells as well as photovoltaic thermal system [165]. As shown in Figure 2-8, a desiccant cooling system mainly consists of a dehumidifier, a regenerator and an auxiliary cooling component [180].

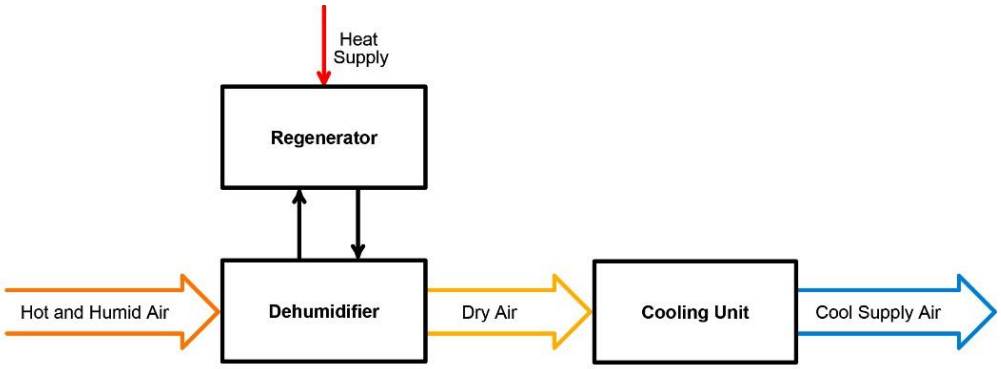


Figure 2-8 Schematic diagram of desiccant cooling

Desiccants are materials with high affinity for water vapour, which can be classified to: (a) adsorbents absorbing moisture without physical and chemical changes and (b) absorbents absorbing moisture accompanied by physical or chemical changes [181]. Typically, desiccants can be either solid or liquid types and most adsorbents are solids and most absorbents are liquids. Dehumidification process occurs when vapour pressure of the desiccant surface is less than that of the process air until an equilibrium state is achieved between the desiccant and air [182]. The water removal process with liquid desiccants is nearly isothermal while it is adiabatic for solid desiccants. To

ensure continuous operation of the desiccant cooling system, the dilute desiccant after a dehumidification process should be regenerated through a regeneration process. In contrast to the dehumidification process, the desiccant regeneration occurs when vapour pressure of the desiccant surface is higher than that of the air, which is commonly realised by heating the desiccant to its regeneration temperature or exposing it to an air stream. Moreover, the regenerator can be powered by a variety of energy sources, like the solar energy and exhaust heat from turbines, which significantly reduce costs and greenhouse gas emissions [183]. For example, Hürdoğan et al. [184] employed solar collectors for regeneration heat supply in a solid desiccant air-conditioning system and Buker and Riffat [185] suggested that not only the solar thermal but also photovoltaic technologies can be utilised for the liquid desiccant cooling system.

Comparatively, the solid desiccant cooling system is less subject to corrosion as most of the solid desiccant materials are environmental-friendly [186]. Ideally, the solid desiccant is expected to have large water adsorption capacity at its operative temperature and easily regenerated at a lower achievable regeneration temperature. Silica gel and zeolite are the two widely adopted materials with strong affinity [187] and extensive researches have been conducted to develop solid desiccant materials with better adsorption and regeneration capabilities as well as long stability, such as nanoporous inorganic material, composite and polymeric desiccants [186]. In general, available solid desiccant cooling systems can be categorized to fixed bed and rotary wheel types and by comparison, the rotary desiccant wheel type has been more favourable. In the desiccant wheel system, the solid desiccant material is impregnated into a support frame and channels can be fabricated in different structures such as honeycomb, triangular and sinusoidal [188] and air to air heat and mass transfer takes

place at a low rotational speed [189]. The solid desiccant cooling system can be operated as a standalone system or coupled to the vapour compression air conditioning system [190]. In such a way, the rotary wheel system has been designed into various configurations to provide different supply conditions, like Pennington, recirculation and Dunkle cycles. Currently, the solar-powered solid desiccant system becomes more preferred with significant reduction in the system operation cost and energy consumption. Many demonstrations of the solar-assisted rotatory wheel system have been available in China and European countries [188]. Saghafifar and Gadalla [191] examined a novel air conditioning system combining the solid desiccant cooling and solar photovoltaic thermal technology for a building in Abu Dhabi, which indicates remarkable energy saving performance. Furthermore, the solid desiccant cooling system has been well accepted in the cogeneration and trigeneration systems. For instance, Hands, et al. [30] presented a comprehensive performance analysis of a large scale solar-assisted trigeneration system with the rotary solid desiccant wheel and compression chiller. They observed 35% of the annual total building cooling load could be met by the desiccant component. Petrov, et al. [192] stated that by adding a desiccant wheel to recover the micro turbine exhaust gas in a micro cogeneration system, the system efficiency increases by 7%. Angrisani, et al. [193] experimentally assessed the performance of a micro trigeneration system with a solid desiccant wheel in southern Italy, with which the supply air temperature of 20.1°C can be provided at an outdoor air temperature of 33.3°C. Because the solid desiccant cooling system commonly has large size and high investment cost, studies for application in the micro trigeneration system are still limited. Thus in terms of application in the micro regeneration system, more compact standardized and packed system designs are suggested for the future development [165].

2.6.2 Liquid desiccant cooling

Compared to the solid desiccant system, the liquid desiccant cooling system is more flexible in utilisation and operation of independent air temperature and humidity controls [194]. The liquid desiccant cooling system enables the humidity control without extra energy consumptions in overcooling and reheating [195]. It has been noted that 40% of the operation cost can be saved by applying a liquid desiccant cooling system compared with the conventional central air conditioning system [195]. Liquid desiccants have been attractive for air dehumidification in indoor conditioning with benefits of lower regeneration temperature and pressure drop on air side [196]. Additionally, they have the capability to improve indoor supply air quality and thus epidemic of respiratory disease can be prevented by absorbing inorganic and organic contaminants in the air [197].

The selection of a liquid desiccant depends on various operating parameters, such as boiling point elevation, energy storage density, regeneration temperature, thermo-physical properties, availability, cost etc. [198]. In terms of thermo-physical properties, the ideal liquid desiccant should have low vapour pressure, low crystallization point, low regeneration temperature, low viscosity, good heat transfer characteristic and appropriate surface tension property [199]. Halide salts are the most commonly selected desiccants, for instance lithium chloride (LiCl), LiBr and $CaCl_2$. Besides, weak organic acid salts, such as potassium and sodium formate are also good alternatives [200] and ionic liquids become promising for a specific achievable dew point temperature at a comparatively lower driving temperature [201]. Among them, LiCl is the most stable desiccant with low vapour pressure, but at higher costs. $CaCl_2$ is the cheapest and most readily available liquid desiccant, but several disadvantages limit its wide application, for example relative higher vapour pressure at a given

temperature and instability with inlet air conditions and desiccant concentration [195]. Different desiccants have different appropriate operative concentration levels [199], and some examples are presented in Table 2-5. Greater dehumidification performance can be achieved by increasing the liquid desiccant solution concentration without going beyond the crystallization limit [202]. The use of highly concentrated solution may cause salt crystallization, which may cause problems of fluid mal-distribution, blockage of the channels, high pumping pressure, and membrane fouling [203].

Table 2-5 Operative concentration levels for different liquid desiccants [199]

Liquid Desiccants	Operative Concentration Level
LiBr	45%-60%
LiCl	30%-45%
$CaCl_2$	35%-45%

A variety of contacting equipment have been proposed to provide contact between air and the liquid desiccant with different characteristics [204]. Common packing types for the liquid desiccant dehumidification system are listed in Table 2-6 with their advantages and disadvantages. The spray, wetted wall and packed tower are commonly applied for the liquid desiccant dehumidification system [205]. However, these typical direct contact packing types have a major problem of liquid desiccant entrainment. Small liquid desiccant droplets would be harmful to the occupant health, building structure and indoor equipment [206]. Alternatively, the membrane-based liquid desiccant dehumidification system successfully eliminates the carryover problem. In such a system, membranes acting as selective barriers that allow heat and moisture transfer between the solution and airstream while prevent the carryover of liquid desiccant or water [206].

Table 2-6 Characteristics of available liquid desiccant dehumidification systems [195, 199, 204-210]

Packing types	Advantages	Disadvantages	Current research fields
Wetted wall (falling film) tower	Stable-flow condition Constant gas-liquid contacting area tower Low initial cost Low pressure drop	Small contact area Difficulty in achieving a thin film over the complete cross section of large tower	Industrial and residential applications System optimisation (e.g. film wetted area, liquid contact angle, etc.)
Spray tower	Low pressure drop on airside Large gas-liquid contacting area for high viscosity liquids with the help of nozzles in spray chamber Simple design of compact size with low cost	Clogged by the dirt Large number of droplets into supply air Low effectiveness in absorption Large pressure drop on liquid side	Industrial and residential applications System design (e.g. sprayed coils, cross flow plate heat exchangers and heat pipes)
Random Packed tower	Cheap Large contacting area Compactness	Large pressure drop on airside High desiccant flow rate for good wetting Undesirable solution distribution over surface	Industrial and residential applications System design (e.g. Berl saddles, Raschig rings and Intalox saddles)

Packing types		Advantages	Disadvantages	Current research fields
Structured Packed columns	Adiabatic	Simple geometric configuration Provides uniform gas-liquid flow path Large air-desiccant contacting area High heat and mass transfer efficiency No additional cooling source to cool liquid desiccant	Large pressure drop imposed on the process air flowing through the packing material Limited performance improvement due to the temperature increase caused by the water vapour absorption Adverse impact on the performance with increasing temperature of liquid desiccant in the moisture removal process Carryover problem of liquid desiccant droplets	Industrial and residential applications Structural optimisation (e.g. cellulose rigid media pads, wood grids, expanded metal lash packing, double spiral rings) Mathematical model for performance evaluation (e.g. finite difference model, effectiveness-NTU model and simplified models)
	Internally Cooled	Utilisation of cooling coil to remove the heat generated from dehumidification process Good dehumidification performance Various types integrated with cooling coil or cooling mediums Reducing device volume High thermal conductivity of material	Large mass flow rates of desiccant solution More equipment requirements and installation difficulty Carryover problem of liquid desiccant droplets	Experiment and theoretical simulation Mathematical model for performance evaluation (e.g. considerations of uniform liquid film thickness and variable liquid film thickness) Materials avoiding corrosion problem

Packing types		Advantages	Disadvantages	Current research fields
Membrane-based	Parallel-plate	Overcome carryover problem of liquid desiccant droplets Simple structure and easy fabrication Less pressure losses in the channels	Low packing density	Membrane material and construction type System feasibility and application Energy analysis
	Hollow Fibre	Overcome carryover problem of liquid desiccant droplets Large packing density and high effectiveness Shell and tube with a bundle of fibre tube	More complex design with two ends sealing problem High pressure losses in the channels Difficulty in modelling of the fluid flow and heat mass transfer	Membrane material and structure System feasibility and application Modelling (e.g. fluid flow, conjugate heat and mass transfer in the membrane module)

In order to further reduce the dehumidified air temperature, different kinds of cooling technologies can be employed in the liquid desiccant cooling system, such as the vapour compression, vapour absorption, direct and indirect evaporative cooling [180]. In particular, evaporative coolers have been mostly considered owing to its lower installation and energy costs. Compared with the vapour compression air-conditioning system, the energy consumption of a evaporative cooler can be reduced by up to 75% [211]. The direct evaporative cooling adds moisture to the cooled air, whereas the indirect evaporative cooling provides only sensible cooling to the process air without any moisture being added, which is more favourable for more humid climates [212]. In terms of the system effectiveness, it ranges from 70% to 90% depending on the temperature for the direct evaporative cooling system, while it varies from 40% to 60% for the indirect evaporative cooling system. The liquid desiccant cooling system with evaporative cooling has been widely developed with good performance and excellent energy saving potential [213]. By installing a liquid desiccant cooling system for an open office building in Seoul, Ham, et al. [214] found 12% saving of the annual primary energy consumption is attainable and Safizadeh, et al. [215] stated that more than 50% of the lifetime operating cost can be saved in Singapore. With the indirect evaporative cooling integrated to a liquid desiccant system, Buker, et al. [216] observed that a drop of 7.5°C in the indoor air temperature is achieved. El-Dessouky, et al. [217] proposed a novel air conditioning system combining a hollow fibre dehumidification system and an indirect/direct evaporative cooler. They observed that wider operating temperature and humidity ranges for application could be feasible in Kuwait (i.e. temperature range of 25°C to 45°C and humidity range of 30 to 100%).

Extensive experimental and theoretical studies have been conducted to investigate effect of various parameters on dehumidification performance of the liquid desiccant

cooling system. For example, the most significant dimensionless parameters affecting the dehumidification performance are identified through theoretical analyses in the literature [218, 219], which are NTU, solution to air thermal capacity ratio and solution concentration. On the other hand, the experimental investigations in the literature [220-222] demonstrate that the dehumidification performance of the liquid desiccant cooling system evidently varies with inlet air condition, solution concentration and packing material density.

Most of the successful demonstrations of the micro trigeneration system integrate direct contact packing liquid desiccant cooling technologies. Currently, more and more research on combining the liquid desiccant cooling with the micro trigeneration system have focused on developments of safe and trouble-free contact equipment, optimal mixed liquid desiccant, higher effective and compact dehumidifier and regenerator design, cost-effective auxiliary cooling technology and control strategy [4, 15, 165]. In particular, the membrane-based liquid desiccant dehumidification system offers great potential.

2.6.3 Membrane-based liquid desiccant cooling

To eliminate the liquid desiccant carryover problem, a membrane-based liquid desiccant dehumidification system is adopted, which involves an indirect contact process for dehumidification. Membrane acting as a selective barrier allows heat and moisture transfer between solution and airstream but prevents the carryover of liquid desiccant solution into supply airstream [206]. Membranes are categorized into dense and porous types depending on the pore dimension. Dense membrane is hydrophilic for vapour transportation, while porous membrane with more open volume and larger pores is hydrophobic [209]. With respect to the form, membranes can be designed as

flat sheets with simple structure and easy fabrication, or hollow fibres with large packing density and high effectiveness but more complex design.

Many studies of the MLDC system have been conducted, which incorporated different renewable energy sources and cooling technologies. Abdel-Salam, et al. [223] proved the feasibility of a membrane-based desiccant air conditioning system powered by solar energy and El-Dessouky, et al. [217] proposed a novel air conditioning system consisting of a membrane dehumidification unit and a direct evaporative cooler, and they observed that 86.2% of energy saving can be achieved compared to a conventional stand-alone vapour compression system. The MLDC system has been explored through modelling simulation; while as yet relatively few studies have been carried out to experimentally investigate the feasibility and performance of the MLDC system. For instance, a comprehensive model of a parallel-plate MLDC system has been developed to address features of the conjugate heat and mass transfer in literature [224]. To overcome the liquid desiccant cooling system shortcomings of complexity and large geometrical size, a compact membrane-based air conditioning system is developed with an evaporative inter-cooler unit for building application in literature [225], whose cooling output is in the range of 570W to 1362W and dehumidifier effectiveness is in the range of 30% to 37% based on the experimental results. Furthermore, limited studies have been conducted to evaluate effect of operating variables on the MLDC system performance by experimental work.

With considerations of the carryover and corrosion problems for building applications, the MLDC system is a favourable option for the micro trigeneration system, but such technology is still in the research and development stage with limited investigations. Elmer, et al. [11] proved the feasibility of a micro trigeneration system with SOFC and a MLDC unit and Jradi and Riffat [160] conducted experimental investigations of an

innovative micro trigeneration system with a liquid desiccant cooling unit to recover waste heat from an ORC unit. In their proposed liquid desiccant cooling unit, an indirect evaporative cooler allows air temperature to drop below the wet-bulb temperature and towards the intake air dew point temperature. Based on their experimental results, the indoor air reduces from 33.8°C to 22.3°C and the relative humidity decreases from 68.6% to 35.5%.

Section 2.6 has reviewed different thermal-activated cooling technologies for the micro trigeneration system, and specifically focused on the liquid desiccant cooling. The liquid desiccant cooling system has higher COP, which is possible to enhance the micro trigeneration system performance in cooling mode. The reviewed work shows that the MLDC system is capable of avoiding the problem of liquid desiccant entrainment that exists in the common direct contact packed liquid desiccant cooling system and such technology is still at the research and development stage with limited studies demonstrating the applications in the micro trigeneration system. Additionally, comprehensive experimental testing of the MLDC system is needed for investigating the effect of a wide range of operating variables on the system performance. In the next Section 2.7, the operating strategy is reviewed on the basis of the existing literature.

2.7 Operating strategy

This section presents a literature review of the operation strategy, which is a critical factor influencing the micro trigeneration system design, energetic, economic and environmental performance [226]. To identify the optimal operating strategy, various factors should be taken into consideration, such as the primary energy consumption, operational cost, emission and waste energy [35, 227]. Basically, the two common

operation modes are namely (a) following the electric load (FEL) when the system operates to first meet the building electricity demand, and (b) following the thermal load (FTL) when the system fulfil the thermal demand first and insufficient electricity would be provided by the grid [228]. It has been seen that the system energy consumption reduces by 11% with a FTL operating strategy compared with that of the FEL and more exhaust heat from the prime mover can be utilised and the system performance is thus improved [229]. However, considerable energy losses are associated with both FTL and FEL strategies. As a consequence, more advanced operating strategies have been established that would effectively interchange between FTL and FEL modes, thus to improve the system performance and enhance associated benefits with less energy waste. For example, following the seasonal operation strategy (FSS) proposed by Mago and Hueffed [230] aims to allow the trigeneration system to operate under either FTL or FEL mode on a basis of the monthly electric-to-thermal load ratio, with a remarkable reduction in the primary energy consumption. Li, et al. [226] presented an advanced operating strategy of the following the electrical-thermal load of buildings (FLB), which is modified from the FSS strategy but based on the hourly electric-to-thermal load ratio. Their simulation results indicate that the FLB strategy matches well with both the electrical and thermal demands for the micro trigeneration system in residential buildings. And, Mago, et al. [231] introduced a following hybrid electric-thermal load (FHL) strategy for a micro trigeneration system, which guarantees the prime mover to operate at an optimal mode in accordance with the electric and thermal loads at any given time without redundant electricity and heat. FHL strategy also contributes to less annual primary energy consumption, operation cost and emission. Moreover, Liu, et al. [28] suggested an hourly operating strategy of

the micro trigeneration system for domestic applications should correspond to the outdoor weather conditions in order to achieve the optimal system performance.

Section 2.7 has discussed several operating strategies for adoption to the micro trigeneration system in the existing literature, which will be useful for designing the proposed micro trigeneration system. Next, Section 2.8 reviews the recent research on the micro trigeneration system.

2.8 Recent research on micro trigeneration

2.8.1 Comprehensive reviews

Many review studies have been conducted to provide comprehensive knowledge of the trigeneration system and related technologies. Table 2-7 presents a summary of eleven review papers regarding the trigeneration system. Among them, a review paper by Sonar, et al. [15] provides a brief review of the micro trigeneration system from the perspectives of technology, research tool and trend, while the rest focus on the trigeneration technology covering topics of the principle, design, operation strategy, component, performance characteristic, optimisation, potential application, future development, etc. For instance, Wu and Wang [20] discussed the up to date global developments of the trigeneration system. Al Moussawi, et al. [4] provided a comprehensive review on the trigeneration system from aspects of the prime mover, heat recovery and thermal energy storage. Jradi and Riffat [5] conducted a detailed literature review in the field of the trigeneration system, including the recent supporting mechanism (policy), prime mover, cooling technology, system configuration and utilisation of renewable energy resource. Al-Sulaiman, et al. [24] comparatively analysed available prime movers for the trigeneration system and summarised the selection criteria listed in the existing literature, while Deng, et al.

[165] mainly reviewed various thermally-activated cooling technologies adopted in trigeneration systems. On the other hand, Liu, et al. [8] provided a summary of the recent research progress on the management, control, system optimisation and sizing of the trigeneration system in different countries. Ünal, et al. [232] critically examined different optimisation modelling techniques for the trigeneration system, by focusing on the optimisation goal and method, input energy resource and associated output. Gu, et al. [233] briefly reviewed the modelling, planning and energy management of the trigeneration system, whereas Cho, et al. [234] outlined approach from the existing literature for the trigeneration system performance assessment, optimisation and development and highlighted emerging trends in the research field.

Table 2-7 Review perspectives of review papers on trigeneration system

References		Perspectives							
Authors	**Year**	**Fuel Types**	**Prime Movers**	**Thermal-activated cooling technologies**	**Heat Recovery**	**Thermal Energy Storage**	**Control, Management, Operating Strategy**	**Optimisation and Sizing**	**Others**
Wu and Wang [20]	2006		-Steam turbine -ICE -Combustion turbine -Micro turbine -Stirling engine -Fuel cells	-Absorption chiller -Adsorption chiller -Desiccant dehumidifier					-Diverse trigeneration configurations -Worldwide development and barriers of the trigeneration system
Al-Sulaiman, et al. [24]	2011	-Natural gas -Distilled Oil -Bio gas	-ICE -Stirling engine -Steam turbine -Gas turbine -Micro turbine -Fuel cells						-Characteristics of available prime movers -Prime mover selection for the trigeneration system
Deng, et al. [165]	2011			-Absorption chiller -Adsorption chiller -Solid desiccant and liquid desiccant cooling					-Researches of thermally-activated cooling in innovative concept, material and technology -Selection of thermally-activated cooling for trigeneration systems

Authors	Year	Fuel Types	Prime Movers	Thermal-activated cooling technologies	Heat Recovery	Thermal Energy Storage	Control, Management, Operating Strategy	Optimisation and Sizing	Others
Cho, et al. [234]	2014	-Solar -Biogas -Biomass -Biofuel	-Fuel cells -ORC				-FEL -FTL -Based load operation	-Energetic analysis -Exergy analysis -CCHP evaluation based field tests, thermodynamic analyses and transient simulation	-Summary of methods for system energetic and exergetic analyses, optimisation, performance improvement and development -Highlights of current research and emerging trends in the trigeneration field
Gu, et al. [233]	2014						-Modelling approach -Planning method -Energy management		-Modelling of prime mover, storage system, loads and renewable energy resources -Trigeneration performance evaluation methods and indicators
Jradi and Riffat [5]	2014	-Solar -Natural gas -Biofuels -Diesel -Waste heat -Biomass	-ICE -Gas turbine -Steam turbine -ORC -Stirling engine -Micro turbine -Fuel cells	-Absorption cooling -Adsorption cooling -Desiccant cooling -Ejector cooling -Vapour compression			-FEL -FTL -FSS		-Trigeneration supporting mechanisms, energy policies and latest developments around the world

Authors	Year	Fuel Types	Prime Movers	Thermal-activated cooling technologies	Heat Recovery	Thermal Energy Storage	Control, Management, Operating Strategy	Optimisation and Sizing	Others
Liu, et al. [8]	2014		-Reciprocating ICE -Combustion turbine -Steam turbine -Micro turbine -Stirling engine -Fuel cells	-Absorption chiller -Adsorption chiller -Desiccant dehumidifier			-Conventional operation strategies (FEL and FTL) -Novel operation strategies	-System configuration -Mathematical modelling (mixed integer and matrix approaches) -Facility sizing	-Development and barriers of trigeneration systems around the world
Sonar, et al. [15]	2014	-Solar -Hydrogen -Alternate fuels (e.g. bioethanol, biodiesel)	-Reciprocating engine -Micro turbine -Stirling engine -Fuel cells	-Sorption cooling (absorption and adsorption) -Desiccant cooling -Vapour ejector refrigeration		-Latent heat storage -Chemical sorbent /bond storage -Metal hydride storage			-Research tool, trend and barrier, associated environmental and economic benefits of the micro trigeneration system

Authors	Year	Fuel Types	Prime Movers	Thermal-activated cooling technologies	Heat Recovery	Thermal Energy Storage	Control, Management, Operating Strategy	Optimisation and Sizing	Others
Ünal, et al. [232]	2015							-Optimisation goal -Optimisation method (e.g. linear and non-linear optimisation, simulation and meta-heuristics) -assessment of optimisation techniques	-Development of optimisation algorithms for design, operation and management in the trigeneration system
Al Moussawi, et al. [4]	2016		-Steam turbine -Gas turbine -Micro turbine -Combined cycle gas turbine -Reciprocating ICE -Stirling engine -ORC -Fuel cells	-Absorption and adsorption chillers -Desiccant dehumidifier	-Unfired unit (e.g. heat recovery muffler, recuperator, regenerator, heat exchanger) -fired unit (e.g. boiler)	-Sensible heat storage -Latent heat storage -Chemical heat storage -Nano-technology based heat energy storage -Heat transfer fluid	-Decision making method (e.g. cost-benefit analysis, elementary method, multi-criteria, sensitivity and risk analysis)	-Design method (e.g. maximum rectangle, energy management sizing, thermos-dynamic sizing, thermos-economic sizing, multi-criteria and fitness function) -Optimisation methods -Selection approach -Evaluation criteria	-Comprehensive review of relevant studies for each perspectives; -Classification, evaluation criteria and selection scheme of the trigeneration system

Authors	Year	Fuel Types	Prime Movers	Thermal-activated cooling technologies	Heat Recovery	Thermal Energy Storage	Control, Management, Operating Strategy	Optimisation and Sizing	Others
Murugan and Horák [87]	2016	-Solar -Wind -Geothermal	-ICE -Stirling turbine -Micro gas turbine -ORC -Fuel cells (SOFC and PMFC) -Thermoelectric converter	-Absorption chiller -Adsorption chiller				-Optimisation techniques -Simulation	-Micro trigeneration system, especially for residential applications

2.8.2 Theoretical research

Numerous theoretical research of the micro trigeneration system have been conducted through numerical modelling and simulation using various software and tools, which are mainly aimed to demonstrate the system feasibility and evaluate the instantaneous or seasonal system performance based on energetic, exergetic, economic and environmental aspects. In general, the energy performance of the micro trigeneration system is commonly examined, through assessments of primary fuel energy usage, electric output, thermal energy, energy efficiency, energy saving, etc. On the other hand, an exergetic analysis provides the quality of supplied and consumed energy of the micro trigeneration system as well as the amount of availability destroyed within the system [235]. Several examples are selected from the existing literature; these have adopted different simulation tools to assess the micro trigeneration system performance.

Sibilio, et al. [47] used the dynamic simulation software TRNSYS to investigate the feasibility of an innovative building-integrated micro trigeneration system. The proposed system is mainly composed of a 6.0kW natural gas-fuelled internal combustion engine, an air-cooled electric water chiller, an auxiliary boiler and a hot water tank, which is devoted to meet electricity, heating and cooling demands for a typical Italian residential building. The system annual performance regarding the energetic, economic and environmental aspects have been simulated under different climate conditions and operating scenarios. Their simulation results demonstrate reduction in the primary energy consumption, annual carbon dioxide equivalent emission and operating cost are 4.3%, 10.6% and 19.9% respectively with the micro trigeneration system installed in Milan, Italy, compared with the conventional separation system based on a natural gas-fired boiler for heating and hot water

demands and an additional electric air-cooled water chiller for cooling. However, effect of different operating variables on the system performance have not assessed comprehensively. Similarly, Rady, et al. [44] designed a micro trigeneration system with concentrated solar collectors, an ORC of 4.3kW nominal electric output power, an absorption chiller of 35kW cooling capacity and a thermal energy storage unit for a medical centre in Egypt. They developed a theoretical system model with equations being solved in the Engineering Equation Solver (EES) program. The daily and monthly system energetic assessments have been presented for both summer and winter operating modes, by examining the solar collector power output, ORC power output, energy conversion efficiency and absorption chiller cooling capacity. Wang, et al. [38] adopted ECLISE simulation software to examine both energy and environmental performance of a micro trigeneration system based on a diesel engine. The proposed micro trigeneration system fuelled with hydrogen achieves an overall efficiency of 83% with electricity output of 6.5kW and COP of 0.66. Wang, et al. [39] developed a micro trigeneration system with direct flame fuel cells and a double-effect absorption chiller and implemented the simulation model with gPROMS software. They have discussed the system energy performance under various operating conditions in Hong Kong and Beijing respectively. The simulation results show a highest trigeneration system overall efficiency of over 90% is attainable. Huicochea, et al. [236] theoretically analysed the thermodynamic performance of a micro trigeneration system with a 28kW micro gas turbine and a double-effect LiBr/water absorption chiller. They established a thermodynamic simulator using MATLAB program, with which the trigeneration system energy performance has been assessed under different operating conditions (i.e. ambient temperature, evaporation temperature and micro gas turbine fuel mass flow rate). Chen, et al. [170] investigated

a residential micro trigeneration system with a proton exchange membrane fuel cell stack and a single-effect LiBr absorption chiller through steady-state mathematical modelling. The simulation model is developed using MATLAB/Simulink software and validated with reference data. A parametric study has been presented to identify the effect of key parameters (e.g. inlet gas condition, fuel cell operating temperature and density) on the fuel cell stack, chiller and overall system performance. In terms of performance analysis, they considered electric and thermal power of fuel cell stack, cooling capacity and COP of absorption chiller, system and cogeneration component energy efficiencies as simulation have been performed for the system operating in both winter and summer modes. Under the optimum operation condition, the maximum system efficiency reaches 70.1% in summer and 82% in winter. Elmer, et al. [11] presented an energetic, economic and environmental performance assessment of a novel SOFC micro trigeneration system with a liquid desiccant cooling unit, which is based on empirical data of SOFC and liquid desiccant components from experiment and existing literature. The proposed SOFC and liquid desiccant cooling technologies are viable for a micro trigeneration system, with which the overall system efficiency achieves 71% based on their theoretical results. The system environmental viability has been confirmed in the UK; with a reduction of up to 51% in the annual carbon dioxide emission has been observed compared to the equivalent base case. However, due to the high capital cost and requirement of stack replacement for SOFC, the system is not economically feasible for domestic applications according to their economic assessment. Ebrahimi, et al. [237] presented energy and exergy analyses of a micro-steam driven trigeneration system, which consists of a closed steam-driven Rankine cycle to provide electricity, heating and cooling loads to a residential building located in Tehran. They developed a comprehensive mathematical model employing the

conservation laws of mass, momentum and energy. Simulations in ASPEN software have been conducted for validating the applicability of designed components in the trigeneration system. Based on simulation results, they assessed the effect of various parameters (e.g. turbine inlet condition, extraction ratio, building heating and cooling demands) on the system performance, considering the fuel energy consumption, cooling and heating loads, COP, overall system efficiency and exergy efficiency. The overall system efficiency reaches 22.82% in summer and 62.15 % in winter at the maximum working load. Compared to the separate production, more than 68.21% and 26.64% of fuel energy consumption can be saved in summer and winter respectively. Their exergy analysis indicates that the biggest exergy destruction takes place in the steam generator. In addition, Huangfu, et al. [238] introduced a micro trigeneration system for domestic and light commercial applications, which comprises a reciprocating internal combustion engine with rated power of 12kW and an adsorption chiller with refrigerating capacity of 9.0kW. They employed methods of engineering economic and thermodynamic analysis to evaluate the system performance comprehensively, involving parameters of economic efficiency, energy output, primary energy consumption and exergy efficiency. In terms of the economic evaluation, factors including initial investment, operating costs and fuel price have been taken into consideration. Their simulation results show that the proposed system is beneficial in low initial cost and short payback period (i.e. approximately £11170/Nm^3 with payback period of 2.97 years for the natural gas price of £0.22/Nm^3).

2.8.3 Experimental work

Number of experimental investigations of the micro trigeneration system have been accomplished to assess the system feasibility and performance under various operating conditions. This section provides several examples of the experimental work

documented in the existing literature. Kong, et al. [175] presented experimental investigations of a micro trigeneration system, which involves a gas engine with rated electric power of 12kW and a silica gel/water adsorption chiller with cooling capacity of 9kW. They built prototype to test the system performance at design load and part load conditions. Energetic analysis has been presented based on experimental data, examining both thermal and electricity performance of the engine, adsorption chiller and whole system. The experimental results indicate that the match of the gas engine and adsorption chiller is feasible in a micro trigeneration system as the overall thermal and electrical efficiencies are both over 70%. Wu, et al. [176] proposed a micro trigeneration comprising an internal combustion engine with a rated electric output of 16kW, an adsorption chiller with cooling capacity of 7.5kW and a thermal management controller to recover and manage the exhaust heat. They conducted experimental tests to examine the system performance under cogeneration and trigeneration modes and processed the experimental data by taking various performance parameters into account, for example input fuel energy, electrical efficiency, exhaust heat efficiency, total engine efficiency, cooling output of chiller and COP. The experimental results demonstrate the system realised electric output of 16kW, heating output of 17.7kW and cooling output of 6.5kW simultaneously. Lin, et al. [239] constructed a micro trigeneration system in laboratory. In the proposed household size system, a Lister-Peter T series diesel engine with capacity of 9.5kW and a commercially available Electrolux absorption refrigerator are employed. They conducted a series of tests to evaluate the engine, refrigerator and overall system performances under different operation conditions; analyses of the fuel consumption, total power output, heat and refrigeration effect, system COP and emissions have been presented. They proved the feasibility of coupling a refrigerator and heat recovery unit

to a diesel engine when the engine load is above 50% with exhaust gas at over 200°C. Angrisani, et al. [240] set up a micro trigeneration system in a laboratory in Frignano, Italy, which is composed of a natural gas fuelled reciprocating internal combustion engine and a triple-state LiCl/water absorption unit. They used model GECC60A2 NR/P manufactured by AISIN as the core cogenerator for power output, which is capable of modulating electricity output according to the end-user's demands up to a maximum capacity of 6.0kW. They monitored and recorded daily electricity load, thermal power and primary energy consumption of the micro trigeneration system, and the system on-site performance under real operating condition was evaluated. Two operation modes are determined, namely winter mode, when thermal energy is used for heating and hot water supply, and warm seasonal mode when the system is operating to satisfy contemporarily the demands for heating, cooling and electricity for a residential building. Based on the gathered data, the proposed micro trigeneration is feasible for application in the residential sector with remarkable reduction in greenhouse gas emissions and operating cost. In addition, they suggested the system energy performance should be experimentally investigated in a wider range of operating conditions and the domestic household thermal and electrical loads profiles should be taken into account as well. Similarly, Ciampi, et al. [45] analysed the on-site performance of a micro-scale trigeneration system located in the University of Naples during a summer period. They adopted the same commercialised cogenerator model as in the literature [240] but coupled with an electric air-cooler water chiller. They evaluated the overall system performance experimentally from energy, economic and environmental points of view. They highlighted that by employing the micro-scale trigeneration system, reduction in the primary energy consumption, operation cost and

CO_2 equivalent emission are 20%, 39% and 23% respectively compared to the conventional separate power generation system.

Section 2.8 has presented a literature review on the recent research of the micro trigeneration system, including relevant review papers, theoretical and experimental investigations. In particular, the assessment methods adopted in the theoretical and experimental studies have been discussed in detail. One of the common approaches to evaluate system performance from energetic, exergetic, economic and environmental perspectives is to assess the instantaneous system performance under various operating conditions by considering various parametric impacts. The method will be fundamental to the theoretical and experimental assessments of the proposed micro trigeneration system in the following chapters. In the next section, conclusions to the literature review are drawn.

2.9 Summary

Extensive literature has been selected with appropriateness in addressing the thesis aim. A thorough literature review has been presented in this chapter covering seven key topics: micro trigeneration system (Section 2.2), concentrating solar collectors (Section 2.3), prime mover (Section 2.4), heat recovery (Section 2.5), thermal-activated cooling (Section 2.6), operating strategy (Section 2.7) and recent research on the micro trigeneration system (Section 2.8). The current research gap in the existing literature can be highlighted as: no work has been reported on such a micro trigeneration system combining CLFR, scroll-based ORC and MLDC. Main findings of the literature review are summarised as follows:

1) Many countries have launched support policies and mechanisms for the trigeneration system. It is worth noting that the micro trigeneration system is promising in domestic applications with benefits in technical, environmental and economic aspects, however it is still under research and development stage with limited available demonstrations.
2) CLFR is promising as a reliable heat source for power generation systems, yet no work has been investigated for its feasibility for the micro trigeneration system. The optical performance comparison between the LFR and CLFR systems has been rarely mentioned in the literature, which could be desirable for realising and promoting the CLFR system application. In addition, the optical design and performance evaluation of the CLFR system with polar orientation through simulation and experiment are limited in the literature.
3) Micro turbine, Stirling engine, Rankine cycle and fuel cells are more preferred for the micro trigeneration system. In particular, ORC demonstrates greater potential for involvement with simplicity, durability, flexibility and cost effectiveness.
4) Available demonstrations of the ORC-based micro trigeneration system are generally, fuelled with natural gas, biomass, solar thermal and fuel cells. Although the scroll expander truly fits the micro scale ORC system, little attention has been paid in the scroll-based ORC micro trigeneration system, which indicates potential for development of such trigeneration system.
5) The heat recovery component of the micro trigeneration system should be selected properly depending on requirement of thermal energy.
6) Absorption and adsorption chillers have been widely employed to the micro trigeneration system, while environmental-friendly desiccant cooling has been more attractive, especially the liquid desiccant cooling technology. The liquid

desiccant cooling is more flexible in utilisation and operation with independent air temperature and humidity controls. Different cooling technologies can be employed to handle the sensible heat load, the low electrical requirement and high COP makes the evaporative based liquid desiccant cooling system a promising option for the micro trigeneration system.

7) Membrane-based liquid desiccant cooling system eliminates the issue of desiccant entrainment and existing investigations confirm its efficient performance for dehumidification and cooling, but such a technology is still in research and development stage with limited studies concerning the application to the micro trigeneration system.
8) The operating strategy of the micro trigeneration should be reasonably proposed in accordance with the specific demands of electricity, heating and cooling for better energy and economic performances.
9) The existing literature demonstrates the respective feasibilities of CLFR, scroll-based ORC and MLDC for power generation systems. This indicates the possibility of integrating these technologies into an efficient micro trigeneration system.
10) A considerable number of theoretical and laboratory experimental studies of the micro trigeneration system have been conducted to prove system feasibility and evaluate system performance, especially for systems incorporating mature technologies, like diesel engine, micro gas engine, absorption and adsorption chillers. However, no work has been previously documented for a micro trigeneration system based on CLFR, scroll-based ORC and MLDC, which highlights the need and opportunity for research.

11) The micro trigeneration system is still under research and development stage, with limited demonstrations of the micro trigeneration system around the world. The literature also reveals the obstacles in development of the micro trigeneration market, such as implementation barriers of the micro trigeneration and the lack of policies, regulation and support framework.

Chapter 3: Micro Trigeneration System Development

3.1 Introduction

As highlighted in Chapter 2, the micro trigeneration system is still under research and development stage with a few available demonstrations around the world. To date, the integration of scroll-based ORC and MLDC for the micro trigeneration system has barely been investigated in the existing literature. In this chapter, a novel micro trigeneration system with a size of $1kW_e$ combining technologies of ORC and MLDC is designed and additionally, CLFR is considered as the primary energy source for powering the scroll-based ORC. Basically, this innovative system is featured with:

- Capability of running on solar energy;
- Multifunction with production of onsite electricity, heating and cooling;
- Reduction in primary energy consumption and greenhouse gas emissions;
- Summer operation by providing cooling and dehumidification;
- Independent control in supply air humidity and temperature without overcooling, reheating and water condensation problems.
- Cost effectiveness

Detailed description of this micro trigeneration system is presented in Section 3.2.

3.2 System description

In this section, description of the micro trigeneration system is presented in the following four parts: a brief introduction of the micro trigeneration system in Section 3.2.1 and explanation of the working principle of each sub-system in Section 3.2.2 (CLFR), Section 3.2.3 (scroll-based ORC) and Section 3.2.4 (MLDC).

3.2.1 Overall system

With an inclusion of CLFR for heat input, the novel micro trigeneration system comprises three main sub-systems: CLFR for energy supply, scroll-based ORC for power generation, MLDC for dehumidification and cooling, as the design concept depicted in Figure 3-1. The micro trigeneration system is capable of operating all the year around with simultaneous production of electricity, hot water supply and cooling. Electricity is generated by the ORC sub-system, hot water is provided with a heat recovery unit utilising the exhaust heat from the scroll expander, meanwhile cooling and dehumidification demands are handled by the MLDC sub-system as the outdoor hot and humid air is dehumidified and cooled to the desired supply condition.

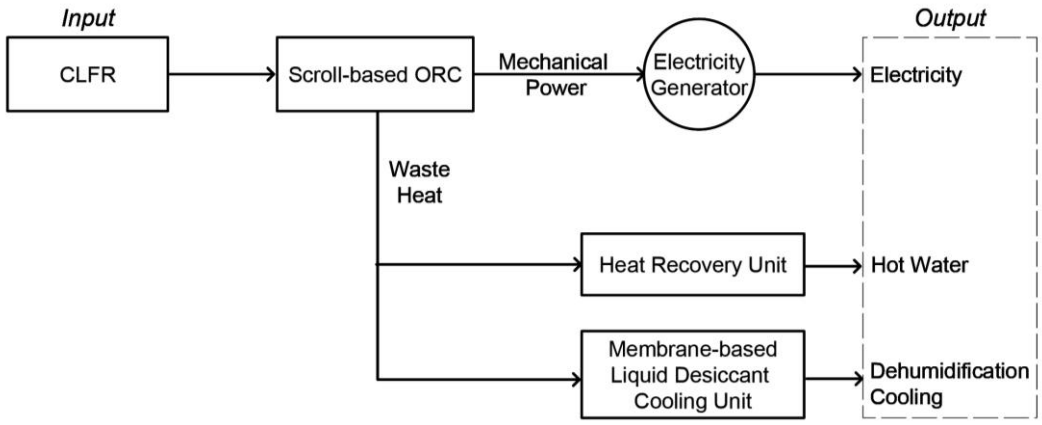


Figure 3-1 Schematic diagram of the proposed micro trigeneration system

The components employed in the micro trigeneration system are listed in Table 3-1.

Table 3-1 Components of the proposed micro trigeneration system

	Components
Primary energy source	CLFR (with flat mirrors and receivers) Auxiliary boiler Steam storage

	Components
ORC sub-system	Evaporator Scroll expander Electricity generator Recuperator Condenser Pump Refrigerant Storage Tank
MLDC sub-system	Membrane-based dehumidifier Membrane-based regenerator Evaporative cooler Fans Tanks Pumps Liquid-liquid heat exchangers Air-air heat exchanger

Design of the micro trigeneration system is presented schematically in Figure 3-2 with the addition of a typical design condition. Basically, the micro trigeneration system is flexible to operate in different modes depending on the end-user's energy demand by controlling valves V1, V2 and V3, for example power generation only, combined heat and power (CHP), combined cooling/dehumidification and power (CCP) and combined heat, power and cooling/dehumidification (CCHP) modes. For CHP and CCHP modes, the hot water supply temperature would be provided in a temperature range of 30-50°C, and the variation in the supply temperature can be realized by adjusting the mass flow rate of the exhaust working fluid. For CCP and CCHP modes, the exhaust temperature of the working fluid leaving from the scroll expander would be sufficient to heat the diluted solution up to a temperature range of 50-60°C in HX2. Additionally, the MLDC sub-system is capable of providing the supply air condition for indoor thermal comfort.

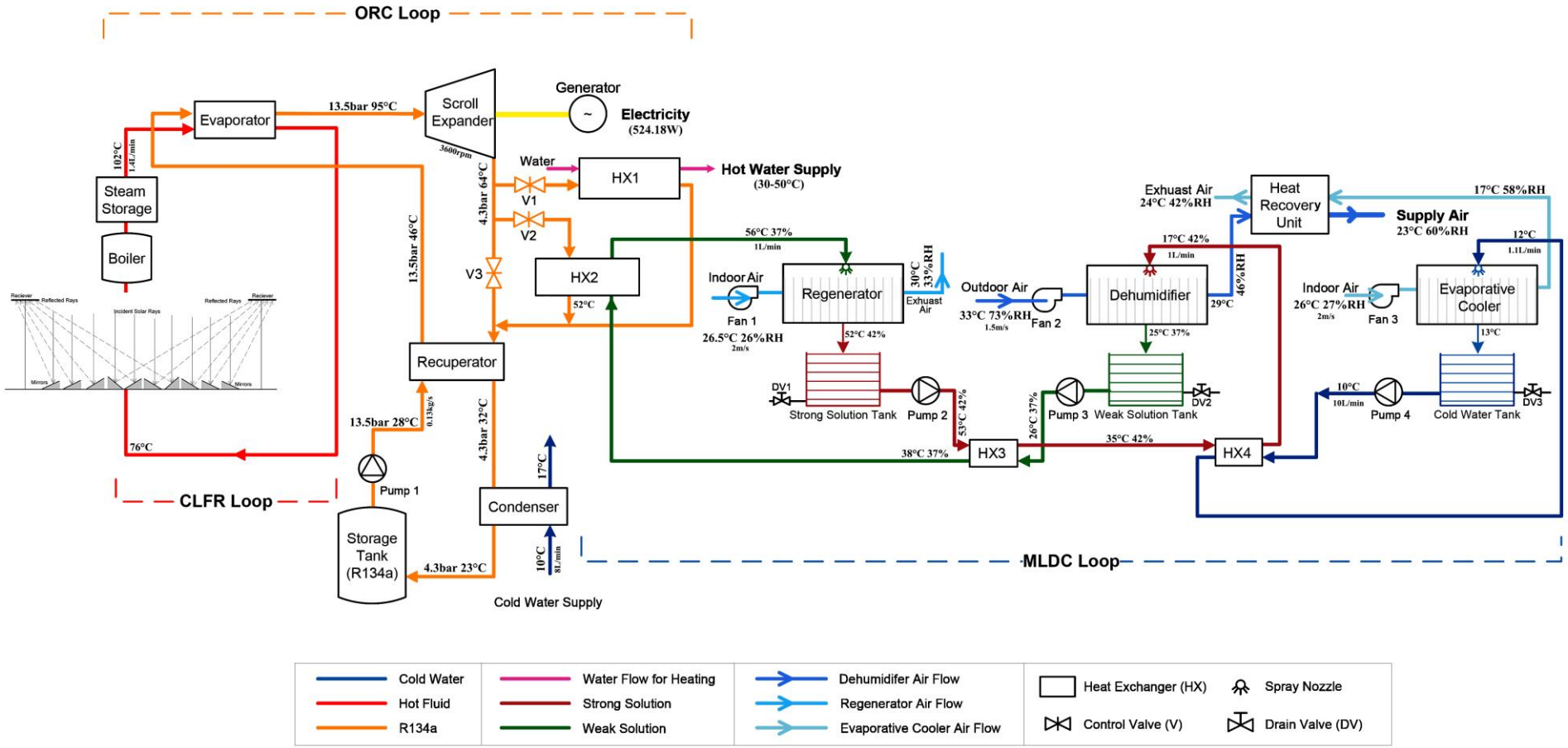


Figure 3-2 Illustration of the micro trigeneration system

3.2.2 Compact linear Fresnel reflector

For the sake of system sustainability, CLFR can be a choice for the primary energy source of the micro trigeneration system. The CLFR sub-system is designed with polar orientation so that series of mirrors at the predefined tilt angels and positions direct the solar rays onto the respective receivers. Considering simplicity and cost effectiveness, flat reflective mirrors and horizontally placed flat receivers are employed. The receivers absorb the reflected solar radiation and convert it into thermal energy so that the heat transfer fluid can be used for heating the refrigerant in the evaporator in the ORC loop. To ensure continuous operation, an auxiliary boiler is essential for providing supplementary heat in case the solar radiation level is too low; steam storage is used to provide a limited buffer to minimise the effect of solar transient due to passing clouds as well as to flatten the solar radiation peak for long time operation.

3.2.3 Scroll-based organic Rankine cycle

Figure 3-3 shows the schematic diagram of the ORC sub-system and a typical operating condition is indicated as well. The ORC sub-system is designed as a regenerative configuration with an additional recuperator, where the remaining heat of the exhaust vapour can be recovered to preheat the working fluid before entering the evaporator. The core component of the ORC sub-system, scroll expander-generator unit, consists of an oil-free scroll expander and a coupled electricity generator. Other main components of the system are refrigerant pump and plate heat exchangers (i.e. evaporator, recuperator and condenser). R134a is selected as the working fluid because of its better thermal efficiency and environmental performance.

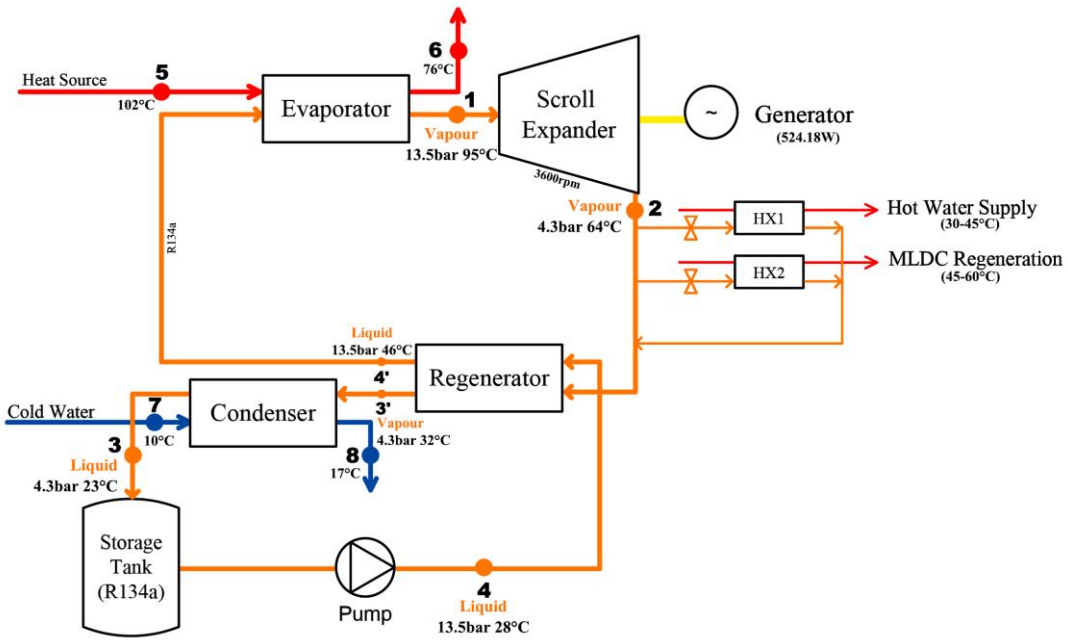


Figure 3-3 Schematic diagram of ORC sub-system

In terms of the cycle working process, a temperature-entropy (*T*-*s*) diagram is presented in Figure 3-4. A refrigerant pump delivers the working fluid R134a to the evaporator where the working fluid is heated to be high-pressure subcritical vapour by the heat source, which is represented as process 4→1 in Figure 3-4. The high-pressure vapour then flows into the scroll expander, where its enthalpy is converted into shaft work to drive the generator for electricity generation (i.e. 1→2). The exhaust low-pressure vapour exits the scroll expander and is led to heat exchangers HX1 and HX2 depending on the operating mode, where heat transfer takes place for: (a) hot water supply in HX1 (CHP and CCHP modes) and (b) heating the dilute liquid desiccant solution in HX2 (CCP and CCHP modes). Afterwards, the low-pressure vapour flows through a recuperator to a condenser, where it is condensed by cold water (i.e. 2→3). A storage tank is added to store the liquefied working fluid after condensation. To enhance the ORC performance, the recuperator allows heat transfer between the liquid working fluid from the storage tank and the mixed low-pressure vapour leaving from HX1 and HX2 (i.e. 2→3' and 4→4'). With an inclusion of the recuperator, the working

fluid temperature entering the evaporator increases, which hence the evaporation load can be reduced; on the other hand, the condenser inlet temperature decreases, which leads to reduction in the condensing heat load as well. A new cycle starts once the preheated working fluid is pumped back to the evaporator.

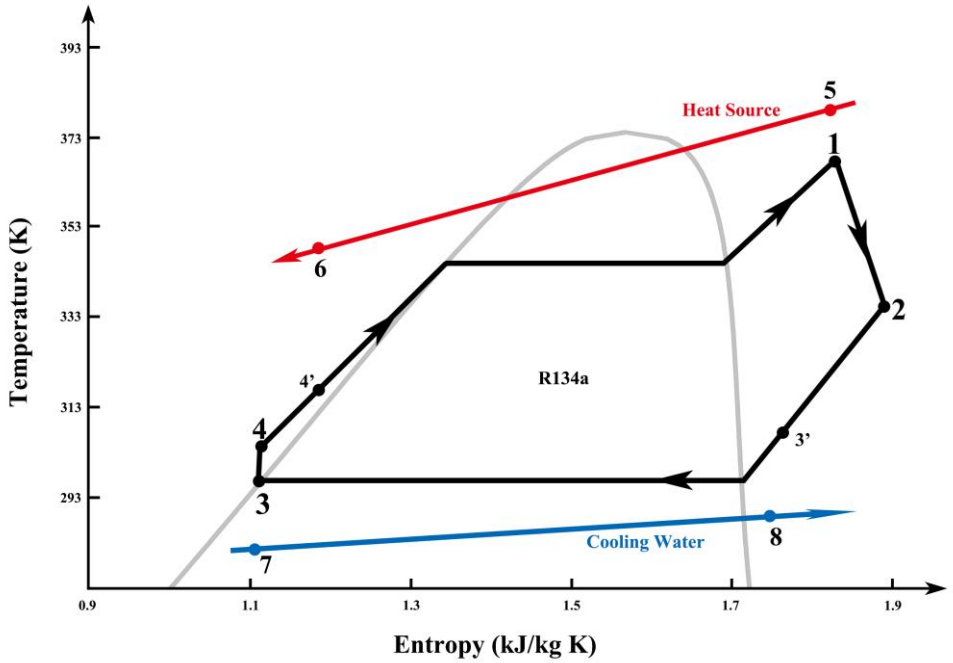


Figure 3-4 Temperature-entropy diagram of ORC sub-system

3.2.4 Membrane-based liquid desiccant cooling

The MLDC sub-system is developed for the proposed micro trigeneration system, as depicted in Figure 3-5. The sub-system mainly involves a membrane-based liquid desiccant dehumidifier and a membrane-based regenerator, an evaporative cooler, an air-air heat recovery unit, heat exchangers (i.e. HX2, HX3 and HX4), pumps and fans. The liquid desiccant used in the system is $CaCl_2$. Additionally, three storage tanks are set up for storing the regenerated and dilute liquid desiccant solution and cold water respectively. In the membrane-based dehumidifier and regenerator, porous membranes allow the $CaCl_2$ solution flowing downwards through solution channels, while airstream passes through air channels to fulfil dehumidification or regeneration.

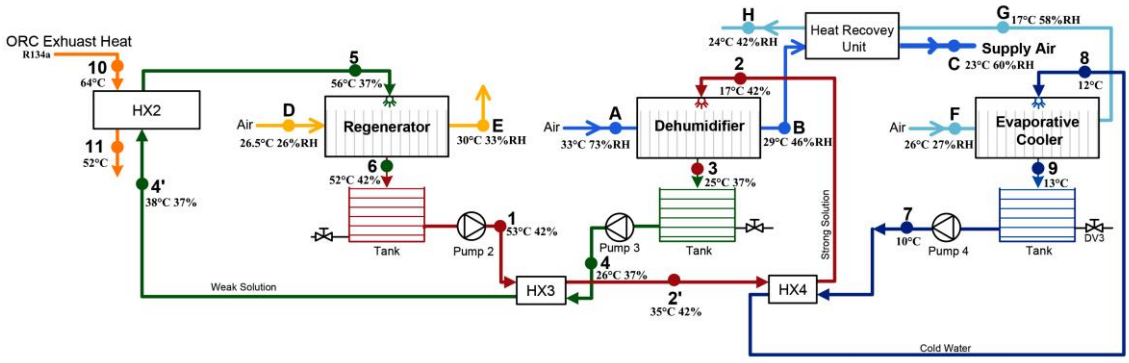


Figure 3-5 Schematic diagram of MLDC sub-system

A psychrometric chart provided under license from the Linric Company has been used to show the psychrometric processes of air flow in the MLDC sub-system, as shown in Figure 3-6. During operation, the outdoor hot and humid air is firstly dehumidified through absorption by the liquid desiccant solution in the dehumidifier (i.e. A→B) and the dried air is then cooled by the secondary airflow exiting from the evaporative cooler in the air-to-air heat recovery unit to the desired supply temperature (i.e. B→C). Regeneration occurs as moisture is vaporised from the liquid desiccant solution and absorbed by the passing airstream (i.e. D→E). On the other hand, air is blown to the evaporative cooler, where direct evaporative cooling takes place (i.e. F→G) and the air leaves for the heat recovery unit to further cool the dehumidified air (i.e. G→H).

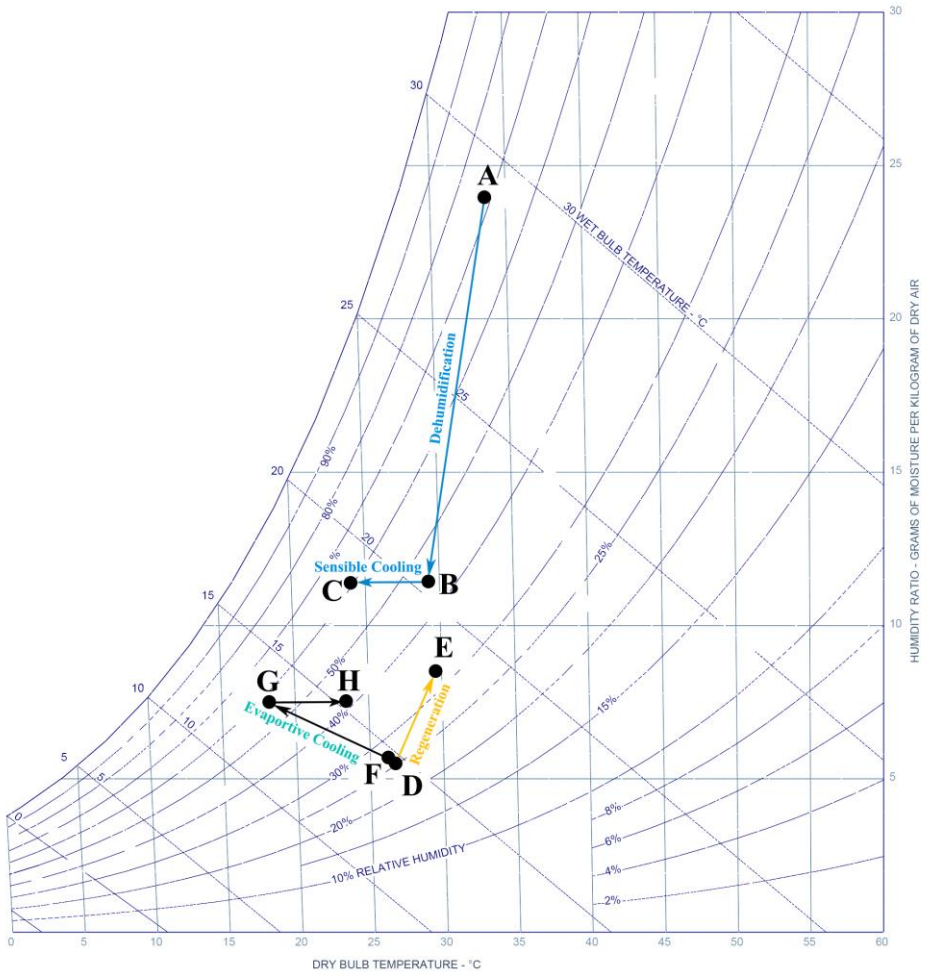


Figure 3-6 Psychrometric process of air in the MLDC sub-system

On the basis of the empirical correlation provided in the literature [241], a psychrometric chart illustrating the correlation of $CaCl_2$ solution equilibrium humidity ratio with solution concentration and temperature has been used to show the psychrometric processes of solution in the MLDC sub-system as seen in Figure 3-7. A liquid pump (i.e. Pump 2) delivers the regenerated solution to the dehumidifier for dehumidification process (i.e. 1→2). After dehumidification, the liquid desiccant solution becomes dilute (i.e. 2→3) and flows directly down into the storage tank. Pump 1 delivers the dilute solution from the storage tank to the heat exchanger HX3 (i.e. 3→4), where heat transfer takes place with the strong desiccant solution from the regenerator storage tank (i.e. 4→4' and i.e. 1→2'). Then the preheated weak solution

is heated by the exhaust heat from the ORC sub-system in HX2 and flows to the regenerator (i.e. 4'→5). In the regenerator, the airstream absorbs the moisture of the diluted desiccant solution thus strong solution is produced (i.e. 5→6). On the other hand, the evaporative cooler can be regarded as the cooling tower to provide cold water to precool the strong solution (i.e. 2'→2).

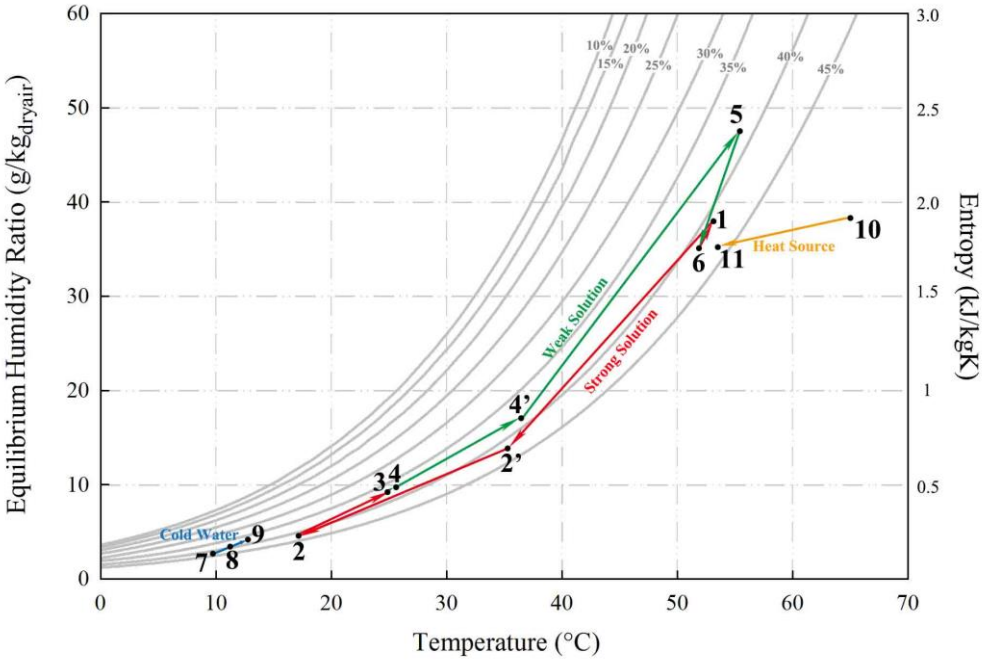


Figure 3-7 Psychrometric process of solution in the MLDC sub-system

3.3 Summary

A comprehensive development of the micro trigeneration system has been described in this chapter, including the system concept, a schematic system diagram and brief description of the working principle of each subsystem. In particular, the CLFR, scroll-based ORC and MLDC sub-systems have been explained in detail including the working principle and how the components connect with each other.

Chapter 4: Optical Performance Evaluation of CLFR

4.1 Introduction

In the micro trigeneration system, the CLFR can be an option for the primary energy source, as the CLFR is capable of subsequently exchanging the absorbed heat to the working fluid of the ORC sub-system. Based on the literature review presented in Section 2.3, studies in the optical design and performance evaluation of the CLFR system through simulation and experiment are very few. The majority of studies investigate the CLFR system with north-south and east-west orientations, while the polar orientated CLFR system has not received much attention. Furthermore, the optical performance comparison between the LFR and CLFR systems has been rarely mentioned in the literature, which would be necessary for accomplishment and wide promotion of the CLFR system application.

This chapter is aimed to demonstrate the feasibility of the CLFR system with polar orientation and present the optical design and performance evaluation. Besides, a comparative study of the concentration characteristics among the LFR, CLFR-complete and CLFR-hybrid systems is performed through geometrical modelling, ray tracing simulation and experimental testing. In order to validate the established geometrical model, experimental investigations are implemented with a small-scale test rig in Nottingham, UK. Additionally, the optical design of the CLFR-hybrid system is assessed theoretically from different design aspects (e.g. mirror array arrangement, solar field area, focal length and receiver tilt angle) by evaluating related geometrical parameters and optical performance. Therefore this chapter is structured in the following sections: Section 4.2 presents the geometrical modelling of the CLFR system; Section 4.3 describes the CLFR experimental set-up, instrumentation and experimental method; Section 4.4 compares optical performance of the LFR and CLFR

systems based on experimental and simulation results; Section 4.5 assesses the optical performance of the CLFR-hybrid system from various design perspectives based on the simulation results and Section 4.6 concludes this chapter.

4.2 Geometrical modelling of CLFR

The main purpose of this section is to develop a generic geometrical model of the CLFR system. The comprehensive model of the CLFR system is formed with two sub-models of the common tilting mirror array and the alternating array. In terms of the CLFR-hybrid system, its modelling requires both sub-models, while for modelling of CLFR-complete system, only sub-model of the alternating array is taken into consideration. The model descriptions together with essential equations are presented as: (a) the sub-model of the common tilting mirror array in Section 4.2.1 and (b) the model of the central alternating array in Section 4.2.2. Besides, a number of metrics are defined for evaluating the optical performance of the LFR and CLFR systems in Section 4.2.3. Furthermore, Section 4.2.4 presents the adopted simulation method, which involves programming in MATLAB and ray tracing simulation in TracePro.

Mathur, et al. [242] firstly developed a generalized methodology for the LFR system employing mirror elements of varying width in 1991 and then Zhang [73] further improved their methodology by considering different receiver configurations and orientations. Following the similar methodology presented in the literature [73, 242], geometrical modelling of the CLFR system is developed in this section. The modelling is on a basis of polar orientation, flat mirrors are defined with variable widths and spacing to eliminate end, shading and blocking effect. Two flat receivers are designed to absorb the reflected solar rays with a given full width ($2B$) and an inclination angle (β). In addition, the sun conical angle (represented by $2\Omega_1 = 32'$) is considered for a

more accurate optical design. The following assumptions are made for the geometrical modelling.

- The system has a perfect tracking scheme to follow the sun movement;
- Only direct/beam solar radiation is considered;
- The sunlight rays are incident axially, which perfectly and normally collimate on mirrors in the solar field;
- Flat mirrors are featured to be specularly reflective.

4.2.1 Common tilting mirror array modelling

For the CLFR-hybrid system, the mirror arrangement of the common tilting array near the receivers is identical to that of the LFR system, while mirror elements in the central field are placed with alternating tilts to focus the sunrays on the respective receivers. The geometrical model for the common tilting array of the CLFR-hybrid system is established, which refers to the modelling of LFR system presented in the literature [73, 242]. Regarding the axially symmetric feature of the CLFR-hybrid system, a basic geometry of the left-sided common tilting mirror array is illustrated in Figure 4-1, which has been redrawn on the basis of the literature [73, 242]. The central point of each mirror element is positioned along the horizontal plane (XX′), the vertical Z-axis passes through the central point of the flat receiver. Original point (*O*) of the defined coordinate system is the intersectional point of the X-axis and Z-axis. For modelling, focal length (*f*) represents the height of the receiver lower edge over the horizontal plane.

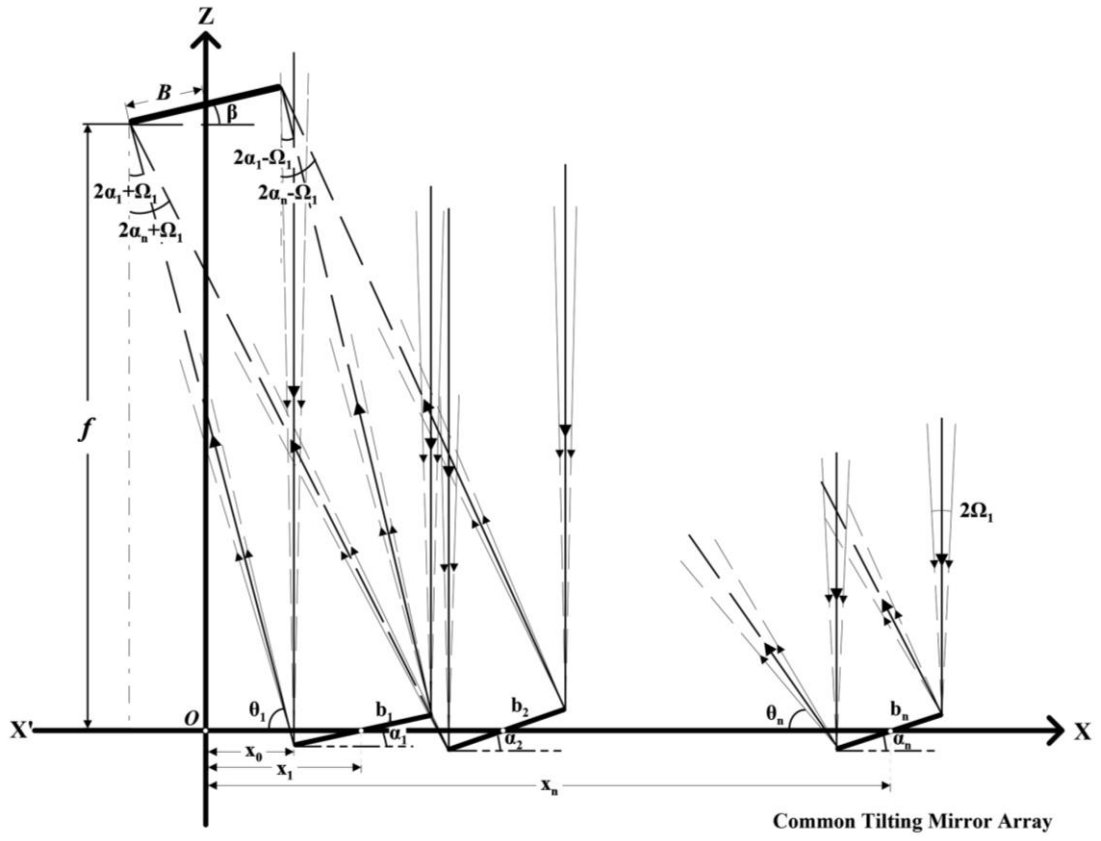


Figure 4-1 Schematic diagram of common tilting mirror array of CLFR system

Each mirror element is characterized by three optical variables: width ($W_n = 2b_n$), tilt angle (α_n), and reference position (x_n) which is determined as the distance from the original point (*O*) to the mirror element centre point. Theoretically, the tilt angle of a mirror element is proposed to ensure the extreme outer sunlight ray impinging on its lower edge strikes at the receiver lower edge after reflection, while the extreme outer ray impinging on the mirror upper edge strikes at the receiver upper edge. The angle between the reflected extreme outer solar ray impinging on the receiver lower edge and horizontal plane XX′ is introduced as θ_n. To avoid projection caused by the flat receiver, mirror elements are precluded underneath the receiver directly. Hence, the lower edge position of the first mirror element is $x_0 = B\cos\beta + (f + 2B\sin\beta)\cdot\tan\Omega_1$. Design variables of the first mirror element are given by:

$$\theta_1 = 90^\circ - 2\alpha_1 - \Omega_1 \tag{4-1}$$

$$\tan\theta_1 = \frac{f + b_1 \sin\alpha_1}{x_0 + B\cos\beta} \tag{4-2}$$

$$\tan\left(2\alpha_1 - \Omega_1\right) = \frac{2b_1\cos\alpha_1 + (f + 2B\sin\beta)\cdot\tan\Omega_1}{f - b_1\sin\alpha_1 + 2B\sin\beta} \tag{4-3}$$

$$W_1 = 2b_1 \tag{4-4}$$

$$\mathrm{x}_1 = x_0 + b_1\cos\alpha_1 \tag{4-5}$$

To eliminate shading and blocking problems, the sunlight rays impinging on the lower edge of the second mirror firstly touches the upper edge of the first mirror element and then strikes at the receiver lower edge after reflection. Following the similar logic, design variables of the nth mirror element are defined as:

$$\theta_n = 90^\circ - 2\alpha_n - \Omega_1 \tag{4-6}$$

$$\tan\theta_{\mathrm{n}} = \frac{f + b_{\mathrm{n}}\sin\alpha_{\mathrm{n}}}{B\cos\beta + x_{\mathrm{n}} - b_{\mathrm{n}}\cos\alpha_{\mathrm{n}}} \tag{4-7}$$

$$\tan\left(2\alpha_{\mathrm{n}} - \Omega_1\right) = \frac{x_{\mathrm{n}} - B\cos\beta + b_{\mathrm{n}}\cos\alpha_{\mathrm{n}}}{f - b_{\mathrm{n}}\sin\alpha_{\mathrm{n}} + 2B\sin\beta} \tag{4-8}$$

$$\frac{2b_1}{\sin\theta_2} = \frac{x_2 - b_2\cos\alpha_2 - x_0}{\sin\left(180^\circ - \theta_2 - \alpha_1\right)} \quad \text{If n=2} \tag{4-9}$$

$$\frac{2b_{\mathrm{n\text{-}1}}}{\sin\theta_{\mathrm{n}}} = \frac{x_{\mathrm{n}} - b_{\mathrm{n}}\cos\alpha_{\mathrm{n}} - x_{\mathrm{n\text{-}1}} + b_{\mathrm{n\text{-}1}}\cos\alpha_{\mathrm{n\text{-}1}}}{\sin\left(180^\circ - \theta_{\mathrm{n}} - \alpha_{\mathrm{n\text{-}1}}\right)} \quad \text{If n>2} \tag{4-10}$$

4.2.2 Alternating mirror array modelling

A schematic diagram of the CLFR-hybrid system for modelling the central alternating mirror array is presented in Figure 4-2. The total solar field width (*W*) of the CLFR-hybrid system is defined as the distance between the two receiver centre points. The gap between the last mirror element in the common tilting array and first adjacent alternating mirror is represented as *D*, and the gap of two consecutive mirror elements with opposite tilting directions in the alternating array is defined as *d*. According to different optical design requirements, *D* and *d* can be adjusted appropriately. To address shading and blocking effect, two different mirror arrangements are proposed depending on the lower edge positions of two adjacent mirrors. One case is that the extreme outer solar ray impinging on the prior mirror element's lower edge touches the lower edge of the latter mirror element and finally strikes at the receiver's lower edge after reflection (e.g. see the arrangement of the first and second mirrors in the alternating array with $b_{c1}\sin\alpha_{c1} \geq b_{c2}\sin\alpha_{c2}$ in Figure 4-2). The other one is that the extreme outer solar ray impinging on the latter mirror's lower edge touches the lower edge of the prior mirror element and strikes at the receiver's lower edge after reflection (e.g. see the arrangement of the third and fourth mirrors in the alternating array with $b_{c3}\sin\alpha_{c3} < b_{c4}\sin\alpha_{c4}$ in Figure 4-2).

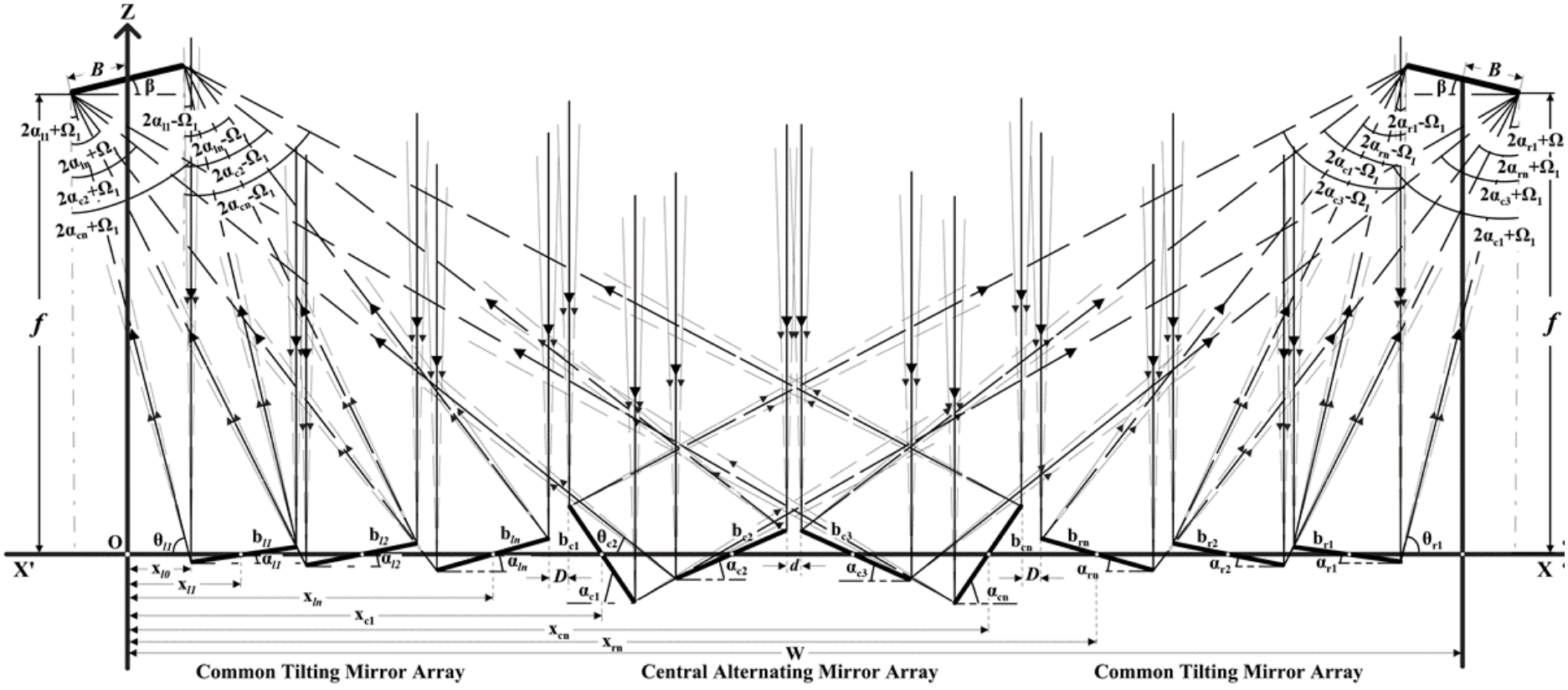


Figure 4-2 Schematic diagram of CLFR-hybrid system

The upper edge position of the last mirror element in the left tilting array is given as $x_{lo} = x_{ln} + b_{ln}\cos\alpha_{ln}$. Consequently, the associated variables of the first alternating mirror element are given by:

$$\theta_{c1} = 90^{\circ} - 2\alpha_{c1} - \Omega_1 \tag{4-11}$$

$$\tan\theta_{c1} = \frac{f + b_{c1}\sin\alpha_{c1}}{W - (x_{lo} + D + 2b_{c1}\cos\alpha_{c1}) + B\cos\beta} \tag{4-12}$$

$$\tan\left(2\alpha_{c1} - \Omega_1\right) = \frac{W - (x_{lo} + D)}{f - b_{c1}\sin\alpha_{c1} + 2B\sin\beta} \tag{4-13}$$

In the central alternating solar field, the even and odd mirror elements have different features as they redirect the solar rays to two respective receivers. Design variables of the even mirror elements are defined as:

$$\theta_{cn} = 90^{\circ} - 2\alpha_{cn} - \Omega_1 \tag{4-14}$$

$$\tan(\theta_{cn}) = \frac{f + b_{cn}\sin\alpha_{cn}}{x_{cn} - b_{cn}\cos\alpha_{cn} + B\cos\beta} \tag{4-15}$$

$$\tan\left(2\alpha_{cn} - \Omega_1\right) = \frac{x_{cn} + b_{cn}\cos\alpha_{cn} - B\cos\beta}{f - b_{cn}\sin\alpha_{cn} + 2B\sin\beta} \tag{4-16}$$

For the case that the prior mirror's lower edge is lower than that of the latter one (i.e. $b_{c(n-1)}\sin\alpha_{c(n-1)} \geq b_{cn}\sin\alpha_{cn}$),

$$\tan(\theta_{c(n-1)}) = \frac{b_{c(n-1)}\sin\alpha_{c(n-1)} - b_{cn}\sin\alpha_{cn}}{(x_{cn} - b_{cn}\cos\alpha_{cn}) - (x_{c(n-1)} + b_{c(n-1)}\cos\alpha_{c(n-1)})} \tag{4-17}$$

For the other case that the prior mirror's lower edge is higher than that of the latter one (i.e. $b_{c(n-1)}\sin\alpha_{c(n-1)} < b_{cn}\sin\alpha_{cn}$),

$$\tan(\theta_{cn}) = \frac{b_{cn}\sin\alpha_{cn} - b_{c(n-1)}\sin\alpha_{c(n-1)}}{(x_{cn} - b_{cn}\cos\alpha_{cn}) - (x_{c(n-1)} + b_{c(n-1)}\cos\alpha_{c(n-1)})} \tag{4-18}$$

On the other hand, variables of the odd mirror elements are given as:

$$\theta_{cn} = 90^{\circ} - 2\alpha_{cn} - \Omega_1 \tag{4-19}$$

$$\tan(\theta_{cn}) = \frac{f + b_{cn}\sin\alpha_{cn}}{W - (x_{c(n-1)} + b_{c(n-1)}\cos\alpha_{c(n-1)} + d + 2b_{cn}\cos\alpha_{cn}) + B\cos\beta} \tag{4-20}$$

$$\tan\left(2\alpha_{cn} - \Omega_1\right) = \frac{W - (x_{c(n-1)} + b_{c(n-1)}\cos\alpha_{c(n-1)} + \mathrm{d}) - B\cos\beta}{f - b_{cn}\sin\alpha_{cn} + 2B\sin\beta} \tag{4-21}$$

$$x_{cn} = x_{c(n-1)} + b_{c(n-1)}\cos\alpha_{c(n-1)} + d + b_{cn}\cos\alpha_{cn} \tag{4-22}$$

Regarding the modelling of the CLFR-complete, the established model of the alternating mirror array can be adopted by defining the upper edge position of the first mirror element on the left side as $x_{co} = B\cos\beta + (f + 2B\sin\beta)\cdot\tan\Omega_1$.

4.2.3 Optical performance evaluation metrics

Basically, optical performances of the LFR and CLFR systems are mainly evaluated by three factors, namely the geometrical concentration, the ground utilisation ratio and the solar illumination on the receiver surface. For the system with horizontally orientated flat receiver(s), the geometrical concentration (*CR*) is defined as the ratio of the total mirror field area to the receiver surface area [243]. Hence, the *CR* of the LFR system is expressed as:

$$CR_{LFR} = \frac{\sum_{n=1}^{N_m} W_n\cos\alpha_n}{2B} \tag{4-23}$$

Where N_m is total number of mirror elements in the LFR system.

For the CLFR-hybrid system, *CR* is given by:

$$CR_{\text{CLFR-hybrid}} = \frac{\sum_{\text{ln}=1}^{N_{\text{m\_ln}}} W_{\text{ln}} \cos\alpha_{\text{ln}} + \sum_{\text{rn}=1}^{N_{\text{m\_rn}}} W_{\text{rn}} \cos\alpha_{\text{rn}} + \sum_{\text{cn}=1}^{N_{\text{m\_cn}}} W_{\text{cn}} \cos\alpha_{\text{cn}}}{4B} \tag{4-24}$$

Where subscripts ln and rn indicate mirror elements in the left-sided and right-sided common tilting arrays respectively, and cn represents an alternating mirror in the central solar field.

For the CLFR-complete system, *CR* is defined as:

$$CR_{\text{CLFR-complete}} = \frac{\sum_{n=1}^{N_{\text{m}}} W_{\text{n}} \cos\alpha_{\text{n}}}{4B} \tag{4-25}$$

On the other hand, the ground utilisation ratio (*K*) implies the ratio of the total mirror field area to the total solar field area. For the LFR system, it is expressed as:

$$K_{\text{LFR}} = \frac{\sum_{\text{n}=1}^{N_{\text{m}}} W_{\text{n}} \cos\alpha_{\text{n}}}{2\cdot(x_{\text{n}} + b_{\text{n}} \cos\alpha_{\text{n}}) - 2B} \tag{4-26}$$

Where $x_{\text{n}} + b_{\text{n}} \cos\alpha_{\text{n}}$ represents half width of the solar field of the LFR system.

For the CLFR-hybrid and CLFR-complete systems, *K* is determined as:

$$K_{\text{CLFR-hybrid}} = \frac{\sum_{\text{ln}=1}^{N_{\text{m\_ln}}} W_{\text{ln}} \cos\alpha_{\text{ln}} + \sum_{\text{rn}=1}^{N_{\text{m\_rn}}} W_{\text{rn}} \cos\alpha_{\text{rn}} + \sum_{\text{cn}=1}^{N_{\text{m\_cn}}} W_{\text{cn}} \cos\alpha_{\text{cn}}}{W - 2B} \tag{4-27}$$

$$K_{\text{CLFR-complete}} = \frac{\sum_{\text{n}=1}^{N_{\text{m}}} W_{\text{n}} \cos\alpha_{\text{n}}}{W - 2B} \tag{4-28}$$

4.2.4 Simulation approach

A comprehensive simulator based on the developed geometrical model is constructed in MATLAB. The programed simulator is able to provide the mirror element profile including the width, tilt angle and reference position for both the LFR and CLFR system with polar orientation. A flow chart showing the overall simulation process is presented in Figure 4-3. To investigate the solar radiation distribution on receiver surfaces, ray tracing simulation is implemented with the advanced TracePro program. The ray tracing simulation is capable of verifying the defined tilt angles and shifts of mirrors whether lateral, shading and blocking problems exist. In TracePro program, flat mirrors are assigned with reflectance of 95% and receivers are defined with absorptance of 0.9. For simulation, the solar field is divided into a large number of equal divisions and in each division, a cone contains a certain number of generated uniform solar rays, which are all defined to be normally impinged onto the solar field. The solar irradiance value as the input parameter in the radiation profile is determined in accordance with the local weather condition. In such a way, the absorbed solar radiation value could be validated with the experimental data under the same weather condition.

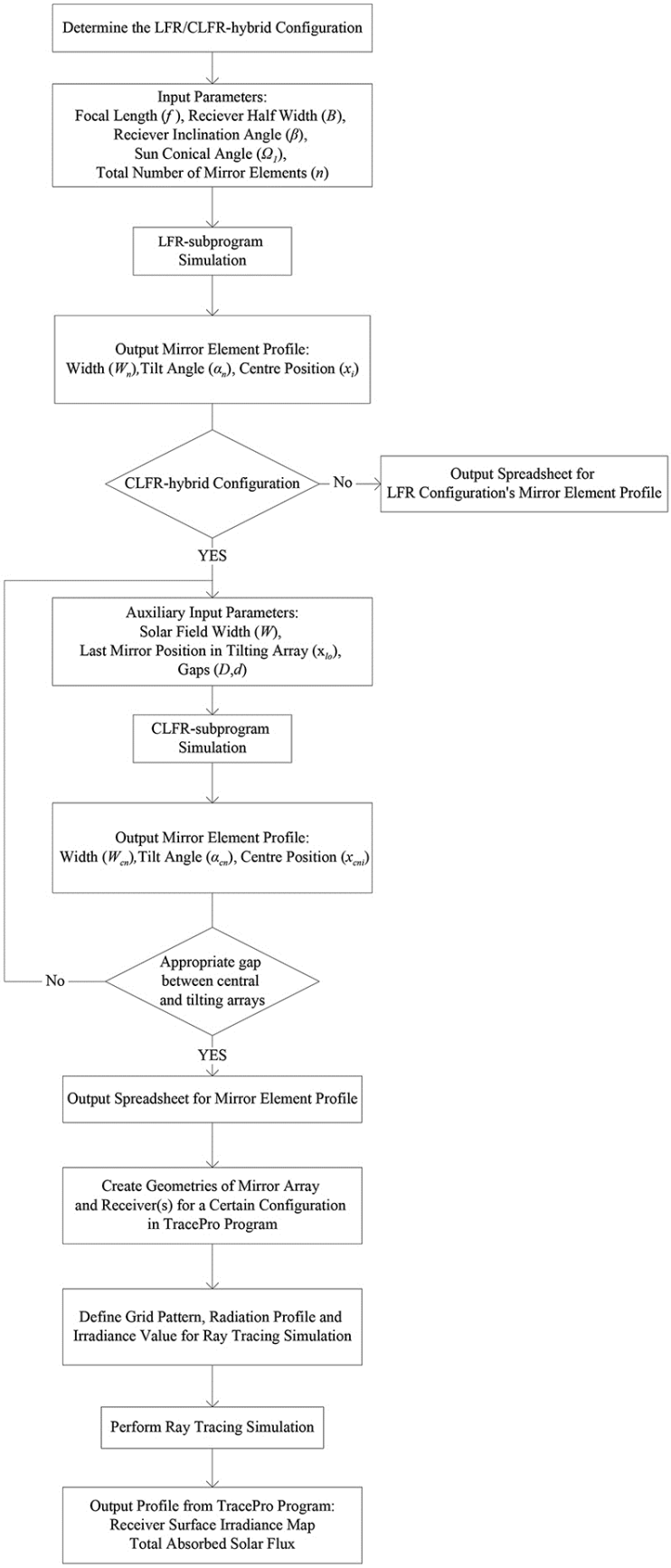


Figure 4-3 Flow chart of CLFR simulation process with MATLAB and TracePro

This section has established the comprehensive modelling for both the CLFR-hybrid and CLFR-complete systems and evaluation metrics regarding the optical performance have been determined as well. In addition, the simulation method of the CLFR system has been discussed. Next, Section 4.3 introduces the experimental set-up of the CLFR system.

4.3 CLFR experimental set-up

A small-scale CLFR test rig is designed and constructed in Nottingham, UK, latitude of 52.97° and longitude of 1.18°. In this section, the experimental instrumentation is firstly introduced in Section 4.3.1 and the experimental method is then explained in Section 4.3.2.

4.3.1 Experiment description

Due to the small-scale set up of the CLFR system, narrow flat mirrors and horizontally placed flat receivers are employed. The CLFR system has an overall solar field area of 2.10m^2, which makes it feasible to track the sun movement freely. Specifications of the CLFR experimental set-up are presented in Table 4-1.

Table 4-1 Specifications of CLFR experimental set-up

Solar Field	
Width	2100mm
Length	1000mm
Focal length range	1000mm-2000mm
Mirror and Receiver Profiles	
Mirror material	Glass
Mirror element length	1000mm
Mirror element thickness	5mm
Receiver width	64mm

Receiver length	1000mm
Receiver inclination angle	0°

As shown in Figure 4-4, the test rig mainly comprises a base framework, a solar field platform with supporting beams, saw-tooth shaped bases, mirror elements and receivers with flexible supporting structures. For the sake of polar orientation, the inclination angle and position of the solar field platform correspond to the solar altitude and azimuth at a specific time. Hence, supporting beams are employed to provide an accurate inclination angle for the solar field platform. A series of flat mirror strips are placed onto the saw-tooth shaped bases at the proposed positions and tilt angles, which are obtained from the theoretical modelling.

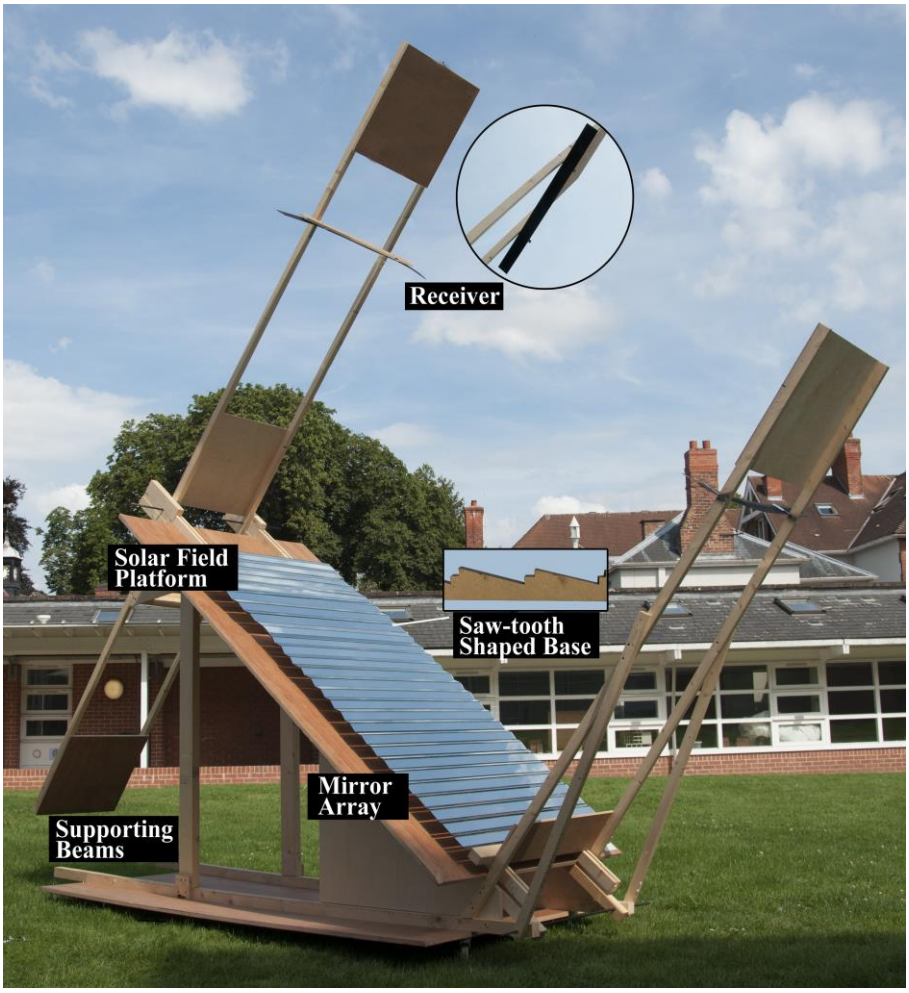


Figure 4-4 Photo of CLFR test rig

4.3.2 Experimental method

On the whole, the experiment is aimed to obtain the total received solar intensity on receiver surfaces. To achieve this, flux measurement is required either using a direct or indirect measuring method. Calorimeter and flux sensor are the common direct measuring instruments to provide flux value on a target, while an indirect device is capable of providing a continuous flux map. In particular, digital camera is mostly preferred as the indirect measuring instrument by offering good resolution. For a good quality digital camera, a sensor is made up of millions of small photosensitive sensors (pixels) and outputs a voltage directly relating to the amount of photons that strike it [244]. The amount of photons hitting each pixel is directly proportional to the flux incident on a target. Under the experimental investigations, a Nikon D90 digital camera is used to produce irradiance maps on receiver surfaces. Reference images of receiver surfaces are also taken under different irradiance levels for calibration. Moreover, a pyranometer is employed to record the solar radiation level during the testing period. In terms of data processing, the image processing toolbox in MATLAB is used to obtain the received solar flux.

The experimental set-up of the CLFR system and the adopted experimental method have been detailed in this section. Next, Section 4.4 provides a comparative study of the optical performance between the LFR and CLFR systems.

4.4 Optical performance comparisons of LFR and CLFR

In this section, optical performances of the LFR, CLFR-hybrid and CLFR-complete systems are investigated through experimental work and simulation, and thus comparisons are presented regarding the mirror array arrangement, concentration, ground utilisation ratio and absorbed solar energy. For the sake of operability with polar orientation, the solar field with a width of 2100mm and a length of 1000mm is determined for the LFR, CLFR-hybrid and CLFR-complete systems at a focal length of 1500mm. In addition, three different arrangements are proposed for the CLFR-hybrid configuration with different ratios of the common tilting mirrors to the alternating ones.

4.4.1 Mirror array arrangement

Table 4-2 lists the total number of mirror elements for each investigated system. It can be observed that the total number of mirror elements varies greatly for different configurations. With the same solar field width and focal length, the CLFR-complete system accommodates 56 pieces of flat mirrors, while the LFR system only allows 42 pieces to be placed in the solar field. It is also seen that with fewer mirrors in the common tilting array, more mirrors could be added in the alternating array. The results imply that the alternating array requires less ground area, which contributes to a more densely packed array arrangement for the CLFR system.

Table 4-2 Total number of mirrors for LFR, CLFR-hybrid and CLFR-complete systems

Configuration	Number of Mirrors		Total Number of Mirror Elements	Percentage of Alternating Mirrors
	Common Tilting Array	Alternating Array		
LFR	42	0	42	0%
CLFR-hybrid A	14	36	50	72%
CLFR-hybrid B	22	24	46	52%
CLFR-hybrid C	28	16	44	36%
CLFR-complete	0	56	56	100%

4.4.2 Concentration and ground utilisation ratios

Optical performance of the five systems is shown in Figure 4-5 on the basis of numerical modelling results. By comparison, the three CLFR-hybrid systems have relative higher concentration and ground utilisation ratios, which are in consistent with the findings in the literature [69]. Although the CLFR-complete system consists of more mirror elements, its concentration is lower than those of the three CLFR-hybrid configurations as a consequence of the large proportion of narrower mirrors located far from the respective targeted receivers. The theoretical analysis reveals that the CLFR-hybrid system could be a favourable alternative to the LFR system with higher concentration and ground usage ratios. It is also noteworthy that the combination of mirror elements placed in the common tilting and alternating arrays influences not only the geometrical aspect but also optical performance. Among the CLFR-hybrid A, B, C systems, the most densely packed CLFR-hybrid A system with comparatively fewer mirrors in the common tilting array has the best optical performance, the geometrical concentration of 15.14 and ground utilisation ratio of 0.95 are obtained respectively.

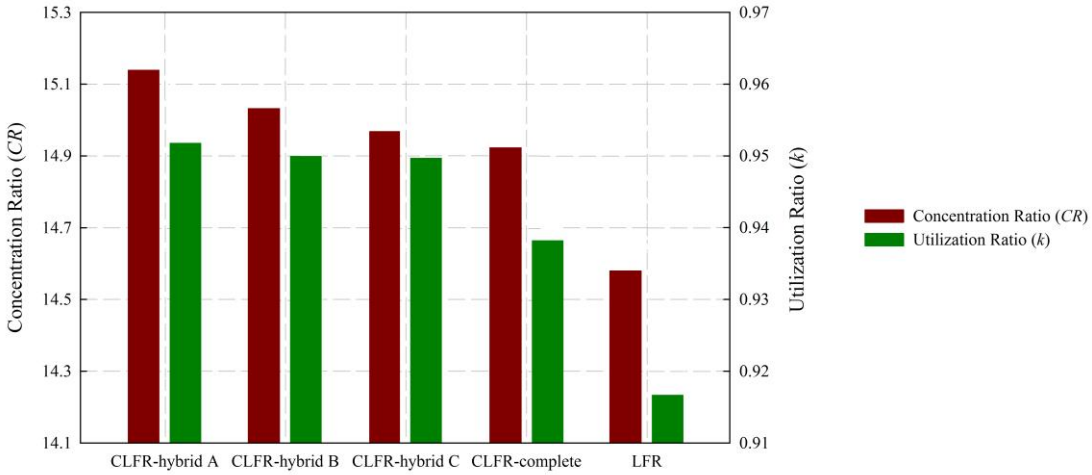


Figure 4-5 Concentration and ground utilisation ratios of LFR, CLFR-hybrid and CLFR-complete systems

4.4.3 Received solar energy

Based on the geometrical profile of the mirror elements derived through modelling, experimental investigations are conducted along with ray tracing simulation to quantify the solar illuminance on receiver surfaces. The total received solar energy on receiver surfaces of the five systems is obtained from experiment and ray tracing simulation as presented in Figure 4-6. The input solar irradiance value in TracePro program is in accordance with the testing weather condition, which is 600W/m^2. It is observed that the variation pattern of simulation results matches with that of the experimental data. The simulation results demonstrate that 1150W of the solar energy is received by the CLFR-hybrid A system, whereas around 1055W is obtained from the experimental testing. With respect to the energy efficiency of the CLFR system, it is defined as the ratio of the total received energy on receiver surfaces to the total incident energy on mirrors [69]. Referring to the experimental data, the energy efficiency of the CLFR-hybrid A system is approximately 91.3%, while 88.47% and 86.03% are obtained for the CLFR-complete and LFR systems.

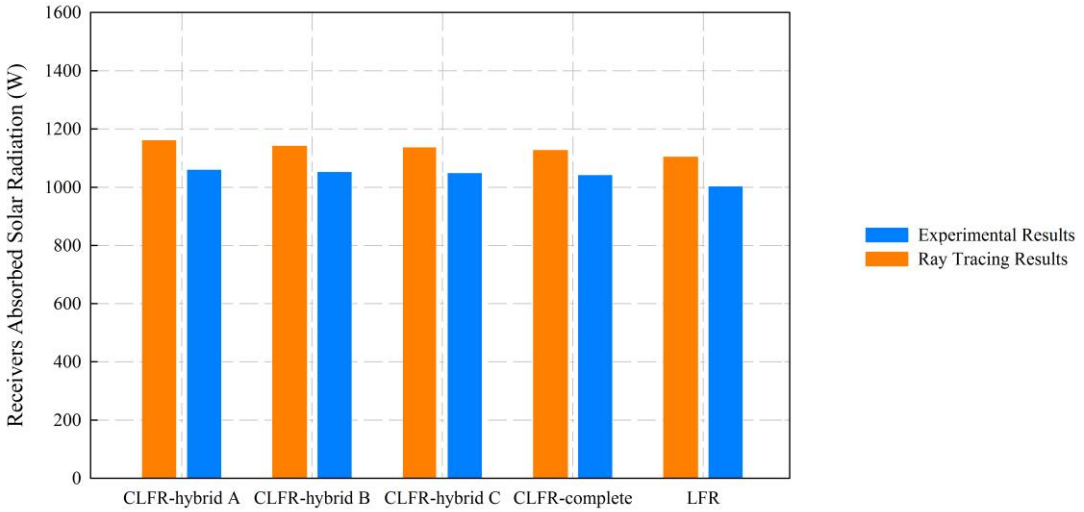


Figure 4-6 Simulation and experimental results of received solar energy for LFR, CLFR-hybrid and CLFR-complete systems

The main reasons for the differences between the simulation and experimental results are as follows: (1) mirrors and receivers are assigned with ideal properties, for example mirror reflectance of 0.95 and receiver absorptance of 0.9 are assumed for ray tracing simulation in TracePro program. However, for the experimental set up, the reflectance of mirrors and absorptance of flat receivers may differ; (2) although the system with polar orientation tracks the sun movement freely, tracking errors may happen during testing, for instance the inaccurate positioning of the test rig; (3) the digital camera captures illuminance images on receiver surfaces, which may be also influenced by the surroundings and (4) errors may occur during the image processing in MATLAB, like for the calibration with reference flux images.

4.4.4 Comparison summary

In this section, comparison of the optical performance between the LFR and CLFR systems has been conducted through both ray tracing simulation and experimental tests. In particular, two different configurations of the CLFR system have been involved, namely the CLFR-complete and CLFR-hybrid. A good agreement has been noted

regarding the variation pattern between the ray simulation and experimental data. The following implications can be summarised:

(1) Compared to the LFR and CLFR-complete systems, better optical performance can be achieved for the CLFR-hybrid system.
(2) Numerical results indicate that the CLFR-hybrid system would be a favourable alternative to the LFR system with higher concentration and ground usage ratios.
(3) The more densely the CLFR-hybrid system is designed with fewer mirrors in the common tilting array, the better the optical performance.

Next, Section 4.5 provides the optical analysis of the CLFR-hybrid system based on theoretical investigations from various optical design perspectives.

4.5 Optical design of CLFR

In this section, a comprehensive optical analysis is presented, in which the optical design of the CLFR-hybrid system is investigated from different design aspects, including the limited solar field area in Section 4.5.1, limited total number of mirrors in Section 4.5.2, given focal length in Section 4.5.3 and variable receiver inclination angle in Section 4.5.4.

4.5.1 With limited solar field area

Based on the previous findings of Section 4.4, the CLFR-hybrid A system with the best optical performance is selected as the basic case to assess the effect of focal length on the optical performance, while the solar field width and length are set as 2100mm and 1000mm respectively. The gaps D and d are accordingly adjusted for the focal length varying from 1100mm to 1900mm. Firstly, the related mirror profile is

evaluated based on the geometrical modelling results. The mirror width variations of the CLFR-hybrid A system at different focal lengths are presented in Figure 4-7. Generally, the farther a mirror element is placed from its targeted receiver, the narrower width and larger tilt angle. However, the mirror width variation is more significant at a smaller focal length. For instance, mirror width varies from 53.7mm to 20.2mm at a focal length of 1100mm, while the variation is from 46.3mm to 25.2mm at a focal length of 1900mm. A similar finding regarding the geometrical aspect has been mentioned by Mathur, et al. [242] as well.

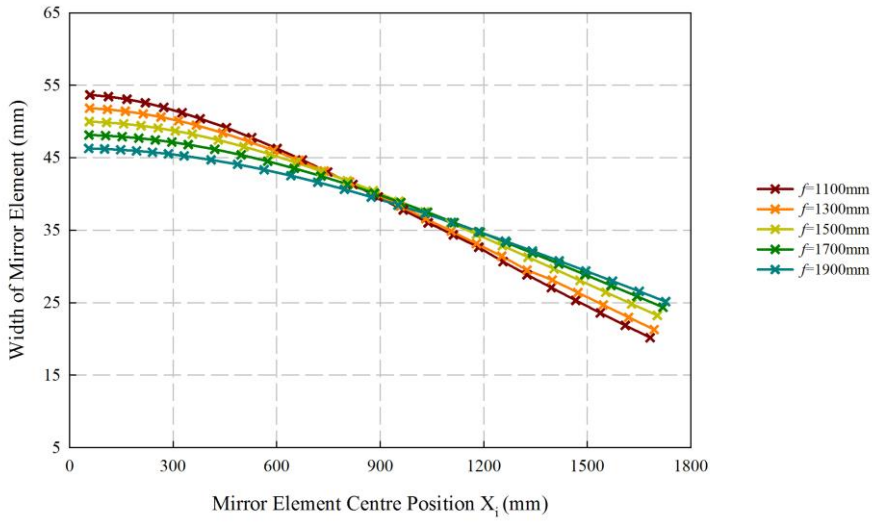


Figure 4-7 Mirror width variations for CLFR-hybrid A system at different focal lengths

In terms of the optical performance, the numerical results presented in Figure 4-8 show that the focal length influences both concentration and ground utilisation ratios when the solar field area is limited to a given value and there exists an optimum focal length. Both ratios gradually increase as the focal length rises from 1100mm to 1500mm, and decrease with a further increase in the focal length. For the investigated solar field area of 2.10m^2, the optimum focal length for the CLFR-hybrid A system is 1500mm, at which both concentration and ground utilisation ratios reach the maximum values.

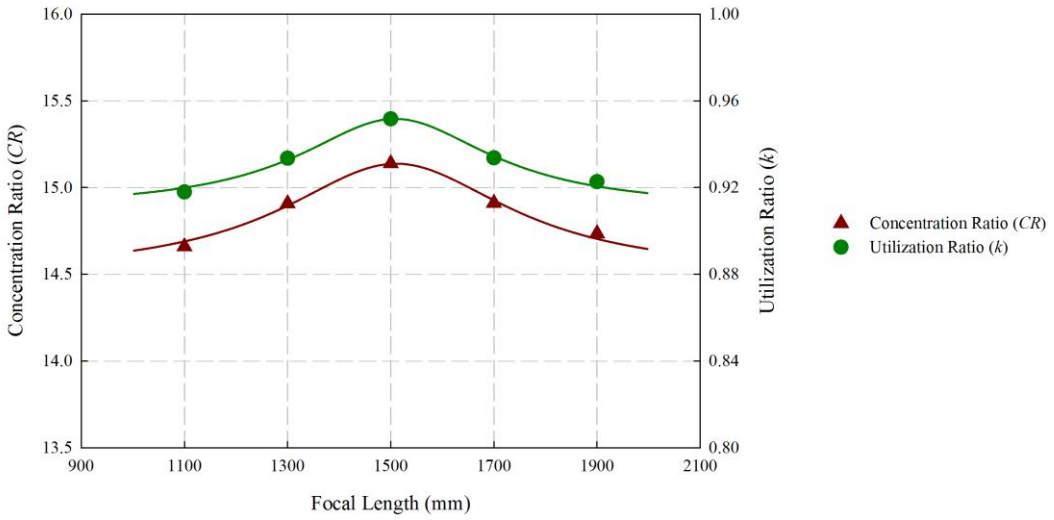


Figure 4-8 Variations of concentration and ground utilisation ratios with focal length for CLFR-hybrid A system

Variations in the concentration and ground utilisation ratios throughout the solar field of the CLFR-hybrid A system at a focal length of 1500mm are demonstrated in Figure 4-9. It can be seen that the concentration increases gradually with the mirror element position, while the ground utilisation ratio decreases conversely due to the increasing shift of mirror elements toward the solar field rim. As the solar field width is limited to 2100mm, the gap variables (i.e. *D* and *d*) in the central alternating array are defined accordingly, which may be larger than the gaps in the common tilting array. This leads to the notable drop in the ground utilisation ratio as the mirror element moves from the common tilting array to the central alternating array.

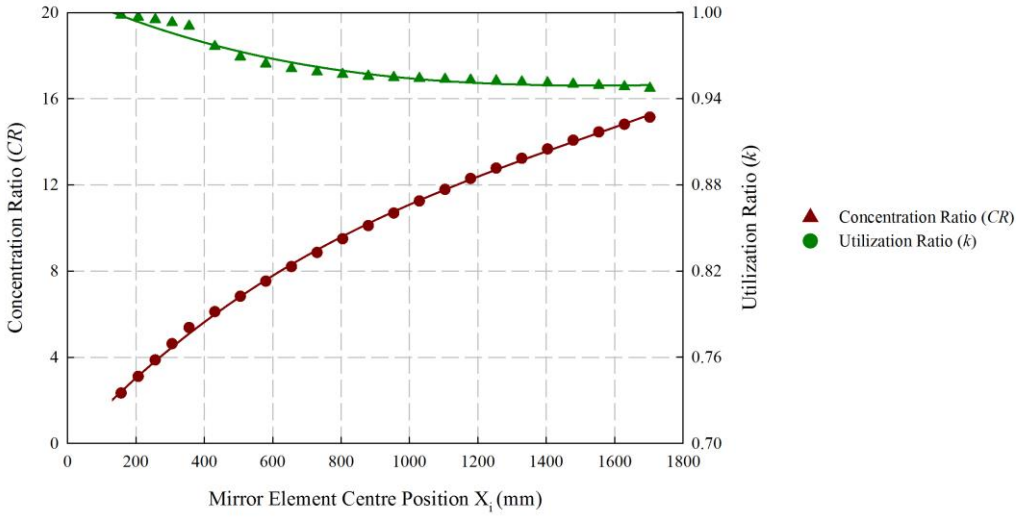


Figure 4-9 Variations of concentration and ground utilisation ratios for CLFR-hybrid A system with a focal length of 1500mm and solar field width of 2100mm

The experimental data for the CLFR-hybrid A system at different focal lengths are shown in Figure 4-10. Comparatively, the focal length has a more significant impact on the optical performance than that of the mirror arrangement. The results also reveal that the focal length should be optimised for optical design of the CLFR-hybrid system with a limited ground area to achieve better optical performance.

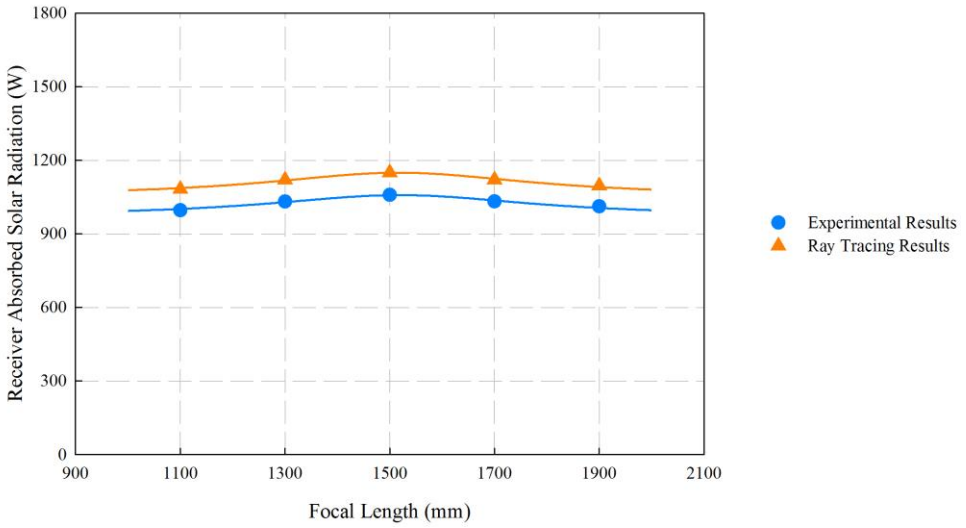


Figure 4-10 Simulation and experimental results of received solar energy for CLFR-hybrid A system

The ray tracing simulation is implemented to verify the proposed optical design on the basis of the geometrical modelling and produce the illuminance map. The ray tracing simulation result of the CLFR-hybrid A system with a solar field width of 2100mm and at a focal length of 1500mm is presented in Figure 4-11. It can be observed that the receivers on both sides receive all reflected rays from the proposed mirror array, which demonstrates the accuracy of the established geometrical model of the CLFR system.

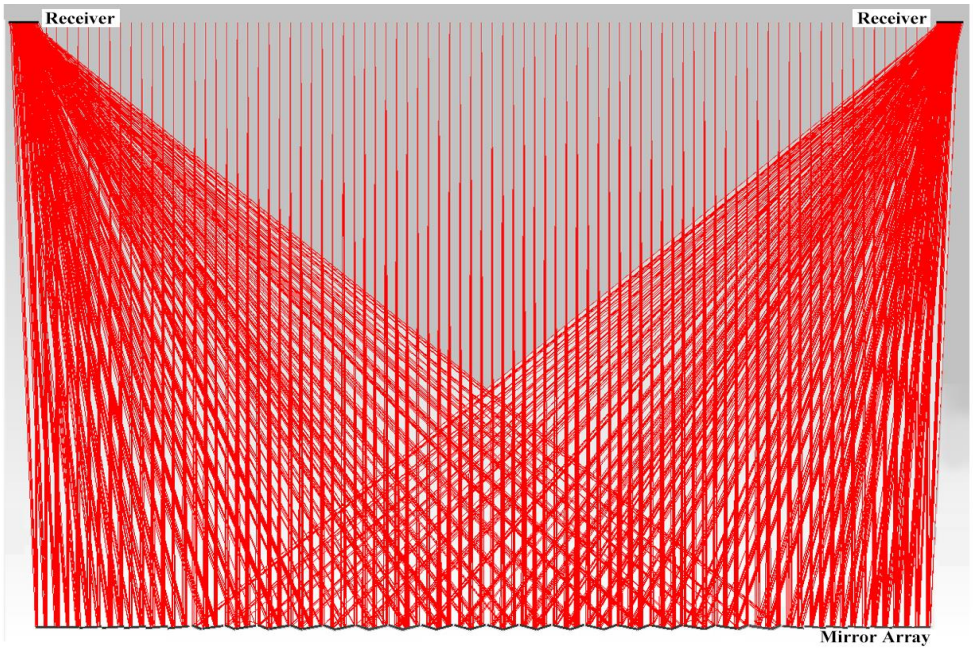
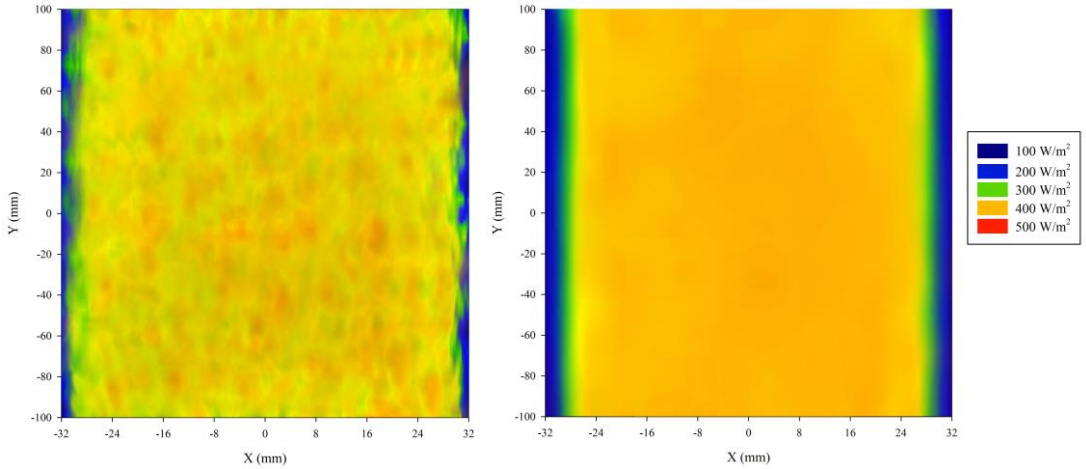


Figure 4-11 Ray tracing simulation result of CLFR-hybrid A

For the sake of simplicity, the solar radiation distribution on the receiver surface is obtained with only one mirror element through both experiment and ray tracing simulation, and related illuminance maps are presented in Figure 4-12. It is noted that almost the entire receiver surface is fully illuminated by the reflected solar rays from the mirror element, which is different from that of the point focusing Fresnel lens. The solar radiation distribution across the receiver surface as seen in the experimental image is not completely uniform, which mainly attributed to its uneven surface pattern. Comparatively, more uniform distribution on the receiver surface can be found in the

TracePro illuminance map except for the boundary regions. This is mainly due to the fact that the total number of generated solar rays for tracing is limited in TracePro program, and the generated rays from the defined solar source could not perfectly strike at the edges of each mirror element.



(a) (b)

Figure 4-12 Illuminance maps of receiver surface for CLFR-hybrid A system (a) experimental (b) ray tracing simulation results

4.5.2 With limited mirrors

Besides the design limitation of the solar field area, the total number of mirror elements could be another restriction for the practical optical design. Investigations are carried out for the CLFR-hybrid system with a fixed total number of mirrors as the focal length and solar field area vary accordingly to accommodate mirrors adequately. As listed in Table 4-3, to ensure 50 mirrors properly placed in the solar field, only a slight variation in the solar field width is observed while the focal length decreases from 2800mm to 700mm.

Table 4-3 Solar field widths for CLFR-hybrid system with the same total number of mirror elements

Configuration	Solar Field Width (mm)	Focal Length (mm)
CLFR-hybrid D	1900	2800
CLFR-hybrid E	2000	2400
CLFR-hybrid F	2050	2000
CLFR-hybrid A	2100	1500
CLFR-hybrid G	2050	1100
CLFR-hybrid H	1950	700

Variations of concentration and ground utilisation ratios for the CLFR-hybrid configurations with the focal length are shown in Figure 4-13. It is worth noting that the CLFR-hybrid A system with a focal length of 1500mm and the largest solar field area is the optimum solution for accommodating 50 mirror elements. The concentration increases as the focal length rises from 700mm to 1500mm, it reaches the maximum value of 15.14 as receivers are located at a height of 1500mm, and then decreases as the focal length continues to increase. Similarly, the ground utilisation ratio reaches the maximum value of 0.95 at a focal length of 1500mm. Thus, the results imply the necessity to identify the optimum focal length and solar field area for the CLFR-hybrid system when the mirror array arrangement is defined with limited total number of mirror elements.

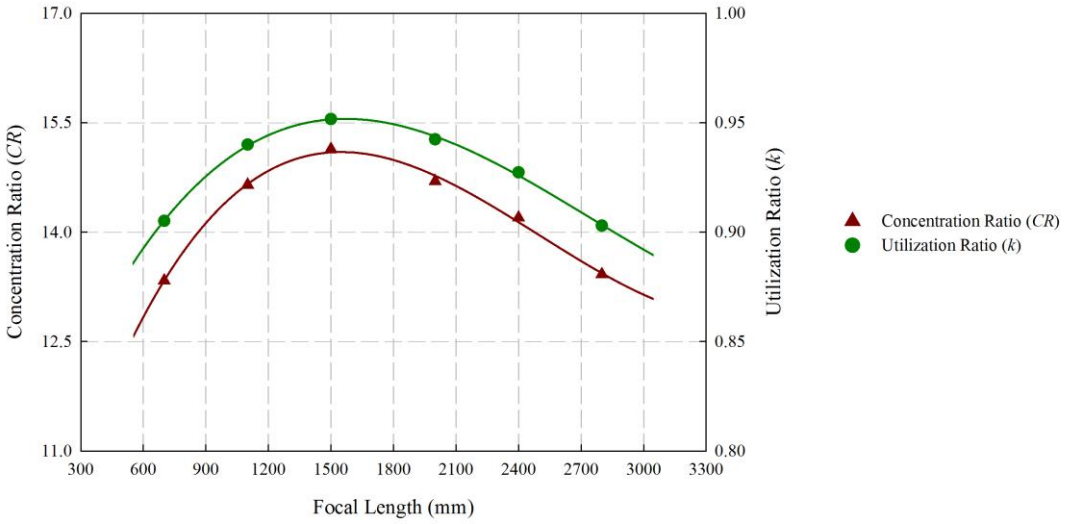


Figure 4-13 Variations of concentration and ground utilisation ratios with focal length for CLFR-hybrid system with 50 mirrors

4.5.3 At a given focal length

Explorations are then conducted to evaluate the optimum arrangement of the CLFR-hybrid A system at a fixed focal length of 1500mm for the solar field width ranging from 1500mm to 5000mm. As shown in Table 4-4, the proportion of mirrors in the central alternating array varies for different configurations. For a larger solar field area, fewer mirrors could be accommodated in the central alternating array while more mirrors are required in the common tilting array to achieve a higher concentration. For instance, approximately 63% of the total number of mirrors are placed in the central alternating array for the smallest solar field with a width of 1523mm, while only 5% of mirrors are found in the central alternating field for the largest solar field with a width of 4997mm. On the other hand, a wider solar field leads to a greater variation range in mirror width at the given focal length. Therefore the number of narrow mirrors should also be taken into consideration, as extremely narrow mirrors located far from the receivers could not be accepted for practical applications.

Table 4-4 Mirror arrangements of the CLFR-hybrid system at a fixed focal length of 1500mm

Configuration	Solar Field Width	Number of Mirrors			Mirror Width Range
		Alternating Array	Common Tilting Array	Total	
CLFR-hybrid I	1523mm	20	12	32	34.5-50mm
CLFR-hybrid J	2061mm	26	20	46	27.3-50mm
CLFR-hybrid M	3018mm	50	32	82	15.2-50mm
CLFR-hybrid L	4001mm	46	70	116	8.5-50mm
CLFR-hybrid M	4997mm	8	148	156	7-50mm

Figure 4-14 illustrates variations of concentration and ground utilisation ratios with the solar field width. It can be clearly seen that a larger solar field with more mirror elements leads to a higher concentration. Nonetheless, in order to avoid the shading and blocking problems, the total gap between adjacent mirrors increases accordingly with the solar field width, which results in a lower ground utilisation ratio. Consequently, a comprehensive procedure should be followed to derive an optimal design of the CLFR-hybrid system, by taking the mirror array arrangement, focal length, concentration characteristic and ground usage into account.

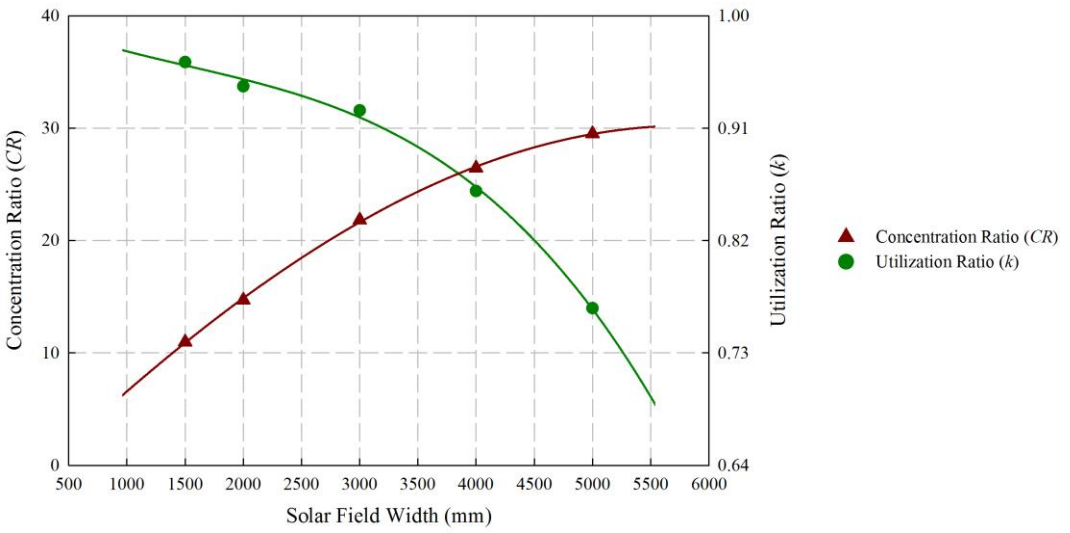


Figure 4-14 Variations of concentration and ground utilisation ratios with solar field width for CLFR-hybrid system at a focal length of 1500mm

4.5.4 With variable receiver inclination angles

Preceding investigations are conducted for the CLFR-hybrid system with horizontally oriented flat receivers, nevertheless flat receivers can be placed at an inclination angle. To evaluate the effect of receiver inclination angle on the optical performance of the CLFR-hybrid system, an angle range of 0° to 90° is considered for both receivers of the CLFR-hybrid A system at a focal length of 1500mm and with a solar field width of 2100mm. Variations of concentration and ground utilisation ratios with the receiver inclination angle are demonstrated in Figure 4-15. It is noteworthy that the highest concertation ratio is achieved with horizontal receivers. Both concentration and ground utilisation ratios decrease remarkably as the receiver inclination angle is over 55°. Though more mirrors could be placed in the solar field for receivers at higher inclination angle, the system concentration is lower due to the larger amount of narrow mirrors. For example, the widths of mirror elements in the common tilting array are less than 10mm for receivers at an inclination angle of 70°, while much wider mirrors (i.e. 48mm) are involved for receivers placed horizontally. On the other hand, the ground utilisation ratio decreases dramatically with the receiver inclination angle. This is due to the fact that the gap between two adjacent mirrors gets much larger as the receiver inclination angle increases. In particular, for vertically orientated receivers, the large inevitable space between the first mirror element and receiver results in the lowest ground utilisation ratio.

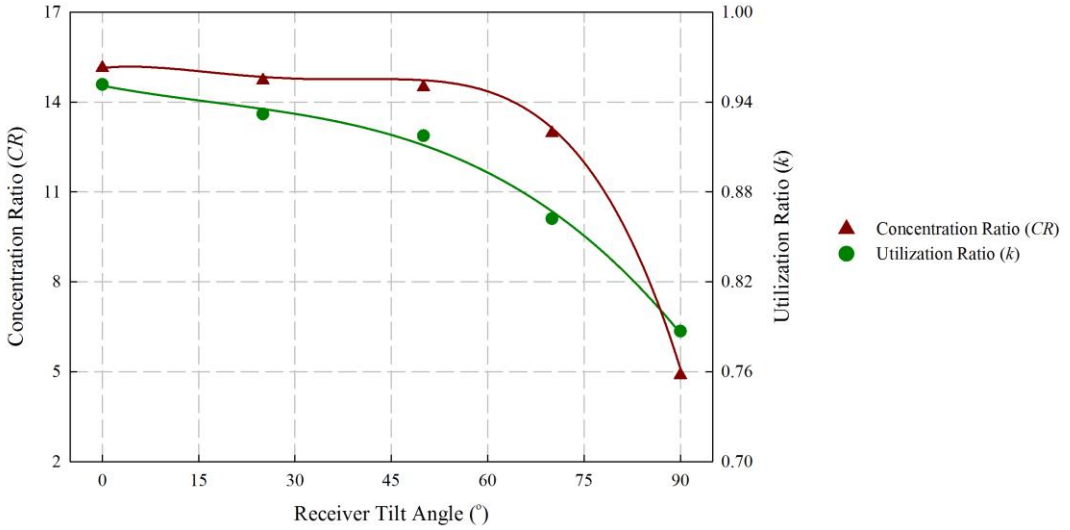


Figure 4-15 Variations of concentration and ground utilisation ratios with receiver inclination angle for CLFR-hybrid A system

4.5.5 Optical analysis summary

This section has presented a comprehensive optical analysis of the CLFR-hybrid system from different design aspects, including the limited solar field area and total number of mirrors, given focal length and variable receiver inclination angle. Following implications can be summarised:

(1) There exists an optimum mirror array arrangement for the CLFR-hybrid system even though a more densely packed mirror array is favourable. The optimum proportion of alternating mirrors in the central alternating array varies widely with the solar field area at a given focal length. The larger the solar field, the more the mirrors should be accommodated in the common tilting array for a higher concentration.

(2) There is an optimum focal length for the CLFR-hybrid system when the mirror array arrangement is fixed and the solar field area is limited.

(3) Horizontal flat receivers are preferred for the CLFR-hybrid system with better optical performance. A receiver inclination angle over 55° results in significant reduction in both concentration and ground utilisation ratios.

Next, Section 4.6 concludes the chapter.

4.6 Summary

In this chapter, a generic geometrical modelling has been established for the CLFR system with polar orientation in Section 4.2, which employs flat mirrors and receivers. Based on the numerical modelling, ray tracing simulation and experimental work, a comparative study regarding the concentration characteristics for the LFR, CLFR-complete and CLFR-hybrid systems has been presented in Section 4.4. Moreover, in Section 4.5, the optical design analysis of the CLFR-hybrid system has been performed from different design perspectives (i.e. limited solar field area, total number of mirror elements, focal length and receiver inclination angle) based on the numerical simulation results. The following conclusions are drawn:

(1) The CLFR system with polar orientation is viable for effectively concentrating the sunlight onto the receivers, where heat transfer fluids could absorb the heat.

(2) The CLFR-hybrid system has the highest concentration and ground utilisation ratios compared to the LFR and CLFR-complete systems. Geometrical concentration of 15.14 and ground utilisation ratio of 0.95 are achieved for the CLFR-hybrid system with 50 pieces of flat mirror elements, a solar field width of 2100mm and a focal length of 1500mm.

(3) Concentration of the CLFR-hybrid system increases with the total number of mirror elements, while its ground utilisation ratio decreases conversely. The

ground usage should be considered to avoid a low ground utilisation ratio while achieving a high concentration.

(4) An optimum mirror array arrangement for the CLFR-hybrid system should be determined with optimum proportion of mirrors in the central alternating array and the common tilting array for a higher concentration.

(5) Once the mirror array arrangement is fixed, an optimum focal length should be determined for the CLFR-hybrid system with limited solar field area.

(6) The CLFR-hybrid system is better to employ horizontal flat receivers for better optical performance.

Overall, the work presented in this chapter contributes to a progress in the field of concentrated solar power, in particular CLFR. It provides a generalized methodology for the optical design of the CLFR system and demonstrates the feasibility of the CLFR system with flat mirrors and polar orientation acting as the energy supply source for the micro trigeneration system.

Chapter 5: Performance Evaluation of Scroll-based ORC

5.1 Introduction

The scroll-based ORC acts as the key component of the micro trigeneration system producing electricity and exhaust heat to be subsequently recovered for heating and cooling/dehumidification demands. In order to effectively integrate ORC into the proposed micro trigeneration system, a preliminary performance evaluation of the ORC system is essential. Therefore, this chapter aims to present a detailed performance evaluation of the scroll-based ORC system based on experimental and simulation data. The scroll expander performance and overall ORC system performance are both assessed under a wide range of operating conditions experimentally and theoretically. This comprehensive assessment facilitates the effective micro trigeneration system integration in Chapter 7.

As previously highlighted in Chapter 2, few experimental and theoretical studies on the operating characteristics of the micro scroll-based ORC system have been documented in the existing literature and most of the published experimental studies have adopted scroll expanders modified from existing refrigeration compressors. More precisely, a parametric study is also necessary to evaluate how the ORC system performs by varying operating variables, for example the pressure ratio, inlet condition and electrical load coupled to ORC system. As a consequence, a micro ORC system with a scroll expander is designed and built in the Marmont laboratory of University of Nottingham, with which experimental investigations with a working fluid of R134a are conducted under various operating conditions. In terms of the numerical modelling, a semi-empirical model of the scroll expander is developed and implemented in MATLAB and then it is validated with experimental data. Simulations are carried out

with the validated model to investigate effect of the working fluid inlet condition (i.e. supply pressure and temperature), scroll expander imposed pressure ratio and rotational speed on the scroll expander performance. Moreover, the influence of the coupled resistive load on the ORC system performance is also clarified through experimental work.

This chapter is split into seven sections: Section 5.2 presents the semi-empirical modelling of the scroll expander; Section 5.3 provides details of the ORC experimental set-up, instrumentation and experimental method; Section 5.4 validates the scroll expander model with experimental data; Section 5.5 analyses the scroll expander performance under a wide range of operating variables based on the simulation results; Section 5.6 experimentally investigates the ORC system performance with various resistive loads and Section 5.7 concludes the chapter and provides implications for the micro trigeneration system integration.

5.2 Scroll expander modelling

The aim of the modelling work is to investigate the scroll expander performance, which thereby can: (a) enhance the modelling knowledge of the scroll expander; (b) facilitate the modelling of the ORC system as well as the entire micro trigeneration system in Chapter 7 and (c) be a pre-design tool for the scroll expander to provide preliminary assessment. In this section, a semi-empirical modelling approach is adopted for computing the scroll expander performance and the modelling development is described at length in Section 5.2.1, and the performance metrics are presented in Section 5.2.2.

5.2.1 Semi-empirical model

A semi-empirical model of the scroll expander is developed based on references [126, 147], with which the evolution of the working fluid state through the scroll expander is decomposed into the following steps as illustrated in Figure 5-1:

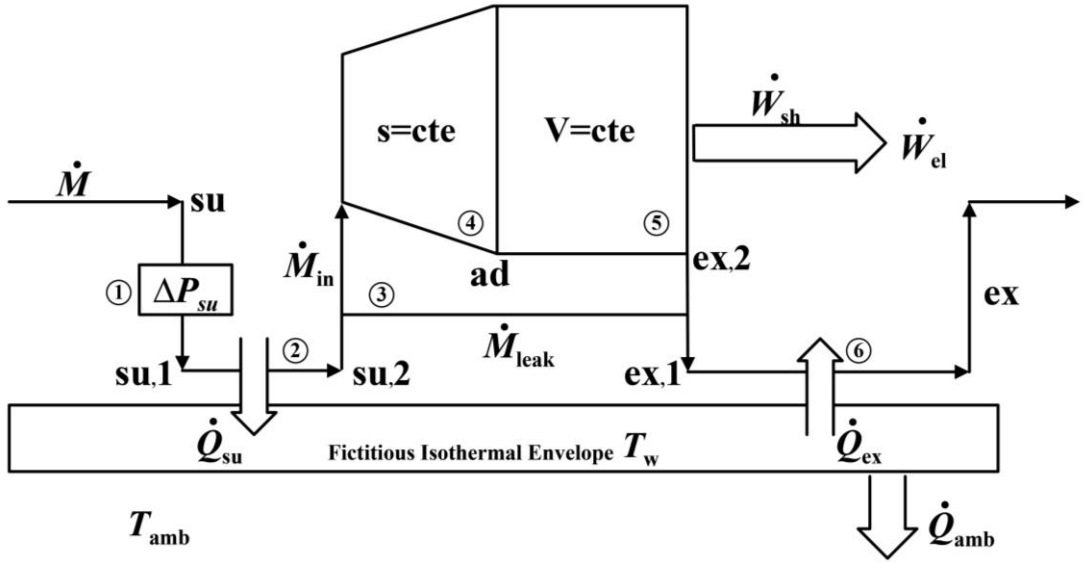


Figure 5-1 Schematic diagram of semi-empirical scroll expander model

1) State su→su,1

Firstly, the working fluid in vapour state entering the scroll expander experiences an adiabatic pressure drop (i.e. $P_{su} \rightarrow P_{su,1}$). The main reasons for the supply pressure drop are: (a) the effective suction port area is affected by the tip of the orbiting scroll and (b) the flow between the suction and adjacent expansion chambers increases at the end of the suction process as the scroll tips are not sealed perfectly. Theoretically, the supply pressure drop (ΔP_{su}) is modelled by comparison to an isentropic flow through a converging nozzle, which can be expressed as:

$$\Delta P_{su} = \frac{(\frac{\dot{M}}{A_{su}})^2 v_{su}}{2} \tag{5-1}$$

Where $\dot{M}$ is working fluid mass flow rate entering the scroll expander, kg/s. A_{su} and v_{su} are cross-sectional area, m^2 and specific volume at the throat of a converging nozzle, m^3/kg.

A_{su} represents an average value of the effective area of the suction port during the suction process, which can be defined by:

$$A_{su} = \frac{\pi d_{h\_su}^{\ 2}}{4} \tag{5-2}$$

Where d_{h_su} is diameter at the throat of a converging nozzle, m.

2) State su,1→su,2

Heat transfer takes place as vapour is at the contact of the metallic mass of the expander and consequently the vapour is cooled down. In order to simulate the supply heat transfer, a fictitious metal envelope of uniform temperature (T_w) is introduced. In general, the envelope represents the metal mass associated to the expander shell, the fixed and orbiting scrolls. Hence, the supply heat transfer is given by:

$$\dot{Q}_{su} = \dot{M}(h_{su,1} - h_{su,2}) = [1 - e^{(\frac{-AU_{su}}{\dot{M} \cdot C_p})}] \cdot \dot{M} \cdot C_p \cdot (T_{su,1} - T_w) \tag{5-3}$$

Where, U_{su} is supply heat transfer coefficient, W/m^2K.

The supply heat transfer coefficient is assumed to vary with the working fluid mass flow rate:

$$U_{su} = U_{su,n}(\frac{\dot{M}}{\dot{M}_n})^{0.8} \tag{5-4}$$

Where, $U_{su,n}$ is nominal heat transfer coefficient corresponding to the nominal mass flow rate ($\dot{M}_n$), W/m^2K.

3) Internal leakage

Basically, the mass flow rate entering the scroll expander ($\dot{M}$) is computed as the sum of the internal mass flow rate ($\dot{M}_{in}$) causing the shaft to rotate and the leakage mass flow rate ($\dot{M}_{leak}$).

$$\dot{M} = \dot{M}_{in} + \dot{M}_{leak} \tag{5-5}$$

The internal working fluid flow is mixed with the leakage flow after expansion process (i.e. State ex,2→ex,1). The internal working fluid mass flow rate ($\dot{M}_{in}$) is related to the scroll expander swept volume and rotational speed, which is expressed as:

$$\dot{M}_{in} = \frac{N_{exp} V_{sw\_exp}}{60 v_{su,2}} \tag{5-6}$$

Where, N_{exp} is scroll expander rotational speed, rpm and V_{sw_exp} is swept volume, m^3.

As the orbiting scroll rotates around the fixed scroll, there exist inevitable internal leakages between the adjacent chambers, which are namely radial and flank leakages. As depicted in Figure 5-2, the flank leakage is resulted from the gap between flanks of the two scrolls, whereas the radial leakage goes through the clearance between the tip wall of one scroll and the base plate of the other scroll. In general, the leakage flow passes directly from the high pressure zone to the low pressure zone without producing any useful work.

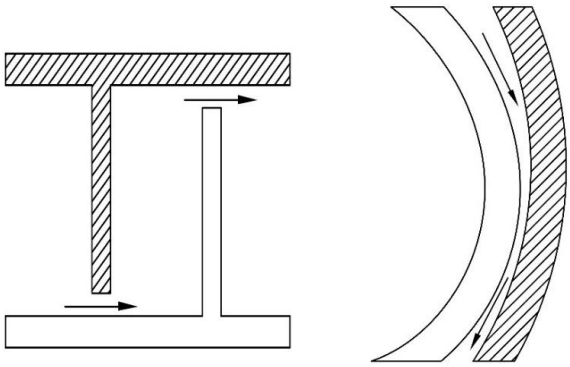


Figure 5-2 Internal leakages of scroll expander (a) radial and (b) flank

To model the internal leakages, all leakage paths are lumped into one unique fictitious leakage clearance. Similarly, the leakage flow rate is computed as an isentropic flow through a simple convergent nozzle with a cross-sectional area (A_{leak}). Hence, the mass flow rate of the leakage flow ($\dot{M}_{leak}$) can be derived with:

$$\dot{M}_{leak} = \frac{A_{leak} v_{f\_leak}}{v_{leak}} \tag{5-7}$$

Where v_{leak} and v_{f_leak} are specific volume and velocity at the throat of a converging nozzle, m^3/kg and m/s.

In terms of the leakage flow pressure, it corresponds to the maximum value between the exhaust and critical pressures:

$$P_{leak} = MAX(P_{ex,2}, P_{crit,leak}) \tag{5-8}$$

Where the critical pressure ($P_{crit,leak}$) is given by considering the working fluid as a perfect gas.

$$P_{crit,leak} = P_{su,2}\left[\left(\frac{2}{\gamma+1}\right)^{\left(\frac{\gamma}{\gamma-1}\right)}\right] \tag{5-9}$$

Where $P_{su,2}$ represents nozzle inlet pressure and γ is isentropic exponent of the working fluid.

4) State su,2→ad

Theoretically, the expansion process starts as the suction chamber ceases to be in communication with the suction line, involving adiabatic expansion (i.e. State su,2→ad) and adiabatic expansion at a constant volume (i.e. State ad→ex,2). More precisely, the adiabatic expansion to the adapted pressure is imposed by the built-in volume ratio of the scroll expander (R_{in}), and the expansion between the supply pressure and adapted pressure is assumed to be isentropic. The specific volume of the working fluid during the adiabatic expansion is calculated with:

$$v_{ad} = R_{in} v_{su,2} \tag{5-10}$$

5) State ad→ex,2

The second expansion process occurs from the adapted pressure to the exhaust pressure. The overall internal expansion process (i.e. State su,2→ex,2) can be expressed as a function of initial and final enthalpy states:

$$\dot{W}_{in} = \dot{M}_{in}(h_{su,2} - h_{ex,2}) = \dot{M}_{in}[h_{su,2} - h_{ad} + v_{ad}(P_{ad} - P_{ex,2})] \tag{5-11}$$

Pressure ratio (*PR*) imposed to the scroll expander is defined as the ratio of working fluid supply and exhaust pressure. Once the scroll expander built-in pressure ratio (PR_{is}) is imposed, the working fluid exhaust pressure (P_{ex}) equals to the built-in exhaust pressure (i.e. P_{su}/PR_{is}) as shown in Figure 5-3(a). However, two other operation conditions may occur practically: under-expansion and over-expansion. When the imposed pressure ratio is higher than the built in ratio, the scroll expander operates at under-expansion state (see Figure 5-3b). On the contrary, over-expansion operation takes place when the imposed pressure ratio is lower than PR_{is} (see Figure 5-3c).

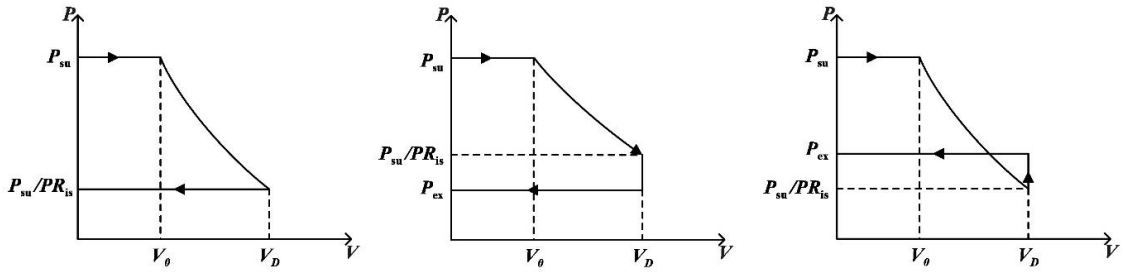


Figure 5-3 *P-V* diagrams of (a) ideal isentropic expansion (b) under-expansion and (c) over-expansion

6) State ex,1→ex

A similar method can be adopted for calculating the exhaust heat transfer as that of the supply heat transfer (i.e. Equation 5-3).

$$\dot{Q}_{ex} = \dot{M}(h_{ex,1} - h_{ex}) = [1 - e^{(\frac{-AU_{ex}}{\dot{M} \cdot C_p})}] \cdot \dot{M} \cdot C_p \cdot (T_{ex,1} - T_w) \quad (5\text{-}12)$$

Where, U_{ex} is exhaust heat transfer coefficient, W/m^{2}K.

5.2.2 Energy balance

Mechanical losses ($\dot{W}_{loss}$) are caused by fictions between the scrolls and losses in the bearings. For the sake of simplicity, all mechanical losses are lumped into one unique mechanical loss torque (T_{loss}), which is independent of the scroll expander rotational speed. Thus, the mechanical losses can be calculated with:

$$\dot{W}_{loss} = \frac{2\pi N_{exp} T_{loss}}{60} \quad (5\text{-}13)$$

Correspondingly, the shaft power of the scroll expander ($\dot{W}_{sh}$) can be derived:

$$\dot{W}_{sh} = \dot{W}_{in} - \dot{W}_{loss} = \dot{W}_{in} - \frac{2\pi N T_{loss}}{60} \quad (5\text{-}14)$$

Ambient heat losses ($\dot{Q}_{amb}$) are associated with the wall temperature to the ambient temperature, which can be obtained by introducing a global heat transfer coefficient (U_{amb}) between the envelope and ambient.

$$\dot{Q}_{amb} = AU_{amb}(T_w - T_{amb}) \tag{5-15}$$

Where T_{amb} is ambient temperature, K.

Thus, the energy balance for the steady-state model is expressed as:

$$\dot{W}_{loss} + \dot{Q}_{su} - \dot{Q}_{ex} - \dot{Q}_{amb} = 0 \tag{5-16}$$

And the electric output of the scroll expander (W_{el}) is determined by the coupled electric generator:

$$W_{el} = \dot{W}_{sh} \cdot \eta_g \tag{5-17}$$

Where η_g is generator efficiency.

5.2.3 Scroll expander performance evaluation metrics

To assess the scroll expander performance, several metrics are taken into account including the scroll expander isentropic efficiency, volumetric efficiency and net efficiency.

The isentropic efficiency (η_{is}) is defined as the ratio of the actual work to work that produced by isentropic expansion process [132].

$$\eta_{is} = \frac{\dot{W}_{sh}}{\dot{M}(h_{su} - h_{ex,is})} \tag{5-18}$$

Where $h_{ex,is}$ is working fluid exhaust specific enthalpy of working fluid in the isentropic expansion process, kJ/kg.

The scroll expander volumetric efficiency (η_v) is determined as the ratio of the internal mass flow rate to the mass flow rate entering the expander [129].

$$\eta_v = \frac{\dot{M}_{in}}{\dot{M}} \tag{5-19}$$

The net efficiency of the scroll expander-generator (η_{ex}) is expressed as the ratio of the electric output power to the isentropic power [146].

$$\eta_{ex} = \frac{\dot{W}_{el}}{\dot{M}(h_{su} - h_{ex,is})} \tag{5-20}$$

Section 5.2 has provided detailed descriptions of the semi-empirical modelling and the scroll expander performance evaluation metrics. Next, Section 5.3 provides the experimental description of the scroll-based ORC system.

5.3 ORC experimental description

A micro scroll-based ORC system is proposed and built in the Marmont laboratory of University of Nottingham. A detailed description of the ORC experimental set-up and instrumentation is provided in Section 5.3.1 and the experimental method with evaluation metrics used to evaluate the ORC system performance is explained in Section 5.3.2.

5.3.1 Experimental set-up

A schematic diagram of the scroll-based ORC system is presented in Figure 5-4 and photos of the test rig are shown in Figure 5-5. With considerations of limited laboratory space and experimental condition, an electric steam boiler is installed acting as the supply heat source provide steam in the ORC system by providing steam, and its

temperature and mass flow rate can be adjusted manually. An oil-free scroll expander manufactured by Air Squared, Inc. is selected with nominal output of 1kW and coupled with a separate electrical generator. The generator is coupled directly to the scroll expander, so it rotates at the same speed as the scroll expander. The scroll expander is fed with working fluid of R134a, which is heated by the steam from the boiler in the evaporator. The high-pressure vapour of R134a flows into the scroll expander, where its enthalpy is converted into shaft work to drive the generator for electricity generation. Afterwards, the low-pressure vapour leaves the scroll expander is condensed by cold water in a condenser and the working fluid flows directly to the storage tank. To improve the ORC performance, a recuperator is included, where heat transfer takes place between the low-pressure vapour leaving from the scroll expander and the liquefied working fluid pumped from the storage tank. After being preheated, the working fluid exits the recuperator to the evaporator, and next cycle begins. A vapour by-pass line is installed to completely isolate the scroll expander for the starting period in case of an emergency. To vary the ORC system operation condition, valves V1-V7 can be adjusted correspondingly and the refrigerant pump can be controlled by a frequency adaptor.

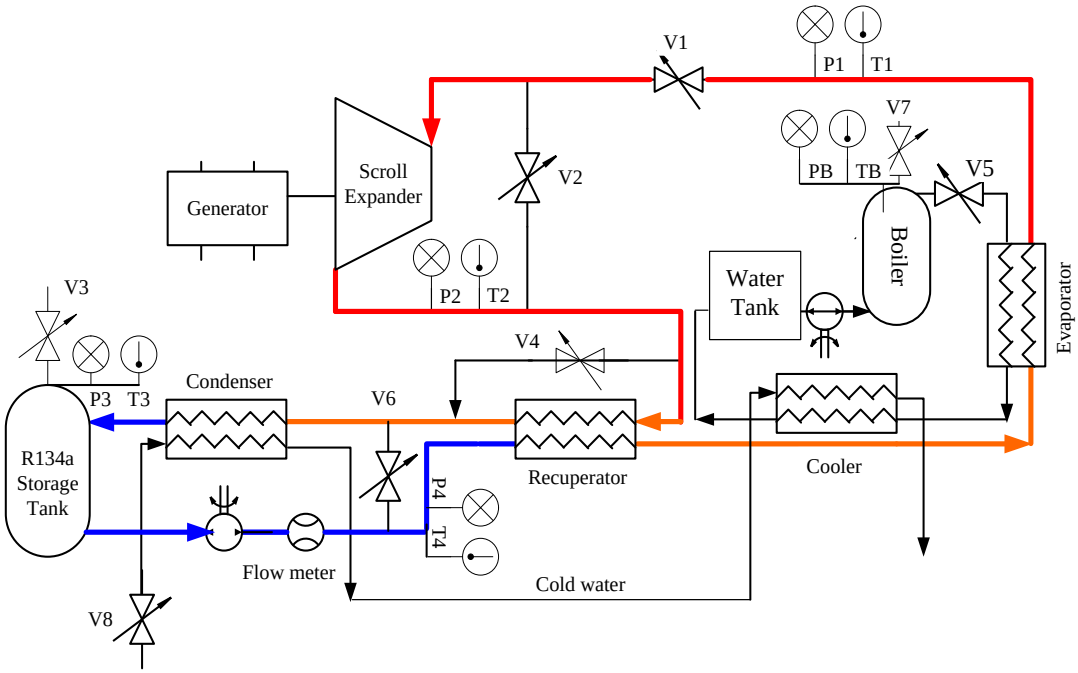
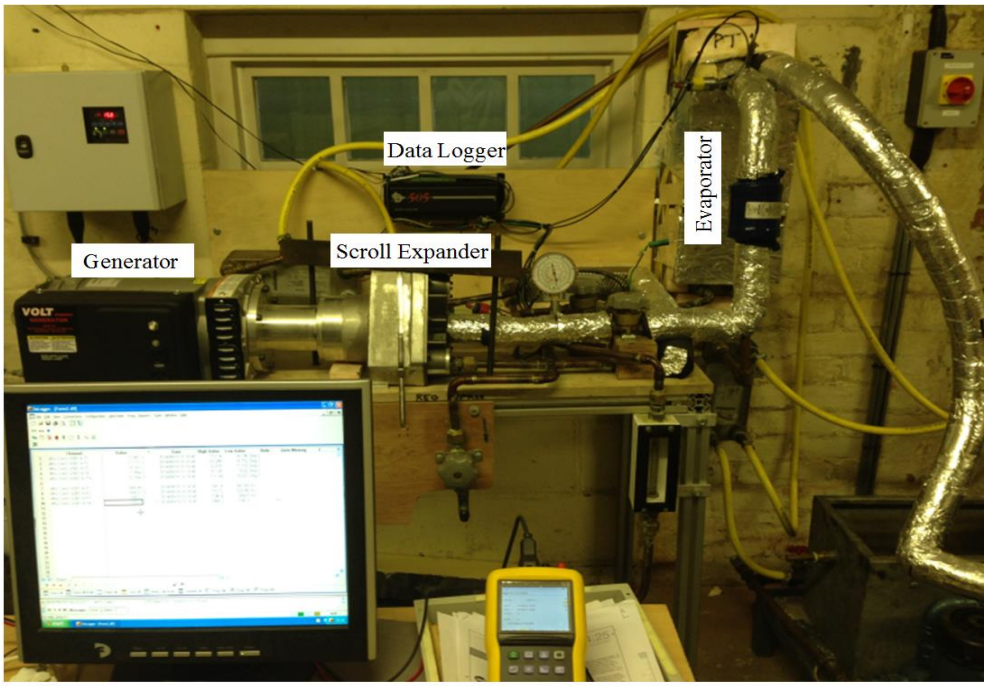


Figure 5-4 Schematic graph of scroll-based ORC system



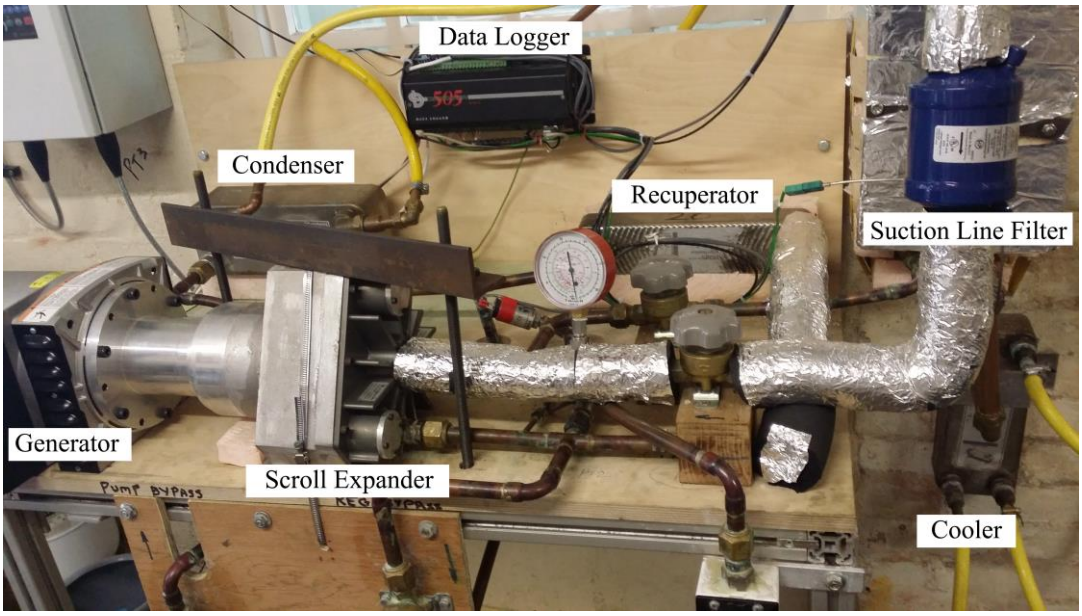


Figure 5-5 Photos of scroll-based ORC test rig

Specifications of the main components in the scroll-based ORC system are listed in Table 5-1. The evaporator, recuperator, condenser and cooler are all brazed plate heat exchangers manufactured by SWEP, but in different dimensions. According to the manufacture data, the scroll expander has a built-in expansion ratio of 3.5 and maximum rotational speed of 3600rpm. The coupled electric generator has an efficiency of 85% with rated power output of 2500W. The magnetic pump delivers the working fluid has a maximum speed of 5000rpm and an efficiency of 75%.

Table 5-1 Specifications of main components in scroll-based ORC system

Equipment	Properties		Manufacturer
Electric Steam Boiler	Rating kilowatts	24kW	Fulton Boiler Works (G.B.) Ltd.
	Rated output	80kg/hr	
Suction Line Filter	Pressure	27.5bar	Emerson Alco Control (ASF-35S5)
	Temperature range	-45°C -50°C	
	Volume	0.8Litre	

Equipment	Properties		Manufacturer
Evaporator	Minimum temperature	-196°C	SWEP (B25T×20)
	Maximum temperature	225°C	
	Test pressure	50bar	
	Heat transfer area	7.6m^2	
	Maximum flow rate	12m^3/h	
Scroll Expander	Displacement	12cm^3/rev	Air Squared, Inc (E15H22N4.25)
	Expansion ratio	3.5	
	Maximum pressure	13.8bar	
	Maximum inlet temperature	175°C	
	Nominal output	1kW	
	Maximum rotational speed	3600rpm	
	Standard fluid	R134a / R245fa	
	Lubrication	Oil-free	
	Coupling	Magnetic	
Electric Generator	Rated Watts	2500W	WANCO, Inc. (Voltmaster AB30L)
	Rated AMPS	20.8A	
	Rated Volts	120V	
	Rated Hertz	60Hz	
	Maximum ambient temperature	40°C	
	Efficiency	85%	
Recuperator	Minimum temperature	-196°C	SWEP (BX8TH×20)
	Maximum temperature	225°C	
	Heat transfer area	1.4m^2	
	Maximum flow rate	4m^3/h	
Condenser	Minimum temperature	-160°C	SWEP (B10H×30)
	Maximum temperature	225°C	
	Heat transfer area	3.8m^2	
	Maximum flow rate	12m^3/h	

Equipment	Properties	Manufacturer	Equipment
Magnetic Pump	Maximum speed	5000rpm	Tuthill (D Series Pump)
	Maximum differential pressure (intermittent)	10.3bar	
	Maximum differential pressure (continuous)	6.9bar	
	Maximum temperature	177°C	
	Efficiency	75%	
Storage Tank	Maximum working pressure	10bar	Zilmet S.p.A (092809)

5.3.2 Experimental method

For experimental testing, series of measuring instruments have been installed to acquire the desired experimental data. For a more rigorous and precise experimental work, it's best to calibrate the measuring instruments depending on the measuring range for investigation. Because of the time constraints, the uncertainties of the measuring instruments have been adopted by reference to the manufacturers' datasheets. The measuring range and accuracies of devices are presented in Table 5-2. Basically, the accuracy of a measuring instrument can be specified in different ways: (a) as a percentage of full scale (i.e. % FS), which is a constant value throughout the measurement range. For instance, OMEGA PXM Series pressure transducers are used to measure the pressure of the working fluid R134a, which feature an accuracy of 0.25% of full scale. K-type temperature sensors with accuracies of ±0.75% FS measure the working fluid temperature. A Platon liquid flow meter with an accuracy of ±1.25% FS is installed to record the working fluid volume flow rate; (b) as a percentage of reading (% RD), which is a function of the indicated measurement as it varies with the measurement reading; and (c) as a combined percentage of reading and percentage of full scale. For example, to derive the electric output of the ORC system, a Chauvin

Arnoux power quality analyser is used to measure the frequency, voltage and current of the output power generated. From the datasheet, the accuracy of measuring voltage is indicated as "0.5% RD +2 counts", where count is defined as a unit change in the last digit of the meter display and the display resolution for voltage measurement is 0.1V, 0.1A for current and 0.01 for frequency. Once a steady-state regime of operation is achieved, a set of measurement data can be recorded by DataTaker 505, which comprises working fluid pressure, temperature, mass flow rate and scroll expander electric output power.

Table 5-2 Measuring instruments with associated accuracies

Parameter	Instrument	Measurement Range	Accuracy
Pressure	Pressure transducer (OMEGA PXM41MD)	0-40 bar G	0.25% FS
Temperature	Type K insulated thermocouple	0-1100°C	±0.75% FS
Voltage	Power Quality Analyser (Chauvin Arnoux CA 8230)	$6V_{RMS}$ - $600V_{RMS}$	±0.5% RD+2 counts
Current		100mA -6500A	±0.5% RD+1 count
Frequency		40Hz – 70Hz	±1 count
Flow rate	Platon Glass Tube Flowmeter	0.05– 1.4 L/min	±1.25% FS
Data Acquisition	DataTaker 505	-	0.15% FS

In order to obtain the thermodynamic properties of the working fluid, both pressure and temperature of the working fluid have been measured and crosschecking has been conducted for validating the data collected from testing. For instance, the working fluid is condensed by cold water to the saturated liquid state and stored in the storage tank; the corresponding pressure and temperature have been measured at the inlet of the storage tank by the thermocouple and pressure transducer, which are indicated as P3

and T3 in Figure 5-4. For crosschecking, the property table of R134a provided in the literature [245] can be referred, by validating the corresponding saturated liquid temperature of R134a at the given pressure or the corresponding pressure at the given saturated temperature. Hence, the validity of the measuring data could be assessed for performance analysis. Moreover, the instruments measure corresponding physical parameters directly with their respective accuracies, but other desired parameters such as working fluid enthalpy and electric output power cannot be measured directly. In such cases, an uncertainty analysis is essential to provide a measure of the error related to a calculated value. A function of the measured physical parameters and the calculated parameter is adopted with reference to the literature [126] and [246]:

$$U_y = \sqrt{\sum_{i=1}^{N} \left(\frac{\partial y}{\partial x_i}\right)^2 \cdot U_{x_i}{}^2} \tag{5-21}$$

Where U_y and U_{xi} are uncertainties of the calculated parameter and each measured variable x_i.

Subsequently, the experimental data can be processed to determine the performance of the scroll expander as well as the complete ORC system. Based on the experimental schematic diagram, the overall working process of the scroll-based ORC system is depicted in Figure 5-6, using a pressure-enthalpy (*P-h*) diagram of R134a reproduced by Potter and Hotchkiss [247].

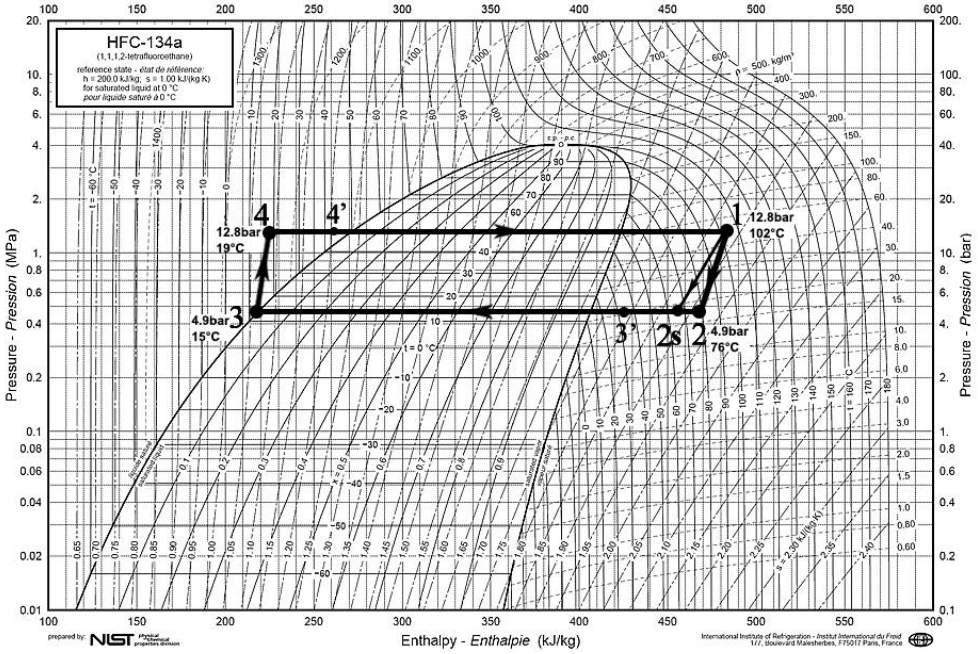


Figure 5-6 *P-h* diagram of scroll-based ORC system

The components of the ORC system are all considered as steady-state flow devices, thus the kinetic and potential energies are neglected. The working fluid R134a is heated in the evaporator (i.e. State 4→4'→1), in which heat is transferred from the electric boiler to the working fluid. Thus, the thermal load (Q_{in}) supplied by the boiler via the evaporator is:

$$Q_{\text{in}} = \dot{M}_f \left(h_1 - h_4 \right) \tag{5-22}$$

Where $\dot{M}_f$ is working fluid mass flow rate, kg/s and *h* is working fluid specific enthalpy, kJ/kg.

Both the desuperheating process (i.e. State 2→3') and the preheating process (i.e. State 4→4') occur in the recuperator. The recovered heat (Q_{re}) in the recuperator is calculated with:

$$Q_{\text{re}} = \dot{M}_f \left(h_2 - h_{3'} \right) = \dot{M}_f \left(h_{4'} - h_4 \right) \tag{5-23}$$

Taking the recovery heat from the recuperator into consideration, Equation 5-22 relating to the heat input can be modified to:

$$Q_{\text{in}} = \dot{M}_f \left(h_1 - h_{4'} \right) \tag{5-24}$$

On the other hand, the input power of the liquid pump (i.e. State 3→4) is defined as:

$$W_{\text{p}} = \dot{M}_f (h_4 - h_3) \tag{5-25}$$

Where the specific enthalpy at State 4 (i.e. h_4) is correlated with the pump efficiency (η_{p}).

The mechanical work delivered by the scroll expander in the expansion process (i.e. State 1→2) is given by:

$$W_{\text{sh}} = \dot{M}_f (h_1 - h_2) \eta_{\text{v}} \eta_{\text{m}} \tag{5-26}$$

Where η_{v} and η_{m} are volumetric and mechanical efficiencies of the scroll expander respectively.

As heat input and power output are the main indicators of the system energy conversion efficiency, the ORC system net electric power (W_{el}) with neglecting the work input by the liquid pump can be expressed as:

$$W_{\text{el}} = W_{\text{sh}} \cdot \eta_{\text{g}} \tag{5-27}$$

Where η_{g} is electric generator efficiency.

In addition, the ORC system electrical efficiency (η_{el}) is determined as the ratio between the electric output power and the heat rate absorbed by the working fluid in the evaporator:

$$\eta_{\text{el}} = \frac{W_{\text{el}}}{Q_{\text{in}}} \tag{5-28}$$

Based on the experimental measurements, the scroll expander performance can be evaluated by the isentropic, volumetric and mechanical efficiencies. The isentropic efficiency of the scroll expander (η_{is}) is calculated as:

$$\eta_{is} = \frac{h_1 - h_2}{h_1 - h_{2s}} \tag{5-29}$$

Where h_{2s} is specific enthalpy at State 2 in an isentropic expansion process, as indicated in Figure 5-6.

The ideal volumetric flow rate at the scroll expander inlet is given as:

$$\dot{V}_{in,\,ideal} = V_{exp} \times \frac{N_{exp}}{60} \tag{5-30}$$

Where N_{exp} represents scroll expander rotational speed, rpm and V_{exp} is the scroll expander volume, m^3. However, the actual volumetric flow rate at the expander inlet is larger than the ideal volumetric flow rate owing to internal leakages, which can be calculated with:

$$\dot{V}_{in} = \dot{M}_f v_{f\_in} \tag{5-31}$$

Where v_{f_in} is vapour specific volume at the scroll expander inlet, m^3/kg.

As a result, the volumetric efficiency of the scroll expander (η_v) can be obtained by:

$$\eta_v = \frac{\dot{V}_{in,\,ideal}}{\dot{V}_{in}} = \frac{V_{exp} \times \frac{N_{exp}}{60}}{\dot{M}_f v_{f\_in}} \tag{5-32}$$

By taking the scroll expander performance into account, the electrical efficiency of ORC system (η_{el}) can be regarded as a function of scroll expander isentropic, volumetric and mechanical efficiencies, and generator efficiency:

$$\eta_{el} = \eta_v \eta_{is} \eta_m \eta_g \frac{(h_1 - h_{2s})}{(h_1 - h_5)} \tag{5-33}$$

Section 5.3 has described the experimental set-up of the scroll-based ORC system and the instrumentation. The experimental method has also been discussed with explanation of the experimental evaluation metrics that would be used to evaluate the ORC system performance in Section 5.6. Next, Section 5.4 presents the validation of the semi-empirical model developed for the scroll expander.

5.4 Model validation with experimental work

To use the semi-empirical model with confidence, validation with reliable experimental data is indispensable. In this section, the input parameters of the established semi-empirical model are firstly identified on a basis of experimental results in Section 5.4.1, with which the model is validated in Section 5.4.2. In addition, potential reasons for discrepancies are discussed in Section 5.4.3.

5.4.1 Identification of input parameters

The semi-empirical model of the scroll expander is developed with MATLAB, which determines the scroll expander performance under various operating conditions. The open source CoolProp library is applied as the main source to retrieve thermo-physical properties for the working fluid R134a. The CoolProp library is capable of implementing accurate equations of state for property calculations. A flow chart of the simulation process in MATLAB is presented in Figure 5-7.

Once the working fluid configuration is determined as R134a, a number of operating variables are required for input, such as the rotational speed of the scroll expander (N_{exp}), working fluid supply pressure (P_{su}), supply temperature (T_{su}) and exhaust pressure (P_{ex}). Besides, several input parameters are necessary for identification to match with the experimental data. Generally, the identification process is

accomplished by minimizing a global error function accounting for errors on the predictions of the mass flow rate, electric power and exhaust temperature.

$$\text{Error} = \sum_{i=1}^{n}\left(\frac{\dot{m}_{s,i}-\dot{m}_{e,i}}{\dot{m}_{e,i}}\right)^2 + \sum_{i=1}^{n}\left(T_{ex,s,i}-T_{ex,e,i}\right)^2 + \sum_{i=1}^{n}\left(\frac{W_{el,s,i}-W_{el,e,i}}{W_{el,e,i}}\right)^2 \quad (5\text{-}34)$$

As long as all the input parameters tuned adequately, the semi-empirical model is capable of producing the following outputs: working fluid mass flow rate ($\dot{M}$), exhaust temperature (T_{ex}), electric power ($\dot{W}_{el}$), ambient heat losses ($\dot{Q}_{amb}$), scroll expander isentropic efficiency (η_{is}), volumetric efficiency (η_v) and net efficiency (η_{ex}).

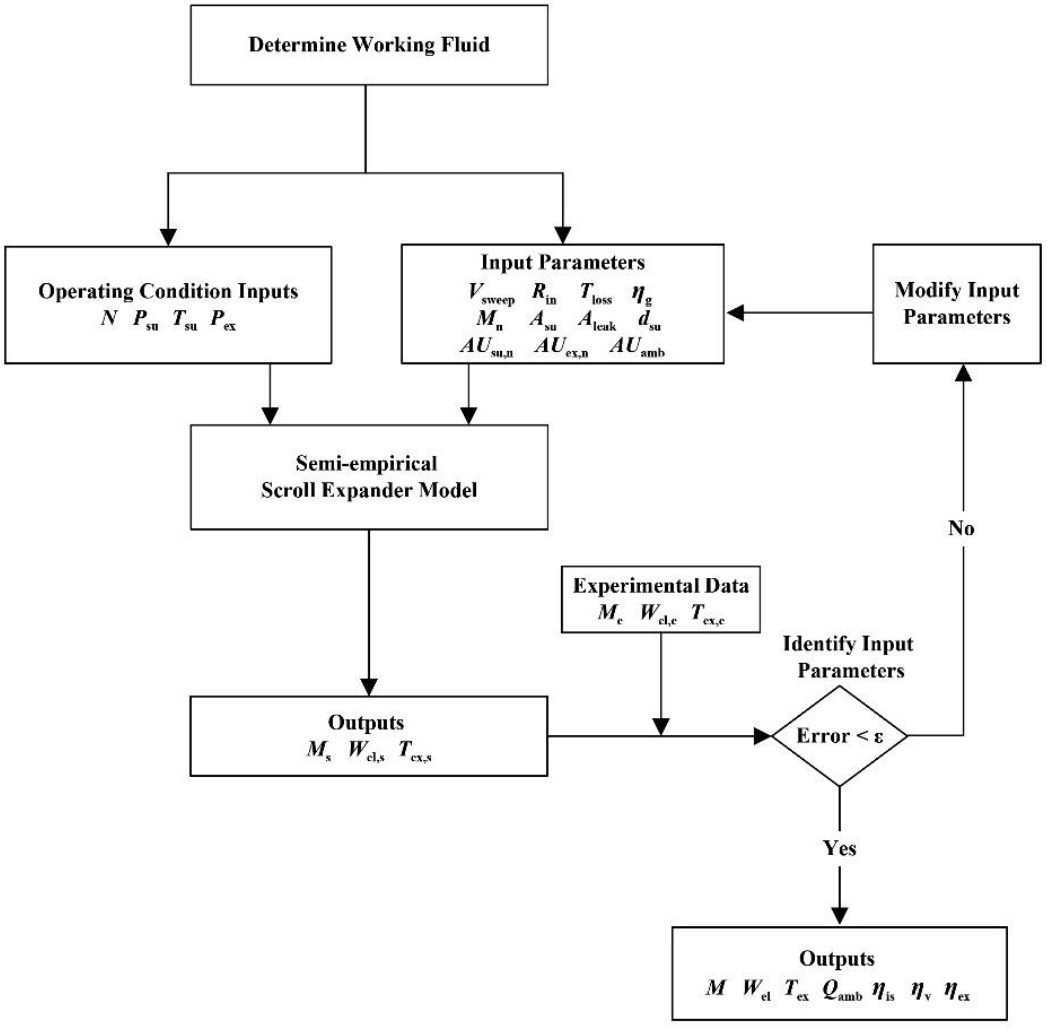


Figure 5-7 Flow chart of overall simulation process

With reference to the experimental data, the input parameters of the semi-empirical model are identified as listed in Table 5-4.

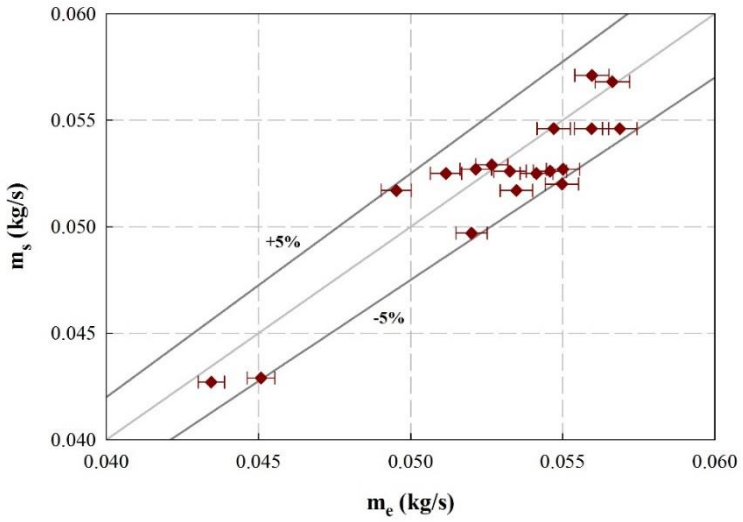
Table 5-3 Identified input parameters of the scroll expander model

Input Parameters	Value
Built-in volume ratio (R_{in})	3.5
Nominal mass flow rate ($\dot{M}_n$)	0.12 kg/s
Scroll expander swept area (V_{sw})	12 cm^3/rev
Supply heat transfer parameter (AU_{su})	30.4 W/K
Exhaust heat transfer parameter (AU_{ex})	40.2 W/K
Leakage area (A_{leak})	1.5 mm^2
Supply port cross-sectional area (A_{su})	22.63 mm^2
Mechanical loss torque (T_{loss})	0.14 N·m
Ambient heat transfer parameter (AU_{amb})	2.5

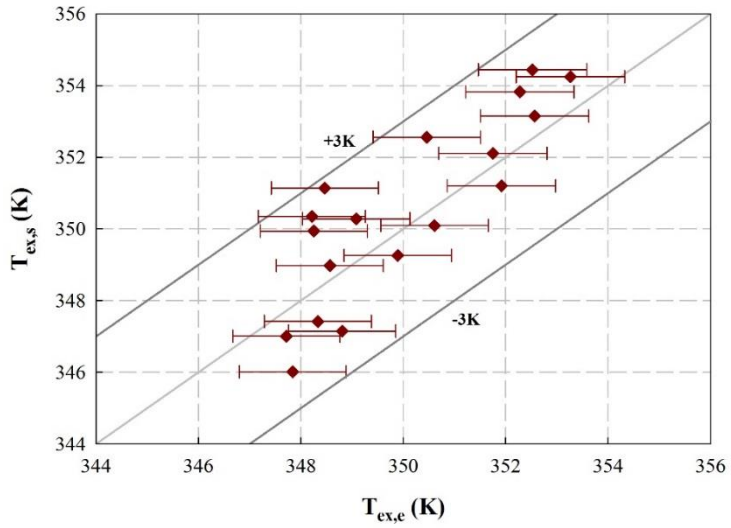
5.4.2 Model validation

As mentioned in Section 5.3, once a steady operation of the ORC system is achieved, a set of measurements are produced including working fluid pressure, temperature and mass flow rate as well as electric output power. For the purpose of validation, the scroll-based ORC system is tested under various operating conditions and comparisons are conducted between the experimental and simulation results regarding the working fluid mass flow rate, exhaust temperature and delivered electric power. The experimental data with error bars are shown alongside the simulation results in Figure 5-8. The simulation results of the working fluid mass flow rate fit within $\pm$ 5% margin, as seen in Figure 5-8(a). The working fluid exhaust temperatures calculated by the

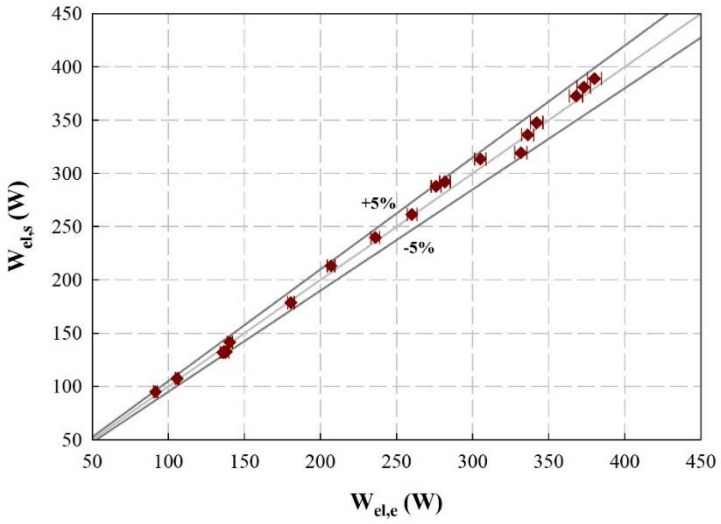
model are clustered around two regions within ± 3K, as observed in Figure 5-8(b). On the other hand, the maximum deviation is approximately 5% for the electric output power, which is indicated in Figure 5-8(c). Hence the comparative results prove the accuracy and validity of the established scroll expander model.



(a)



(b)



(c)

Figure 5-8 Comparisons of between calculated and measured results for: (a) working fluid mass flow rate, (b) working fluid exhaust temperature and (c) electric output power

5.4.3 Validation summary

The experimental results have been compared with simulation results of the semi-empirical model of the scroll expander fed with R134a. The validation demonstrates that the model produces results within a reasonable error range to simulate the scroll expander performance. Consequently, the validated model can be used with confidence for the scroll expander parametric analysis in Section 5.5 and for integration into the complete micro trigeneration system in Chapter 7. Potential reasons for the discrepancies between the experimental and simulation results have been also explained as follows:

1) The semi-empirical model simplifies the working process of the scroll expander by adopting a lumped method, while detailed geometries of scroll expander chambers are not taken into account and state changes of the working fluid inside the scroll expander are also neglected.
2) For the sake of simplicity, the internal leakage of the scroll expander is modelled by lumping both radial and flank leakages into one fictitious leakage

clearance, which may be not precise enough to reflect the real leakage condition inside the scroll expander.

3) Experimental tests have been conducted under variable environmental conditions, for instance the laboratory indoor temperature maybe changeable because of occupancy and equipment operation, which would not be accurately manifested in the semi-empirical model. The ambient temperature during experimental testing has also been measured and recorded; the maximum temperature variation is approximately 4.6K.
4) Inevitable experimental errors exist due to accuracies of the measurement instruments, measurement methods and etc.

Next, using the validated model, Section 5.5 provides a comprehensive parametric analysis for the scroll expander under a wide range of operating conditions.

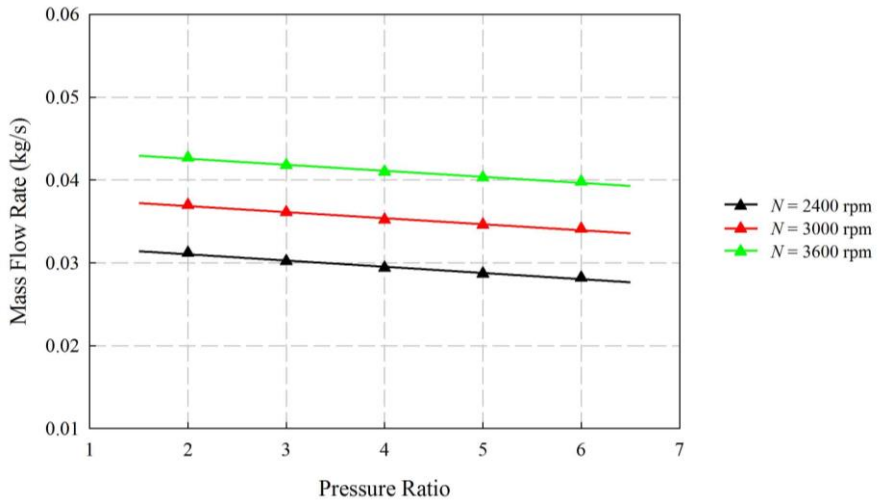
5.5 Scroll expander parametric analysis

In this section, the validated semi-empirical model is employed to simulate the scroll expander performance under different operating conditions. Based on the simulation results, effect of a variety of operating variables are investigated: the imposed pressure ratio in Section 5.5.1 and Section 5.5.2, the scroll expander supply pressure in Section 5.5.3, the scroll expander supply temperature in Section 5.5.4 and the scroll expander rotational speed in Section 5.5.6.

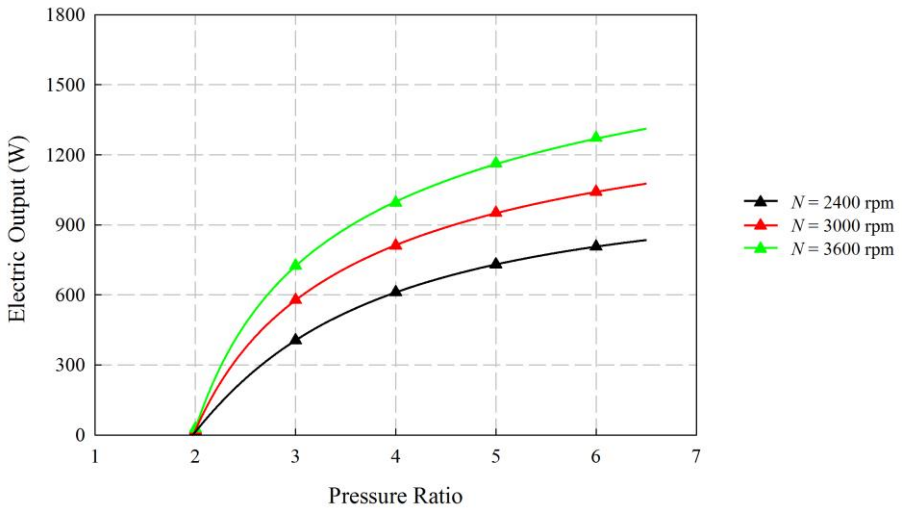
5.5.1 Effect of scroll expander pressure ratio at constant supply pressure

As a matter of fact, the imposed pressure ratio of the scroll expander may deviate from the built-in pressure ratio, thus either under-expansion or over-expansion may take place. Investigations are conducted to evaluate how the pressure ratio affects the scroll

expander performance at different rotational speeds, as the scroll expander supply pressure is maintained at 13.5bar and the exhaust pressure varies from 2.25bar to 6.75bar. Due to the constant supply condition of the scroll expander, the internal mass flow rate of the working fluid is independent of the pressure ratio as indicated in Equation 5-6, however the working fluid mass flow rate entering the scroll expander decreases in line with the pressure ratio as shown in Figure 5-9(a). This is because that the exhaust pressure reduces with the increasing pressure ratio at a constant supply pressure and thus less leakage would be obtained. Nevertheless, the electric output increases dramatically with the imposed pressure ratio. The electric output of the scroll expander increases from 13.39W at *PR*=2 to 806.61W at *PR*=6 when the scroll expander runs at *N*=2400rpm, and an increase of the electric output is about 1244.94W at *N*=3600rpm. More precisely, the rate of increase in the electric output decreases gradually. As noted in Figure 5-9(b), the variation of the electric output levels off as the pressure ratio exceeding 6.



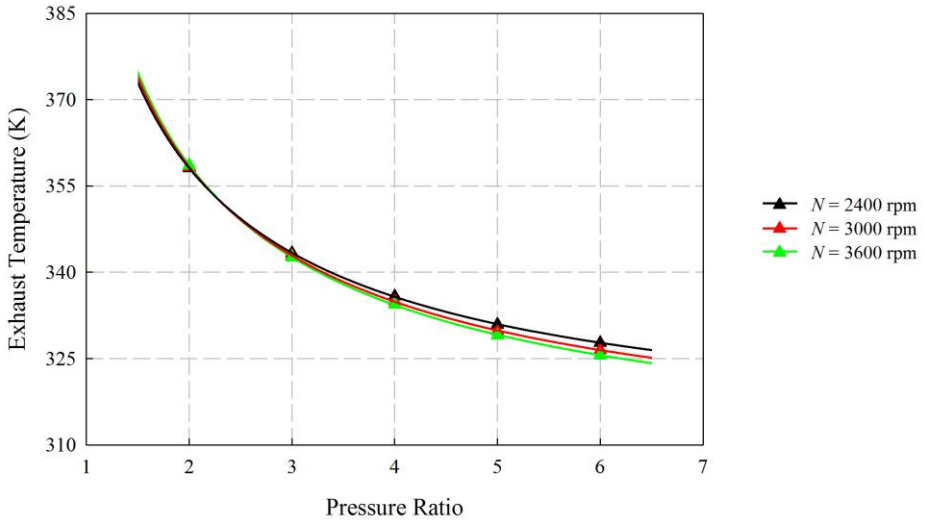
(a)



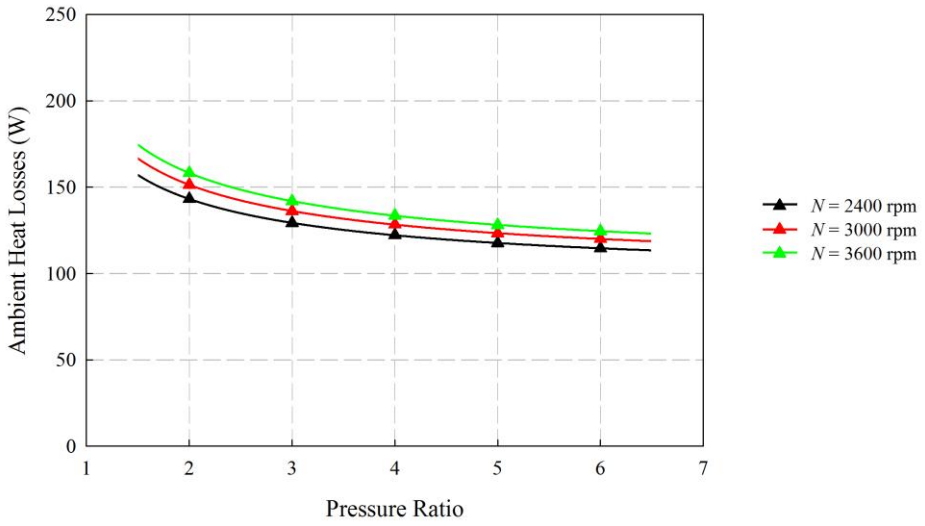
(b)

Figure 5-9 Variations of (a) working fluid mass flow rate and (b) scroll expander electric output with pressure ratio

When different pressure ratios are imposed to the scroll, the working fluid exhaust temperature and ambient heat losses vary accordingly as shown in Figure 5-10. The higher the pressure ratio, the lower the working fluid exhaust temperature is. Consequently, less ambient heat losses are obtained. For instance, the exhaust temperature reduces by 9.22% at N=3600rpm and the ambient heat losses decline by 21.30% as the pressure ratios increases from 2 to 6. It is also worth noting that the pressure ratio influences the ambient heat losses less markedly when the scroll expander operates at the under-expansion state.



(a)

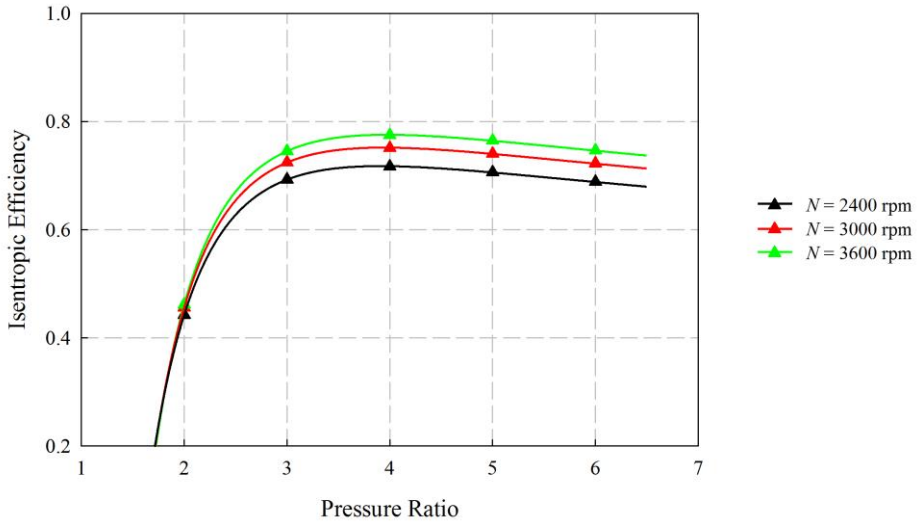


(b)

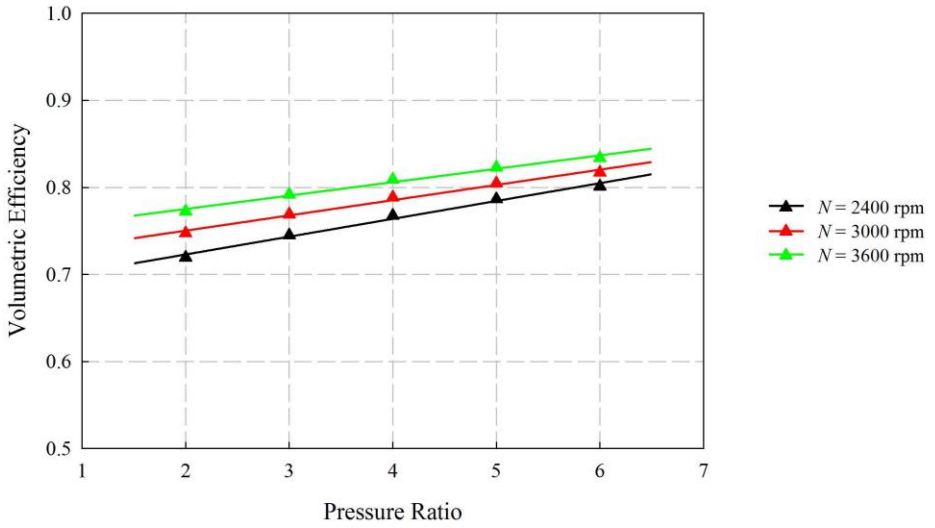
Figure 5-10 Variations of scroll expander (a) exhaust temperature and (b) ambient heat losses with pressure ratio

Figure 5-11(a) demonstrates that the maximum scroll expander isentropic efficiency is achieved when the imposed pressure ratio matches with the scroll expander built-in volume ratio at a given rotational speed. For instance, at a pressure ratio approximately of 4, the scroll expander isentropic efficiency reaches the highest value of 0.78 at N=3600rpm. When the scroll expander operates at the over-expansion state, the higher the pressure ratio, the higher the isentropic efficiency until reaching the maximum efficiency, however it gradually declines once the under-expansion occurs. As

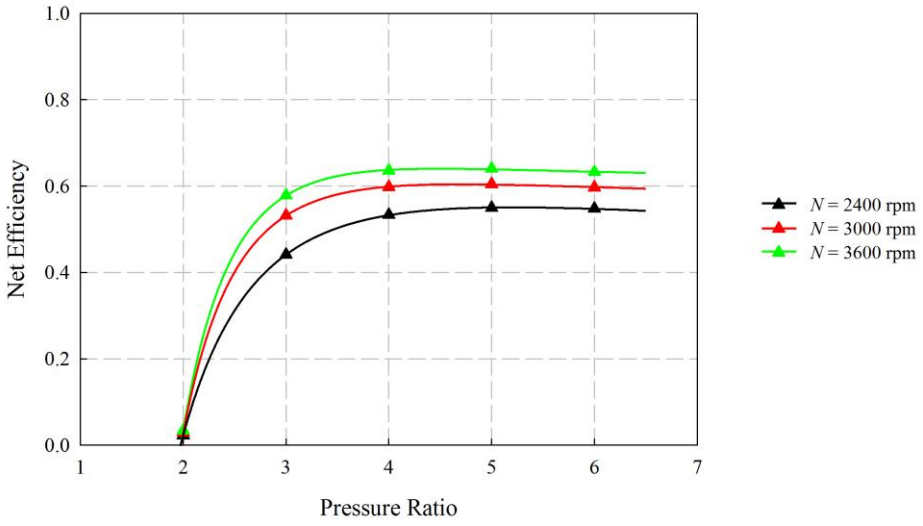
indicated in Equation 5-19, the internal leakage characteristic of the scroll expander is also an important factor that affecting the volumetric efficiency. Because more leakage of the scroll expander is observed at a lower pressure ratio, a lower volumetric efficiency can be noted in Figure 5-11(b). On the other hand, the scroll expander net efficiency firstly rises sharply as the pressure ratio increases from 2 to 4 and then remains steady as the pressure ratio above 4. The results indicate that both under and over expansion influence the scroll expander performance negatively, especially when the scroll expander working at the over-expansion state, where the expander working condition is deteriorated [129] with lower system stability [248].



(a)



(b)

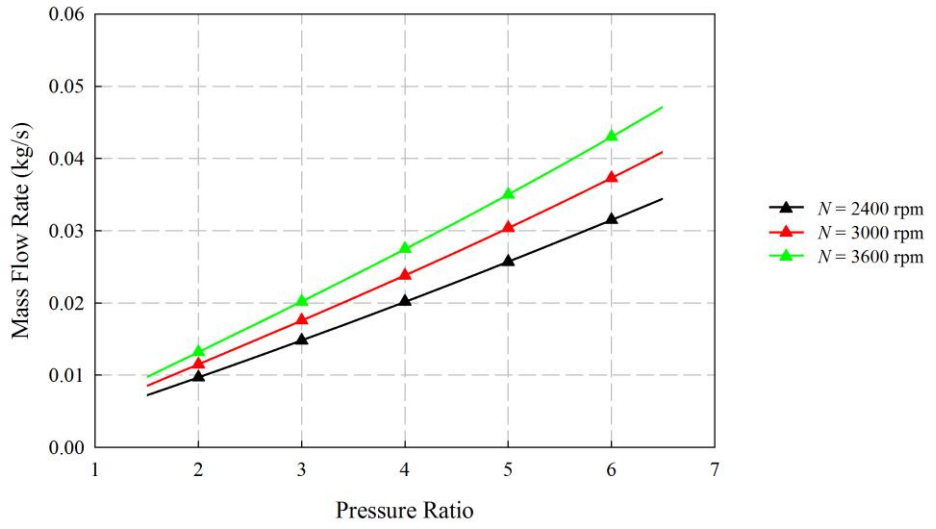


(c)

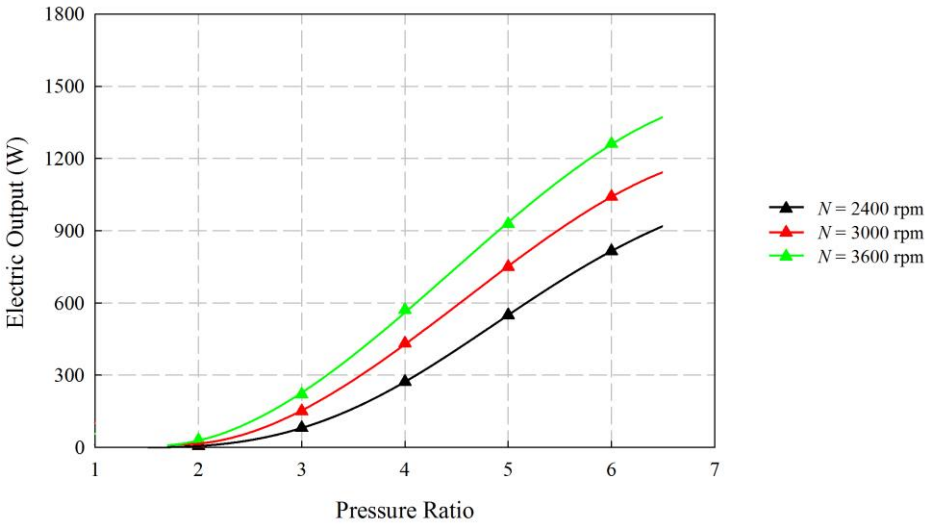
Figure 5-11 Variations of scroll expander (a) isentropic, (b) volumetric and (c) net efficiencies with pressure ratio

5.5.2 Effect of scroll expander pressure ratio at constant exhaust pressure

Different from the simulations conducted in Section 5.5.1, in this section the effect of the pressure ratio is evaluated as the scroll expander operates at a constant exhaust pressure of 2.25bar and the supply pressure ranges from 4.5bar to 13.5bar. Due to the fact that the working fluid supply pressure rises, a rising trend of the working fluid mass flow rate at a given rotational speed is seen from Figure 5-12(a). Hence, the electric output power increases significantly. When the scroll expander operates at N=3600rpm, the mass flow rate increases rapidly from 0.01kg/s at PR=2 to 0.04kg/s at PR=6 and the electric output rises from 2.52W to 1270.76W accordingly.



(a)

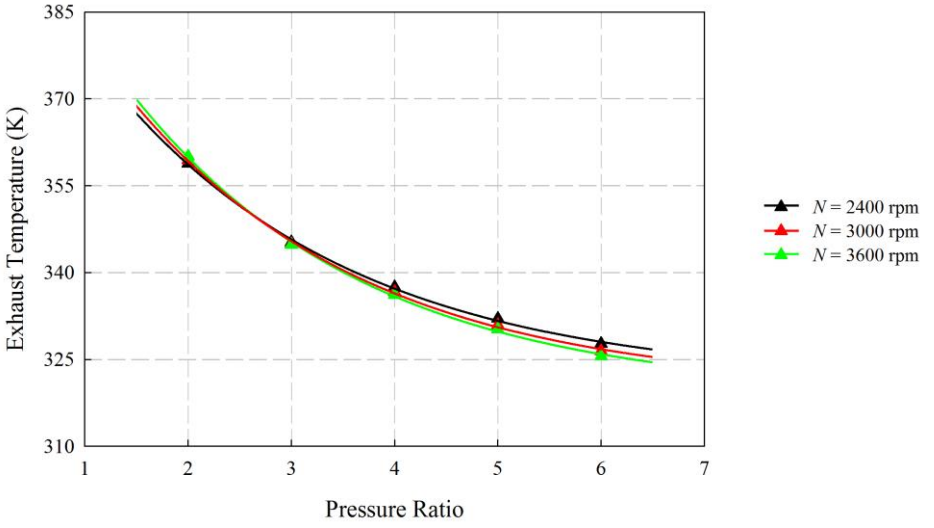


(b)

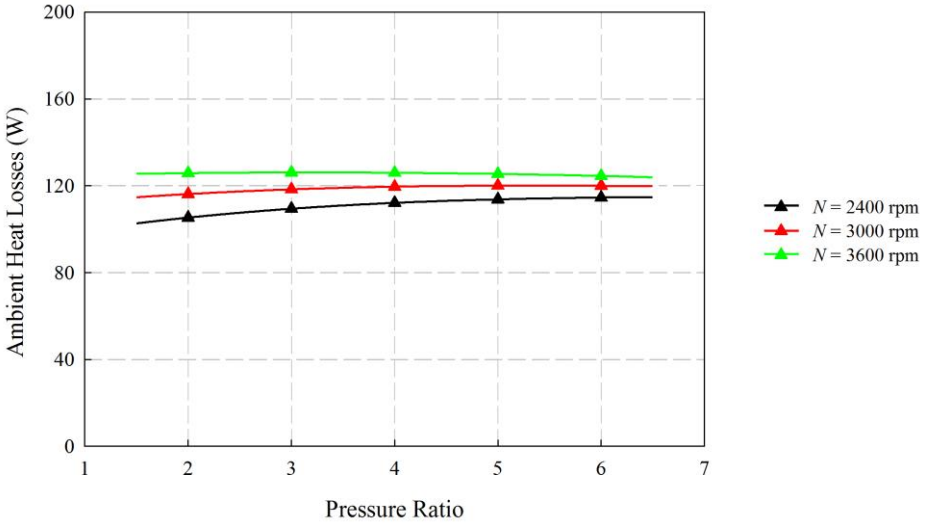
Figure 5-12 Variations of (a) working fluid mass flow rate and (b) scroll expander electric output with pressure ratio

On the other hand, the working fluid exhaust temperature varies steeply with the pressure ratio. As shown in Figure 5-13(a), the exhaust temperature reduces by 31.12K and 34.51K at *N*=2400rpm and 3600rpm respectively. In terms of the ambient heat losses, the associated effect of the pressure ratio is sensitive to the rotational speed. At *N*=3600rpm, a slight variation of the ambient heat losses is obtained, while a more noticeable increase with the pressure ratio is observed at *N*=2400rpm. The reason is that although the supply heat transfer increases in line with the working fluid supply

pressure, the exhaust heat transfer direction between the envelope and working fluid depends on the imposed pressure ratio. For example, the supply heat transfer rate is 36.54W and the exhaust heat transfer from the envelope to the working fluid is 32.87W at *N*=2400rpm and *PR*=2, while at *PR*=6 the supply heat transfer increases up to 87.32W and the exhaust heat transfer takes place from working fluid to the envelope conversely (i.e. 8.65W).



(a)



(b)

Figure 5-13 Variations of scroll expander (a) exhaust temperature and (b) ambient heat losses with pressure ratio

Similar to the observation discussed in Section 5.5.1, an optimum pressure ratio exists for the scroll expander, at which the isentropic efficiency achieves the highest at a given rotational speed as implied in Figure 5-14(a). The imposed pressure ratio affects the isentropic efficiency of the scroll expander more considerably for the over-expansion operation. At N=3600rpm, the isentropic efficiency improves from 0.29 at PR=2 to the highest 0.76 at approximately PR=4.6, and then it decreases by around 5.40% with the pressure ratio further increasing to 6. In terms of the volumetric efficiency of the scroll expander, the related effect is not remarkable, as the volumetric efficiency only increases by 1.10% over the investigated range at N=3600rpm. It is apparent from Figure 5-14(b) that the scroll expander net efficiency dramatically increases at the over-expansion state, and then a stable net efficiency is noted as the pressure ratio above the built-in pressure ratio. This is mainly attributed to the smaller variation in the electric output when the scroll expander operates at the under-expansion state. The simulation results reveal the importance of the imposed pressure ratio on the scroll expander performance for both constant supply pressure and exhaust pressure operating conditions. The scroll expander is thereby recommended for operating at the built-in pressure ratio in order to minimize the negative effect of the imposed pressure ratio especially for the over-expansion operation, which has also been stated in the literature [146].

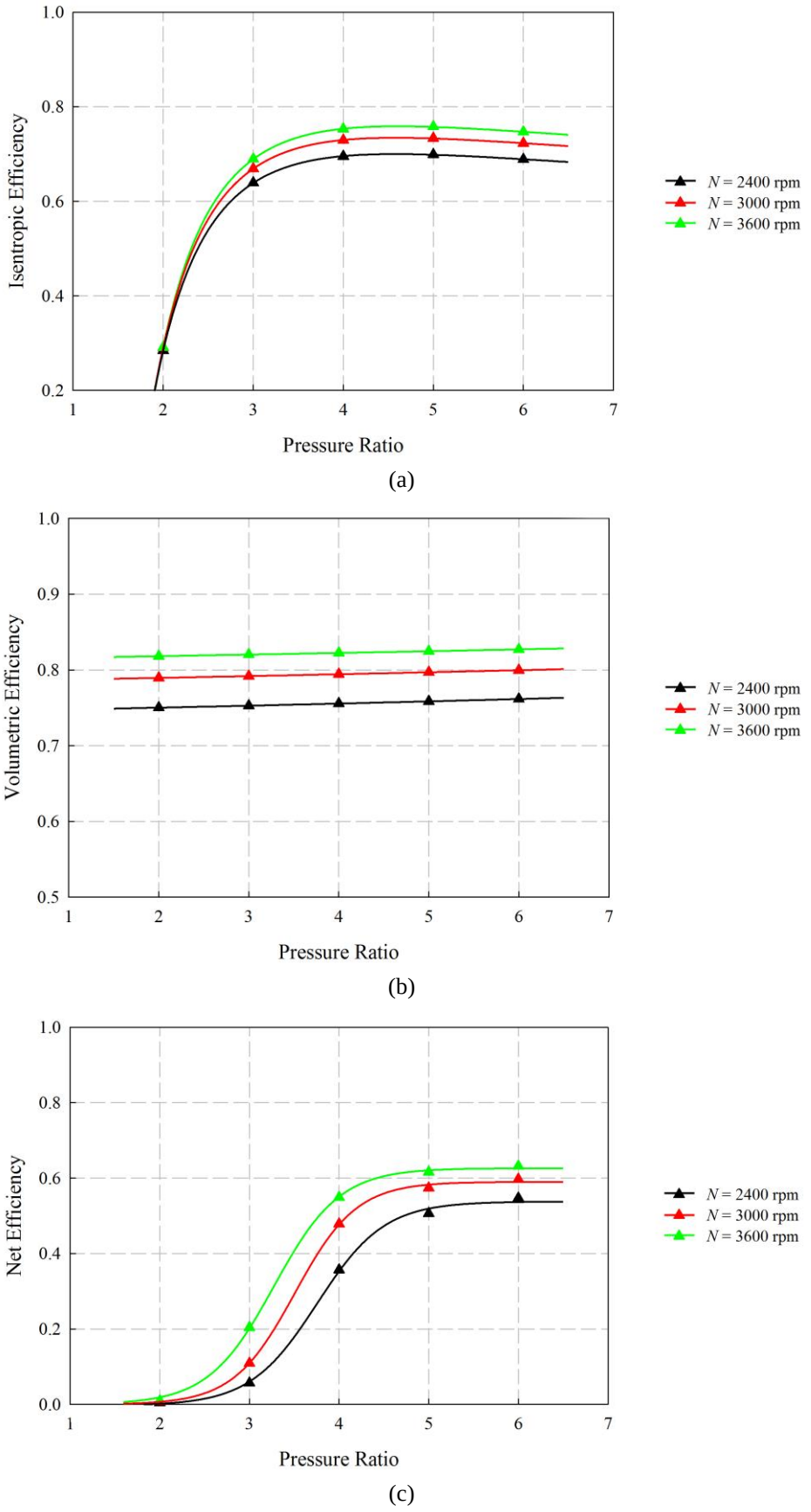
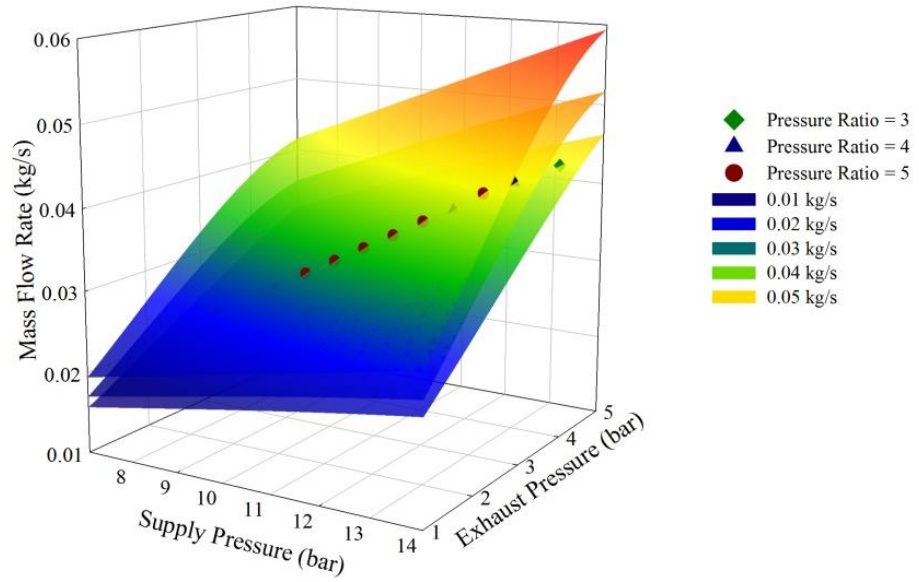


Figure 5-14 Variations of scroll expander (a) isentropic, (b) volumetric and (c) net efficiencies with pressure ratio

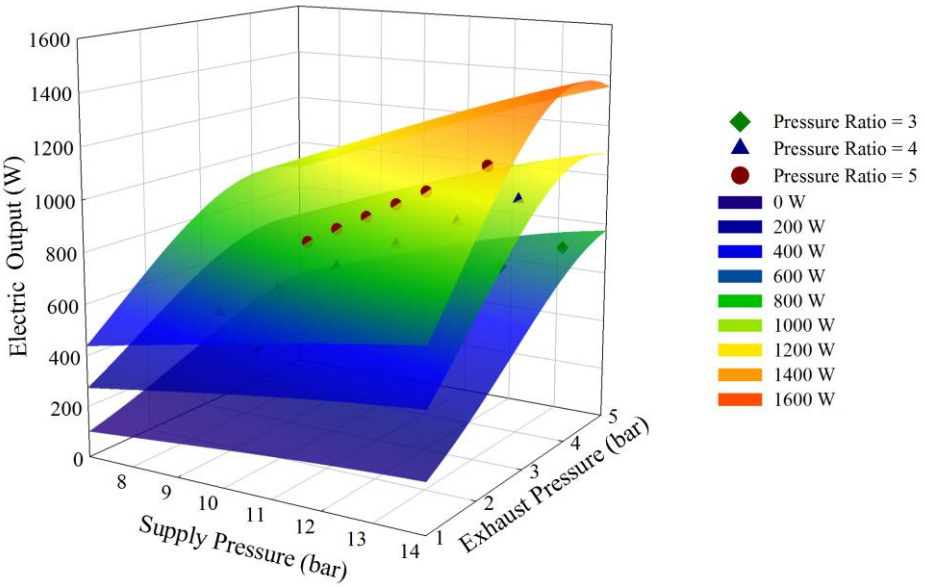
5.5.3 Effect of scroll expander supply pressure

To explore the influence of working fluid supply pressure on the scroll expander performance, the working fluid supply pressure ranges from 8.5bar to 13.5bar while the scroll expander operates at a constant rotational speed of 3600rpm and supply temperature of 378.15K. Three constant pressure ratios are imposed for simulation (i.e. *PR*=3, 4, 5), at which the exhaust pressure varies in accordance with the variable supply pressure. Figure 5-15 presents variations of the mass flow rate and electric output with the supply and exhaust pressures at different pressure ratios respectively in 3D view. It can be observed that the mass flow rate increases markedly with the increment of the supply pressure at a given pressure ratio, which results from the increasing working fluid density. As a result, more electric output is produced at a higher supply pressure.

Comparatively, the effect of the supply pressure is less significant at a higher pressure ratio. For instance, at *PR*=3, the mass flow rate rises by approximately 32% as the supply pressure rises from 10.5bar to 13.5bar and more electricity is generated with an improvement of 49.22%, while the rates of increase in the mass flow rate and electric output are 29.25% and 32.81% respectively at *PR*=5.



(a)

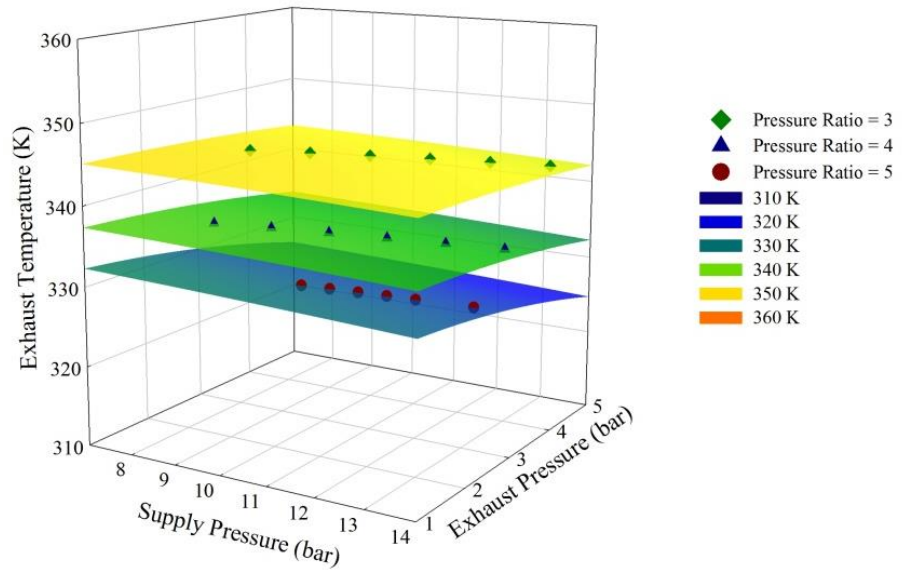


(b)

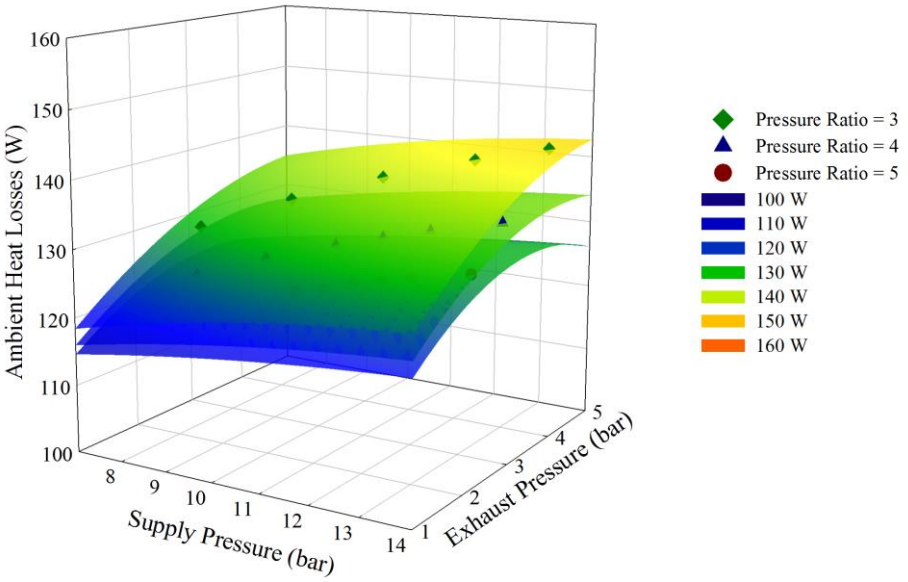
Figure 5-15 Variations of (a) working fluid mass flow rate and (b) scroll expander electric output with supply pressure

A less noticeable influence of the supply pressure on the working fluid exhaust temperature is noted in Figure 5-16(a). The exhaust temperature decreases from 344.44K at P_{su} =8.5bar to 342.60K at P_{su} =13.5bar for the scroll expander operating at *PR*=3. On the other hand, a higher supply pressure leads to a higher envelope temperature and thus more ambient heat losses are caused. As illustrated in Figure 5-

16(b), the ambient heat losses increases by 7.56% as the supply pressure increases from 8.5bar to 13.5bar at *PR*=3.



(a)

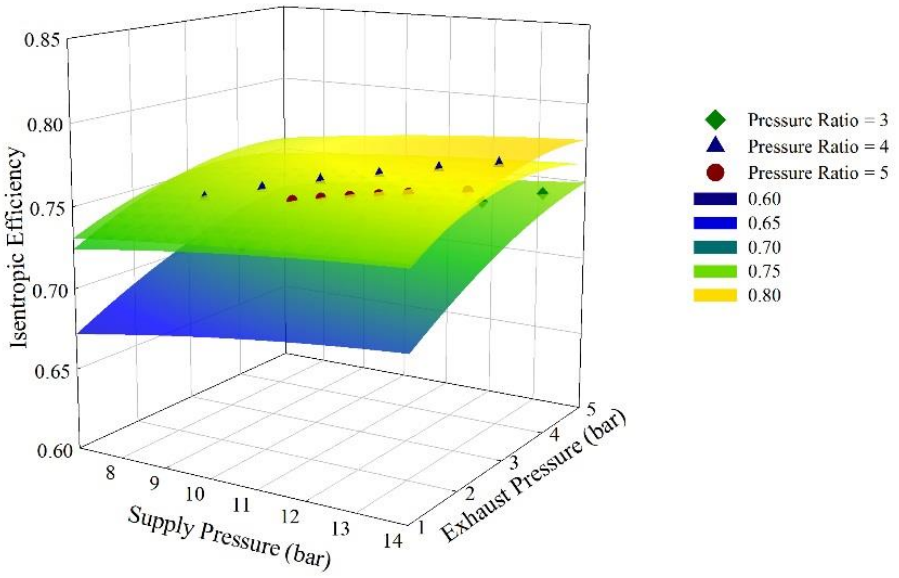


(b)

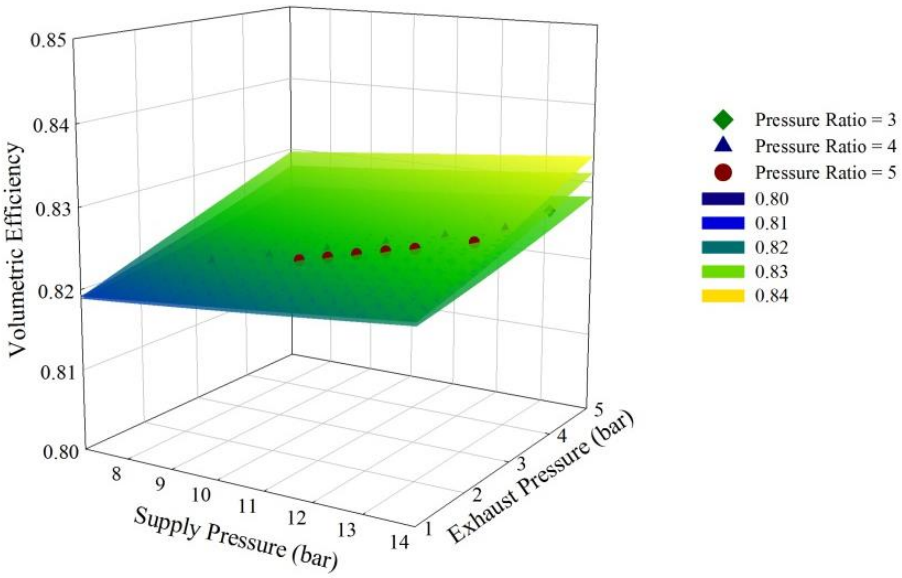
Figure 5-16 Variations of scroll expander (a) exhaust temperature and (b) ambient heat losses with supply pressure

Figure 5-17 shows the variations of the scroll expander isentropic, volumetric and net efficiencies with the supply pressure. As the supply pressure increases from 8.5bar to 13.5bar, the scroll expander isentropic efficiency improves by 4.92% at *PR*=3. Though

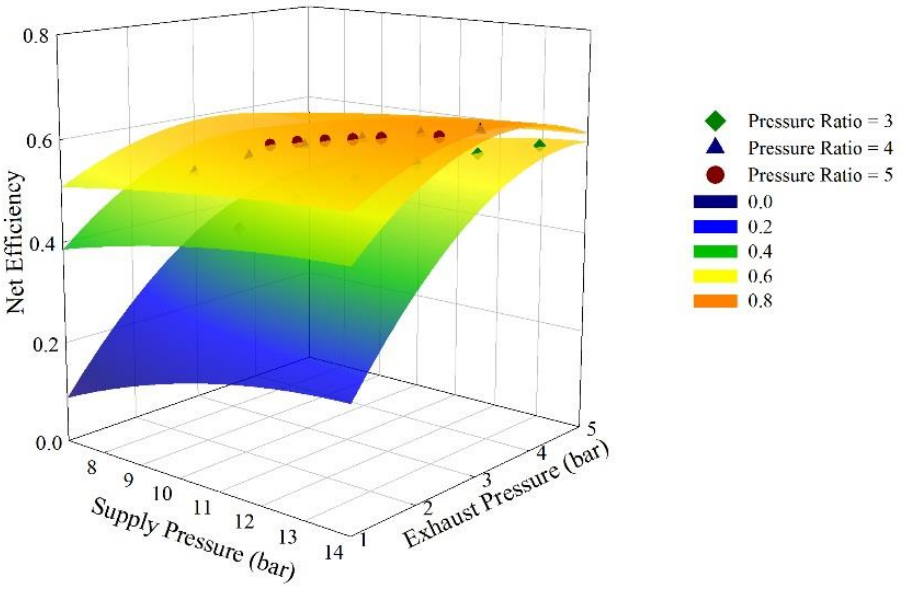
the working fluid mass flow rate increases with the supply pressure, the scroll expander volumetric efficiency is insensitive to the increment of the supply pressure. Over the investigated supply pressure range, the scroll expander volumetric efficiency increases only from 0.82 to 0.83, while the net efficiency rises greatly by 47.70%. The results indicate that by increasing the supply pressure at a constant pressure ratio, an improvement in the scroll expander performance can be achieved, which is line with the finding presented in the literature [117].



(a)



(b)



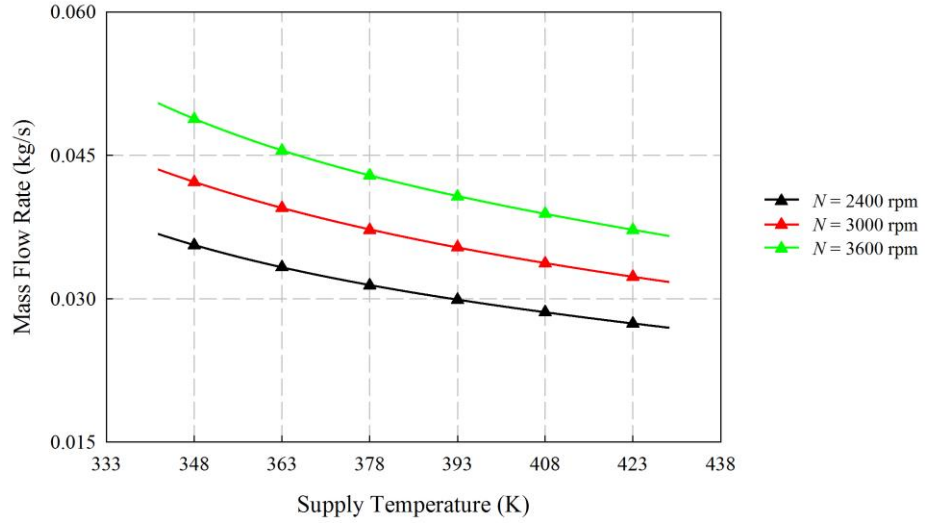
(c)

Figure 5-17 Variations of scroll expander (a) isentropic, (b) volumetric and (c) net efficiencies with supply pressure

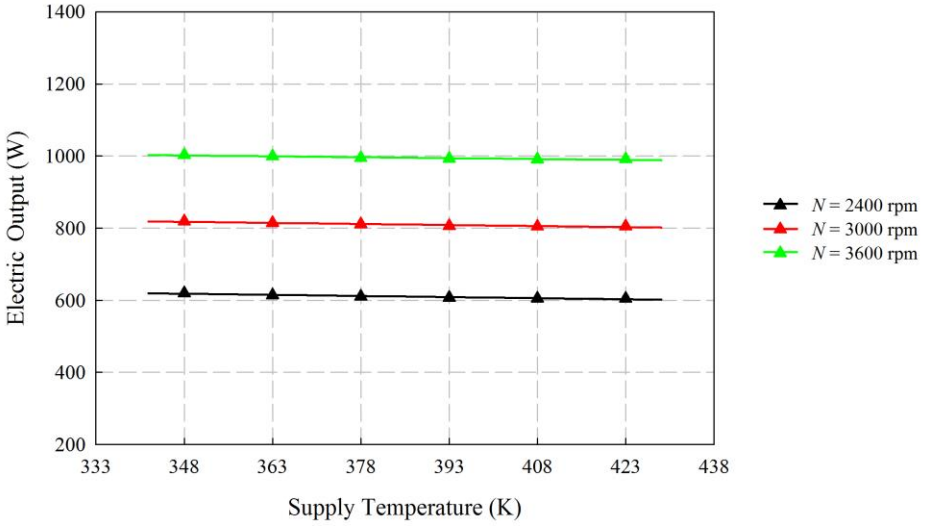
5.5.4 Effect of scroll expander supply temperature

By changing the working fluid supply temperature, the scroll expander performance would be affected accordingly. The scroll expander supply temperature is simulated in a range of 348K to 423K at a constant pressure ratio of 3.97 (i.e. P_{su} =13.5bar and P_{ex} =3.4bar). Figure 5-18 demonstrates the variations of the mass flow rate and electric output power with the supply temperature at different rotational speeds (i.e. N=2400, 3000 and 3600rpm). There is an evident decline tendency in the mass flow rate at a given rotational speed as shown in Figure 5-18(a), which is due to the fact that the working fluid density reduces with the increasing supply temperature at a constant supply pressure. Moreover, the effect of the supply temperature on the mass flow rate is independent of the scroll expander rotational speed. For example, at N=2400rpm, the mass flow rate reduces by 23.03% as the supply temperature rises by 75K, and the rate of decrease at N=3600rpm is approximately 23.77%. On the contrary, a negligible effect of the supply temperature on the scroll expander electric output is noted in

Figure 5-18(b). Over the investigated supply temperature range, the reduction in the electric output is only 15.33W at *N*=2400rpm and 13.52W at *N*=3600rpm respectively.



(a)

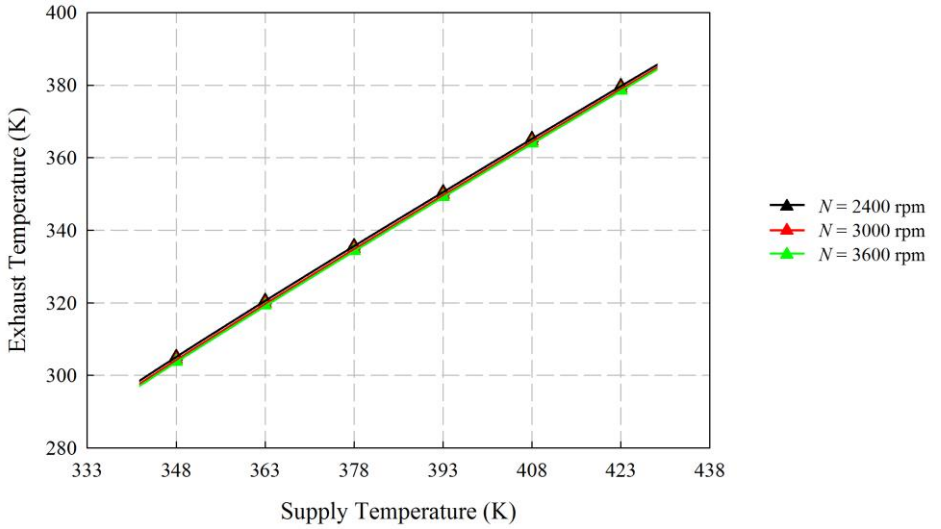


(b)

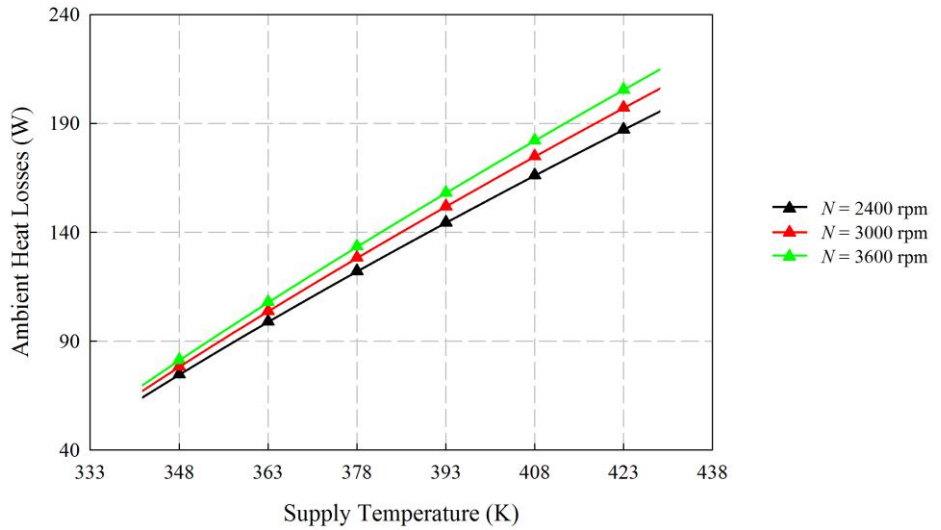
Figure 5-18 Variations of (a) working fluid mass flow rate and (b) scroll expander electric output with supply temperature

In addition, the higher temperature the working fluid is supplied to the scroll expander, the higher the exhaust temperature and the more the ambient heat losses as presented in Figure 5-19. At *N*=3600rpm, the working fluid exhaust temperature rises from 303.81K at T_{su} =348.15K to 378.56K at T_{su} =423.15K, and the associated ambient heat losses increase by 124.26W accordingly. The increase in the supply temperature leads

to more heat transfer between the envelope and ambient, in other words more ambient heat losses are resulted.



(a)

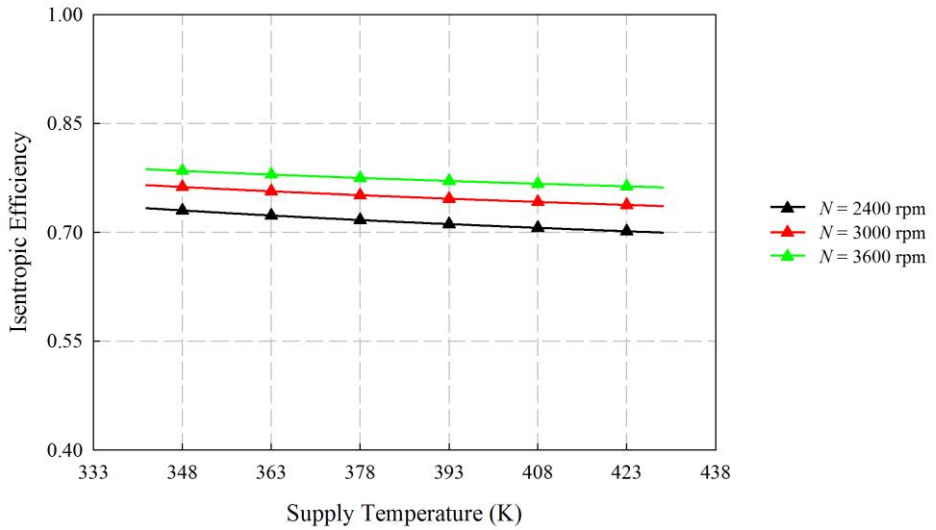


(b)

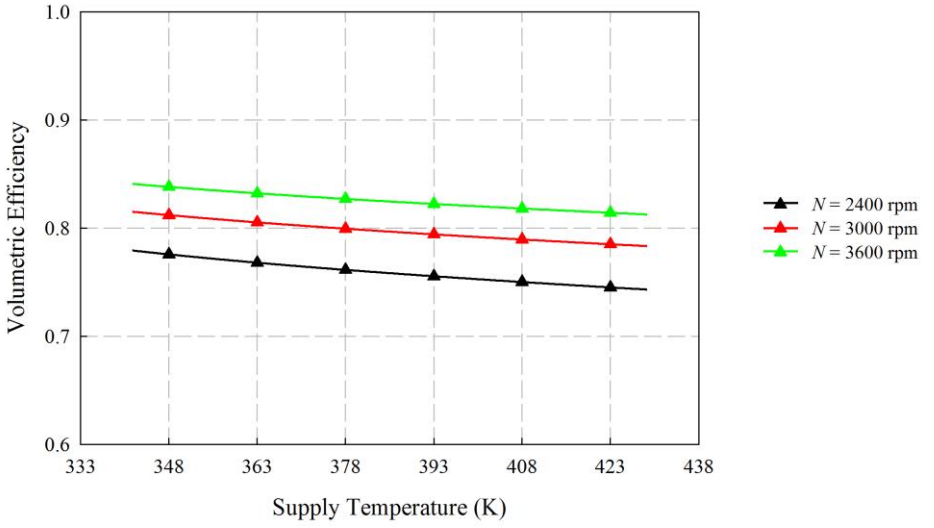
Figure 5-19 Variations of scroll expander (a) exhaust temperature and (b) ambient heat losses with supply temperature

It can be noted from Figure 5-20 that the working fluid supply temperature has a negative influence on the scroll expander performance. However, the influence is not very distinguished, and it becomes less at a higher rotational speed. As the scroll expander supply temperature rises by 75K, the rates of decline in the isentropic, volumetric and net efficiencies are 3.91%, 3.93% and 4.58% at *N*=2400rpm, whereas

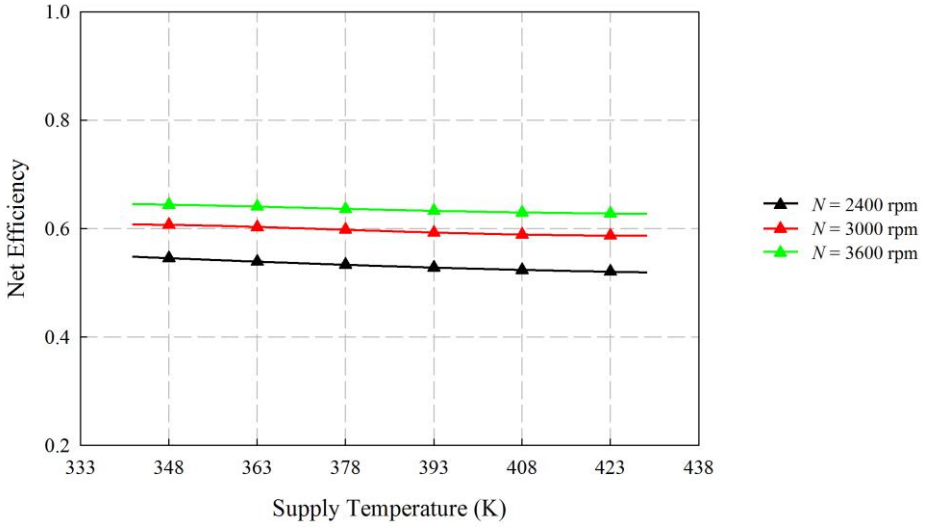
the isentropic efficiency reduces by 2.71%, the volumetric and net efficiencies decrease by 2.85% and 2.51% at *N*=3600rpm. The results reveal that the superheated working fluid results in worse scroll expander performance at a constant pressure ratio. However a different observation has been presented in the literature [249], indicating that superheating of the working fluid is preferred for improvement in the power generation and ORC system efficiency. The reason for the difference is explained as follows: To figure out the influence of supply temperature on the scroll expander performance, only one parameter (i.e. the supply temperature) has changed while other parameters were kept constant for simulation presented in this section. Nevertheless, the study in the literature [249] has been conducted by concerning a variation of the heat source supply temperature, which subsequently influences the supply temperature of the scroll expander. In such a way, the operating condition of the scroll expander as well as the corresponding performance varied.



(a)



(b)



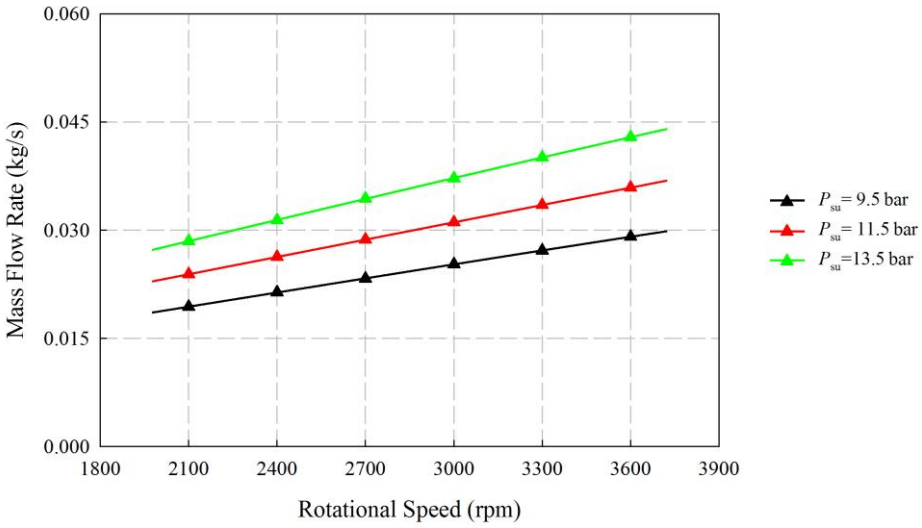
(c)

Figure 5-20 Variations of scroll expander (a) isentropic, (b) volumetric and (c) net efficiencies with supply temperature

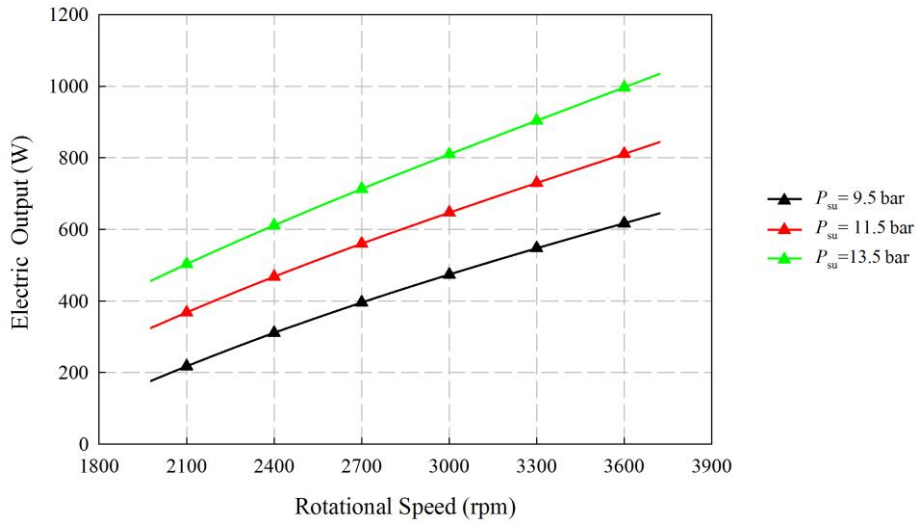
5.5.5 Effect of scroll expander rotational speed

Simulations are also conducted for the scroll expander running at various rotational speeds with a constant pressure ratio (i.e. *PR*=4). There is an evident linear relationship between the working fluid mass flow rate and the rotational speed as seen in Figure 5-21(a), which can be justified by Equation (5-6). The higher the scroll expander rotational speed, the higher the working fluid mass flow rate and consequently the

more the electric output are achieved (Figure 5-21b). At P_{su} =13.5bar, the mass flow rate rises by 50.53% and 493.61W more electric output is produced as the scroll expander rotational speed increases from 2100rpm to 3600rpm. A greater effect of the rotational speed on the electric output is noticed at a lower supply pressure. For instance, at P_{su} =9.5bar, the rate of increase in the electric output power is approximately 183.78% over the investigated rotational speed range, while 98.09% is obtained at P_{su} =13.5bar.



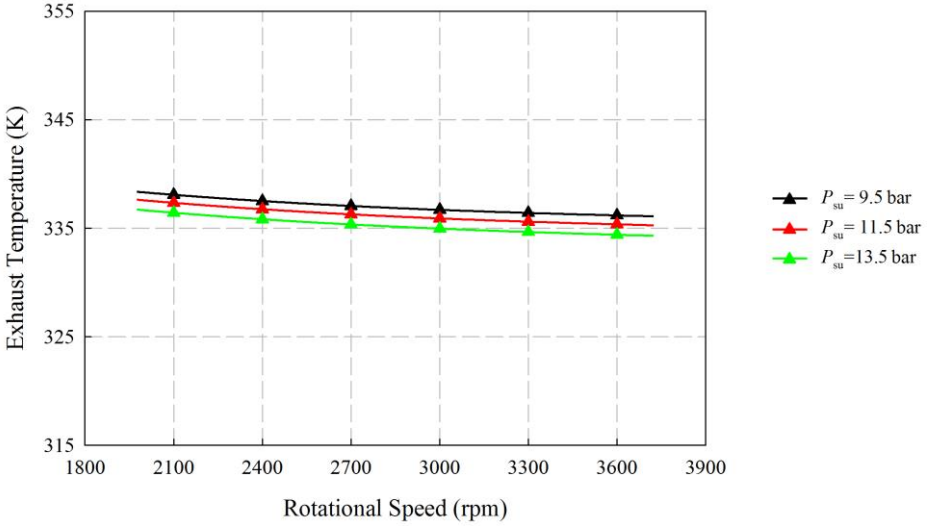
(a)



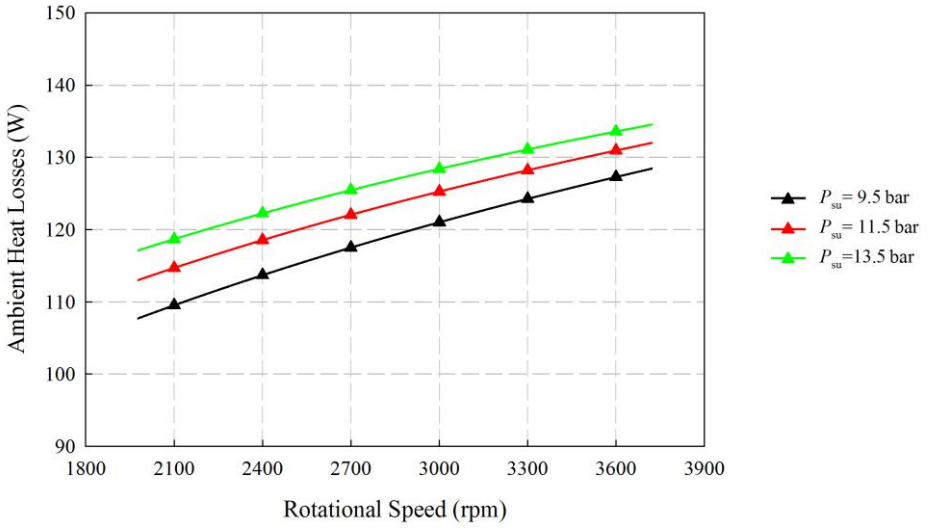
(b)

Figure 5-21 Variations of (a) working fluid mass flow rate and (b) scroll expander electric output with rotational speed

However, the rotational speed of the scroll expander has an insignificant effect on the working fluid exhaust temperature as only slight variations with the rotational speed are noted in Figure 5-22(a). For P_{su} =13.5bar, the exhaust temperature decreases from 336.44K at N=2100rpm to 334.41K at N=3600rpm. On the contrary, a higher rotational speed accounts for a higher working fluid mass flow rate, more mechanical losses, supply and exhaust heat transfers, which thereby leads to more ambient heat losses. As seen in Figure 5-22(b), the ambient heat losses increase by 16.20% and 12.55% when the scroll expander rotates from 2400rpm to 3600rpm at P_{su} =9.5 and 13.5bar.



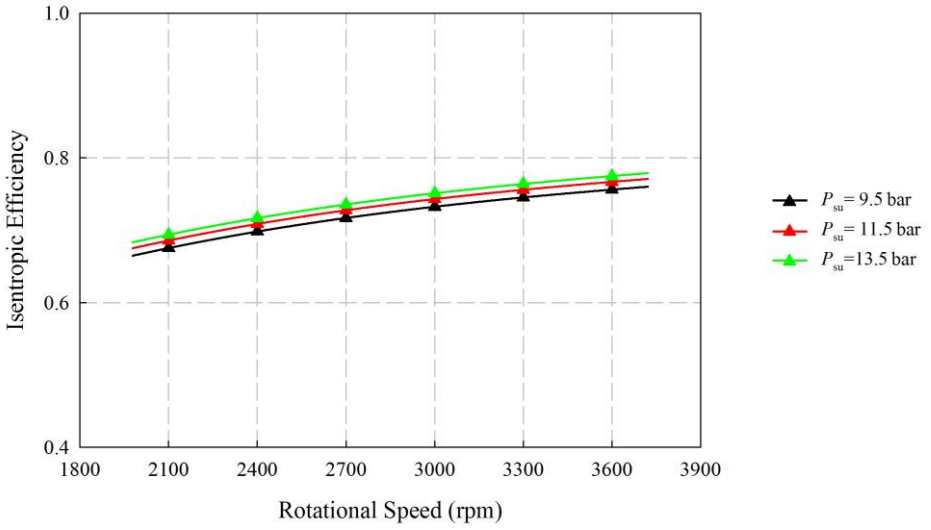
(a)



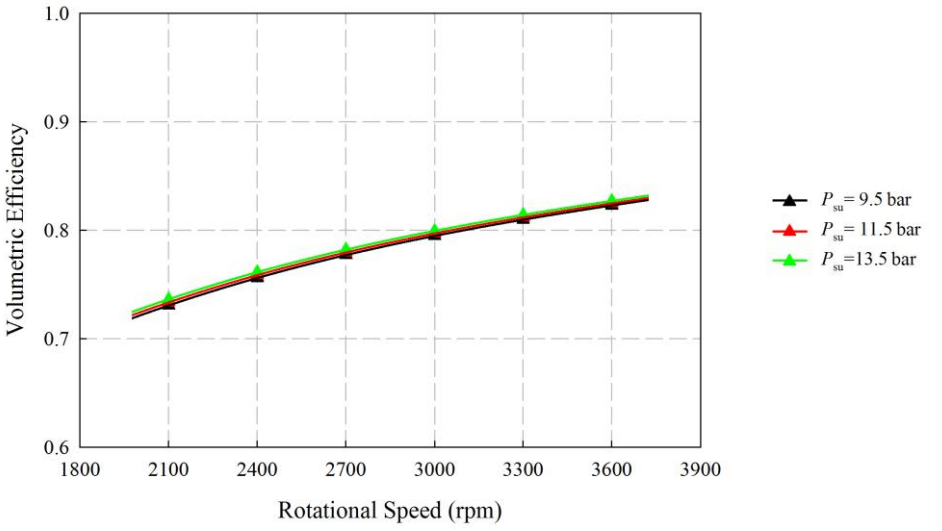
(b)

Figure 5-22 Variations of scroll expander (a) exhaust temperature and (b) ambient heat losses with rotational speed

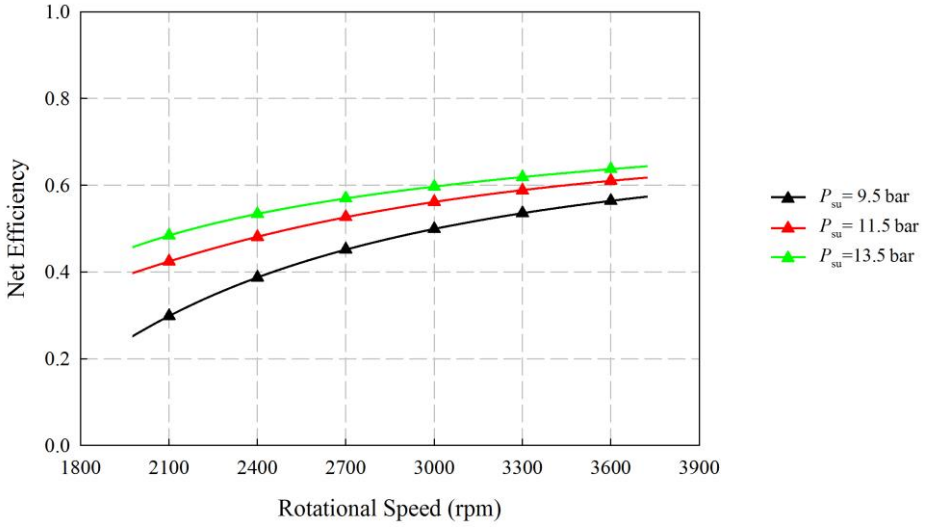
Figure 5-23 confirms the positive impact of the rotational speed on the scroll expander performance. With more shaft power produced, the isentropic efficiency of the scroll expander improves from 0.69 to 0.78 as the rotational speed increases to 3600rpm at P_{su} =13.5bar. Meanwhile, the volumetric and net efficiencies rise by 12.30% and 31.59% respectively. The lower volumetric efficiency at a low rotational speed is mainly attributed to the larger leakage flow. Furthermore, variations of the three efficiencies become more stable as the rotational speed further increases, which indicate that the scroll expander performance is not greatly dependent on the rotational speed when the rotational speed is beyond the maximum rotational speed. Practically, the scroll expander is suggested to operate at a higher rotational speed but within its capacity to ensure better energy performance and this has also been considered in the literature [129].



(a)



(b)



(c)

Figure 5-23 Variations of scroll expander (a) isentropic, (b) volumetric and (c) net efficiencies with rotational speed

5.5.6 Parametric analysis summary

Section 5.5 has presented a comprehensive parametric analysis of the scroll expander on the basis of the simulation results and the effect of the working fluid inlet condition (i.e. supply pressure and temperature), scroll expander imposed pressure ratio and rotational speed have been investigated. The following findings are summarised:

- Once the imposed pressure ratio matches with the built-in expansion ratio, the maximum isentropic efficiency of the scroll expander is attainable.

- The scroll expander performance deteriorates as the imposed pressure ratio deviating from the built-in pressure ratio; in particular a more considerable effect of the pressure ratio is observed when the scroll expander operates at over-expansion state.
- By increasing the working fluid supply pressure at a constant pressure ratio, better scroll expander performance can be achieved, with more electric output power as well as higher isentropic, volumetric and net efficiencies.
- Superheated working fluid negatively influences the scroll expander performance when the scroll expander operates at a constant pressure ratio.
- The higher the rotational speed of the scroll expander, the more the electric output power and the better the scroll expander performance.

Next, Section 5.6 presents experimental investigations of the scroll-based ORC system with different electrical resistive loads.

5.6 Experimental investigations of ORC system

As discussed in Chapter 2, limited studies have been conducted regarding the effect of the coupled electrical resistive load on the scroll expander and ORC system performances. Hence, in this section, based on the experimental investigations, a detailed analysis of the performances for both the scroll expander and the ORC system is presented for operation with variable resistive loads. A series of tests have been performed with the scroll-based ORC system and six different resistive consumers are selected for load simulation, which were 18.6Ω, 19.4Ω, 26.2Ω, 34.7Ω, 64.0Ω and 75.6Ω respectively. The evaluation presented in this section is structured as: Section 5.6.1 discusses the influence of the electrical resistive load on the electric output

characteristic of the ORC system; Section 5.6.2 analyses how the electrical resistive load affects the imposed pressure ratio of the scroll expander; Section 5.6.3 presents variations of the electric output with the pressure ratio and rotational speed of the scroll expander and the impact of the electrical resistive load on the efficiencies of the scroll expander and ORC system are clarified in Section 5.6.4.

In addition, error bars are included in the experimental result analysis, which are associated with the calculated uncertainties.

5.6.1 Variation of electric output with resistive load

The resistive load coupled to the scroll expander-generator unit results in shaft resisting torque. For a low resistive load, the generated current is high based on the interaction between electromagnetic and mechanical loads, thus the corresponding shaft resisting torque is high owing to the proportional relation between the current and the torque. To ensure the scroll expander-generator unit runs smoothly, the shaft torque produced by the scroll expander should be equal to the total resisting torques induced by the generator and various frictions. Variations of the electric output power with the resistive load at different rotational speeds (i.e. 3432, 3144, 3006, 2730rpm) are presented in Figure 5-24. As can be seen, the output power decreases with the resistive load at a given rotational speed. However, the decreasing rate of output power declines gradually as the resistive load gets higher. When the scroll expander rotates at a speed of 3432rpm, the output power is 557.2W for a resistive load of 18.6Ω, while only 20% of the power can be produced for a resistance of 75.6Ω. Moreover, the linear relationship between the electric output and rotational speed is clearly indicated for all resistive loads. The increasing rate for the lower resistive load is much higher than that for the higher one. As the scroll expander rotational speed rises from 2730rpm to

3432rpm, 257.7W more electric power can be generated for the resistive load of 18.6Ω, while the increase is only approximately 68.5W for the resistance of 75.6Ω. The results reflect the significant role of the resistive load in the ORC system output power. Similarly, an experimental study of a small ORC power generation system with five different load resistances (20Ω, 60Ω, 100Ω, 140Ω and 180Ω) has been also presented in the literature [152]. Their measurement data also have confirmed that the decreasing rate of the electric output power with the resistive load becomes larger at a higher rotational speed, but at a different rate owing to the different working fluids and operating conditions.

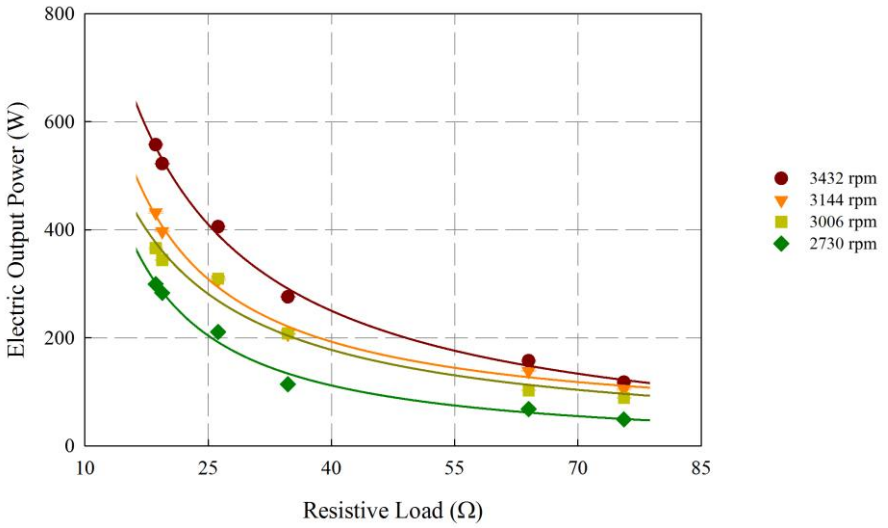
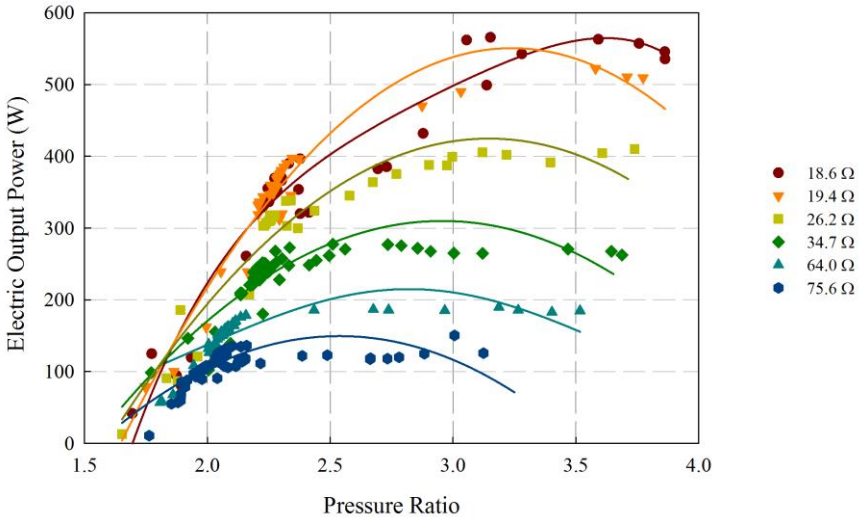


Figure 5-24 Variations of electric output power with resistive load

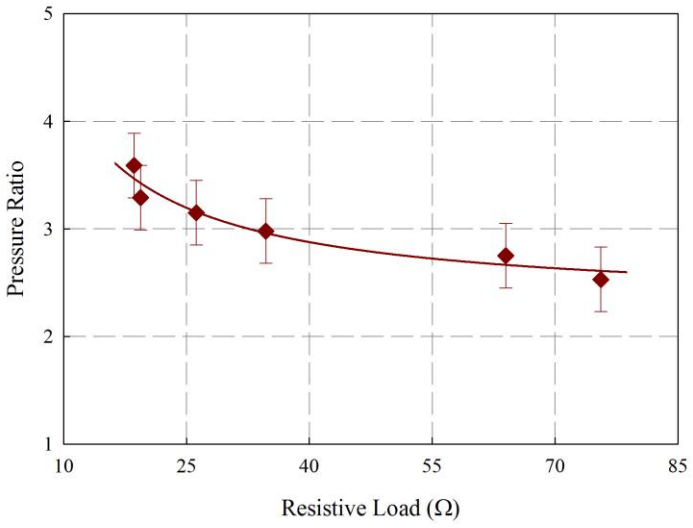
5.6.2 Variation of electric output with pressure ratio

Due to the fact that the evaporation and condensation pressures of the working fluid are influenced by the temperatures of heat source and heat sink respectively, an adjustment in the pressure ratio of the scroll expander could be realised by controlling the supply conditions of boiler and cold water for testing. Variations of the electric output with the pressure ratio of the scroll expander for the six different resistive configurations are shown in Figure 5-25(a). For a given resistive load, the output

power increases with the pressure ratio until reaching a maximum and then it decreases gradually. Moreover, it can be also observed that the resistive load has a marked impact on the optimal pressure ratio of the scroll expander from Figure 5-25(b). Initially, the optimal pressure ratio decreases sharply with the increasing resistive load and then the decreasing rate declines gradually. Because of the correlation between the shaft torque and the output power, less power can be produced at a lower pressure ratio of the scroll expander. The optimal pressure ratio for the resistive load of 18.6Ω is approximately 3.6 and the maximum output power of 564.5W is achieved, while only 154.2W electric power is generated for the resistance of 64.0Ω under an optimal pressure ratio of 2.8. The relationship implies that a lower electrical resistive load contributes to the larger amount of electric output under a higher optimal pressure ratio.



(a)



(b)

Figure 5-25 Variations of (a) electric output power with pressure ratio and (b) optimal pressure ratio with resistive load

5.6.3 Variation of electric output with pressure ratio and rotational speed

A set of 3D images presented in Figure 5-26 show variations of the electric output power with the scroll expander rotational speed and pressure ratio for all resistive loads. In particular, with the resistive load of 18.6Ω, the output power increases dramatically with the pressure ratio and rotational speed, and reaches the maximum value of 564.5W under a pressure ratio of 3.6 and a rotational speed of 3450rpm, and then it decreases as the pressure ratio is higher than 3.6 and the scroll expander rotates faster. Therefore, the load characteristic in correlation to the expander-generator unit plays an important role in achieving an optimal performance of the ORC system.

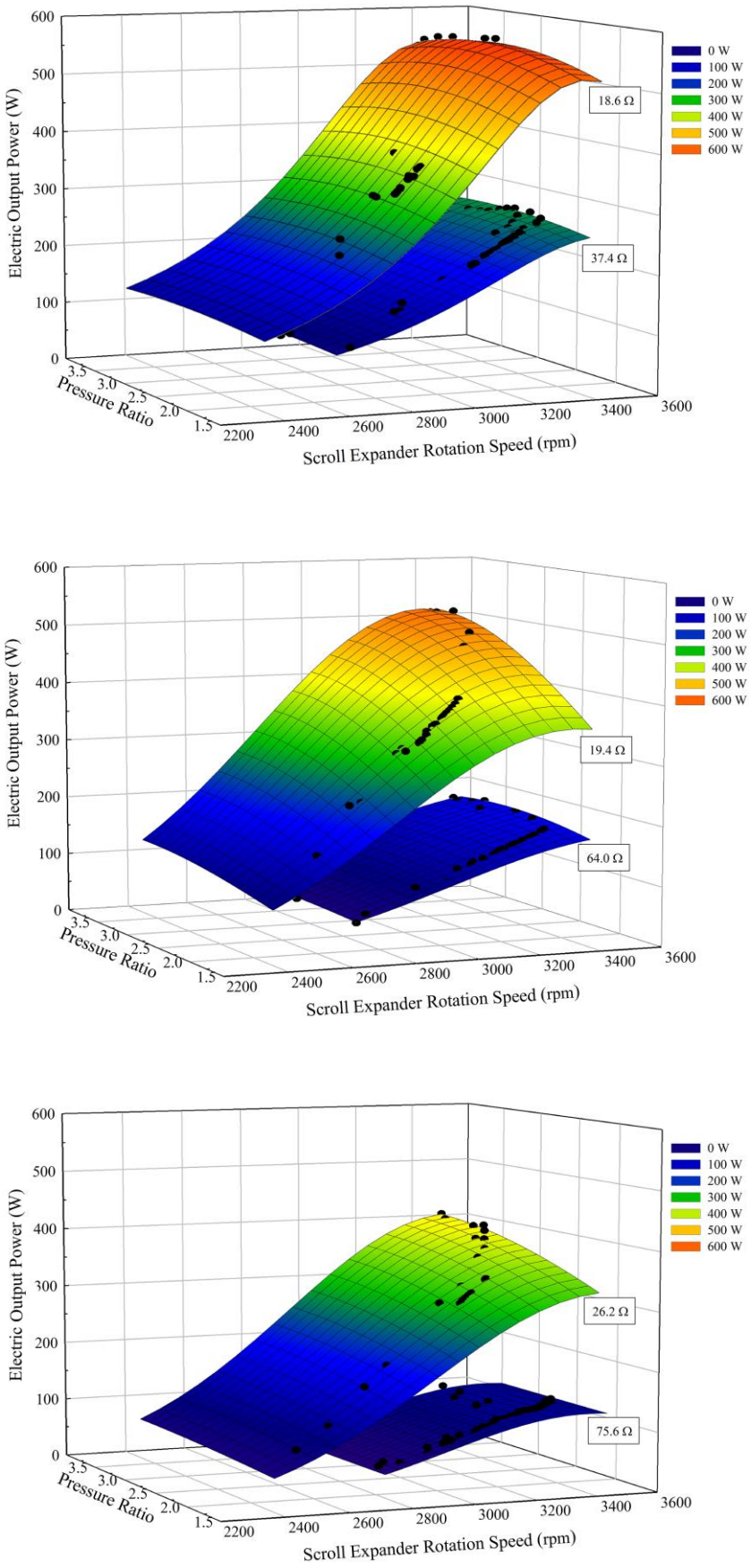


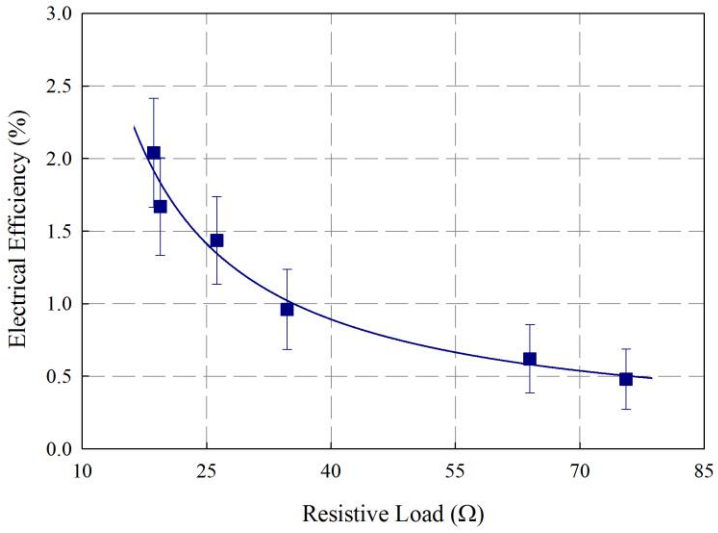
Figure 5-26 Variations of electric output power with pressure ratio and rotational speed

5.6.4 Variation of electrical and scroll expander efficiencies with resistive load

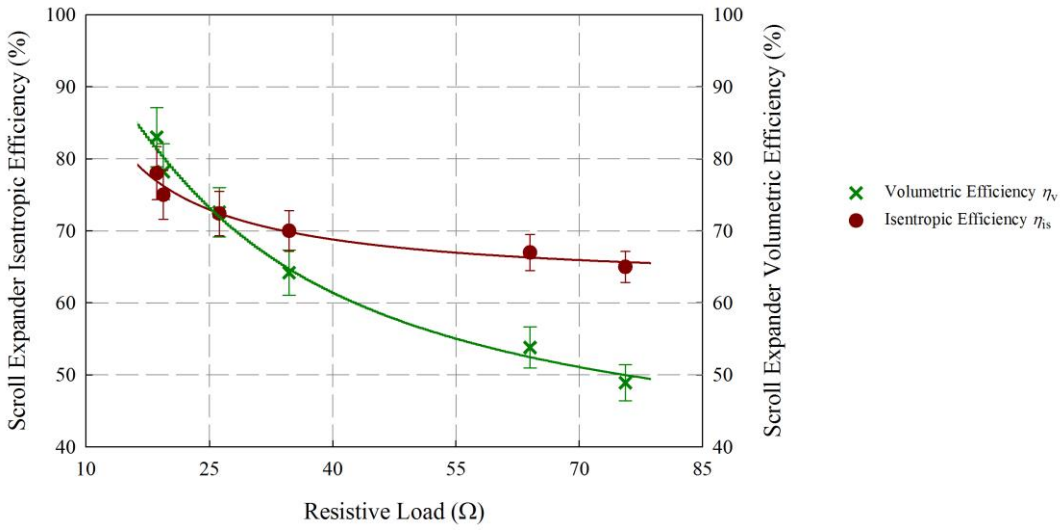
Additionally, the maximum electrical efficiency of the ORC system under the optimal pressure ratio for each resistive load is presented in Figure 5-27(a). A dramatically decreasing tendency can be observed for the electrical efficiency curve, which is similar to that of the output power in Figure 5-24. The maximum electrical efficiency reaches 2.04% for the resistive load of 18.6Ω; however it reduces by 70% for the resistance of 64.0Ω.

Referring to Equation 5-32, the electrical efficiency of the ORC system relates directly to the performance characteristic of the scroll expander. To evaluate the effect of the resistive load on the scroll expander isentropic and volumetric efficiencies, investigations are carried out under the optimal pressure ratio operating condition for the six resistive loads. Different resistive loads cause different resisting torques, which also influence the operation of the scroll expander as demonstrated in Figure 5-27(b). The results clearly show that the lower resistive load results in both higher isentropic and volumetric efficiencies of the scroll expander. Compared with the decreasing rate of isentropic efficiency, the resistive load influences the volumetric efficiency less significantly. For the resistive load of 18.6Ω, the isentropic and volumetric efficiencies are 78% and 83% respectively while the isentropic efficiency reduces to 65% and the volumetric efficiency decreases by 41.7% for a higher resistive load of 75.6Ω. A similar variation of the scroll expander isentropic efficiency with the resistive load has also been presented in the literature [151]. For example, based on the obtained experimental data, the isentropic efficiency is 78% for the resistive load of 18.6Ω and 70% for the resistive load of 34.7Ω, in other words, the efficiency decreases by 8% as the resistive load nearly doubles. The electrical loads in the literature [151] were adjusted by changing the number of the bulbs parallel connected to the power

generator, based on their experimental results, the isentropic efficiency of the scroll expander is 55% for 12 bulbs and 47% for 6 bulbs, that is to say the reduction in the isentropic efficiency is also 8% when the resistive load doubles.



(a)



(b)

Figure 5-27 Variations of (a) ORC electrical efficiency and (b) isentropic and volumetric efficiencies of scroll expander with resistive load

5.6.5 Experimental investigations summary

Section 5.6 has presented the experimental work for the scroll-based ORC system with different electrical resistive loads, in which the effect of the resistive load on the performances of both the scroll expander and ORC system has been investigated. Some implications are drawn as follows:

1) Different resistive loads coupled to the scroll expander-generator unit result in different shaft resisting torques. A low resistive load leads to a high linear increasing rate in the electric output with the scroll expander rotational speed. The electric output power decreases with the resistive load at a fixed rotational speed, while the associated decreasing rate reduces gradually.
2) There exists an optimal pressure ratio with the maximum electric output at a given electrical resistive load. However, the optimal pressure ratio decreases markedly with the resistive load.
3) The optimal pressure ratio at a corresponding rotational speed could be determined based on the variations of the electric output power with the pressure ratio and rotational speed. For a resistive load of 18.6Ω, the optimal pressure ratio is 3.6 with the maximum electric output power of 564.5W at a rotational speed of 3450rpm.
4) The electrical efficiency of the ORC system decreases significantly with the resistive load. The maximum electrical efficiency reduces by 70% for the resistance of 64.0Ω compared with a load of 18.6Ω. A lower resistive load leads to in both higher isentropic and volumetric efficiencies of scroll expander. The scroll expander volumetric efficiency drops by 41.7% as the resistive load increases from 18.6Ω to 75.6Ω, while the isentropic efficiency decreases from 78% to 65%.

5.7 Summary

This chapter has presented a comprehensive evaluation of the ORC system with a scroll expander through experimental testing and theoretical modelling, including performance assessments of the scroll expander and the ORC system under a variety of operating conditions. A semi-empirical model of the scroll expander has been developed to describe the scroll expander thermodynamic behaviour and the electromechanical losses of the generator have also been taken into account. The validation results have proved the validity and accuracy of the model, with maximum deviations of 5% for the working fluid mass flow rate and electric output power and 3K for the exhaust temperature. Based on the simulation with the validated model, effect of the working fluid inlet condition (i.e. supply pressure and temperature); scroll expander imposed pressure ratio and rotational speed have been investigated respectively with the working fluid of R134a. On the other hand, a comprehensive assessment based on experimental work has been performed regarding influence of the electrical resistive load on the performance of the scroll-based ORC system. Main findings of the theoretical and experimental investigations are presented as follows:

(1) Both the numerical and experimental data demonstrate the capability of the micro scroll-based ORC to efficiently produce electric power and the exhaust heat temperature of the scroll expander is adequate for subsequent heat recovery (i.e. typically above 65°C under investigated operating conditions), which thereby affirms the feasibility of integration to the micro trigeneration system.

(2) Either a higher working fluid supply pressure or a higher rotational speed of the scroll expander contributes to better scroll expander performance, whereas an small negative impact of the superheated supply working fluid is observed.

(3) For the investigated scroll expander, a maximum isentropic efficiency of 78% can be reached once the imposed pressure ratio matches with the built-in volume ratio. However, both under and over-expansion operations negatively influence the scroll expander performance, in particular the over-expansion operation should be avoided practically due to the associated lower system stability and a more considerable negative effect of the pressure ratio.

(4) The electrical resistive load coupled to the scroll expander-generator unit indeed affects not only the electric output characteristic of the scroll expander but also the ORC system performance.

(5) The experimental data also indicate that an optimum pressure ratio of the scroll expander exists with the maximum electric output. Nevertheless, the optimal pressure ratio of the scroll expander decreases markedly as the resistive load gets higher.

(6) Based on the experimental tests, the optimum pressure ratio of the scroll expander is approximately 3.6 at a rotational speed of 3450rpm for a resistive load of 18.6 Ω. The maximum electric output of 564.5W is obtained with corresponding isentropic and volumetric efficiencies of 78% and 83% respectively.

The validated model of the scroll expander can be adopted as a useful tool for pre-design and preliminary assessment of the scroll expander as well as the scroll-based ORC system. The work presented in this chapter facilitates an effective integration of the scroll-based ORC system to the proposed micro trigeneration system in Chapter 7. Furthermore, the investigations provide contributions to the knowledge of modelling and simulation of the scroll expander and comprehensive experimental assessment of

the scroll-based ORC system. Next, Chapter 6 presents a detailed performance evaluation of the MLDC system based on experimental work.

Chapter 6: Performance Evaluation of MLDC

6.1 Introduction

In the proposed micro trigeneration system, the inclusion of MLDC is aimed to handle the cooling and dehumidification demands with utilisation of the exhaust heat from the scroll-based ORC sub-system. In order to gain the knowledge of the MLDC and prove the feasibility of an effective combination with the scroll-based ORC for the micro trigeneration system, experimental investigation of a MLDC system is conducted in this chapter, the MLDC dehumidification, regeneration, evaporative cooling as well the overall system performances are investigated under a wide range of operating conditions.

As stated in Chapter 2, the liquid desiccant cooling system is regarded as an environmental-friendly and economical air conditioning alternative to the conventional mechanical vapour compression system, owing to its flexibility in utilising low-grade energy sources [194] and capability of efficient independent humidity and temperature controls [197]. By adding the evaporative cooling into the liquid desiccant system, such a system has been proved with remarkable energy and cost saving potential [213]. More specifically, the MLDC system successfully eliminates the liquid desiccant carryover problem by adopting membranes as selective barriers for heat and mass transfer between the solution and airstream [206]. To date, the MLDC system is still under the research and development stage and the majority of the existing studies are based on modelling and simulation, whereas relatively few studies have been conducted to experimentally investigate the effect of various operating variables on the MLDC system performance. In this chapter, a novel MLDC

system is developed with the following characteristics to address the issues of temperature and humidity controls as well as carryover of liquid desiccant droplets:

- Low-grade heat sources can be utilised to regenerate the liquid desiccant $CaCl_2$ (i.e. in a temperature range of 50.0°C to 80.0°C).
- Independent control in the supply air temperature and humidity in the hot and humid climate without overcooling, reheating and water condensation problems.
- The carryover problem of liquid desiccant solution droplet into supply airstream is avoided by adopting semi-permeable micro porous membranes in both the dehumidifier and regenerator.
- An indirect approach is employed to handle the sensible cooling load, where heat transfer takes place between the cool airstream from the direct evaporative cooler and the dehumidified airstream.

Very few similar studies have been found in the literature on experimental investigation of an integrated liquid desiccant cooling system combining the membrane-based dehumidifier, regenerator and evaporative cooler. In this chapter, experimental tests of the MLDC system are conducted under variable controlled laboratory conditions, which generate greater understandings of the MLDC system and its performance. The main aims of the experimental work in this chapter are to: (a) demonstrate the MLDC system feasibility in the hot and humid climate and (b) identify the impacts of changes in environmental and operating condition on the performance of the dehumidifier, regenerator, evaporative cooler and complete MLDC system. Thus, this chapter is structured into seven sections: Section 6.2 describes the MLDC experimental set-up, instrumentation and experimental method; Section 6.3 introduces the performance evaluation metrics for analysis; Section 6.4 assess the MLDC system

dehumidification performance under various operating conditions; Section 6.5 evaluates the MLDC system regeneration performance by varying the inlet air flow rate, hot water supply temperature and desiccant solution concentration; Section 6.6 presents investigation on the overall MLDC system performance under various operating conditions (i.e. different cold water and regeneration temperatures) and Section 6.7 summarises the chapter and discusses potentials for the micro trigeneration system integration.

6.2 Experimental set-up of MLDC

A MLDC test rig is designed and built in the Marmont laboratory of University of Nottingham. Aqueous $CaCl_2$ is selected as the liquid desiccant solution. This section describes the MLDC experimental set-up with instrumentation in Section 6.2.1 and detailed descriptions of the membrane-based unit are presented in Section 6.2.2. The experimental method together with measuring instrumentation is explained in Section 6.2.3.

6.2.1 System description

The proposed MLDC system consists of four main components: a dehumidifier, a regenerator, an evaporative cooler and an air-to-air heat exchanger, in which four processes are involved as illustrated in Figure 6-1:

- *Dehumidification process*: the outdoor hot and humid air is dehumidified by liquid desiccant solution in the dehumidifier;
- *Regeneration process*: the indoor return airstream passes through the regenerator and absorbs moisture from the dilute desiccant solution;
- *Direct evaporative cooling process*: the evaporative cooler lowers the indoor return air temperature through water evaporation;

- *Sensible cooling process*: the airstream from the evaporative cooler is used to cool the dehumidified air to meet the desired supply air requirement in the air-to-air heat exchanger.

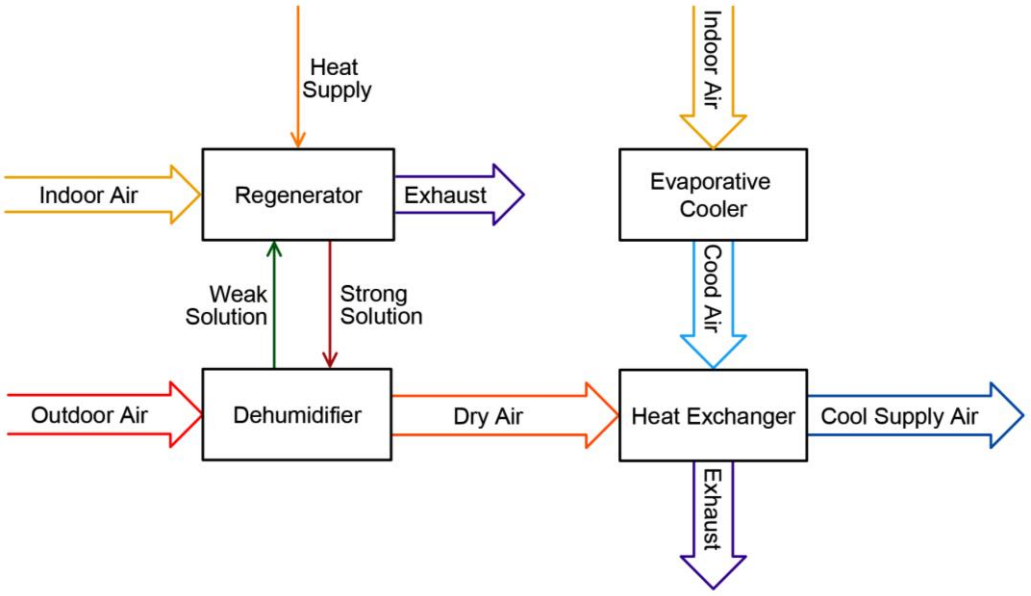


Figure 6-1 Block diagram of MLDC system

A schematic diagram of the MLDC experimental set-up is presented in Figure 6-2 and main instruments with their specifications are listed in Table 6-1. For experimental testing, a 3kW electric boiler is used to provide hot water for the regeneration purpose. Three AC axial fans are fitted in the dehumidifier, regenerator and evaporative cooler respectively. Two 15W single phase magnetic-driven pumps are used to circulate the regenerated and dilute desiccant solutions. In order to enhance the dehumidification performance, a liquid-to-liquid heat exchanger (HX2) allows heat recovery between the regenerated and dilute solutions, and cold water is utilised to further cool the regenerated solution prior to flowing into the dehumidifier. Ball valves (i.e. V1, V2, V3, and V4) are installed to control the desiccant solution and water flow rates.

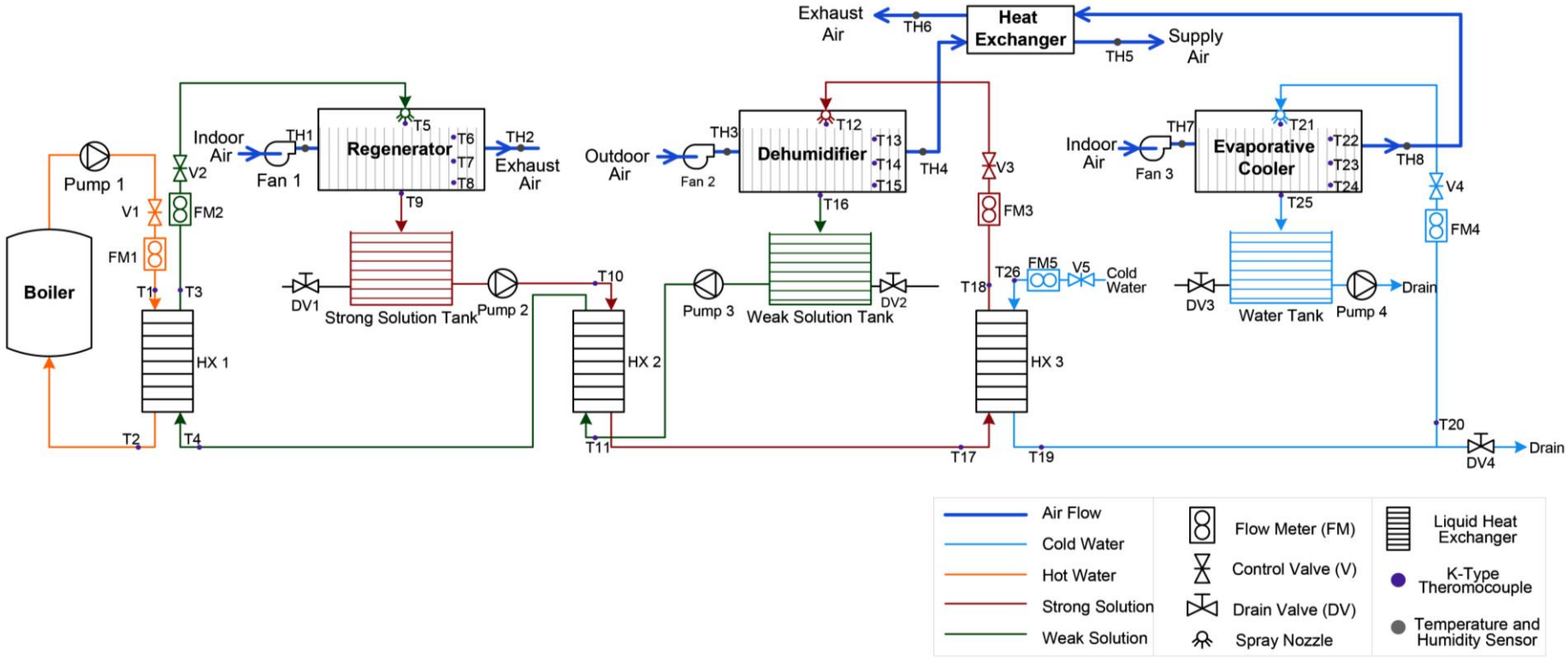


Figure 6-2 Schematic graph of MLDC system

Table 6-1 Specifications of main equipment in MLDC system

Equipment	Properties		Manufacturer
Magnetic pump	Power	15W	Shanghai Jiaxing Pumps Co., Ltd.
	Maximum frequency	50Hz	
	Maximum speed	2600rpm	
	Maximum capacity	10L/min	
AC axial fan	Power	45W	ebm-papst Mulfingen GmbH & Co. KG
	Nominal speed	2800rpm	
Boiler	Capacity	3kW	Wilo SE
	Supply temperature range	50-80°C	
	Water storage	120Litre	
	Circulating pump	45W	
	Water flow rate	0-6L/min	

6.2.2 Membrane-based unit

Both the dehumidifier and regenerator are membrane-based units with specifications presented in Table 6-2. The evaporative cooler has the same dimensions as the membrane-based unit, whereas its air channels are formed only by fibre sheets, providing wet surfaces for water evaporation.

Table 6-2 Specifications of membrane-based unit

Membrane-based unit dimension	Length	410mm
	Width	230mm
	Height	210mm
Membrane thickness		0.11mm
Air channel barrier thickness		0.13mm
Solution channel	Quantity	21
	Width	4.30mm

Air channel	Quantity	21
	Width	7.73mm

The membrane-based unit has a series of separate channels in the cross-flow manner for the airstream and desiccant solution, as depicted in Figure 6-3. The semi-permeable micro-porous hydrophobic membranes allow heat and moisture transfer between the airstream and desiccant solution while the liquid desiccant cannot permeate. Each solution channel is formed by two flat membrane sheets. During operation, the desiccant solution passes through the permeable barrier on the top and then flows downwards in the solution channels. Simultaneously, the gap between two solution channels allows the airstream to pass through for dehumidification or regeneration, where fibre materials are added only as supporting barriers.

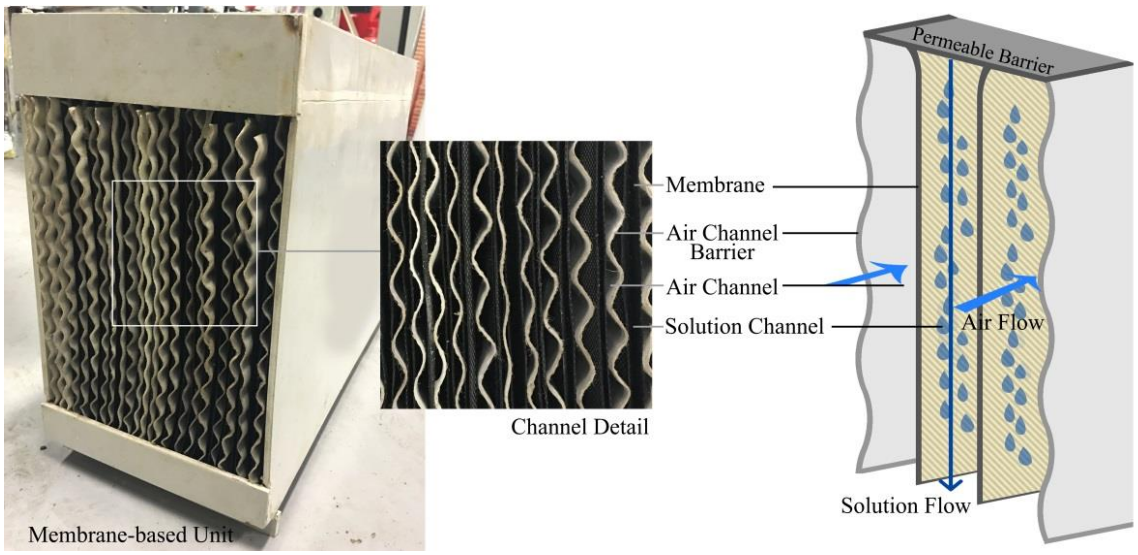
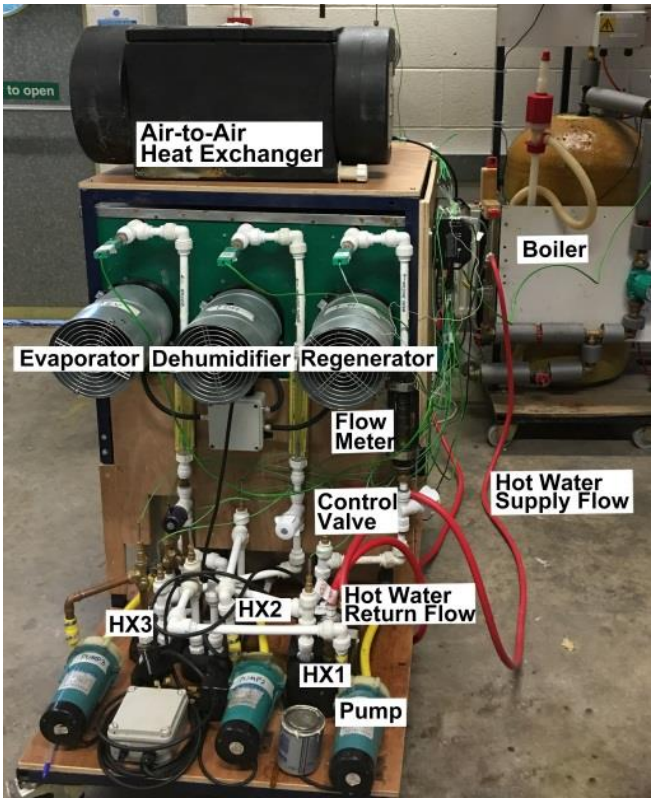


Figure 6-3 Illustration of membrane-based unit

6.2.3 Experimental method

Photos of the experimental rig are provided in Figure 6-4. An environmental chamber in the Marmont laboratory is used to provide inlet air for the dehumidifier unit, which is capable of simulating various desired hot and humid climate conditions. On the other

hand, an air conditioner is used to supply air for the regenerator and evaporative cooler. With consideration of the surrounding effect, components such as air ducting, pipe work and heat exchangers are well insulated.



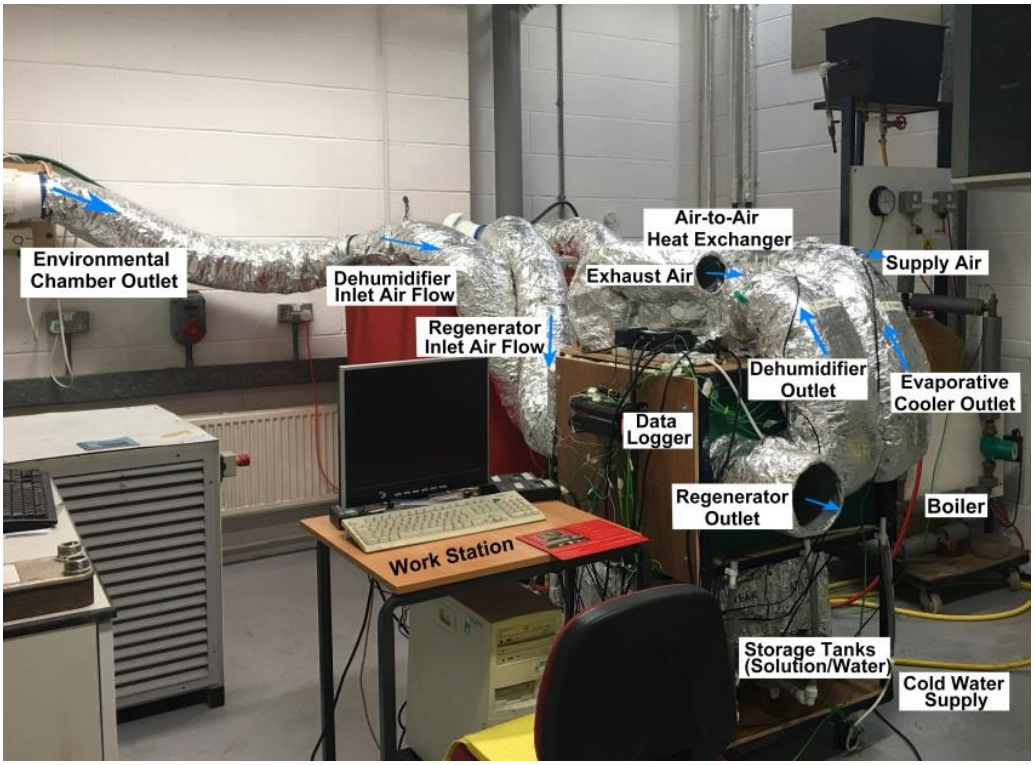


Figure 6-4 Photos of MLDC test rig

The main measurement devices with their associated accuracies are presented in Table 6-3, which have been drawn from manufacturers' datasheets. A Testo anemometer is used to measure air velocity, with an accuracy of ± (0.03m/s+5% FS). Air temperatures and relative humidity at inlets and outlets of the dehumidifier, regenerator, evaporative cooler and air-to-air heat exchanger are obtained by Sensirion humidity sensors, which have an accuracy of 1.8% RH (relative humidity) and a temperature accuracy of ±0.2°C. In addition, K-type thermocouples are used to measure the desiccant solution and water temperatures, and a data acquisition system is employed to record the data during operation. Once the desired inlet conditions for the three units are achieved, the entire system runs continuously until the steady state is reached and then the measured data is collected with a computer.

Table 6-3 Measurement devices with associated accuracies

Instruments	Parameters	Measurement Range	Accuracy
Testo thermo-anemometer	Air velocity	0-10 m/s	±(0.03m/s+5% FS)
Sensirion humidity sensor	Air temperature	-40 - +125°C	±0.2°C
	Air relative humidity	0 - 100%	±1.8% RH
K-type thermocouple	Liquid temperature	0-1100°C	±0.75% FS
Data logger DT500	Data Acquisition		±0.15%
Brannan hydrometer 200 Series	Solution density	1.0-1.6 g/m^3	±0.002g/m^3
Parker Easiflow meter	Liquid flow rate	1-15 L/min	±5% FS
Parker liquid flow indicator	Liquid flow rate	4-22 L/min	±2% FS

For experimental investigations, tests are conducted at various concentrations of $CaCl_2$ solution. Practically, the solution concentration (C_{sol}) is a function of solution density and temperature, which is expressed as [250]:

$$\rho_{sol}(C_{sol},T_{sol}) = \rho_w(T_{sol})\cdot[1+0.8360\cdot(\frac{C_{sol}}{1-C_{sol}}) - 0.4363(\frac{C_{sol}}{1-C_{sol}})^2 + 0.1056(\frac{C_{sol}}{1-C_{sol}})^3]$$

(6-1)

where, T_{sol} and ρ_{sol} are solution temperature, °C and density, kg/m^3. The solution density is measured by a Brannan hydrometer. ρ_w is saturated water density at T_{sol}, kg/m^3.

Desiccant solution and water volumetric flow rates are measured by Parker liquid flow meters, which are calibrated with water at 20°C. To equate the volumetric flow rate readings from the installed flow meters to the actual solution flow rates in the dehumidifier and regenerator, a correction correlation is used [251]:

$$v_{sol} = v_w\sqrt{\frac{(m_{float}-V_{float}\rho_{sol})\rho_w}{(m_{float}-V_{float}\rho_w)\rho_{sol}}} \quad (6\text{-}2)$$

where, v_{sol} and v_w are volumetric flow rates of the desiccant solution and water respectively, L/min. m_{float} and V_{float} are flow meter float weight in kg and volume, m^3.

Refereed to Section 5.3.2, the uncertainty analysis is carried out to correlate the uncertainty of a calculated variable. Error bars associated with the respective uncertainties are provided in Section 6.4-6.7.

Section 6.2 has presented descriptions of the MLDC experimental set-up, instrumentation and experimental method. Next, Section 6.3 provides the performance evaluation metrics used for the system performance assessment.

6.3 Performance evaluation metrics

A wide range of metrics are required to assess the dehumidification, regeneration, evaporation and overall system performance of the MLDC system comprehensively. In this section, the involved evaluation metrics are explained. The rate of mass change occurring in the dehumidifier and regenerator is referred as moisture removal rate ($\dot{M}_{\mathrm{r}}$) to evaluate the dehumidification and regeneration performance of the MLDC system, which is given as:

$$\dot{M}_{\mathrm{r\_DH}} = \dot{m}_{\mathrm{air\_DH}} \cdot (\omega_{\mathrm{in\_DH}} - \omega_{\mathrm{out\_DH}}) \tag{6-3}$$

$$\dot{M}_{\mathrm{r\_RE}} = \dot{m}_{\mathrm{air\_RE}} \cdot (\omega_{\mathrm{out\_RE}} - \omega_{\mathrm{in\_RE}}) \tag{6-4}$$

where, $\dot{m}_{\mathrm{air}}$ is mass flow rate of the airstream passing through the dehumidifier/regenerator, kg/s. ω_{in} and ω_{out} are air humidity ratios at the dehumidifier/regenerator inlet and outlet respectively, $\mathrm{kg/kg_{dryair}}$, which are calculated based on the measured air temperature and relative humidity [252].

Dehumidification effectiveness ($\varepsilon_{\mathrm{DH}}$) which is defined as the ratio of the actual change in moisture content to the maximum moisture transfer:

$$\varepsilon_{\mathrm{DH}} = \frac{\omega_{\mathrm{in\_DH}} - \omega_{\mathrm{out\_DH}}}{\omega_{\mathrm{in\_DH}} - \omega_{\mathrm{eq\_DH}}} \tag{6-5}$$

Where, $\omega_{\mathrm{eq\_DH}}$ is equilibrium humidity ratio of the desiccant solution at the inlet condition, $\mathrm{kg/kg_{dryair.}}$ Referred to the empirical correlation derived by Cisternas and Lam [241], a psychrometric chart illustrating the correlation of $CaCl_2$ solution equilibrium humidity ratio with solution concentration and temperature is presented in Figure 6-5.

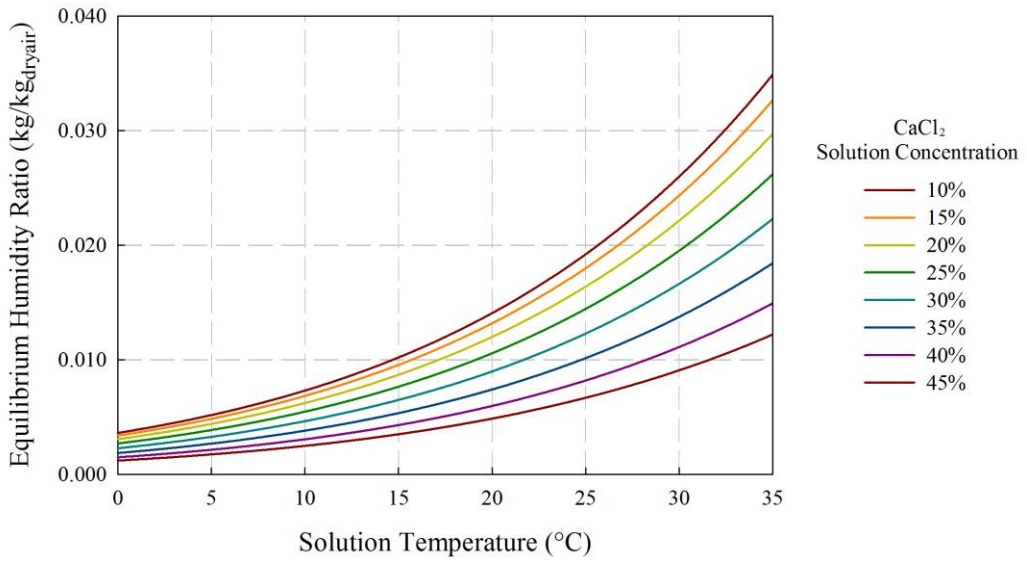


Figure 6-5 $CaCl_2$ solution equilibrium humidity ratio with concentration and temperature

In addition, the evaporative cooling effectiveness (ε_{EV}) of the MLDC system is defined to evaluate the evaporative cooler performance, which is expressed as:

$$\varepsilon_{EV} = \frac{T_{in\_EV} - T_{out\_EV}}{T_{in\_EV} - T_{wb\_in\_EV}} \tag{6-6}$$

where, T_{in_EV} and T_{out_EV} are air dry bulb temperatures at the evaporative cooler inlet and outlet respectively, °C. $T_{wb\_in\_EV}$ is air wet bulb temperature at the evaporative cooler inlet, °C.

Based on the airstream enthalpy difference between the inlet and outlet, the dehumidifier cooling output ($\dot{Q}_{DH\_cooling}$) and the MLDC system total cooling output ($\dot{Q}_{cooling}$) are determined respectively:

$$\dot{Q}_{DH\_cooling} = \dot{m}_{air\_DH}(h_{in\_DH} - h_{out\_DH}) \tag{6-7}$$

$$\dot{Q}_{cooling} = \dot{m}_{air\_DH}(h_{in\_DH} - h_{supply}) \tag{6-8}$$

where, $h_{\text{in\_DH}}$ and $h_{\text{out\_DH}}$ are specific enthalpies of the airstream entering and leaving the dehumidifier respectively, J/kg, and h_{supply} is supply air enthalpy, J/kg.

The overall performance of the MLDC system is assessed by the overall coefficient of performance (COP), which is defined as:

$$\text{COP} = \frac{\dot{Q}_{\text{cooling}}}{\dot{Q}_{\text{RE}}} \tag{6-9}$$

where $\dot{Q}_{\text{RE}}$ is regenerator thermal input power, W:

$$\dot{Q}_{\text{RE}} = \dot{m}_{\text{w\_RE}} \cdot c_{\text{p\_w\_RE}} (T_{\text{w\_f}} - T_{\text{w\_r}}) \tag{6-10}$$

where, $\dot{m}_{\text{w\_RE}}$ and $c_{\text{p\_w\_RE}}$ are hot water mass flow rate, kg/s and specific heat capacity, J/kg K. $T_{\text{w\_f}}$ and $T_{\text{w\_r}}$ are hot water supply and return temperatures in the heating circuit respectively, °C.

Section 6.3 has listed all the performance evaluation metrics for evaluating the MLDC system comprehensively. In the next Section 6.4, a detailed evaluation of the MLDC system dehumidification performance is provided.

6.4 MLDC dehumidification performance evaluation

In this section, the influence of various operating variables on the MLDC dehumidification performance is analysed. As defined in Section 6.3, the MLDC dehumidification performance is mainly assessed by the dehumidification moisture removal rate, the dehumidification effectiveness and the dehumidifier cooling output. A series of tests have been conducted for MLDC dehumidification performance evaluation and the base operating condition is listed in Table 6-4. Based on the $CaCl_2$

solution operative concentration level for dehumidification as previously presented in Table 2-5, a concentration range of 30% to 42% was selected for testing. Solution flow rate in the dehumidifier remained the same at 1L/min throughout the investigation, which is capable of providing sufficient wetting surface in the membrane unit for continuous operation. Hot and cold water was supplied at flow rates of 2L/min and 12L/min respectively.

Table 6-4 Operating condition for MLDC dehumidification performance evaluation

Operating variables	Value
$CaCl_2$ solution concentration	30% - 42%
$CaCl_2$ solution flow rate	1L/min
Hot water flow rate	2L/min
Cold water flow rate	12L/min

6.4.1 Influence of inlet air condition

Experimental tests have been firstly conducted to evaluate the dehumidification performance under various inlet air conditions at $CaCl_2$ solution concentration of 39%. The inlet air conditions provided by the environmental chamber are shown in Figure 6-6. To simulate different weather conditions in the hot and humid region, the dehumidifier inlet air has been set in the temperature range from 28.0°C to 40.0°C and relative humidity range from 65% to 95%. The absolute humidity ratio varied from 16.39g/kg_{dryair} to 36.48g/kg_{dryair} accordingly. Throughout testing, the cold water has been supplied at a constant temperature of 12°C.

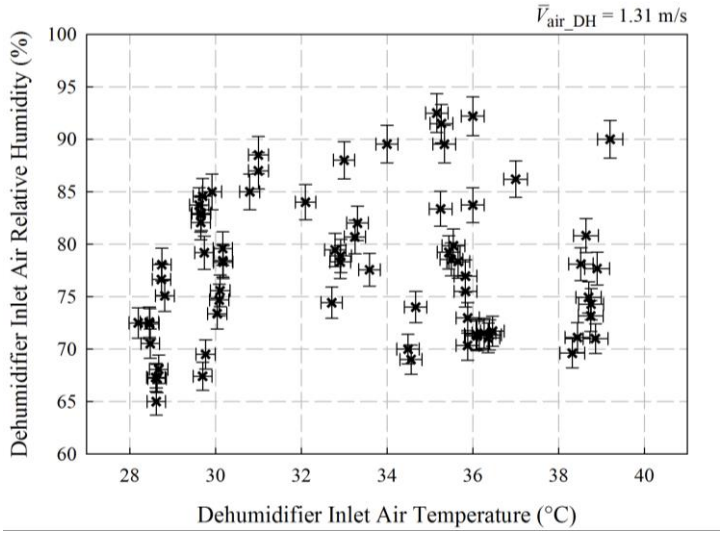
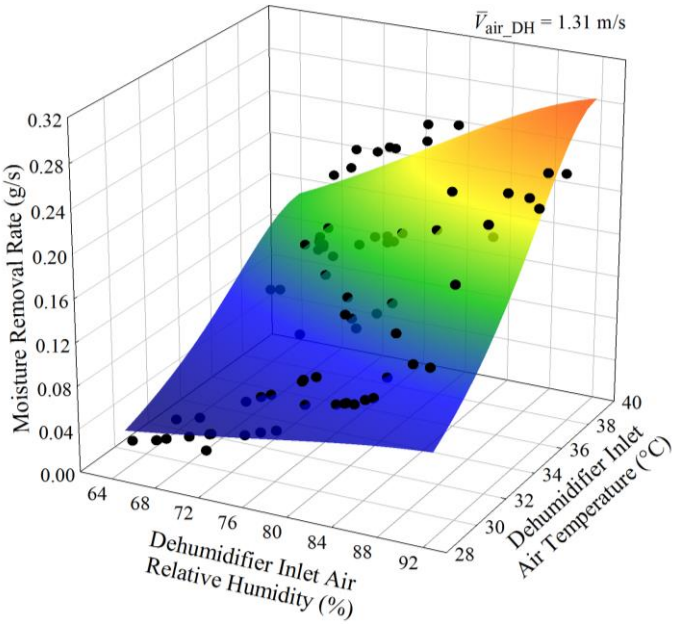


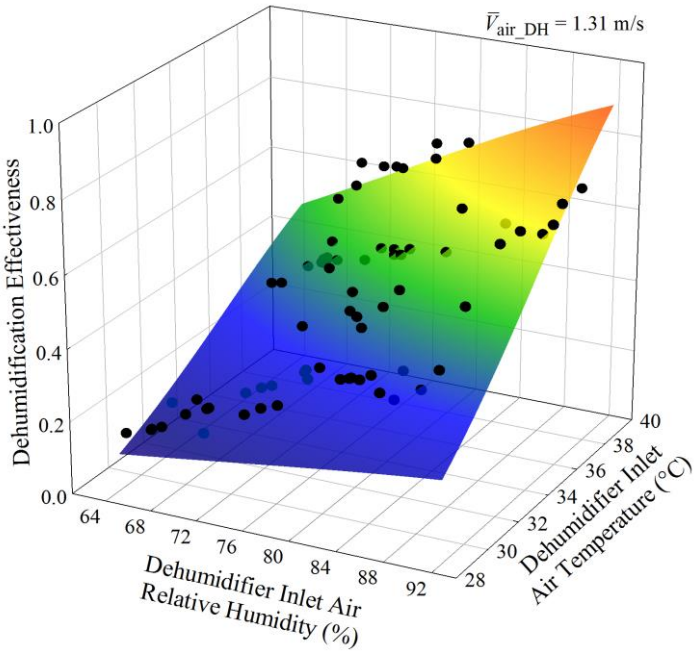
Figure 6-6 Dehumidifier inlet air condition range

As shown in Figure 6-7, the dehumidification performance improves with inlet air temperature and relative humidity. The higher the air temperature and relative humidity, the higher the vapour pressure and the more mass transfer occurs owing to the greater vapour pressure difference between the airstream and desiccant solution. Consequently, corresponding increases in the dehumidification moisture removal rate, effectiveness and cooling output are observed. For example, when the dehumidifier inlet air temperature is maintained at 36.0°C, the moisture removal rate increases from 0.15g/s to 0.25g/s as the air relative humidity rises from 71% to 92%, and correspondingly the dehumidification effectiveness increases from 0.50 to 0.68 and the dehumidifier cooling output increases from 332.6W to 642.3W. This is because of the increase in inlet air humidity ratio with relative humidity at a constant temperature, which causes more mass transfer in the dehumidification process. Similarly, the dehumidification performance improves with inlet air temperature under a constant relative humidity condition. For instance, at an inlet air relative humidity level of 75%, the moisture removal rate increases from 0.06g/s at air temperature of 29.0°C to 0.22g/s at air temperature of 39.0°C and simultaneously, the dehumidification

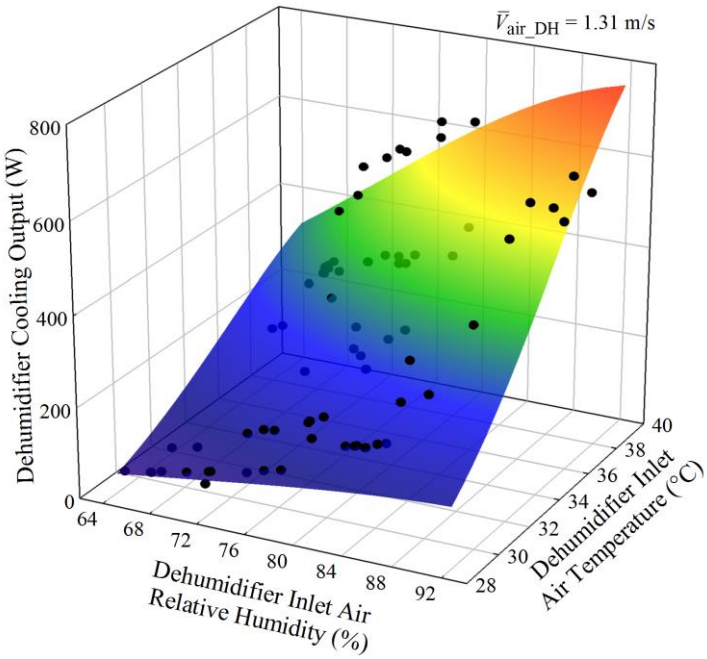
effectiveness improves by 0.34 and the cooling output increases by 451.6W. This is due to the fact that the inlet air humidity ratio increases with air temperature while the relative humidity remains constant. Thus more heat and mass transfer takes place and the associated cooling load increases. The effect of inlet air condition on the dehumidification performance in this study is consistent with those in the literature [160, 203, 221, 225, 253]. For instance, the dehumidifier performance of a MLDC system with a potassium formate desiccant solution has been experimentally investigated under various inlet air conditions in the literature [225]. Their experimental data have demonstrated that at the inlet air relative humidity of 60%, the moisture removal rate increases by approximately 35.69% as the inlet air temperature rises from 30°C to 35°C and over the inlet air relative humidity range of 50% to 70%, the dehumidification effectiveness improves from 0.32 to 0.47 and the dehumidifier cooling output increases by 303W at the inlet air temperature of 35°C. The results presented in this section indicate that the outdoor weather condition significantly affects the dehumidification performance and by comparison, the inlet air temperature has a more notable impact on the dehumidification performance.



(a)



(b)



(c)

Figure 6-7 Influence of inlet air condition on dehumidifier (a) moisture removal rate, (b) dehumidification effectiveness and (c) cooling output

6.4.2 Influence of air flow rate

In order to assess the impact of inlet air flow rate on the dehumidification performance, tests were carried out for the $CaCl_2$ solution concentration ranging from 30% to 42% with the inlet air temperature of 34.0°C and relative humidity of 72%. The supply temperature of the cold water is maintained at 11°C throughout testing. The influence of dehumidifier air flow rate is presented in Figure 6-8, it can be noted that the variation in the dehumidification performance is not very significant. At solution concentration of 42%, the moisture content change in the dehumidification process is 8.62g/kg_{dryair} at air flow rate of 34.17m^3/h, and it reduces to 7.47g/kg_{dryair} at air flow rate of 45.88m^3/h. This is due to the fact that the dehumidification capability decreases with air flow rate. However, the moisture removal rate is a function of air flow rate and moisture content change, which increases with air flow rate as displayed in Figure 6-8(a). For instance, the moisture removal rate increases by 16.72% over the investigated air flow rate range at concentration of 36%. As indicated in Figure 6-8(b), the dehumidification effectiveness decreases with dehumidifier air flow rate at a given solution concentration. The influence of dehumidifier air flow rate on the dehumidifier moisture removal rate and the dehumidification effectiveness demonstrated in this section is in a good agreement with those in the literature [254]. With LiCl as the liquid desiccant for a liquid desiccant cooling system in the literature [254], the dehumidifier moisture removal rate increases from 0.17g/s to 0.21g/s as the inlet air flow rate rises from 70kg/h to 115kg/h, while the dehumidification effectiveness reduces from 0.67 to 0.51 accordingly. Moreover, a high dehumidifier air flow rate causes a large volume of air being conditioned in the dehumidifier, thus the dehumidifier cooling output increases correspondingly as shown in Figure 6-8(c).

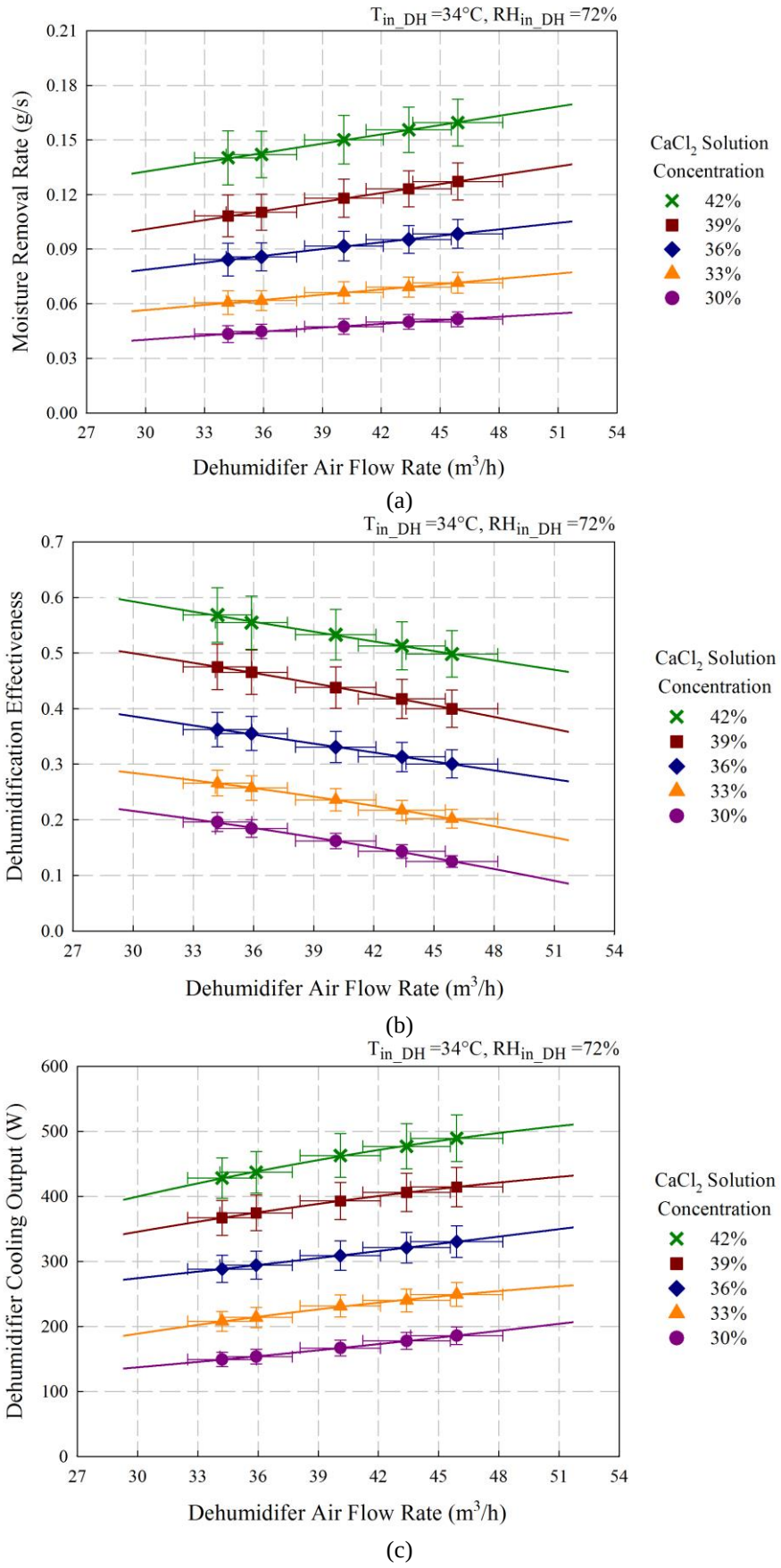


Figure 6-8 Influence of air flow rate on dehumidifier (a) moisture removal rate, (b) dehumidification effectiveness and (c) cooling output

6.4.3 Influence of cold water temperature

In the proposed MLDC system, cold water was utilised to pre-cool the regenerated solution prior to flowing into the dehumidifier and the effect of cold water temperature on the dehumidification performance is then examined. The dehumidifier inlet air condition was maintained constant, while cold water was supplied in the temperature range of 10.0°C to 20.0°C. Temperature variations in the dehumidifier sprayed solution and outlet air with cold water temperature are illustrated in Figure 6-9. It can be seen that the desiccant solution spray temperature rises in accordance with cold water temperature from 13.9°C to 24.2°C at $CaCl_2$ solution concentration of 42%, and the dehumidifier outlet air temperature increases from 29.5°C to 33.1°C correspondingly.

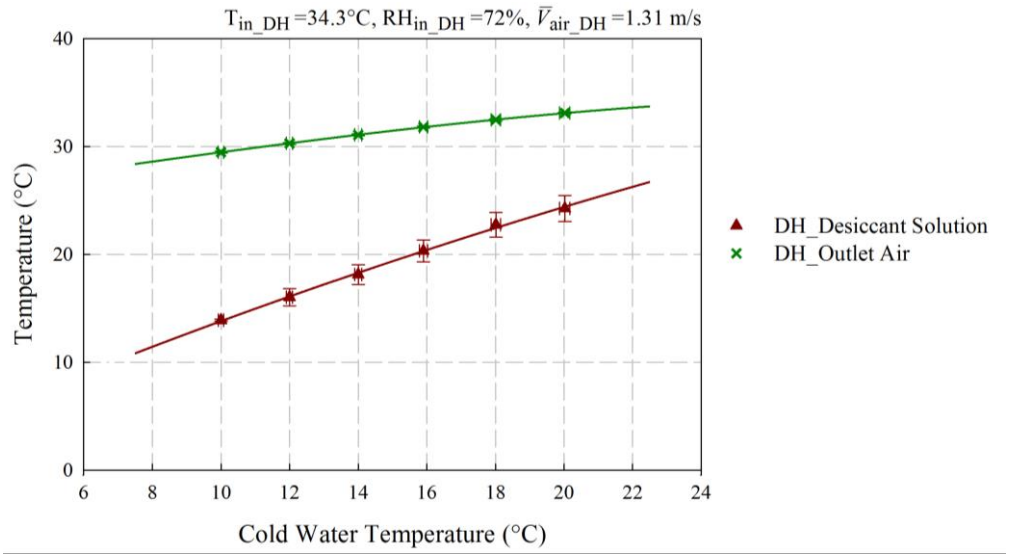
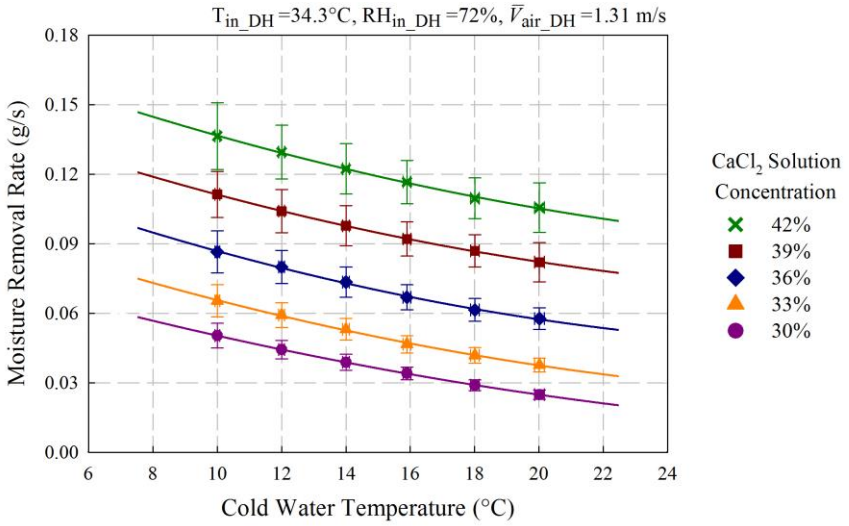


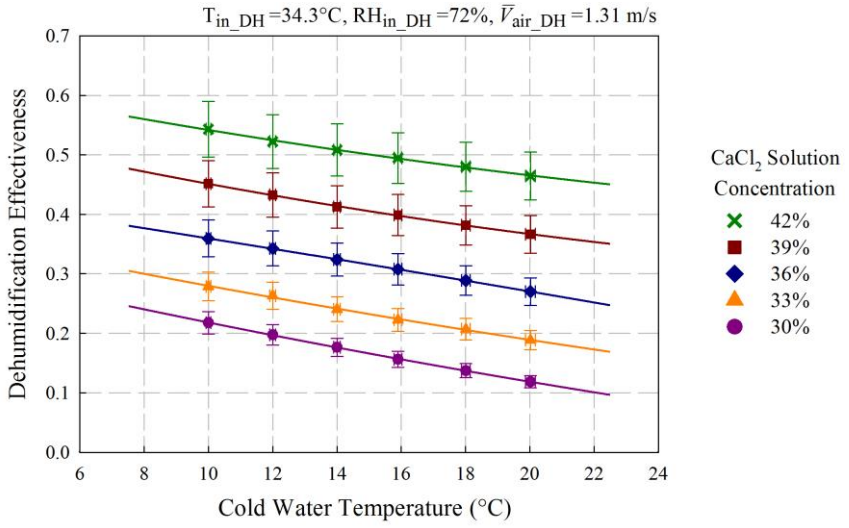
Figure 6-9 Variations of dehumidifier solution spray temperature and outlet air temperature with cold water temperature

Apparently, an increase in the desiccant solution spray temperature has a negative impact on the dehumidification performance as demonstrated in Figure 6-10. At $CaCl_2$ solution concentration of 42%, the dehumidifier moisture removal rate reduces by 32.04% as cold water temperature increases by 10°C, the dehumidification

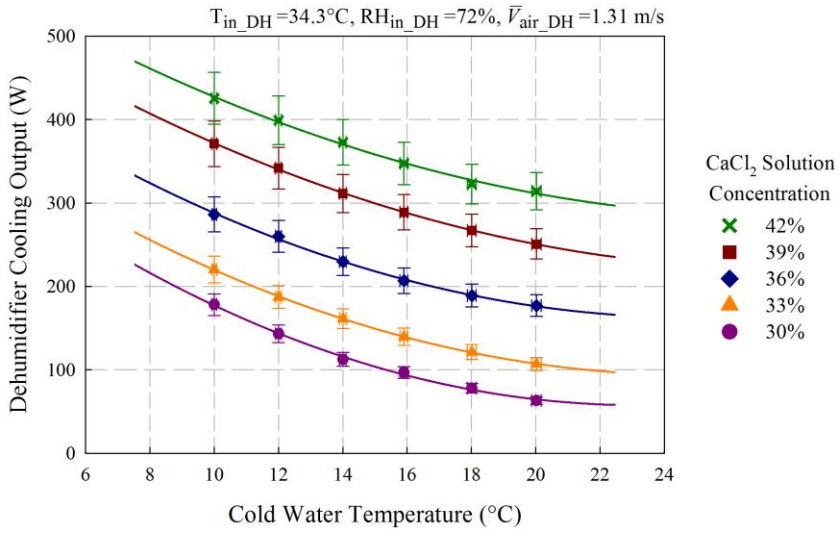
effectiveness decreases by 21.12% and the dehumidifier cooling output decreases by 28.23%. This is because that a higher desiccant solution temperature causes higher vapour pressure on the solution side, so less mass transfer occurs in the dehumidification process with a smaller vapour pressure difference between the solution and airstream. The experimental results imply that an enhancement in the dehumidification performance can be achieved by lowering the desiccant solution spray temperature in the dehumidifier, which has also been stated in the literature [203].



(a)



(b)



(c)

Figure 6-10 Influence of cold water temperature on dehumidifier (a) moisture removal rate, (b) dehumidification effectiveness and (c) cooling output

6.4.4 Influence of solution concentration

It is noteworthy that the solution concentration has a significant influence on the dehumidification performance, which has been confirmed by many researchers in the literature [210, 254-256]. A higher solution concentration contributes to better dehumidification performance as seen previously in Figure 6-8 and Figure 6-10. Under the investigated operating condition (i.e. the dehumidifier inlet air flow rate of 35.93m^3/h and cold water supply temperature of 10°C), the dehumidifier moisture removal rate is only 0.05g/s at $CaCl_2$ solution concentration of 30%, while it increases to 0.14g/s at concentration of 42%, simultaneously, the dehumidification effectiveness improves from 0.22 to 0.56 and the dehumidifier cooling output increases from 178.2W to 425.4W. This is mainly attributed to the larger vapour pressure difference between the airstream and desiccant solution at a higher concentration, thus more moisture can be removed during the dehumidification process. A similar impact of LiCl solution concentration on the dehumidification performance has been presented in the literature [254]. Based on their experiential data, the dehumidifier moisture

removal rate increases from 0.06g/s at solution concentration of 26% to 0.21g/s at concentration of 39% and the dehumidification effectiveness improves from 0.34 to 0.61 consequently.

6.4.5 Dehumidification performance evaluation summary

In this section, the dehumidification performance of the MLDC system has been assessed by investigating the effect of different operating variables through experimental work. It has been noted that the MLDC system is feasible for effective dehumidification with $CaCl_2$ solution. Based on the experimental results, the following findings can be obtained:

- The MLDC system dehumidification performance is significantly influenced by the local weather condition, both the dehumidifier moisture removal rate and dehumidification effectiveness increase with inlet air temperature and humidity.
- The dehumidifier cooling output increases with the inlet air flow rate, nevertheless its dehumidification effectiveness deceases simultaneously.
- The $CaCl_2$ solution concentration has a marked impact on the dehumidification performance. The higher the concentration, the better the dehumidification performance. As the $CaCl_2$ solution becomes stronger from the concentration of 30% to 42%, the dehumidifier dehumidification effectiveness improves by 0.37.

Next, the MLDC regeneration performance is evaluated under various operating conditions in Section 6.5.

6.5 MLDC regeneration performance evaluation

In this section, the impact of different operating variables on the MLDC regeneration performance is clarified on the basis of experimental data, including the influence of the air flow rate in Section 6.5.1, the regeneration hot water supply temperature in Section 6.5.2 and solution concentration in Section 6.5.3. As defined in Section 6.3, the main regeneration performance evaluation parameters are the regeneration moisture removal rate and regenerator thermal input power. $CaCl_2$ solution flow rate in the regenerator was set at 1L/min throughout the investigation, so as to ensure sufficient wetting surfaces in the regenerator for continuous operation. Hot and cold water were supplied at flow rates of 2L/min and 12L/min respectively.

6.5.1 Influence of air flow rate

The regenerator inlet air temperature and relative humidity were set at 26.0°C and 30% respectively, while its air flow rate increased from 43.82m^3/h to 148.44m^3/h for experimental testing. The increase in the regenerator air flow rate leads to a reduction in the moisture absorption capability. Nevertheless, the regeneration performance, which is assessed by the moisture removal rate, improves with air flow rate as shown in Figure 6-11. At $CaCl_2$ concentration of 30%, the moisture removal rate reaches 0.08g/s at air flow rate of 148.44m^3/h, while only 0.01g/s is achieved at flow rate of 43.82m^3/h. A similar variation trend of the regenerator performance with air flow rate has been indicated in the literature [210], in which the moisture removal rate improves by 44.45% as the regenerator air flow rate increases by 0.12kg/s.

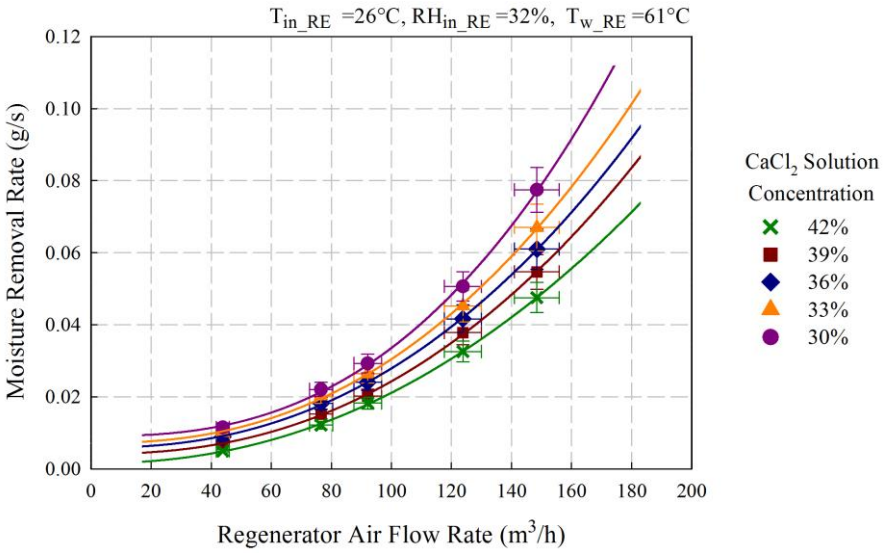


Figure 6-11 Influence of air flow rate on regenerator moisture addition rate

The variation of the regenerator thermal input power with air flow rate at $CaCl_2$ solution concentration of 42% is presented in Figure 6-12. Over the investigated air flow rate range, the hot water temperature difference in the heating circuit varied from 4.1°C to 5.2°C, as a result, the regenerator thermal input power was in the range of 568.9W to 728.6W. The higher air flow rate, the more thermal input power is required for heating the dilute solution. The finding is consistent with the statement presented in the literature [256] that the regenerator air flow rate is a critical parameter influencing the regeneration performance. Therefore, the required thermal input power should be taken into account to determine the regenerator air flow rate.

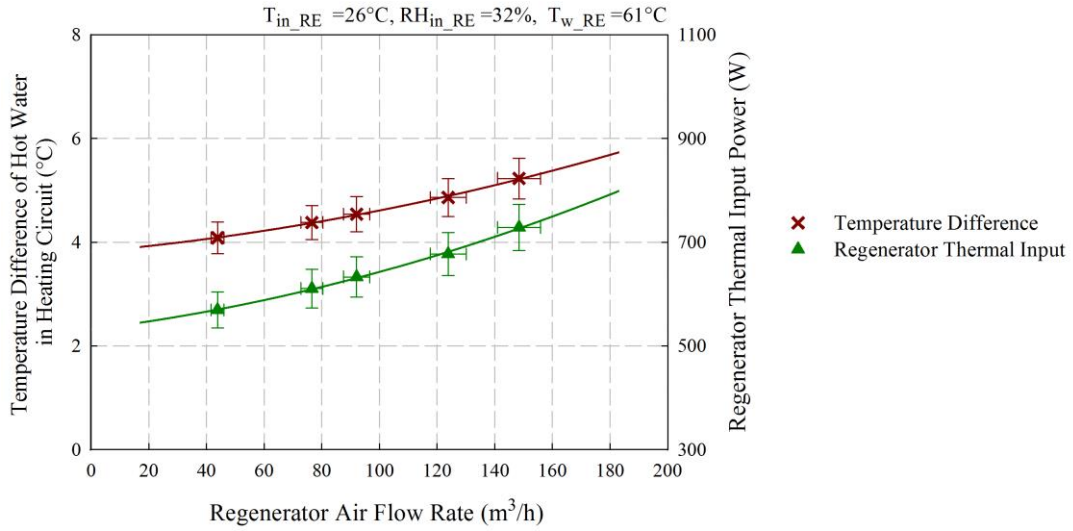


Figure 6-12 Influence of air flow rate on regenerator thermal input power

6.5.2 Influence of regeneration hot water temperature

Hot water from an electric boiler is utilised for regeneration purpose. In order to identify the influence of the regeneration temperature on the regeneration performance, the hot water supply temperature was set in the range of 55.0°C to 80.0°C while the regenerator inlet air was maintained at a temperature of 26.0°C and relative humidity of 33%. The impact of hot water supply temperature on the regeneration removal addition rate is indicated in Figure 6-13. It can be observed that the regeneration performance greatly improves with hot water temperature. For instance, the moisture removal rate increases by 72.32% as hot water temperature rises from 55.0°C to 80.0°C at $CaCl_2$ solution concentration of 42%, while it doubles at $CaCl_2$ concentration of 30%. A higher hot water supply temperature causes higher vapour pressure of the desiccant solution in the regenerator; hence more mass transfer from the solution to airstream occurs because of a greater vapour pressure difference. Based on the experimental data of a liquid desiccant cooling system using LiBr aqueous solution presented in the literature [210], an approximately 30% increase in the moisture

removal rate has also been observed as hot water supply temperature rises from 31°C to 42°C.

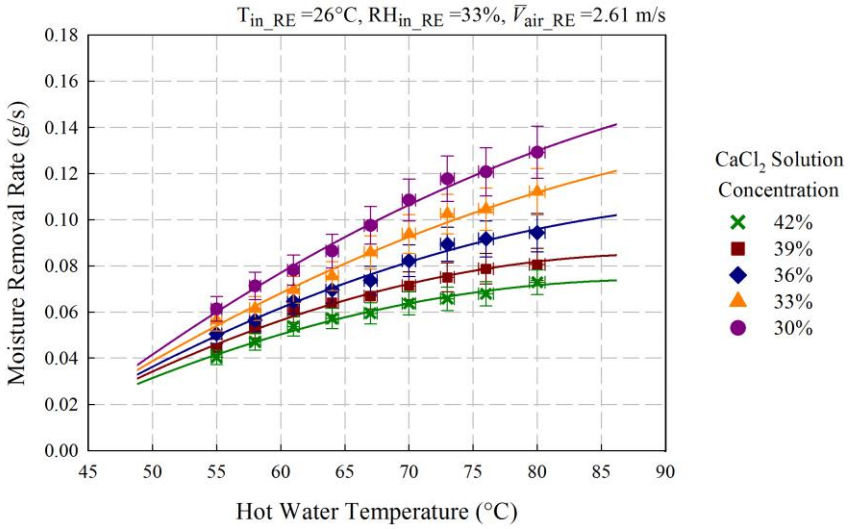


Figure 6-13 Influence of hot water temperature on regenerator moisture addition rate

A considerable increase in the regenerator thermal input power with hot water temperature is observed, as illustrated in Figure 6-14. At $CaCl_2$ solution concentration of 42%, the thermal input power doubles as the hot water supply temperature rises from 55.0°C to 80.0°C. The higher the hot water temperature, the better the regeneration performance, but simultaneously more thermal input power is required.

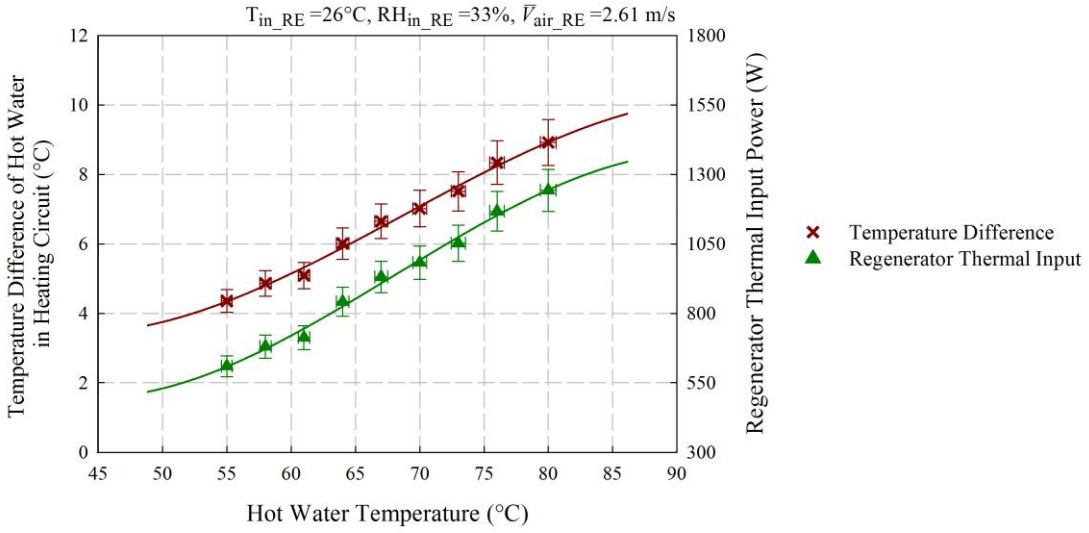


Figure 6-14 Influence of hot water temperature on regenerator thermal input power

6.5.3 Influence of solution concentration

It can be noted that better regeneration performance can be achieved at a lower solution concentration as shown in Figure 6-11 and Figure 6-13. For example, at regenerator air flow rate of 148.44m^3/h, the moisture removal rate increases by 63.83% as the $CaCl_2$ solution concentration decreases from 42% to 30%. In the regeneration process, less mass transfer takes place at a higher concentration due to the lower vapour pressure. Similar effect of LiCl solution concentration on the regeneration performance has been demonstrated in the literature [257]. Based on their observations, the regenerator moisture removal rate reduces by 10.14% as the concentration of LiCl solution increases from 32% to 35%.

Moreover, a more significant variation of the moisture removal rate with hot water supply temperature is observed at a lower concentration as presented in Figure 6-13. It is also worth noting that the rate of increase in the moisture removal rate with hot water temperature slows down gradually. For example, at $CaCl_2$ concentration of 42%, only a slight change in the moisture removal rate (i.e. 0.01g/s) has been observed over the investigated hot water temperature range of 65.0°C to 80.0°C. Thus, an appropriate regeneration temperature range should be determined for the adequate regeneration performance based on the operative solution concentration so that excessive thermal input power can be avoided and thereby the overall system energy performance can be enhanced.

6.5.4 Regeneration performance summary

The regeneration performance of the MLDC system under various operating conditions has been investigated experimentally in Section 6.5 and the following findings are provided:

- The regeneration performance improves with regenerator air flow rate and hot water supply temperature, whereas the required thermal input power increases accordingly. At $CaCl_2$ solution concentration of 42%, the regenerator moisture removal rate increases by 72.32% as the hot water supply temperature rises from 55.0°C to 80.0°C, however regenerator thermal input power doubles.
- To avoid excessive thermal input power for the liquid desiccant solution regeneration, the hot water temperature should be supplied within an appropriate range based on the solution operating concentration.
- The solution concentration has a marked impact on the MLDC regeneration performance. At a higher solution concentration, the regeneration capability is degenerated, and the associated crystallization risk should be noted as well. As the $CaCl_2$ solution becomes stronger from the concentration of 30% to 42%, the regenerator moisture removal rate decreases by 58.38% correspondingly.

Next, the MLDC evaporative cooling performance is assessed experimentally in Section 6.6.

6.6 MLDC evaporative cooling performance evaluation

Tests have been carried out to identify the effect of cold water supply temperature on the evaporative cooling performance in this section. Variations of the cooler outlet air temperature and evaporative cooling effectiveness are shown in Figure 6-15. Under the constant inlet air condition of the evaporative cooler, the evaporative cooler outlet air temperature increased from 19.4°C to 23.8°C and the evaporative effectiveness decreased from 0.72 to 0.37 as cold water supply temperature increased from 10.0°C to 20.0°C. In the proposed MLDC system, the cold water supplied at a lower temperature not only evidently leads to better evaporative cooling performance [212]

but also contributes to an improvement in the dehumidification performance as previously discussed in Section 6.4.3.

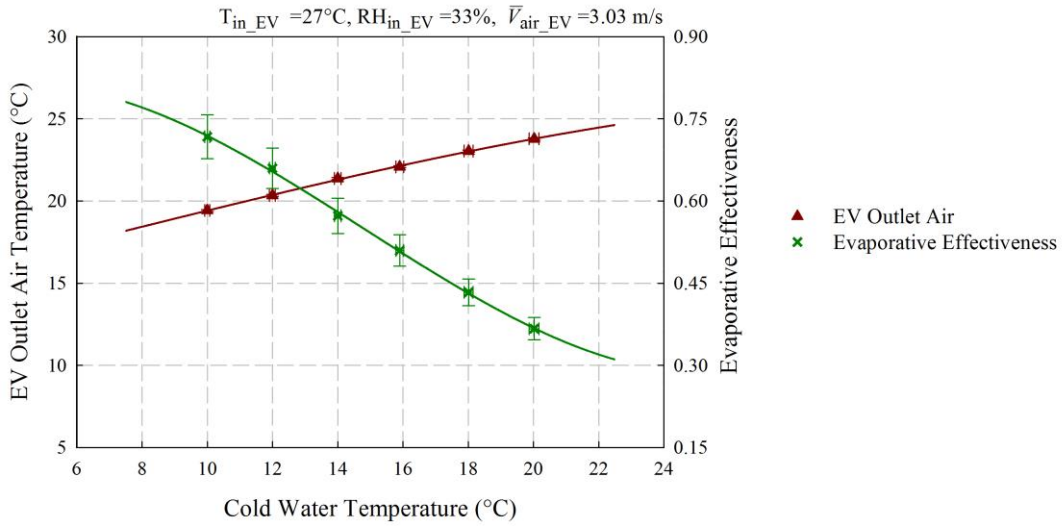


Figure 6-15 Variations in evaporative cooler outlet air temperature and evaporative effectiveness with cold water temperature

Next, Section 6.7 presents a comprehensive assessment of the overall MLDC system performance under variable operating condition.

6.7 MLDC overall system performance evaluation

With respect to the MLDC system steady operation at a given solution concentration, the performance balance between the dehumidifier and regenerator is of great importance as desiccant mass imbalance problems may occur over time, such as the dilution of the solution with insufficient regeneration and a more concentrated solution with excessive regeneration. As referred to Section 6.4 and Section 6.5, measures can be taken to balance the dehumidification and regeneration performances. For instance, the improvement of the dehumidification performance can be realised by increasing the dehumidifier air flow rate. On the other hand, the regenerator moisture removal rate can be enhanced to by increasing the regenerator air flow rate and hot water temperature. Alternatively, the regenerator could be designed with a large dimension,

which has also been stated in the literature [225], so that a large contact area for more heat and mass transfer in the regeneration process could be provided. Furthermore, the crystallization problem may appear for the high concentrated solution, which causes the risks of fluid mal-distribution, channel blockage, high pumping pressure, and membrane fouling [210]. For example, at $CaCl_2$ solution concentration of 42%, solution begins crystalizing at a temperature of 16.0°C.

6.7.1 Influence of cold water temperature

Under the stated operating conditions, the effect of cold water temperature on the MLDC system performance is assessed at $CaCl_2$ solution concentration of 36%. Declines in the system total cooling output and COP with cold water temperature are observed in Figure 6-16. The system total cooling output reduces from 486.7W at cold water temperature of 10.0°C to 339.6W at cold water temperature of 20.0°C, and the COP decreases from 0.70 to 0.59 accordingly. As mentioned in Section 6.4.3, the cold water temperature also influences the desiccant solution spray temperature in the dehumidifier, the solution spray temperature increases from 13.9°C to 24.2°C as the cold water temperature rises from 10°C to 20°C. A similar effect of solution temperature has been presented in the literature [203], the system COP reduces from 0.75 to 0.65 as LiCl solution temperature at the dehumidifier inlet increases from 15°C to 25°C. The results imply that cooler water is preferred for better dehumidification and system performances, which has been also suggested by Gandhidasan [196]. In addition, varying the cold water temperature could also be a solution to reach the desired supply air temperature. According to the experimental data, the supply air temperature rises from 20.4°C to 24.8°C as the cold water temperature rises from 10°C to 20°C.

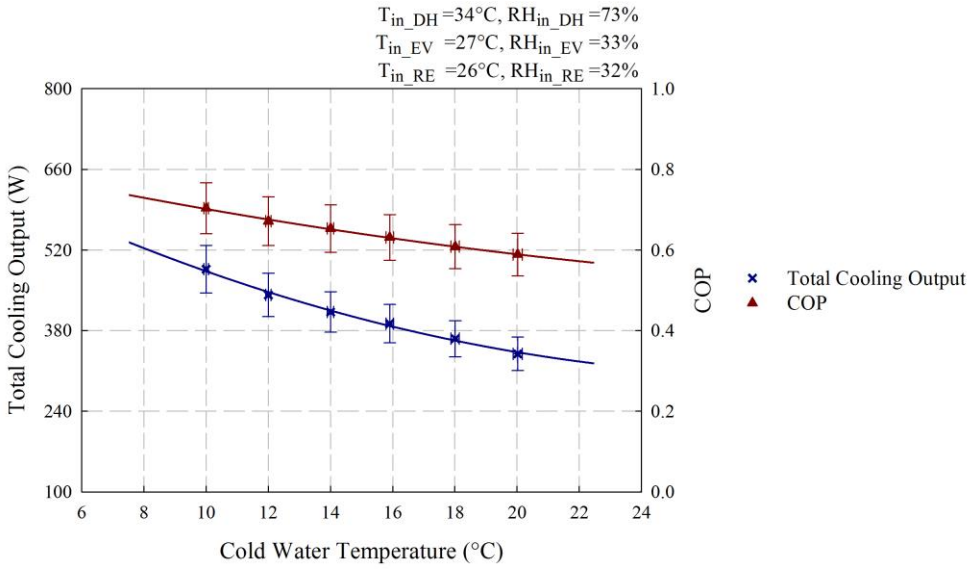


Figure 6-16 Influence of cold water temperature on system cooling output and COP

6.7.2 Influence of regeneration temperature

The effect of hot water supply temperature on the MLDC system performance is indicated in Figure 6-17. The desiccant solution temperature at the regenerator inlet varies in line with the hot water temperature. As a result, an evident reduction in the system COP with the regenerator desiccant solution temperature and more thermal input power is associated. At $CaCl_2$ solution concentration of 36%, the regenerator thermal input power increases by 635.3W while the system COP reduces by 21.33% as the hot water supply temperature rises from 55.0°C to 80.0°C. It has also been indicated in the literature [203], as the system COP decreases by approximately 17% when the temperature of LiCl solution rises from 40°C to 65°C at the regenerator inlet. The results reveal that more thermal input power is required to attain a higher regeneration temperature and thereby a lower system COP is obtained.

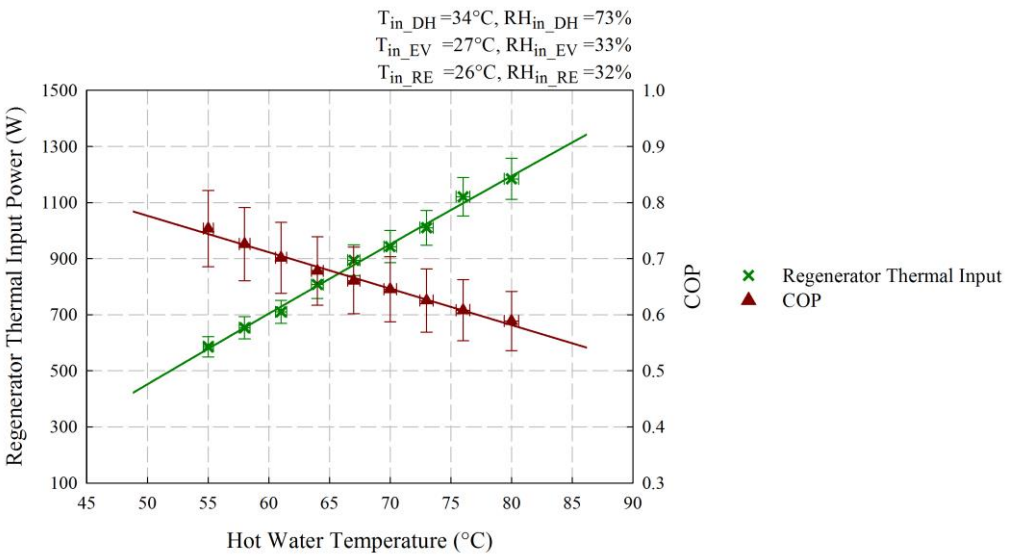


Figure 6-17 Influence of hot water temperature on regenerator thermal input power and system COP

6.7.3 System performance evaluation summary

In this section, the MLDC system performance has been evaluated through experimental work. With $CaCl_2$ solution, the MLDC system is feasible for operating in the hot and humid region with efficient independent temperature and humidity controls. Based on the experimental results, the following implications can be identified:

- The MLDC system mass balance between the dehumidifier and regenerator is of vital importance for steady operation. Appropriate adjustments should be applied for the match the moisture removal rates between the dehumidifier and regenerator at a given solution concentration.
- The overall system performances decrease with cold water supply temperature and the supply air temperature increases accordingly. Based on the experimental data, the MLDC system is capable of providing the supply air at a temperature range of 20.4°C to 24.8°C as the cold water temperature rises from 10.0 °C to 20.0°C.

- The dehumidification effectiveness of 0.30 and system COP of 0.70 are achieved at $CaCl_2$ solution concentration of 36% under the investigated operating condition.

Next, Section 6.8 concludes this chapter and implications are also provided.

6.8 Summary

In this chapter, the hybrid MLDC system with $CaCl_2$ solution has been evaluated through experimental work regarding the dehumidification, regeneration, evaporative cooling and overall system performance. The experimental data has evidently demonstrated the feasibility of the MLDC system for providing cooling and dehumidification demands in the hot and humid region. Under the investigated operating condition with an outdoor temperature of 34°C, the MLDC system provides dehumidification effectiveness of 0.3, COP of 0.7 and a supply air temperature of 20.4°C. On the basis of the experimental results, the following conclusions are drawn:

(1) The MLDC system with $CaCl_2$ as the liquid desiccant is feasible for running with low-grade heat sources, as sufficient regeneration can be attainable in a heat source supply temperature range of 55°C to 80°C. Therefore the MLDC system can be incorporated with the scroll-based ORC system forming an effective integration in the micro trigeneration system, as the exhaust heat temperature from the scroll expander suffices the regeneration requirement of the dilute $CaCl_2$ solution in the MLDC system.

(2) Practically, the system mass balance between the dehumidifier and regenerator is crucial for steady operation of the MLDC system.

(3) The inlet air condition greatly affects both the dehumidification and regeneration performance of the MLDC system.

(4) Depending on the operating environment, the MLDC system dehumidification performance varies as it improves with the dehumidifier inlet air temperature and humidity.

(5) Based on the operating solution concentration, the heat source supply temperature for regeneration should be controlled appropriately without excess energy being wasted.

(6) The dehumidification, evaporative cooling and overall system performance decrease with cold water supply temperature, however the supply air temperature rises.

(7) The solution concentration influences the MLDC system performance considerably. The MLDC system is better running with liquid desiccant solution at a concentration for better the dehumidification and overall system performance. Nevertheless, the more thermal input power for the solution regeneration and crystallization risks in the normal operating temperature range should be noted as well.

The work presented in this chapter provides contribution to knowledge of the comprehensive experimental testing of a liquid desiccant cooling system and evaluating effect of a wide range of operating conditions on the system performance. Furthermore, the work facilitates an effective pairing of MLDC and scroll-based ORC system for the proposed micro trigeneration system in Chapter 7. Next Chapter 7 presents a detailed performance evaluation of the overall micro trigeneration system with scroll-based ORC and MLDC through theoretical modelling.

Chapter 7: Performance Evaluation of Micro Trigeneration System

7.1 Introduction

Owing to the benefits in technical, environmental and economic aspects, the onsite micro power generation system have been a highly-anticipated solution to fulfil the domestic energy requirements [160]. As highlighted in Chapter 2, to date a micro trigeneration system combining the scroll-based ORC and MLDC has been rarely explored in the literature. This chapter mainly presents a validated steady-state micro trigeneration system model, which has advantages in simplicity and effective prediction of the system performance in a wide range of operating conditions. A comprehensive analysis of the trigeneration system energy performance in different operating modes (i.e. single power generation, CHP, CCP and CCHP) is produced. The work in this chapter provides a contribution to knowledge of theoretical modelling and analysis of the micro trigeneration system.

The schematic diagram of the proposed micro trigeneration system is presented in Figure 7-1 and this multifunctional system is featured with:

- Simultaneous production of onsite electricity, heating and cooling.
- Capability of running on low-grade heat sources.
- Reduction in primary energy consumption, thermal loss and greenhouse gas emissions.
- Summer operation by meeting the cooling and dehumidification demands.
- Independent control in supply air humidity and temperature without overcooling, reheating and water condensation problems.
- Cost effectiveness

The aims of this chapter are to (a) develop a comprehensive model of the micro trigeneration system and validate with experimental data; (b) demonstrate the feasibility of combining scroll-based ORC and MLDC technologies for an efficient micro trigeneration system, (c) conduct a comparison of energy performance for the single power generation, cogeneration and trigeneration operating modes; (d) investigate effect of different operating variables on the system energy performance under various operating conditions through simulation and (e) provide recommendations for practical operation of the micro trigeneration system. Therefore, this chapter is organised in the following sections: Section 7.2 establishes the micro trigeneration system modelling; Section 7.3 presents validation of the developed system model with experimental data; Section 7.4 compares the system energy performance for single power generation, CHP, CCP and CCHP modes; Section 7.5 provides a theoretical performance analysis of the trigeneration system in cogeneration mode; Section 7.6 evaluate the energy performance of the trigeneration system in trigeneration mode based on simulation results and Section 7.7 summarises the chapter and provides recommendations for practical operation.

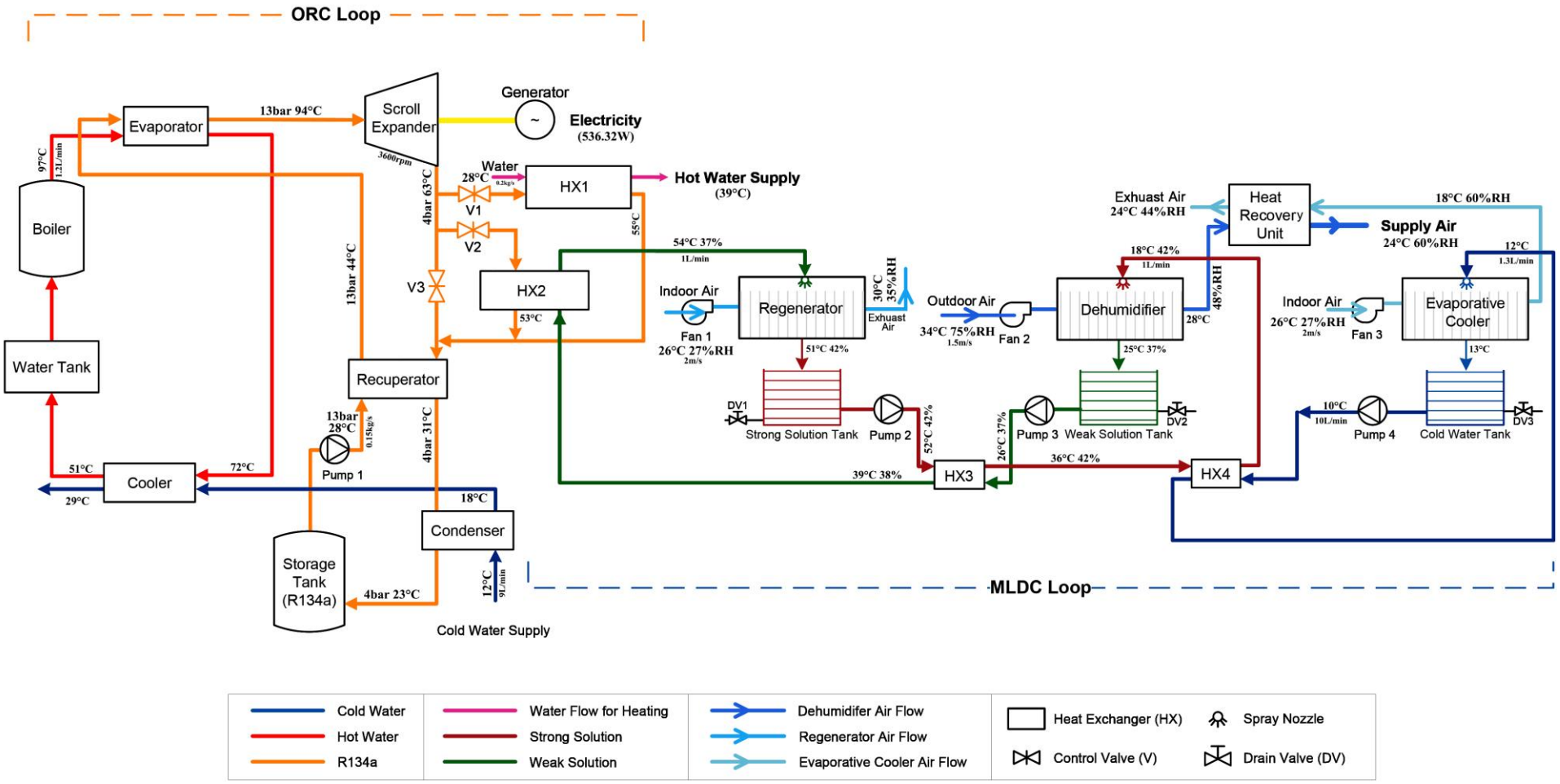


Figure 7-1 Schematic diagram of micro trigeneration system with scroll-based ORC and MLDC

7.2 Micro trigeneration system modelling

In terms of modelling, the micro trigeneration system can be regarded as a closed-loop cycle with several connected components, which mainly consists of the scroll expander, heat exchangers, pumps, membrane-based dehumidifier, membrane-based regenerator and evaporative cooler. The system component modelling is implemented individually and subsequently linked in series to form a steady-state trigeneration system model, which predicts the trigeneration system performance under static equilibrium. In this section, modelling of the involved components is described respectively with reference to a number of the literature [126, 147, 258, 259], and the overall system energy performance evaluation metrics are presented as well.

7.2.1 Scroll expander

The scroll expander modelling (i.e. EXP) with a complete description of the governing equations has been presented in Section 5.2. As mentioned in Section 5.4.1, the identification of eight parameters of the scroll expander has been accomplished using experimental data. In general, the input variables of the semi-empirical scroll expander modelling are listed in Table 7-1: the working fluid properties (i.e. pressure, enthalpy and temperature) at inlet and outlet of the scroll expander and scroll expander rotational speed. The scroll expander static performance under a variety of operating conditions can be explored, with the output variables of: the exhaust enthalpy of the working fluid, the working fluid mass flow rate delivered by the scroll expander, shaft and electric power produced.

Table 7-1 Parameters of scroll expander model

EXP Model	Parameters	Descriptions	Unit
Inputs	P_{exp_su}	Inlet pressure of working fluid	Pa

	h_{exp_su}	Inlet enthalpy of working fluid	J/kg
	P_{exp_ex}	Exhaust pressure of working fluid	Pa
	N_{exp}	Scroll expander rotational speed	rpm
	T_{exp_ex}	Exhaust temperature of working fluid	K
Outputs	h_{exp_ex}	Exhaust enthalpy of working fluid	J/kg
	M_{dot}	Working fluid mass flow rate	kg/s
	W_{sh}	Shaft power	W
	W_{el}	Electric power	W

7.2.2 Pump

The role of a refrigerant pump is to move and pressurize the organic working fluid R134a in the ORC loop. In principle, an isentropic process takes place inside the pump, where the working fluid entropy remains unchanged while passing through the pump. A semi-empirical pump model (i.e. PP) is developed to characterize the pump performance. Basically, the pump power consumption and volumetric flow rate vary with the pump speed (N_{pp}) and the pressure difference between pump inlet and outlet (i.e. $\dot{M}_{pp} = P_{pp\_ex} - P_{pp\_su}$) [147]. The semi-empirical pump model using physics-based equations requires the several input variables as listed in Table 7-2, including the pump basic specification (i.e. displacement volume and volume), rotational speed, losses (i.e. leakage surface area and power loss factor), working fluid property at inlet and outlet of the pump (i.e. pressure and enthalpy).

Table 7-2 Parameters of pump model

PP Model	Parameters	Descriptions	Unit
Inputs	V_{pp_sw}	Pump displacement volume	m^3
	A_{pp_leak}	Pump leakage surface area	m^2
	N_{pp}	Pump speed	rpm
	W_{pp_loss}	Pump constant power losses	W

	K_{pp_loss}	Pump proportional loss factor	-
	P_{pp_su}	Inlet pressure of working fluid	Pa
	h_{pp_su}	Inlet enthalpy of working fluid	J/kg
	P_{pp_ex}	Exhaust pressure of working fluid	Pa
Outputs	T_{pp_ex}	Exhaust temperature of working fluid	K
	h_{pp_ex}	Exhaust enthalpy of working fluid	J/kg
	M_{pp}	Working fluid mass flow rate	kg/s
	W_{pp}	Mechanical power input	W

In terms of the output variables, the pump model predicts the working fluid mass flow rate delivered by the pump ($\dot{M}_{pp}$), in which the internal leakage is modelled as an incompressible flow through an equivalent orifice.

$$\dot{M}_{pp} = \frac{N_{pp}}{60 \cdot V_{pp\_sw} \cdot \rho_{pp\_su}} - A_{pp\_leak}\sqrt{2\rho_{pp\_su} \cdot (P_{pp\_ex} - P_{pp\_su})} \tag{7-1}$$

Where ρ_{pp_su} is density of the working fluid at the pump inlet, kg/m^3.

The mechanical power of the pump (W_{pp}) is determined by taking mechanical losses into account. The mechanical losses (W_{pp_loss}) are obtained by means of constant losses added to a term proportional to the isentropic power.

$$W_{pp} = W_{pp\_loss} + K_{pp\_loss} \cdot \frac{\dot{M}_{pp}}{\rho_{pp\_su}} \cdot (P_{pp\_ex} - P_{pp\_su}) \tag{7-2}$$

Therefore, the pump exhaust temperature (T_{pp_ex}) can be determined by exhaust enthalpy (h_{pp_ex}) and pressure (P_{pp_ex}) of the working fluid thermodynamically:

$$h_{pp\_ex} = h_{pp\_su} + \frac{W_{pp}}{\dot{M}_{pp}} \tag{7-3}$$

7.2.3 Heat exchangers

As depicted in Figure 7-1, a number of plate heat exchangers are involved in the micro trigeneration system and serve various purposes: (a) evaporator-transfers heat from the hot water supplied by the electric boiler to the working fluid; (b) HX1-captures exhaust heat from the scroll expander for supplying hot water; (c) HX2-captures exhaust heat from the scroll expander to heat the dilute solution in MLDC; (d) recuperator-allows heat transfer between the working fluid leaving from HX1 and HX2 with the liquefied working fluid pumped from storage tank; (e) condenser-condenses the working fluid by cold water; (f) HX3-provides heat transfer between dilute solution and regenerated solution and (g) HX4-precools the regenerated solution by cold water before entering the dehumidifier. A counter-flow arrangement has been assumed for the heat exchanger modelling and the effectiveness-number of heat transfer units (NTU) method has been adopted to conveniently predict the working fluid temperature at the heat exchanger outlet. As listed in Table 7-3, the input variables of the heat exchanger model (i.e. HEX) are heat exchanger specification (i.e. total surface area), and hot and cold fluids properties at inlet of the heat exchanger (i.e. pressure, temperature and mass flow rate).

Table 7-3 Parameters of heat exchanger model

HEX Model	Parameters	Descriptions	Unit
Inputs	A_{tot}	Heat exchanger total surface area	m^2
	P_{hf_su}	Inlet pressure of hot fluid	Pa
	T_{hf_su}	Inlet temperature of hot fluid	K
	m_{hf}	Mass flow rate of hot fluid	kg/s
	P_{cf_su}	Inlet pressure of cold fluid	Pa
	T_{cf_su}	Inlet temperature of cold fluid	K
	m_{cf}	Mass flow rate of cold fluid	kg/s

Outputs	T_{hf_ex}	Exhaust temperature of hot fluid	K
	T_{cf_ex}	Exhaust temperature of cold fluid	K

The following assumptions have been made for modelling the heat exchanger.

1) The heat exchanger operates under steady-state conditions (i.e. uniform temperature and flow rate of fluids at entrances of the heat exchanger);
2) On each fluid side, the fluid flow rate and heat transfer surface area are distributed uniformly through the heat exchanger;
3) The thermophysical properties of each fluid are constant throughout the heat exchanger, for instance the fluid specific heat;
4) The overall heat transfer coefficient is constant (i.e. independent of temperature, time and position) throughout the heat exchanger;
5) Heat loss to or heat gain from the surroundings is negligible.

In the effectiveness-NTU method, the heat exchanger effectiveness (ε) is defined as the ratio between the actual heat transfer rate (q) to the maximum possible heat transfer rate that would be transferred within the heat exchanger (q_{max}) [260]:

$$\varepsilon = \frac{q}{q_{max}} \tag{7-4}$$

The maximum heat transferable rate between two fluids in the heat exchanger at the given inlet temperatures can be obtained with:

$$q_{max} = C_{min}(T_{hf\_su} - T_{cf\_su}) \tag{7-5}$$

Where C is heat capacity rate of the fluid. It can be expressed as $C = \dot{M} \cdot cp$, $\dot{M}$ is fluid mass flow rate and cp is fluid specific heat at constant pressure. Subscripts of hf

and cf denote hot and cold fluid respectively, and $C_{\min}$ is the minimum of C_{hf} and C_{cf}. $T_{\text{hf\_su}} - T_{\text{cf\_su}}$ represents fluid inlet temperature difference.

In terms of the counter-current flow heat exchanger, the relationship between the heat exchanger effectiveness and NTU is expressed as [261]:

$$\varepsilon = \frac{1-\exp[-NTU(1-\frac{C_{\min}}{C_{\max}})]}{1-\frac{C_{\min}}{C_{\max}}\cdot\exp[-NTU(1-\frac{C_{\min}}{C_{\max}})]} \tag{7-6}$$

Where $C_{\max}$ is the higher of two heat capacity rates of C_{hf} and C_{cf}.

The number of transfer units (NTU) is defined as a ratio of the overall thermal conductance to the smaller heat capacity rate [262], which is calculated with:

$$\text{NTU} = \frac{UA}{C_{\min}} \tag{7-7}$$

Where U is overall heat transfer coefficient and A is total heat transfer area, m^2.

Hence, the heat transfer rate from the hot fluid to the cold fluid within the heat exchanger (q) is given by:

$$q = \varepsilon \cdot q_{\max} = m_{\text{hf}} \cdot cp_{\text{hf}} \cdot (T_{\text{hf\_su}} - T_{\text{hf\_ex}}) = m_{\text{cf}} \cdot cp_{\text{cf}} \cdot (T_{\text{cf\_su}} - T_{\text{cf\_ex}}) \tag{7-8}$$

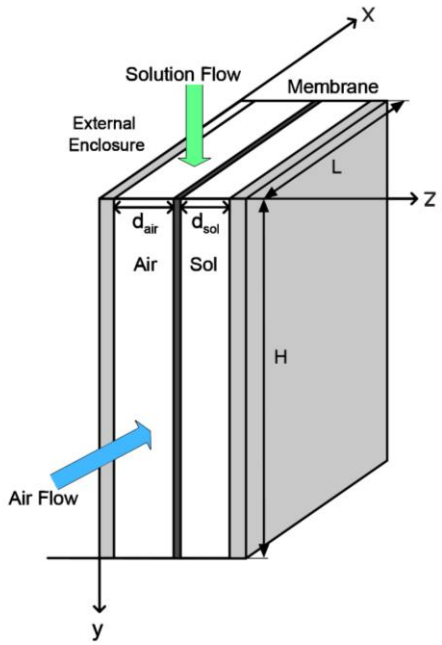
Accordingly, the exhaust temperatures for hot and cold fluid can be determined by:

$$T_{\text{hf\_ex}} = \frac{q}{m_{\text{hf}} \cdot cp_{\text{hf}}} \tag{7-9}$$

$$T_{\text{cf\_ex}} = \frac{q}{m_{\text{cf}} \cdot cp_{\text{cf}}} \tag{7-10}$$

7.2.4 Membrane-based unit

In the MLDC, the membrane-based dehumidifier/regenerator unit consists of air and solution channels arranged in parallel, which are separated by semi-permeable membranes. Both heat and vapour can be transferred through membranes, whereas the liquid desiccant solution is prevented from passing through. In view of the complexity of MLDC modelling, a steady-state cross flow mathematical model has been developed for the membrane-based dehumidifier, and the regenerator and evaporator models have been implemented by a simplified empirical approach. A single-layer membrane unit has been established using one air channel and one neighbouring solution channel as the domain for dehumidifier modelling. As depicted in Figure 7-2, air flows along x axis positive direction, while desiccant solution flows along y positive direction, heat and mass are exchanged in z direction.



Height (H)	0.25m	Length (L)	0.30m
Membrane Thickness (δ)			0.0005m
Solution Channel Thickness (d_{sol})			0.0016m
Air Channel Thickness (d_{air})			0.005m

Figure 7-2 Schematic diagram of a cross-flow single-layer membrane unit

For modelling, air and solution flows are considered to be laminar since their Reynolds numbers are less than 2000 [224]. The flowing assumptions are made to simplify the flow model:

1) The membrane-based unit is well-insulated with negligible heat transfer taking place between the unit and ambient.
2) Thermodynamic and physical properties of air and solution flows are constant and independent of temperature and humidity.
3) Flows with uniform velocity are fully developed with negligible entrance effect.
4) Both air and solution flows are fully developed and the bulk properties (i.e. temperature and humidity) of two flows only vary along channel length.
5) The membrane properties are uniform in the unit.
6) Heat and mass transfer through membrane only occurs normally to the membrane in z axis direction and axial diffusion is neglected.
7) Water vapour is transferred in the membrane and condensed at the membrane-solution interface. The heat released during the process is added to the solution side since the convective heat transfer coefficient on solution side is much higher than that on air side.
8) The channel boundaries are flat with no fins or any heat transfer enhancements.

Based on the mathematical models in the literature [263] [224] and [264], modifications are adopted to develop a simplified numerical model of coupled heat and mass transfer for a single-layer membrane unit using $CaCl_2$ as the liquid desiccant. Figure 7-3 illustrates the incremental control volume for heat and mass balances in the solution and air channels respectively.

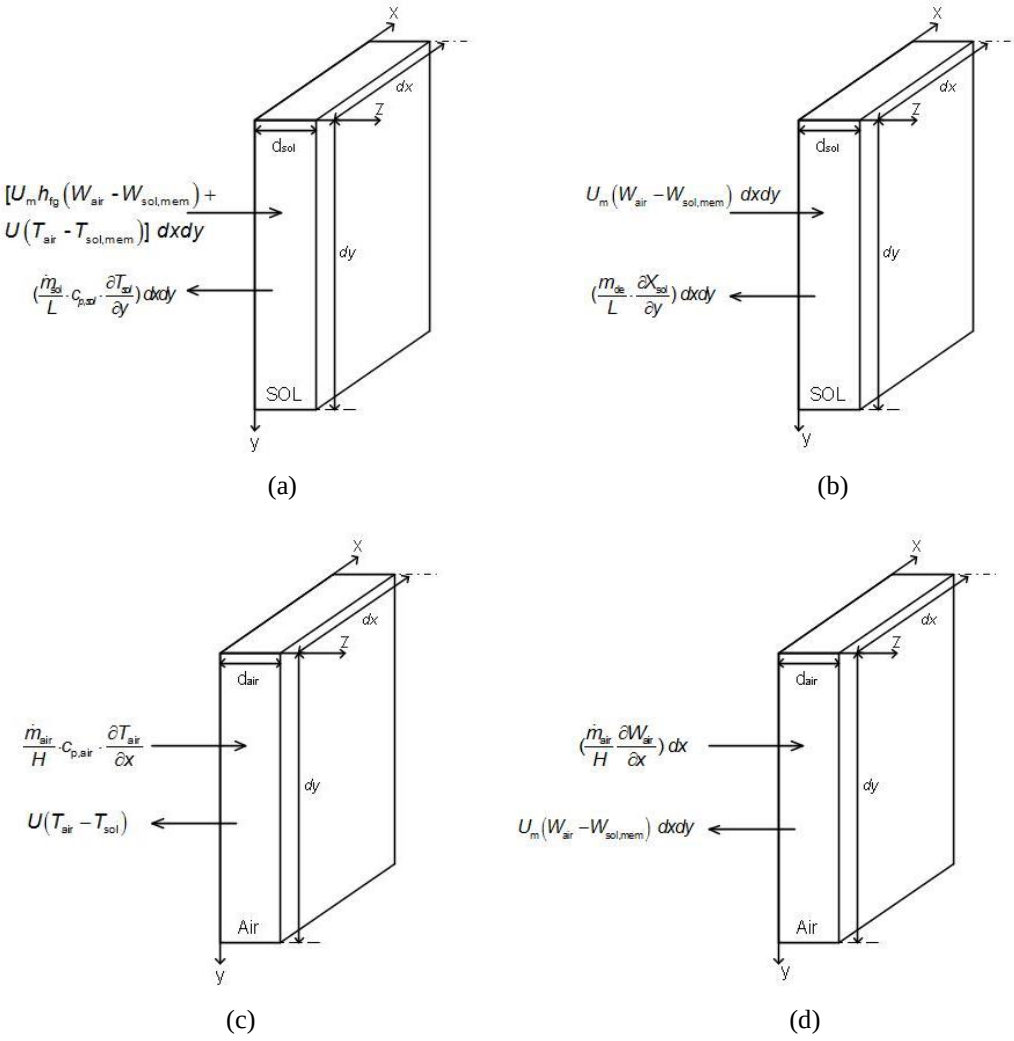


Figure 7-3 Control volumes for (a) heat balance, (b) mass balance in solution channel, (c) heat balance and (d) mass balance in air channel

Explanations for parameters involved in the MLDC model are presented in Table 7-4:

Table 7-4 Parameters for MLDC modelling

Parameters	Explanations	Unit
$\dot{m}_{de}$	Liquid desiccant mass flow rate	kg/s
$\dot{m}_{air}$	Air mass flow rate	kg/s
$\dot{m}_{sol}$	Solution mass flow rate	kg/s
ω_{air}	Specific humidity of air	kg/kg
$\omega_{sol,mem}$	Solution specific humidity on the membrane surface	kg/kg

Parameters	Explanations	Unit
C_{p_sol}	Solution specific heat	kJ/kg K
C_{p_air}	Air heat capacity	kJ/ kg K
h_{fg}	Water condensation heat	J/kg
T_{sol}	Solution temperature	°C
T_{air}	Air temperature	°C
$T_{sol,mem}$	Membrane surface solution temperature	°C

The solution mass fraction (X_{sol}) is defined as the mass ratio between water and desiccant, with which the liquid desiccant solution concentration (C_{sol}) can be derived:

$$X_{sol} = \frac{m_{water}}{m_{de}} \tag{7-11}$$

$$C_{sol} = \frac{1}{1+X_{sol}} \tag{7-12}$$

Where m_{water} and m_{de} are masses of water and desiccant respectively, kg.

Regarding to the heat and mass transfer inside the two channels, overall convective mass transfer coefficient (U_m) and heat transfer coefficient (*U*) are defined respectively, which can be obtained by dimensionless Nusselt number (*Nu*) and Sherwood number (*Sh*) under conjugate transfer condition.

$$U_m = \left(\frac{1}{h_{m,air}} + \frac{\delta}{k_{m,mem}} \right)^{-1} \tag{7-13}$$

Where $h_{m,air}$ is air side mass transfer coefficient, kg/m^{2}K and $k_{m,mem}$ is membrane mass conductivity, kg/ms.

$$U = \left(\frac{1}{h_{\text{air}}} + \frac{\delta}{k_{\text{mem}}} + \frac{1}{h_{\text{sol}}} \right)^{-1} \tag{7-14}$$

Where h_{air} is air side heat transfer coefficient, W/m^{2}K, k_{mem} is membrane heat conductivity, W/mK and h_{sol} is solution side heat transfer coefficient, W/m^{2}K.

With referred to validated heat and mass transfer models for various membranes by Huang, et al. [224], the corresponding *Nu* and *Sh* values under the defined conjugate transfer condition of this model are adopted directly.

Besides the heat and mass transfers occurring in the air and solution channels, the membrane heat and mass transfer should be also considered, which takes place at the membrane surface as the heat from vapour condensation is added to the solution side. The overall heat transfer coefficient is used for heat transfer from air channel to membrane, which includes the resistance of convective heat transfer of the solution. The heat transfer boundary conditions are based on thermal energy balance through the membrane:

$$h_{\text{sol}} \left(T_{\text{sol,mem}} - T_{\text{sol}} \right) = U \left(T_{\text{air}} - T_{\text{sol,mem}} \right) + h_{\text{fg}} U_{\text{m}} \left(\omega_{\text{air}} - \omega_{\text{sol,mem}} \right) \tag{7-15}$$

Where $h_{\text{m,sol}}$ is solution convective mass transfer coefficient, kg/m^{2}s and $C_{\text{sol,mem}}$ is solution concentration on membrane surface.

Similarly, mass transfer boundary conditions are based on mass balance through the membrane:

$$U_{\text{m}} \left(\omega_{\text{air}} - \omega_{\text{sol, mem}} \right) = h_{\text{m,sol}} \left(C_{\text{sol}} - C_{\text{sol,mem}} \right) \tag{7-16}$$

The governing equations are then normalized to outline important parameters. The normalization procedure is explained in Figure 7-4. In particular, NTU is obtained

based on the minimum capacity ratio (i.e. $\dot{m}_{\text{air}}c_{p,\text{air}} < \dot{m}_{\text{sol}}c_{p,\text{sol}}$). The normalized equations for the membrane-based unit modelling are provided in Table 7-5.

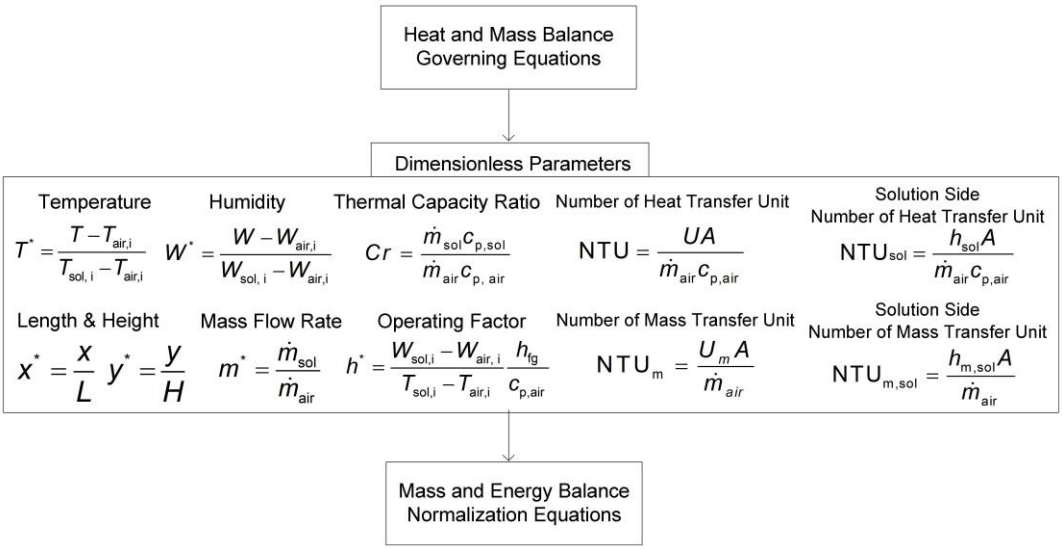


Figure 7-4 Normalization process with dimensionless parameters for governing equations

Table 7-5 Normalized equations for heat and mass balances

Descriptions	Normalized Equations
Solution side heat balance	$\frac{\partial T^*_{\text{sol}}}{\partial y^*} - NTU_{\text{m}}h^*\frac{1}{Cr}\left(\omega^*_{\text{air}} - \omega^*_{\text{sol,mem}}\right) - NTU\cdot\frac{1}{Cr}\left(T^*_{\text{air}} - T^*_{\text{sol}}\right) = 0$
Solution side mass balance	$\frac{\partial X_{\text{sol}}}{\partial y^*} - \frac{1}{m^*}\cdot\left(\omega_{\text{sol,in}} - \omega_{\text{air,in}}\right)\cdot NTU_{\text{m}}\left(1 + X_{\text{sol}}\right)\left(\omega^*_{\text{air}} - \omega^*_{\text{sol,mem}}\right) = 0$
Air side heat balance	$\frac{\partial T^*_{\text{air}}}{\partial x^*} + NTU_{\text{m}}\left(T^*_{\text{air}} - T^*_{\text{sol}}\right) = 0$
Air side mass balance	$\frac{\partial \omega^*_{\text{air}}}{\partial x^*} + NTU_{\text{m}}\left(\omega^*_{\text{air}} - \omega^*_{\text{sol,mem}}\right) = 0$
Membrane surface heat balance	$NTU_{\text{sol}}\left(T^*_{\text{sol,mem}} - T^*_{\text{sol}}\right) = NTU\left(T^*_{\text{air}} - T^*_{\text{sol,mem}}\right) + NTU_{\text{m}}h^*\left(\omega^*_{\text{air}} - \omega^*_{\text{sol,mem}}\right)$
Membrane surface mass balance	$NTU_{\text{m}}\cdot\left(\omega_{\text{sol,in}} - \omega_{\text{air,in}}\right)\cdot\left(\omega^*_{\text{air}} - \omega^*_{\text{sol,mem}}\right) = NTU_{\text{m,sol}}\left(C_{\text{sol}} - C_{\text{sol,mem}}\right)$

For modelling, air specific humidity is used instead of vapour pressure since it is more straightforward and the vaporisation heat can be easily derived. The relationship between the specific humidity and vapour pressure is given by [265]:

$$\omega = 0.62198 \frac{P_v}{P_a - P_v} \tag{7-17}$$

Where P_a and P_v are atmospheric pressure and vapour pressure respectively, Pa.

Similarly, the equivalent specific humidity ratio of the desiccant solution is adopted for modelling, which can be calculated with equilibrium state of air at the interface. The differential membrane surface humidity governing equations can be obtained from surface temperature and solution concentration. The equilibrium water vapour pressure of desiccant solution is a function of solution temperature and concentration. An empirical correlation is derived by Cisternas and Lam [241] as expressed:

$$Log\ P_v = KI\left[A - \frac{B}{T - E_s}\right] + \left[C - \frac{d}{T - E_s}\right] \tag{7-18}$$

Where K is an electrolyte parameter relating to solute; A, B, C, D and E_s are parameters regarding to solvent. As $CaCl_2$ is selected as the liquid desiccant, the psychrometric chart of $CaCl_2$ solution has been previously presented in Figure 6-5.

7.2.5 Performance evaluation metrics

Theoretically, the energy performance of the micro trigeneration system is mainly assessed by three parameters: the electrical efficiency, the thermal efficiency and the system overall efficiency. The electrical efficiency (η_{el}) represents the useful power produced by the micro trigeneration system, which is expressed as:

$$\eta_{el} = \frac{W_{net}}{Q_{in}} = \frac{W_{net}}{Q_{ev}} \tag{7-19}$$

Where W_{net} is system net power output as the difference between the scroll expander output power and the pump input power (i.e. $W_{net} = W_{el} - W_{pp}$) and Q_{ev} represents heat absorbed by the working fluid in the evaporator, W.

The thermal efficiency (η_{th}) is the thermal energy proportion in the entire micro trigeneration system, which indicates how much energy is recovered rather than wasted.

$$\eta_{th} = \frac{Q_{th}}{Q_{in}} = \frac{Q_{th}}{Q_{ev}} \tag{7-20}$$

Where Q_{th} is total thermal output discharged by the scroll expander and distributed to the heat recovery and MLDC units respectively, W.

The coefficient of performance (COP) of the MLDC is defined as:

$$\text{COP} = \frac{Q_{cooling}}{Q_{th\_MLDC}} \tag{7-21}$$

Where $Q_{cooling}$ is cooling output of the MLDC and Q_{th_MLDC} is heat input of the MLDC regenerator, which is recovered from the exhaust heat of the scroll expander, W.

The micro trigeneration system overall efficiency ($\eta_{overall}$) is determined as the ratio of the overall trigeneration system energy conversion (i.e. electricity, heating and cooling) over the total energy input to the system:

$$\eta_{overall} = \frac{W_{net} + Q_{HR} + Q_{cooling}}{Q_{ev}} \tag{7-22}$$

Where Q_{HR} is thermal output of heat recovery unit, W.

All the evaluation metrics has been included as the output variables for the micro trigeneration system modelling.

7.2.6 Modelling method

MATLAB provides highly self-defined mathematical model environment and provides comprehensive numerical equation solvers compared to EES or other potential simulation software. Referred to the methodology presented in the literature [147], the integrated micro trigeneration system modelling is implemented by linking the established components together in series in MATLAB. The open source CoolProp library is applied as the main source to retrieve thermo-physical properties of the working fluid R134a applicable for the micro trigeneration system. Maim assumptions adopted in the system modelling are: (a) the trigeneration system operate in steady state and (b) the pressure drops in heat exchangers and pipelines are neglected.

A flow chart of theoretical modelling is shown in Figure 7-5. The input variables of the system model mainly include heat source of ORC, cold and hot water properties, ambient environment temperature, solution and air inlet conditions of MLDC. As the entire system model is regarded as a closed loop with all the components combined and connected in series, fluid properties and variables of every individual component will interact with each other. For example, the working fluid condition at the pump outlet also acts as the supply condition for the evaporator. In order to obtain the steady-state result, a comprehensive iteration process is necessary. At the start of implicit iteration, a good initial guess is essential for saving calculation time and shortening the simulation process. In principle, on a basis of the steady-state condition guessed for each component, the iteration process gradually narrows down the discrepancy among variables of components, and finally the steady-state result will be determined

once reasonable residual is reached. For the sake of efficient simulation in MATLAB, a pre-conditioner solver and an overall cycle solver are programmed. The pre-conditioner mainly functions to implement the guess process implicitly, while the cycle solver assigns the guessed results to the components at the beginning of iteration, which starts from the pump model. Each iteration result serves as the initial input for the next calculation loop, while residuals between the loop input and output are calculated accordingly. The overall system steady-state result is produced when the average residual is narrowed to a given criterion. Basically, three main outputs of the micro trigeneration system, including the electric generated, hot water supply temperature, cooling output of MLDC can be produced by the model. In addition, for performance evaluation in this chapter, the output variables of the model are generated in a comprehensive profile format, as presented in Table 7-6.

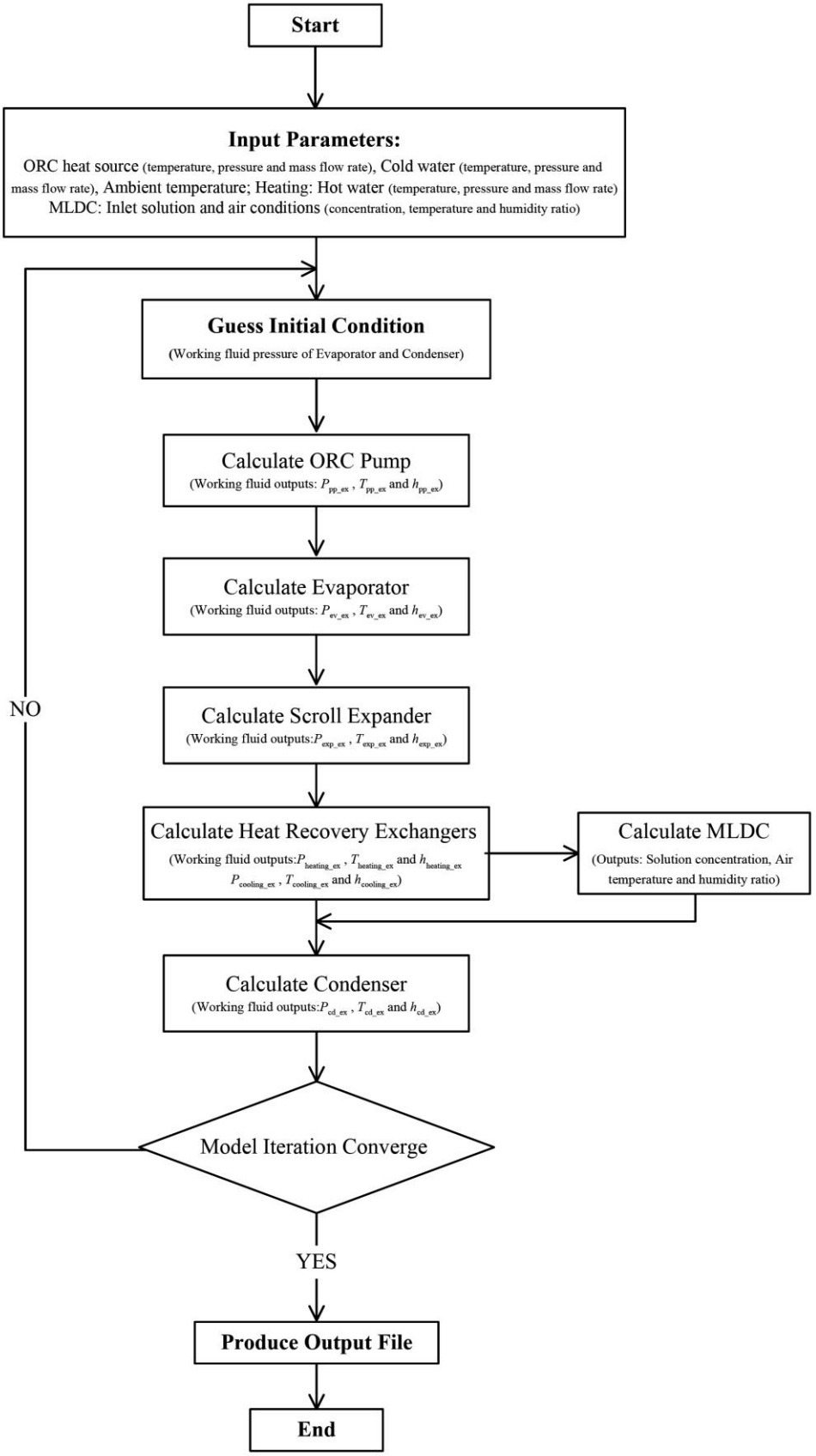


Figure 7-5 Modelling flow chart

Table 7-6 Outputs of the micro trigeneration system model

Scroll expander	Shaft power W_{sh}
	Electric power W_{el}
Hot water supply	HX1 outlet T_{hf_ex}
Thermal energy	Input thermal of heat source Q_{ev}
	Recovered thermal energy for heating $Q_{th\_heating}$
	Recovered thermal energy for cooling $Q_{th\_coolling}$
	MLDC cooling output $Q_{cooling}$
	Total recovered thermal energy Q_{th}
MLDC	COP
System net power output W_{net}	
Efficiency	Scroll expander isentropic efficiency η_{is}
	Scroll expander volumetric efficiency η_{vo}
	Electrical efficiency η_{el}
	Thermal efficiency η_{th}
	Overall system efficient $\eta_{overall}$

In this section, the complete system modelling has been presented in detail with descriptions of each individual component modelling as well as modelling method. Next, Section 7.3 presents the validation of the system model with the experimental work.

7.3 Model validation with experimental work

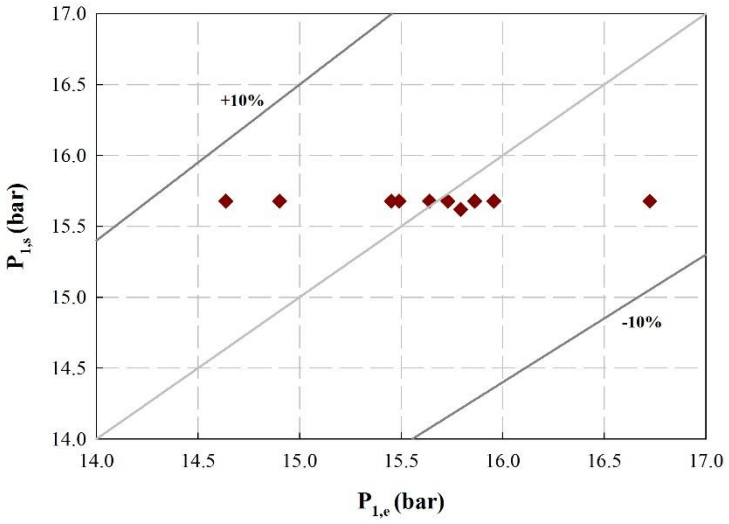
To use the model with confidence, the model validation is conducted with experimental data. In this section, the validation is mainly focused on the main components of the micro trigeneration system (i.e. ORC), by comparing simulation results with experimental data. The experimental testing of the ORC has been

described previously in Section 5.3 with R134a as the working fluid. The parameters involved in the model validation are namely the working fluid pressures at inlet and outlet of the scroll expander (i.e. P_1 and P_2), the working fluid mass flow rate (m), the electricity output (W_e) and working fluid temperatures at various locations. Ten tests have been selected for validation and the experimental data alongside the simulation results, the operating conditions are listed in Table 7-7, and validation results are presented in Figure 7-6 and Figure 7-7.

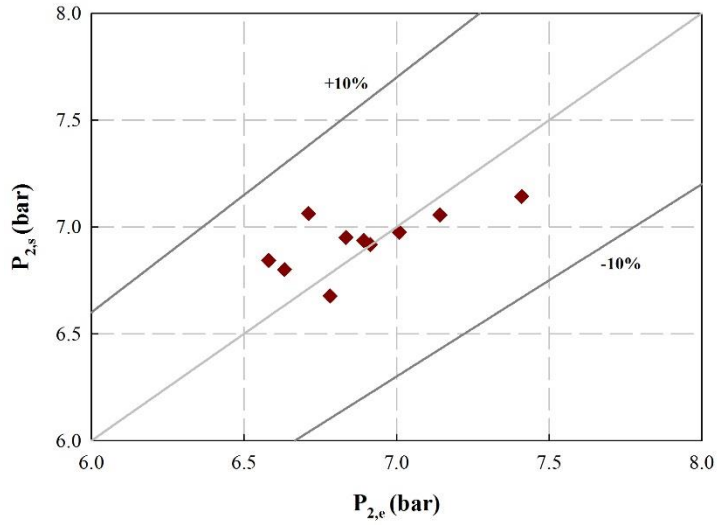
Table 7-7 Operating variables for validation

Operating variables	Range
Hot water temperature	368-378K
Hot water mass flow rate	0.12kg/s
Scroll expander rotational speed	3000-3600rpm
Pump rotational speed	3300-3600rpm
Cold water temperature	283-287K
Cold water mass flow rate	0.20kg/s

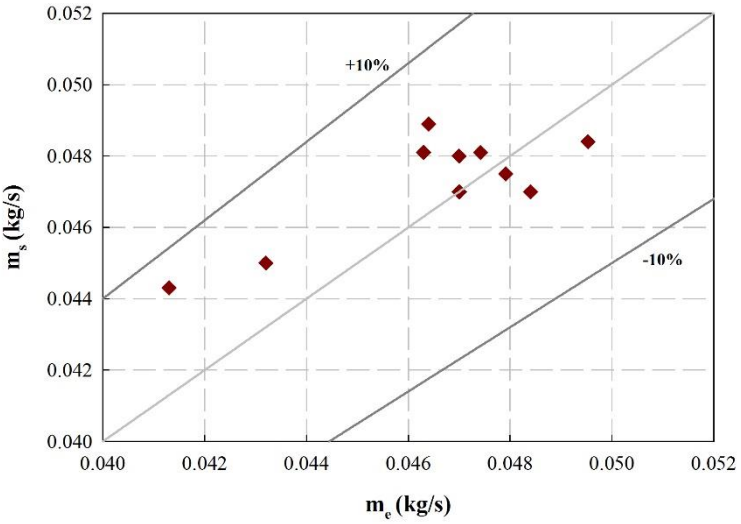
Figure 7-7 presents the comparisons between the measured and simulated data for the working fluid pressure, working fluid mass flow rate and electricity output. Error bars of ±10% are included to illustrate the degree of agreement between the experimental and simulation results. Over the 10 tests, good agreements between the simulation and experimental results are observed for both the inlet and outlet pressures (i.e. P_1 and P_2), with a maximum deviation of ±8%. On the other hand, the simulation results of the working fluid mass flow rate and generated electric power match well with the experimental data, where predictions fit within ±8% margin.


17.0
16.5
16.0
15.5
15.0
14.5
14.0
+10%
-10%
$P_{1,s}$ (bar)
14.0
14.5
15.0
15.5
16.0
16.5
17.0
$P_{1,e}$ (bar)

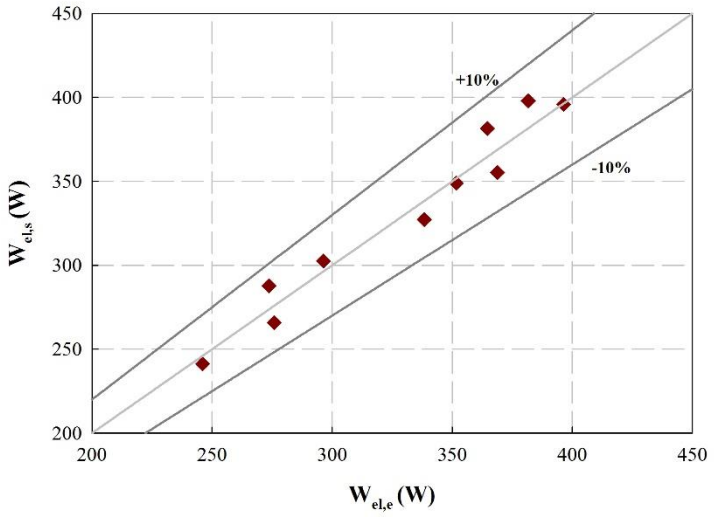
(a)


8.0
7.5
7.0
6.5
6.0
+10%
-10%
$P_{2,s}$ (bar)
6.0
6.5
7.0
7.5
8.0
$P_{2,e}$ (bar)

(b)


0.052
0.050
0.048
0.046
0.044
0.042
0.040
+10%
-10%
m_s (kg/s)
0.040
0.042
0.044
0.046
0.048
0.050
0.052
m_e (kg/s)

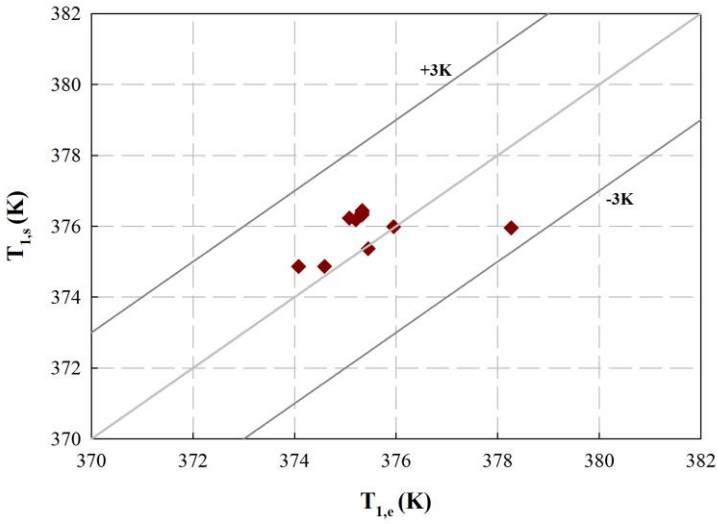
(c)



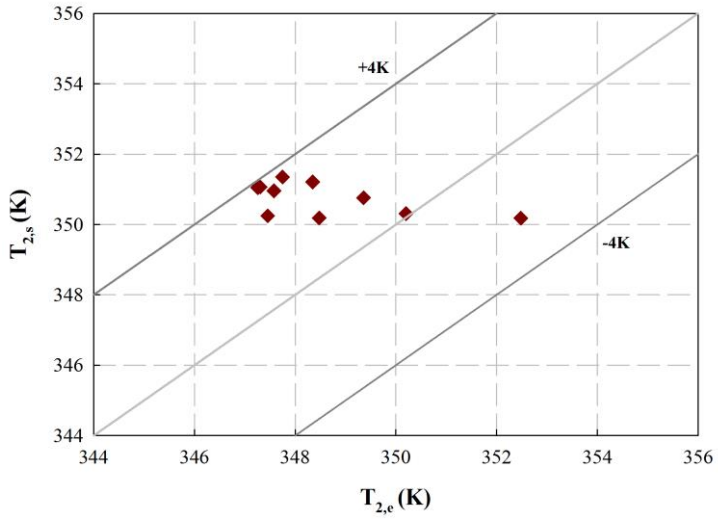
(d)

Figure 7-6 Comparison of the calculated and measured results for: (a) scroll expander supply pressure (b) scroll expander exhaust pressure (c) working fluid mass flow rate and (d) electric output power

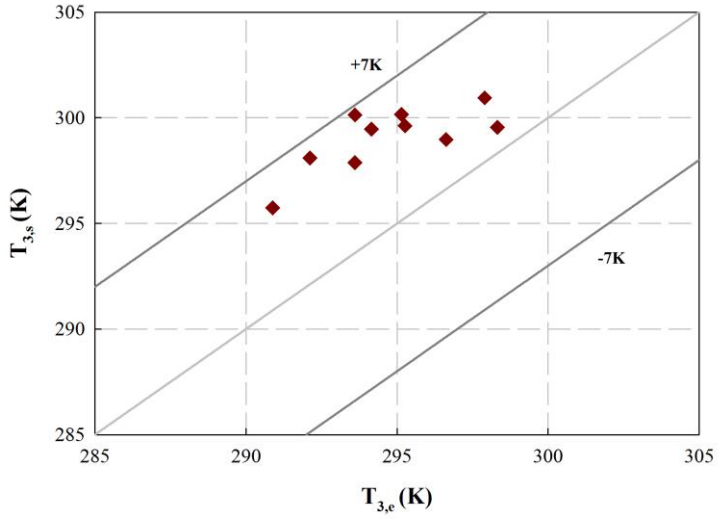
Regarding to the validation of temperature variables, working fluid temperatures at inlet and outlet of the scroll expander (i.e. T_1 and T_2) as well as the condenser outlet (i.e. T_3) are compared to the experimental data, which are measured by thermocouple sensors during testing. As show in in Figure 7-7(a) and 7-7(b), the calculated working fluid temperatures at inlet and outlet of the scroll expander (i.e. T_1 and T_2) correspond well to the experimental data, which are all clustered around two regions within ±3K and ±4K respectively. However, a more notable difference of the condenser outlet temperature between the prediction and measurement is seen in Figure 7-7(c), as the calculated condenser outlet temperatures are fluctuating within the margin of +7K.



(a)



(b)



(c)

Figure 7-7 Comparison of the calculated and measured results for working fluid temperature at: (a) scroll expander inlet (b) scroll expander outlet (c) condenser outlet

Overall the developed micro trigeneration system model works within an acceptable error range for the parameters required to evaluate the micro trigeneration system. Consequently, the model can be used confidently in the following parametric studies presented in Section 7.4, 7.5 and 7.6. The discrepancies between the experimental and simulation results may be caused by the following reasons:

1) Average values of experimental conditions are used as the modelling input.
2) Semi-empirical modelling has been adopted for the scroll expander and pump, which simplifies the working processes inside the scroll expander and pump. The internal leakages of the scroll expander are modelled by lumping leakages paths into one fictitious leakage clearance and the mechanical losses are obtained by considering a proportional loss factor for the pump, which may not precisely simulate the real leakage condition.
3) Pressure losses due to friction in the pipe and heat exchangers are assumed to be negligible.
4) The ambient temperature maybe not constant throughout the testing period, which cannot be accurately manifested in the modelling.
5) Due to the accuracies of the measurement instruments and measuring method, inevitable experimental errors exist.

This section has presented the validation of the micro trigeneration system model with experimental data for a wide range of parameters. Reasonable agreements have been found for all the investigated parameters between the simulation and experimental data. Next, a detailed comparison of the system energy performance under different operating modes is provided in Section 7.4.

7.4 System energy performance in different operating modes

The proposed micro trigeneration system enables various operating modes to meet the end-user's energy demands, which include: (a) ORC-based single power generation mode for electricity only; (b) CHP mode for electricity and hot water supply; (c) CCP mode for electricity and cooling/dehumidification demands and (d) CCHP mode for electricity, hot water supply and cooling/dehumidification demands. Based on the validated model, the micro trigeneration system performance can be simulated in different operating modes by varying the input variables. For simulation, the working fluid of R134a and liquid desiccant of $CaCl_2$ are chosen for the micro trigeneration system. In this section, comparisons of the micro trigeneration system performance are conducted among the four operating modes for generating similar amount of electric output power. More specifically, by adjusting the distribution ratio of the recovered thermal power for heating and cooling/dehumidification demands, the micro trigeneration system performs differently in CCHP mode. Hence, as the micro trigeneration system operates in CCHP mode, three distribution ratios are selected for the comparative study (i.e. 30%, 50% and 70%) in this section.

A number of evaluation metrics with regard to the micro trigeneration system energy performance are taken into account for comparison, as previously stated in Section 7.2.5, including the electric power generated, scroll expander isentropic efficiency, thermal power recovered for heating, recovered thermal power for cooling, total recovered thermal power, total useful energy power, system electrical efficiency, thermal efficiency, COP of MLDC and overall system efficiency. Table 7-8 shows the simulation results of the micro trigeneration system in different operating modes. Apparently, the feasibility of the proposed micro trigeneration system is proved based on the simulation data. The micro trigeneration system operating in the CHP, CCP and

CCHP modes exhibits better energy performance compared to that of the separate power generation mode. Comparatively, CCP mode demonstrates the highest overall system efficiency of 42.04%, while only 5.74% is achieved for the single power generation. The results also imply that by integrating a heat recovery component in a single power generation system for hot water supply, the overall system efficiency improves by additional 33.32% and an integration of the MLDC contributes an improvement of additional 36.30% in the overall system efficiency. For the micro trigeneration system operating in CCHP mode, the more thermal power is recovered for cooling/dehumidification demand, the higher overall system efficiency can be reachable owing to the more total useful energy output. With 40% more recovered thermal energy is distributed for cooling demand, the improvement in the overall system efficiency is approximately 4.1%. On the contrary, the COP of MLDC decreases accordingly because the heat input power added for heating the dilute solution plays a more predominant role than the cooling output of the dehumidifier.

Table 7-8 Energy performance of micro trigeneration system in different operating modes

Parameters	**Power only**	**CHP**	**CCP**	**CCHP_1**	**CCHP_2**	**CCHP_3**
				H:30 C:70	**H:50 C:50**	**H:70 C:30**
Input power (W)	12996	13198	13173	13109	13128	13134
Electric output (W)	825.57	825.18	825.33	825.50	825.54	825.39
Scroll expander exhaust temperature (K)	337.64	337.51	337.52	337.49	337.49	337.49
Scroll expander isentropic efficiency (%)	65.88	65.74	65.72	65.75	65.78	65.76

Parameters	Power only	CHP	CCP	CCHP_1	CCHP_2	CCHP_3
				H:30 C:70	H:50 C:50	H:70 C:30
Working fluid mass flow rate (kg/s)	0.05	0.05	0.05	0.05	0.05	0.05
Recovered thermal energy for hot water supply (W)	-	4385.03	-	1206.52	2311.01	2716.21
Recovered thermal energy for MLDC (W)	-	-	4781.00	3440.45	2238.21	1730.89
Total useful energy output (W)	758.12	5142.21	5538.33	5404.47	5304.76	5202.49
Electrical efficiency (%)	5.83	5.74	5.75	5.76	5.76	5.75
Thermal efficiency (%)	-	33.23	36.29	35.28	34.53	33.76
COP	-	-	0.21	0.26	0.37	0.45
Overall system efficiency (%)	5.85	38.96	42.04	41.23	40.41	39.61

In this section, the simulation results have demonstrated the pairing of ORC and MLDC for a micro trigeneration system is viable. It has also been found from the comparison that the micro trigeneration system in cogeneration and trigeneration modes exhibits better energy performance compared to the single power generation mode. Next, a comprehensive parametric study of the micro trigeneration system performance in CHP mode is presented in Section 7.5.

7.5 Parametric study of system performance in cogeneration mode

In this section, the micro trigeneration system is simulated in CHP mode, which only provides electricity and hot water supply. For the parametric study in this section, the system energy performance is assessed by a number of metrics as defined in Section 7.2.5, namely the generated electricity, the recovered thermal energy for hot water supply, the electrical efficiency, the thermal efficiency and the CHP efficiency. Based on the simulation results, the effect of different operating variables on the system performance are investigated as well: (a) the effect of hot water supply temperature in Section 7.5.1; (b) the effect of hot water supply mass flow rate in Section 7.5.2; (c) the effect of cold water supply temperature in Section 7.5.3; (d) the effect of cold water supply mass flow rate in Section 7.5.4 and (e) the effect of scroll expander rotational speed in Section 7.5.5. For the parametric study in this section, the typical operating condition for simulation is presented in Table 7-9, and the ranges of the operating variables used in the investigation are also listed.

Table 7-9 Operating variables for simulation

Operating variables	Value	Simulation Range
Hot water temperature	370K	365-385K
Hot water mass flow rate	0.12kg/s	0.10-0.15kg/s
Scroll expander rotational speed	3600rpm	2800-3600rpm
Refrigerant pump rotational speed	3600rpm	-
Cold water temperature	3000rpm	280-292K
Cold water mass flow rate	285K	0.15-0.35kg/s

7.5.1 Hot water supply temperature

As depicted in Figure 7-1, hot water is supplied from the electric boiler to the evaporator for heating up the working fluid R134a in the ORC loop, so that the working fluid enters the scroll expander at a high temperature and pressure vapour state. To investigate the impact of the hot water supply temperature on the system performance, simulations are conducted for the micro trigeneration system operating in CHP mode with hot water supply temperature ranging from 365K to 385K. Figure 7-8 demonstrates temperature variations of the working fluid at scroll expander supply and exhaust respectively. Apparent linear relationships with the hot water supply temperatures are observed for both the working fluid inlet and outlet temperature. Over the investigated hot water supply temperature range, the scroll expander supply and exhaust temperatures rise linearly from 364.97K to 385.01K and from 330.88K to 350.69K respectively.

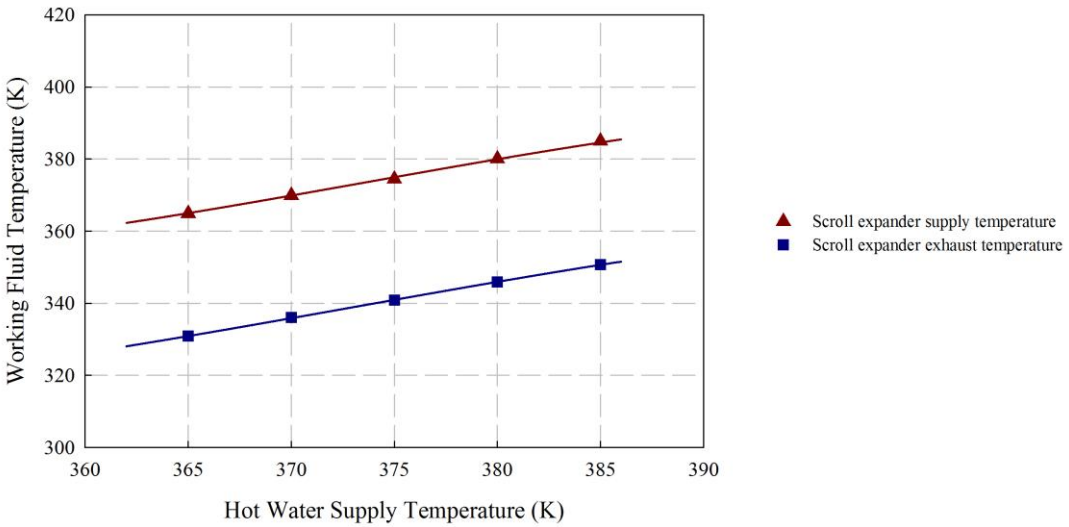


Figure 7-8 Influence of hot water supply temperature on scroll expander supply and exhaust temperatures

As the supply condition varies with the hot water supply temperature, the scroll expander performs differently. Figure 7-9 presents the scroll expander operating

pressure ratios and isentropic efficiencies at different hot water supply temperatures. It can be clearly seen that higher hot water supply temperature leads to higher supply temperature and pressure of the scroll expander, thus a higher pressure ratio is imposed and a higher isentropic efficiency can be achieved. For example, at a hot water supply temperature of 365K, the scroll expander is operated at a pressure ratio of 2.63 and its isentropic efficiency is approximately 66.27%, while with hotter water supplied to the system (i.e. 385K), the scroll expander isentropic efficiency improves by 5.46% as the scroll expander operates at a pressure ratio of 2.87.

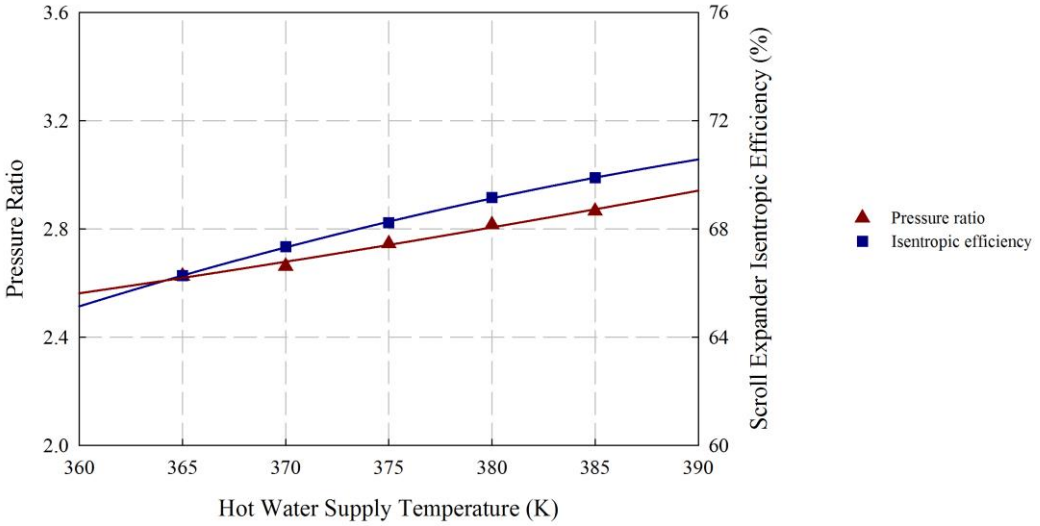


Figure 7-9 Influence of hot water supply temperature on scroll expander pressure ratio and isentropic efficiency

At a higher hot water supply temperature, more heat transfer occurs between the hot water and working fluid in the evaporator and the working fluid leaves for the scroll expander at a higher volume flow rate and enthalpy. Evidently, more heat input is provided to the system with the increasing hot water supply temperature as indicated in Figure 7-10. As the hot water supply temperature rises, working flow per unit mass flow rate produces more power owing to the increasing supply temperature and pressure as well as the mass flow rate. As a consequence, more thermal power can be recovered for heating purpose. For instance, over the simulated hot supply temperature

range, the electric output power and the recovered thermal power increase by 11.86% and 28.81% respectively, whereas meanwhile 9.87% more heat input is required to power the scroll expander.

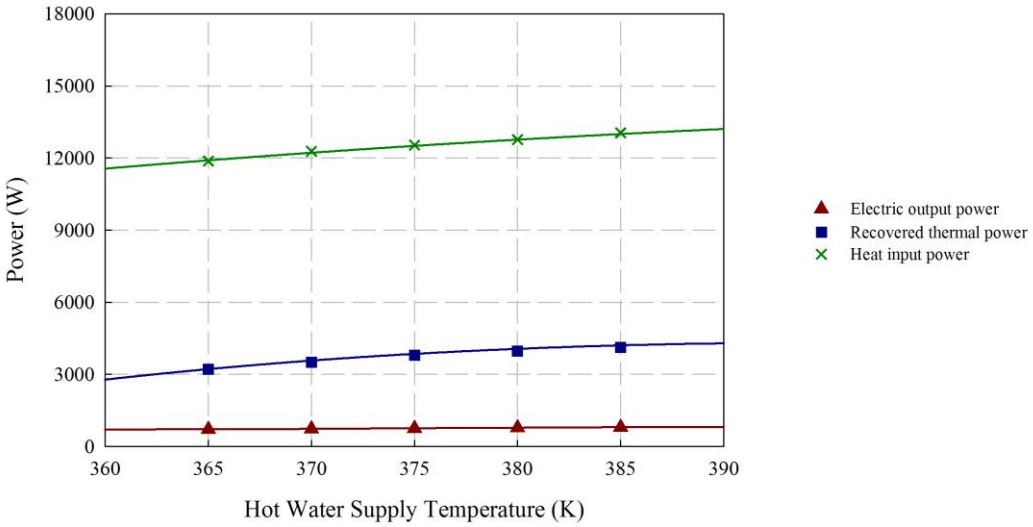


Figure 7-10 Influence of hot water supply temperature on heat input power, electric output power and recovered thermal power

Figure 7-11 presents the impact of the hot water supply temperature on the system electrical, thermal and CHP efficiencies. As the hot water supply temperature increases from 365K to 385K, only approximately 85.39W more electricity is produced by the scroll expander, thus the variation in the system electrical efficiency is not significant (i.e. an increase rate of 3.84%). Comparatively, higher rates of increase in the system thermal and CHP efficiencies are noted. The thermal efficiency increases by 16.71% and the CHP efficiency improves by 14.39% as the hot water supply temperature rises by 20K. It is also worth noting that as the hot water supply temperature increases gradually, the rates of increase in the thermal and CHP efficiencies decline accordingly. For instance, as the hot water supply temperature rises from 380K to 385K, the thermal and CHP efficiencies improve by only 0.94% and 0.74% respectively.

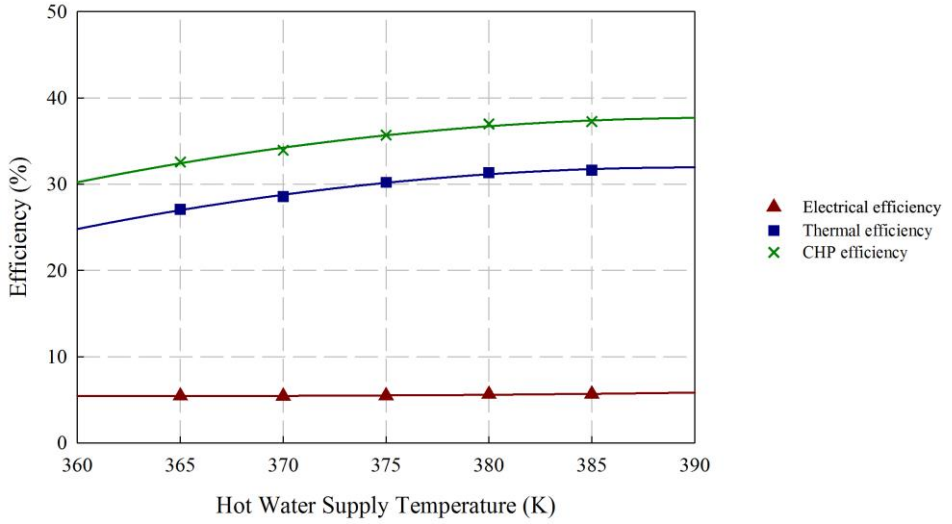


Figure 7-11 Influence of hot water supply temperature on system electrical, thermal and CHP efficiencies

The results imply that the improvement in the energy performance of the micro trigeneration system would be limited as the temperature difference between the hot water and working fluid further increases, which is attributed to the heat transfer mechanism in the evaporator. Over the hot water temperature range for simulation, the working fluid R134a is heated by the hot water and leaves the evaporator at the superheated vapour state. By varying the hot water temperature, the variation in the superheated degree of the vapour could be realised and the results reveal that superheating of the working fluid contributes to an improvement in the electric production as well as system efficiency. Basically, in terms of the boiling process occurring in the evaporator, the working fluid is firstly heated by the hot water to the superheated liquid through convective heat transfer, and then followed by saturated nucleate boiling, where a sufficient degree is reached for boiling nucleation to occur and vapour bubbles are generated [266]. Generally, nucleate boiling takes place when the surface temperature is higher than the saturation temperature by 4 to 30°C. In the nucleate boiling mode, the larger the temperature difference between the hot water and working fluid, the more the heat flux can be achieved. As the vapour production further

progresses with a larger temperature difference, the transition from the saturated nucleate boiling leads to the departure from nucleate boiling. At the departure from nucleate boiling point, the heat flux occurred in the evaporator reaches a maximum value and is called the critical heat flux [267], beyond which the vapour bubbles merge to form a continuous vapour film and less effective heat transfer takes place at low mass vapour quality with a notable reduction in the heat transfer coefficient [268]. Hence, when further increases the hot water temperature, the heat absorbed by the working fluid in the evaporator would level off gradually.

7.5.2 Hot water supply mass flow rate

Alternatively, varying the hot water mass flow rate is another way to realise changes in the hot water supply condition. To identify the effect of the hot water mass flow rate on the system energy performance, the hot water is simulated in a mass flow rate range of 0.10kg/s to 0.15kg/s. As the hot water mass flow rate increases, in other words, more hot water is supplied to transfer heat to the working fluid in the evaporator. In such a way, the scroll expander performance improves in accordance with the hot water mass flow rate as illustrated in Figure 7-12. When the hot water mass flow rate is 0.10kg/s, the scroll expander isentropic efficiency is 66.19% at a pressure ratio of 2.57, while at a hot water mass flow rate of 0.15kg/s, the scroll expander operates at a pressure ratio of 2.89 and its isentropic efficiency rises up to 70.01%.

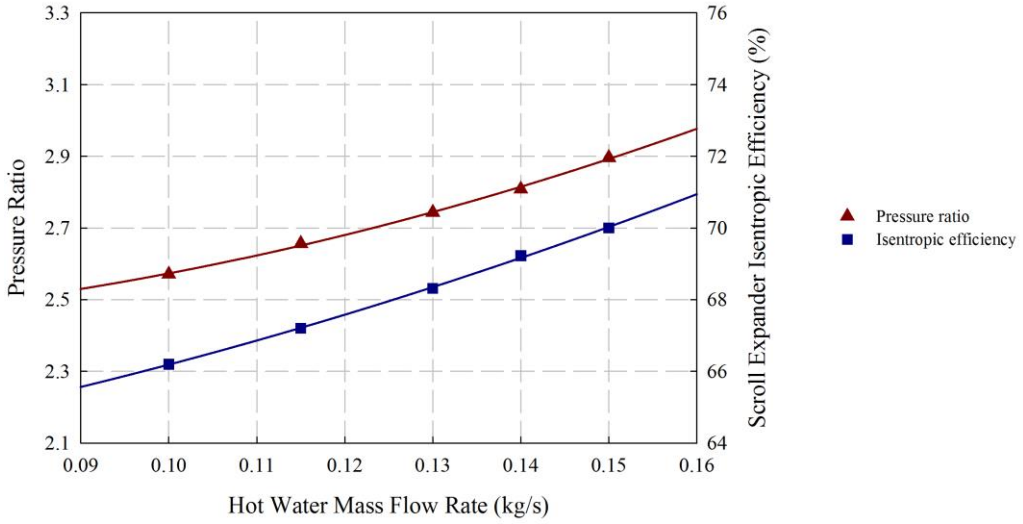


Figure 7-12 Influence of hot water mass flow rate on scroll expander pressure ratio and isentropic efficiency

The increase in the hot water mass flow rate allows more heat input into the micro trigeneration system, as indicated in Figure 7-13. The results imply that though a higher mass flow rate of the hot water leads to more electric output and more recovered thermal energy, more heat input power are required simultaneously. For instance, as the hot water mass flow rate increases from 0.10kg/s to 0.15kg/s, the heat input power increases by 12.38% and the rates of increase in the electricity and recovered thermal output are 19.53% and 19.32% respectively. In addition, as the mass flow rate further increases, the variation in the heat input power becomes gentler which is related to the critical heat flux of the boiling process occurring in the evaporator, as mentioned in Section 7.5.1.

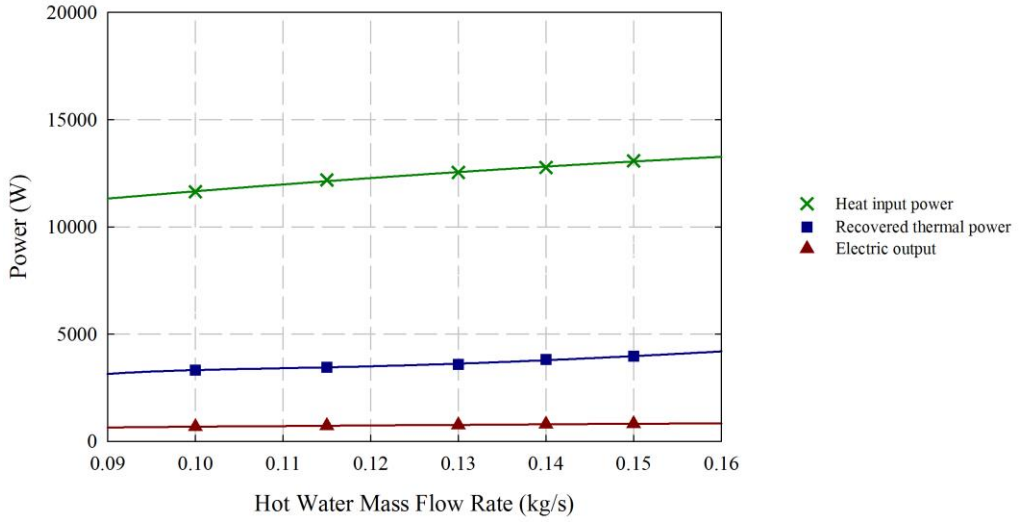


Figure 7-13 Influence of hot water mass flow rate on heat input power, recovered thermal power and electric output

Figure 7-14 presents the impact of the hot water mass flow rate on the system electrical, thermal and CHP efficiencies. Due to the increases in the heat input power, recovered thermal energy and electric output; variations in the efficiencies are not marked. Over the investigated mass flow rate range, the electrical efficiency varies from 4.95% to 5.69%, the thermal efficiency increases by 8.07% and the CHP efficiency improves by 6.44%. The results demonstrate that an improvement in the system energy performance can be attainable by providing the hot water at a higher mass flow and the actual heat transfer in the evaporator should be noted since it affects the heat input of the evaporator. Basically, the increase in the hot water mass flow rate directly influences the working fluid temperature at the evaporator outlet and thus the degree of superheat is affected as well. In terms of the evaporator, there exists a pinch point for the two-phase plate heat exchanger, which limits the capacity of the heat exchanger and increases irreversibility. From the previous studies [269-271], it has been noted that the pinch point of the evaporator plays an important role and its position is influenced by the inlet temperature of the working fluid and hot water. When the degree of superheat rises, it would cause an increase of the temperature difference at

pinch point in the evaporator as well as the irreversibility in the heat transfer process, which thus would result in the reduction of the heat exchanger efficiency and the attenuation in the increment of electric power generated could be observed. Therefore, the degree of superheat should be optimised based on the working fluid type, properties and parameter, heat source parameters and evaporator configuration, which has been also stated in the literature [112, 272].

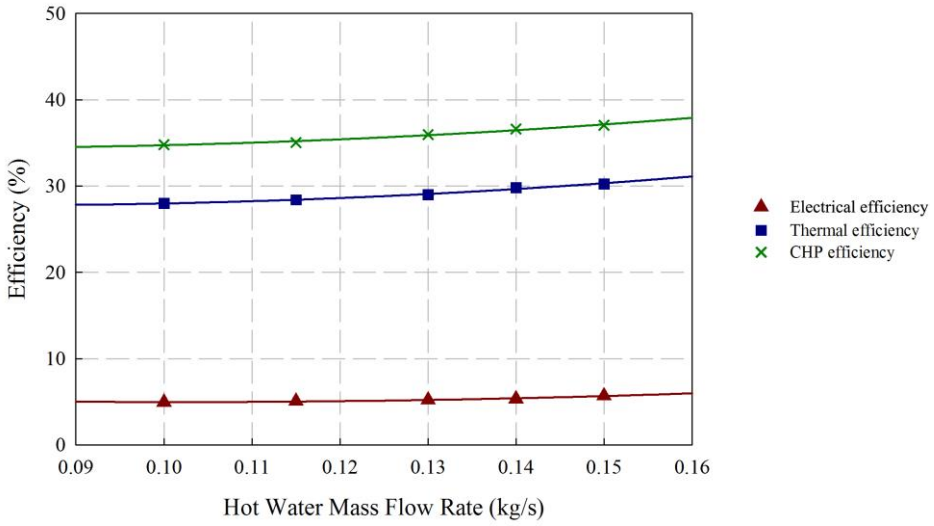


Figure 7-14 Influence of hot water mass flow rate on system electrical, thermal and CHP efficiencies

7.5.3 Cold water supply temperature

As presented in Figure 7-1, when the micro trigeneration system operates in the CHP mode, the low-pressure vapour of R134a exiting from the scroll expander firstly flows into the heat exchanger HX1 for heat recovery to provide hot water supply, and afterwards it enters the recuperator and is condensed by cold water. In such a way, the liquefied working fluid will be stored in the storage tank and pumped to the evaporator for the continued operation. By varying the cold water supply temperature from 280K to 292K while keeping the other parameters constant, its impact on the system energy performance is assessed in this section.

Apparently, the working fluid temperature at the pump inlet increases linearly with the cold water supply temperature as observed in Figure 7-15. As the cold water temperature rises from 280K to 292K, the pump supply temperature increases from 284.91K to 293.93K. A higher cooling water temperature results in a higher condensing temperature and hence higher condensing pressure is obtained, which directly influences the scroll expander exhaust pressure. When the scroll expander operates at a higher exhaust pressure, the scroll expander supply pressure increases correspondingly with the cold water supply temperature to ensure the steady operation. As the cold supply water rises by 12K, the scroll expander supply and exhaust pressures increase by 6.86% and 24.79% respectively.

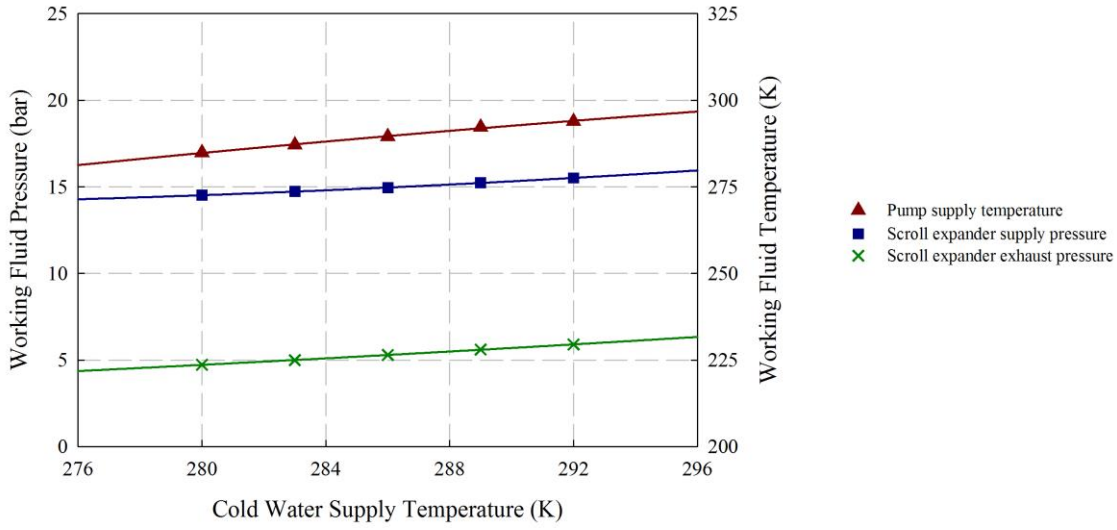


Figure 7-15 Influence of cold water supply temperature on pump supply temperature and scroll expander supply and exhaust pressures

Because the increase rate of the condensing pressure is larger than that of the supply pressure, the scroll expander pressure ratio decreases with the cold water supply temperature as shown in Figure 7-16. As a consequence, the scroll expander efficiency is lowered. At a cold water supply temperature of 280K, the scroll expander operative pressure ratio is 3.07 with an isentropic efficiency of 71.31%, while the isentropic

efficiency declines by 7.29% and the pressure ratio reduces to 2.64 as the cold water temperature rises by 12K.

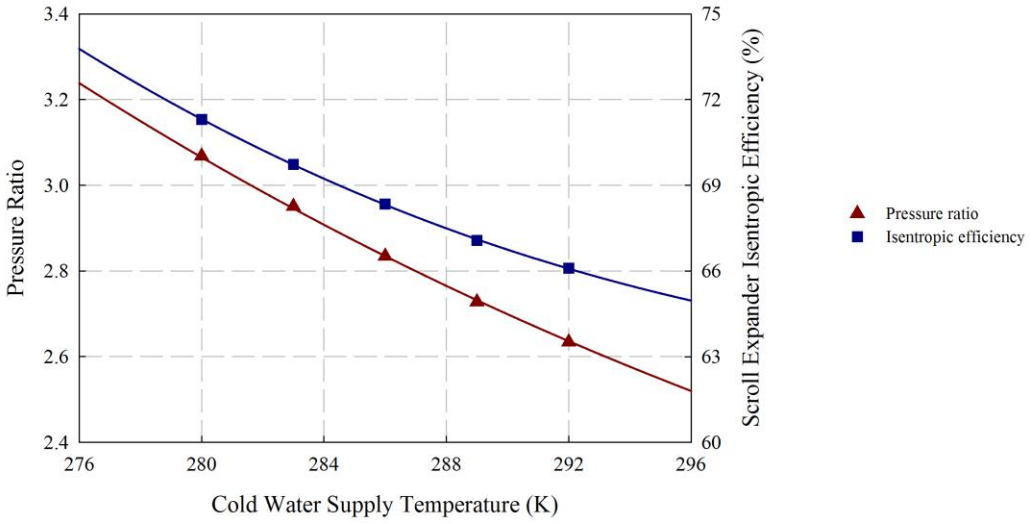


Figure 7-16 Influence of cold water supply temperature on scroll expander pressure ratio and isentropic efficiency

The increasing evaporating pressure with a higher cold water temperature results in a higher evaporating temperature and a higher working fluid density in the evaporator. However the hot water supply temperature is maintained at 365K, thus the heat transfer between the hot water and working fluid reduces and less heat input power is required as noted in Figure 7-17. With a higher cold water temperature, the scroll expander operates at a lower pressure ratio, which degenerates the power generation ability of the scroll expander. The decreasing power output is mainly determined by the increasing condensing pressure with a higher cold water temperature. On the other hand, less thermal power is recovered owing to the reduction in the heat input, condensing output and power output at a higher cold water supply temperature. For instance, at a cold water supply temperature of 280K, the system heat input power is 12519.26W, the electric output power is around 855.98W and 3673.05W thermal power is recovered, while 2.42% less heat input power is observed at a cold water

supply temperature of 292K, the electric output power reduces by 16.74% and recovered thermal power declines by 9.82% respectively.

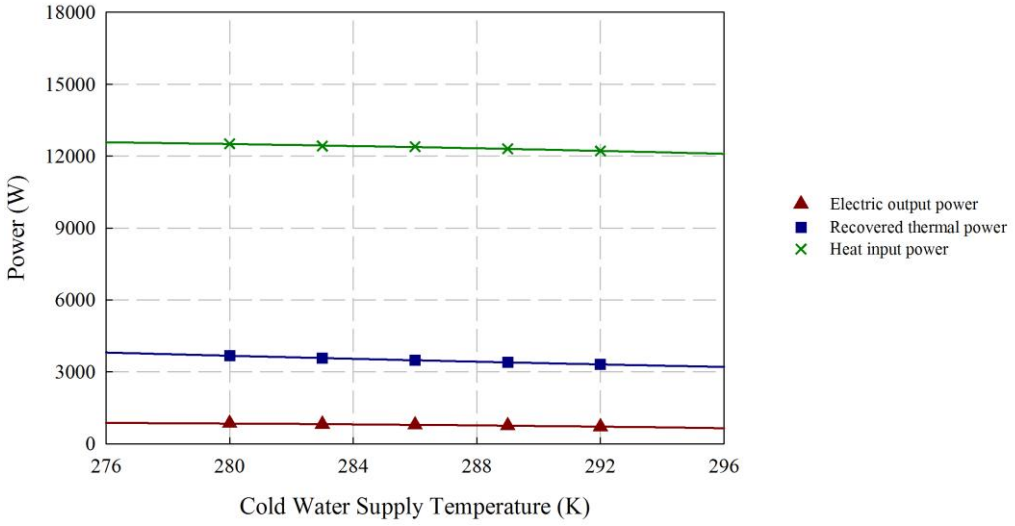


Figure 7-17 Influence of cold water supply temperature on heat input power, electric output power and recovered thermal power

Negative impacts of a higher cold water supply water temperature on the system electric, thermal and CHP efficiencies are demonstrated in Figure 7-18. The higher the cold water temperature, the lower the electrical, thermal and CHP efficiencies of the micro trigeneration system are. Over the investigated cold water supply temperature range, the CHP efficiency decreases by 9.06% and the electrical efficiency lowers by 16.74%, and 7.58% of decrease for the thermal efficiency. The result reveals the importance of supplying cooler water to the micro trigeneration system for better energy performance, which has also been stated in the literature [159]. Similar to the heat transfer mechanism of the evaporator explained in Section 7.5.1 and 7.5.2, condensation process taking place in the condenser also involves convection, drop nucleate, transition and film-wise modes [266]. By lowering the cold water supply temperature, the temperature difference between the cold water and working fluid increases and drives more heat transfer especially in the drop nucleate process.

However, there exists a critical heat flux in the condenser, beyond which a much less effective heat transfer would occur. Thus it is also noteworthy that the cold water supply temperature should be reasonable to avoid detrimental effects on the system power generation and efficiency due to the condensate sub-cooling [273] .

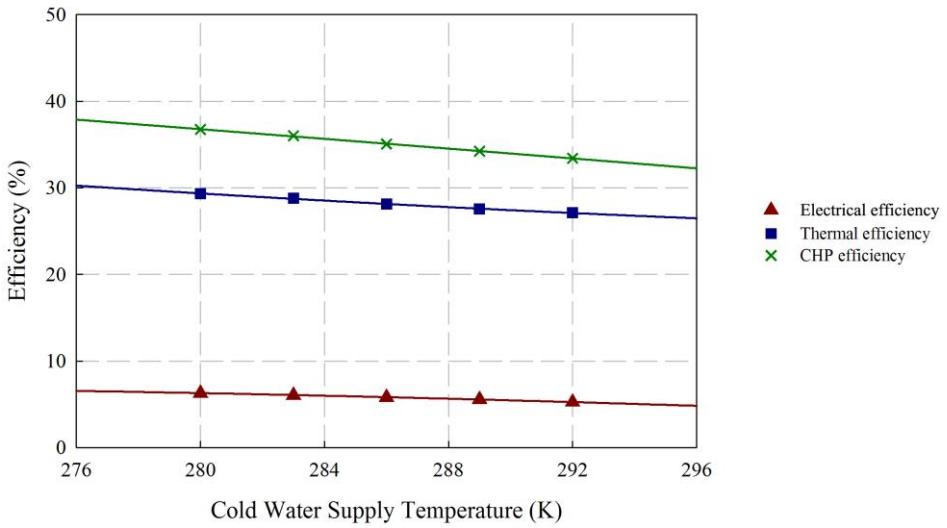


Figure 7-18 Influence of cold water supply temperature on system electrical, thermal and CHP efficiencies

7.5.4 Cold water supply mass flow rate

Then investigations are carried out to identify the effect of the cold water supply mass flow rate on the system energy performance by varying the cold water mass flow rate from 0.15kg/s to 0.35kg/s. It is noted from Figure 7-19, the scroll expander pressure ratio rises in line with the increase in the cold water mass flow rate, which thus leads to higher isentropic efficiency. This is mainly attributed to more cold water being supplied for condensing the working fluid in the condenser. When the cold water mass flow rate is 0.15kg/s, the scroll expander isentropic efficiency is approximately 62.45% at a pressure ratio of 2.45, and it rises to 69.57% at a cold water mass flow rate of 0.35kg/s and scroll expander operates at a pressure ratio of 2.84. Moreover, the rate of increase in the isentropic efficiency gradually reduces, which indicates that when the

cold water mass flow rate exceeds a critical value, the scroll expander performance levels off as sufficient cooling power is provided for condensation of the working fluid.

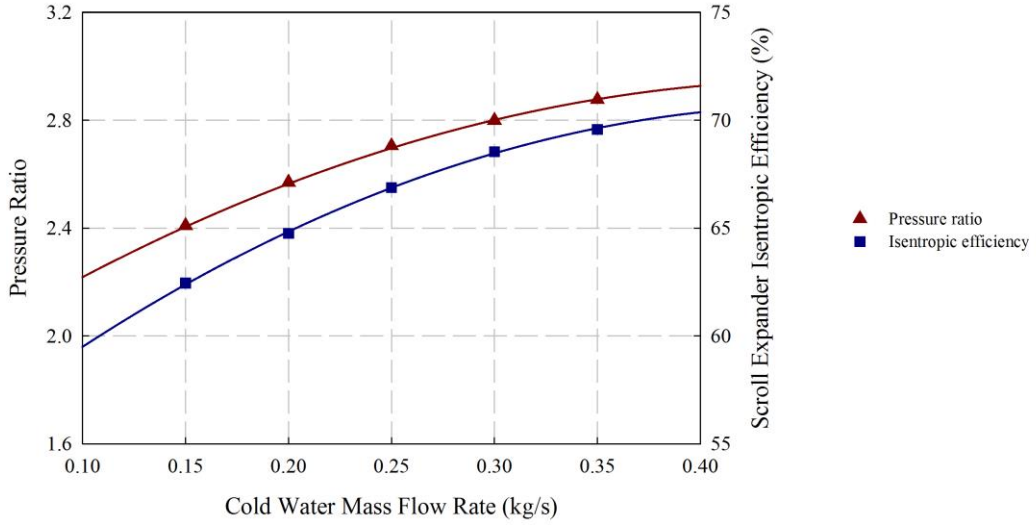


Figure 7-19 Influence of cold water mass flow rate on scroll expander pressure ratio and isentropic efficiency

At a higher cold water mass flow rate, the larger temperature difference between the cold water and working fluid leads to more heat transfer taking place in the drop nucleate condensation mode and hence the working fluid exits the condenser at a lower temperature. In other words, more heat input is demanded for the evaporator to recover the temperature difference caused by larger cold water flow in the condenser. In terms of the power output, slight tendencies of rising with the cold water mass flow rate are noted in the heat input power and recovered thermal power as seen in Figure 7-20. Over the investigated cold water mass flow rate range of 0.15kg/s to 0.35kg/s, the heat input power increases by 4.17% and the recovered thermal power varies by only 2.32%. Contrarily, there is an evident increase in the electric output, which is because of the higher pressure ratio. Approximately 275.41W more electric power is produced by the scroll expander as the mass flow rate rises by 0.20kg/s.

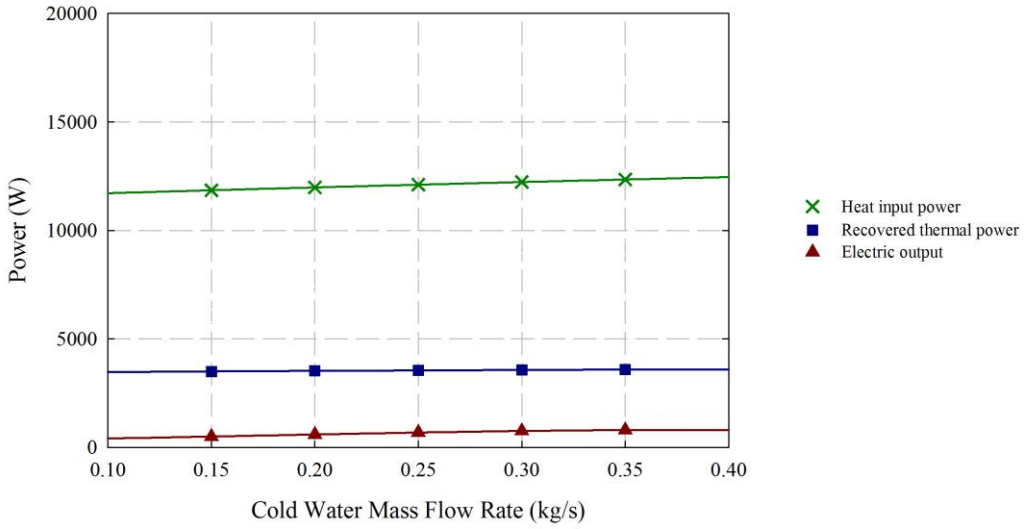


Figure 7-20 Influence of cold water mass flow rate on heat input power, recovered thermal power and electric output

In terms of the system efficiencies as shown in Figure 7-21, the thermal efficiency decreases by only 1.77% owing to the slight increases in the input heat power and the recovered thermal power. Nevertheless, a more remarkable influence is observed on the system electrical efficiency with an improvement of 51.57%. Due to the larger increment in the electric output power compared to that of the heat input power, the system CHP efficiency increases by 6.09% in accordance with the increase in the cold water mass flow rate. Similar to the findings discussed in Section 7.5.2, although a higher cold water mass flow rate is favourable for better system energy performance, it is necessary to take into account the corresponding configurations and parameters of the working fluid, cold source and condenser for designing the cold source supply condition (i.e. mass flow rate and temperature) without causing negative effect of the condensate sub-cooling.

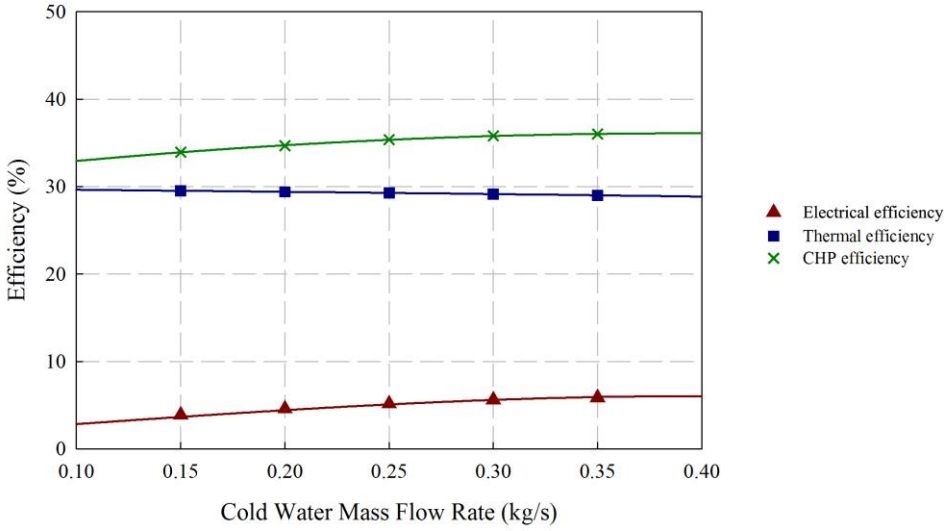


Figure 7-21 Influence of cold water mass flow rate on system electrical, thermal and CHP efficiencies

7.5.5 Scroll expander rotational speed

The scroll expander as the core power generation component of the micro trigeneration system can operate at different rotational speeds, therefore the micro trigeneration system performance differs. As previously presented in Table 5-2, the selected scroll expander has a maximum rotational speed of 3600rpm, hence in this section, the impact of the scroll expander rotational speed on the system energy performance is investigated for a range of 2800rpm to 3600rpm. As discussed previous in Section 5.5.5, by increasing the scroll expander rotational speed, the scroll expander operating pressure ratio increases and thus a higher isentropic efficiency can be obtained. It is seen from Figure 7-22, the pressure ratio increases from 2.86 to 3.28 and the isentropic efficiency improves significantly from 67.27% to 74.14% as the scroll expander rotational speed increases by 800rpm.

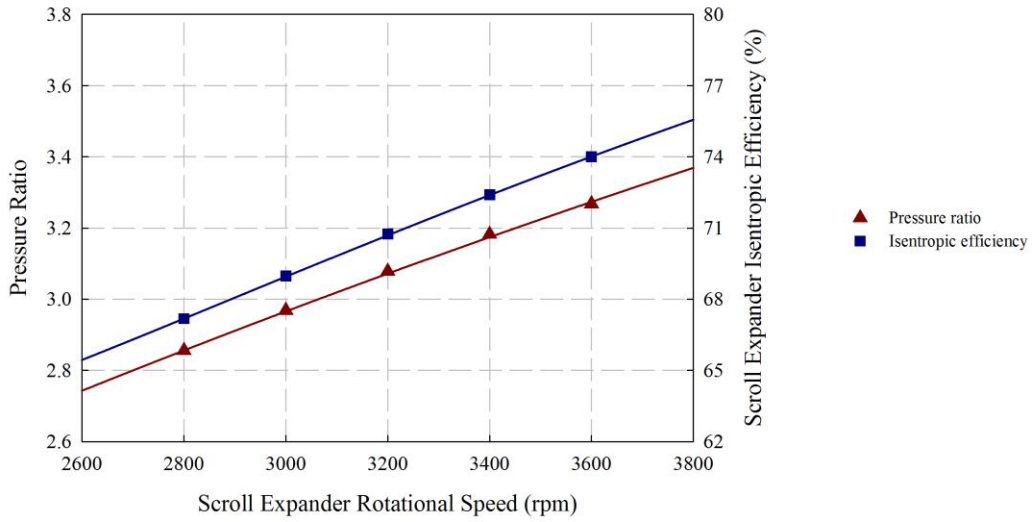


Figure 7-22 Influence of scroll expander rotational speed on scroll expander pressure ratio and isentropic efficiency

Figure 7-23 shows the influence of the scroll expander rotational speed on the heat input, electric output and recovered thermal power. The higher the rotational speed, the more energy is required for heat input and more electric power is generated owing to the larger pressure ratio. As a result, more thermal energy from the scroll expander could be utilised at a higher rotational speed. For instance, as the scroll expander rotational speed increases from 2800rpm to 3600rpm, the heat input power increases by 18.08%, the electric output power increases by 29.73% and 22.49% more thermal energy is recovered for hot water supply.

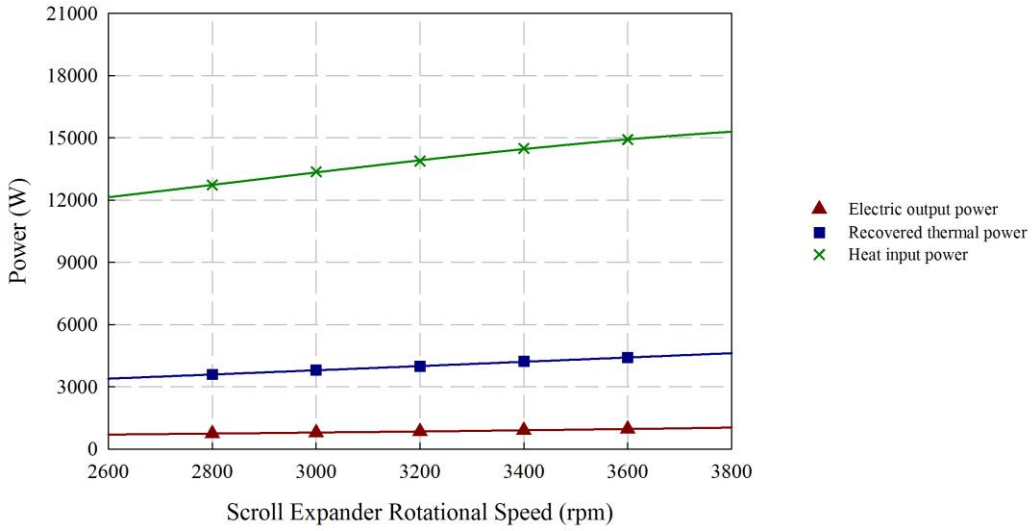


Figure 7-23 Influence of scroll expander rotational speed on heat input power, electric output power and recovered thermal power

Figure 7-24 demonstrates the positive impact of the scroll expander rotational speed on the system efficiencies. Compared to the heat input power and recovered thermal power, the electric output power is more sensitive to the scroll expander rotational speed. The electrical efficiency improves by 12.77% when the scroll expander rotational speed increases from 2800rpm to 3600rpm, whereas the improvements in the thermal and CHP efficiencies are 5.16% and 3.74% respectively. The results reveal that when electricity is the top consideration for energy supply, a significant improvement in the electric output power can be attainable by speeding up the scroll expander.

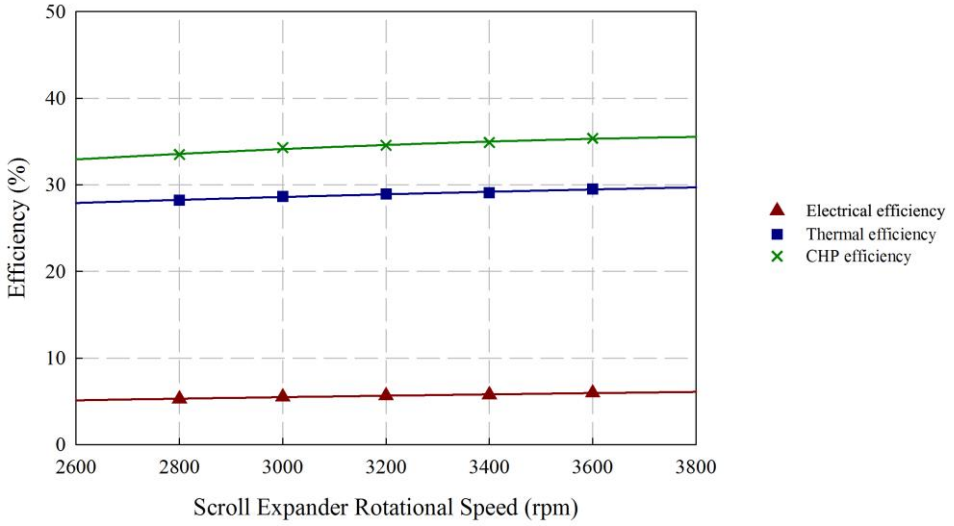


Figure 7-24 Influence of scroll expander rotational speed on system electrical, thermal and CHP efficiencies

7.5.6 Cogeneration performance summary

In this section, with the validated system model, the micro trigeneration system has been simulated to operate in CHP mode with production of electricity and hot water supply. Based on the simulation results, the effect of various operating variables on the micro trigeneration system have been discussed, including hot and cold water supply conditions as well as scroll expander rotational speed. The following findings are identified:

- The higher the hot water supply temperature, the higher the scroll expander supply temperature and the better the scroll expander performs. Consequently, more recovered thermal power can be utilised for heating demand and higher system electrical, thermal and CHP efficiencies are observed. However, the increment of the power output is attenuated gradually owing to the heat transfer mechanism in the evaporator as the degree of superheat increases.
- By increasing the hot water supply mass flow rate, a higher pressure ratio of the scroll expander is imposed and thus a higher isentropic efficiency and more

electricity output can be achieved. However, the associated impacts on the electrical, thermal and CHP efficiencies are not significant.

- Both higher hot water supply temperature and mass flow rate lead to superheating of the working fluid leaving the evaporator, and better system performance could be achieved without condensation in the scroll expander as liquid droplets would be detrimental. The degree of superheat should be optimised based on the working fluid, heat source and evaporator configurations and parameters.
- Colder water and a higher cold water mass flow rate are preferred for providing better condensation effect to the working fluid and hence better energy performance of the micro trigeneration system can be reachable. Nevertheless, the cold water supply condition should be controlled within a reasonable range in order to provide sufficient cooling effect for condensation in the micro trigeneration system and to avoid negative effect of the condensate sub-cooling at a larger temperature difference between the cold water and working fluid.
- Comparatively, the scroll expander rotational speed plays a more predominant role in the electricity output than in the system thermal and CHP efficiencies. When the scroll expander operates at a higher rotational speed, more electricity is produced and more thermal energy can be recovered for hot water supply.

Next, a parametric study of the micro trigeneration system performance is presented for operation in trigeneration mode.

7.6 Parametric study of system performance in trigeneration mode

In this section, the micro trigeneration system is simulated in CCHP mode with production of power, heating and cooling/dehumidification. The recovered thermal power from the scroll expander is distributed evenly for hot water supply and regeneration of dilute solution. Similar to the assessment presented in Section 7.5, the energy performance of the micro trigeneration system is evaluated by several defined metrics: the electricity generated, the total thermal energy recovered for heating and cooling/dehumidification demand, the electrical efficiency, COP of the MLDC and CCHP efficiency. Three operating variables are selected for the parametric study of the micro trigeneration system performance in this section: (a) hot water supply temperature in Section 7.6.1, (b) cold water supply temperature in Section 7.6.2 and (c) scroll expander rotational speed in Section 7.6.3. A similar typical operating condition has been adopted as that shown in Table 7-9 in Section 7.5, and the ranges of operating variables investigated in this parametric study are explained in the following sections.

7.6.1 Hot water supply temperature

As discussed in Section 7.5.1, the supply state of hot water from the boiler influences the scroll expander supply condition as well as the system energy performance in CHP mode. Similarly, to clarify how the hot water supply temperature influences the energy performance of the micro trigeneration system in CCHP mode, simulations are conducted for the hot water supply temperature ranging from 363K to 383K. Figure 7-25 demonstrates the temperature variations at the scroll expander inlet and outlet. Evident linear relationships are observed, as the hot water temperature increases from

363K to 383K, the scroll expander supply and exhaust temperatures increases by 5.32% and 6.03% respectively.

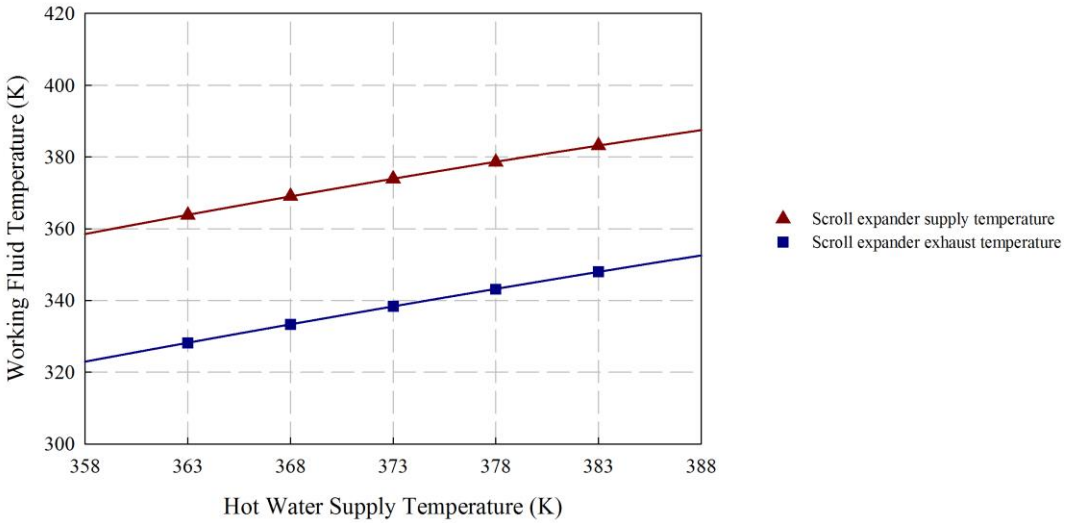


Figure 7-25 Influence of hot water supply temperature on scroll expander supply and exhaust temperatures

Based on the simulation condition, the working fluid leaves the evaporator at the superheated vapour state and the degree of superheat varies with the hot water supply temperature. It can be noted from Figure 7-26 that a higher water supply temperature contributes to a higher scroll expander operating pressure ratio and isentropic efficiency. For instance, when the hot water is supplied at a temperature of 363K, the scroll expander operates at a pressure ratio of 2.57 with an isentropic efficiency is 63.68%, whereas the operative pressure ratio reaches up to 2.86 as the hot water supply temperature increases to 383K and an isentropic efficiency of 68.92% is obtained.

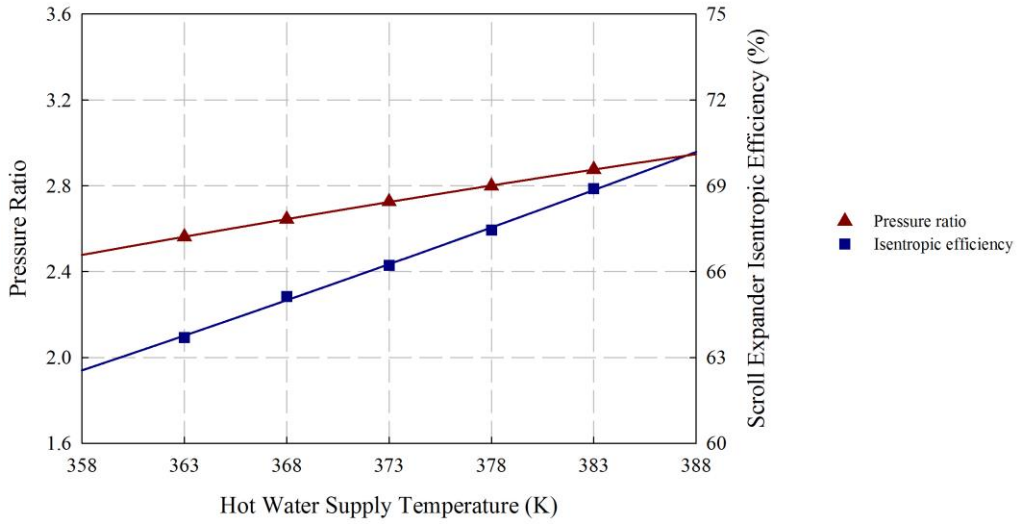


Figure 7-26 Influence of hot water supply temperature on scroll expander pressure ratio and isentropic efficiency

Figure 7-27 presents the variations in electric, recovered thermal power and heat input power with the hot water supply temperature. As a matter of course, the electric output power increases in accordance with the scroll expander operating pressure ratio. However, an apparent increase in the heat input power is notable for the hot water providing at a higher temperature. By increasing the hot water supply temperature by 20K, 10.59% more input heat power is desired. On the other hand, owing to the better scroll expander performance, more thermal power can be utilised for both heating and cooling purposes when hot water is provided at a higher temperature. For instance, over the simulated range, the electric output power increases by 14.48% and meanwhile the total recovered thermal power increases from 3238.32W to 4527.77W.

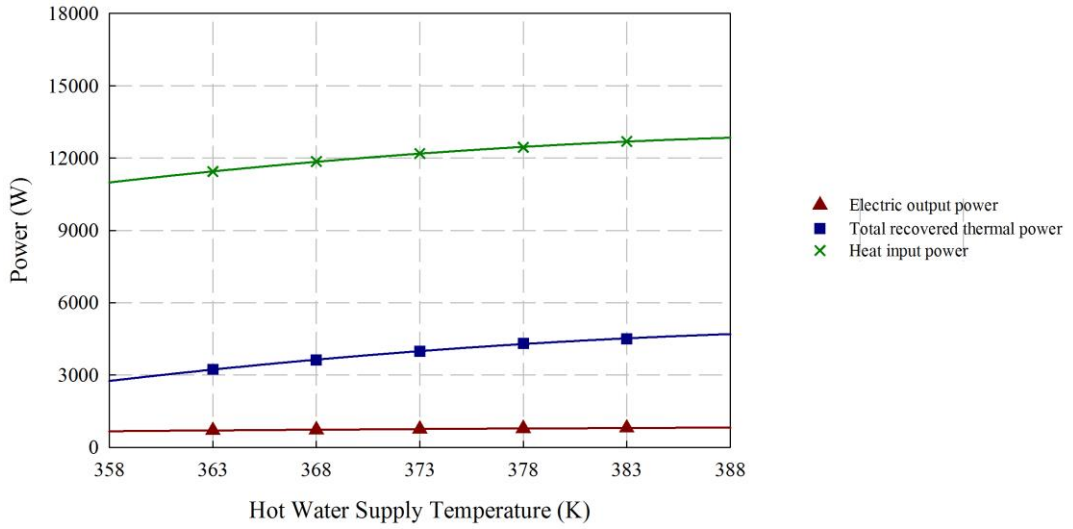


Figure 7-27 Influence of hot water supply temperature on heat input power, electric output power and total recovered thermal power

The increases in the electric, recovered thermal and heat input power with hot water supply temperature are also reflected in the system efficiencies. As demonstrated in Figure 7-28, the CCHP efficiency improves markedly while the electrical efficiency is less sensitive to the rising hot water supply temperature. Contrarily, a reduction in the COP of MLDC is noted with increasing hot water supply temperature, which is mainly attributed to the more recovered thermal power added for heating the weak solution. Over the investigated hot water supply temperature range, the electrical efficiency variation is only approximately 5.04%, while the COP reduces from 0.40 to 0.35 and CCHP efficiency improves from 33.80% to 41.55%. Moreover, their associated rates of increase gradually decrease, as the actual heat transfer in the evaporator from hot water to the working fluid may gradually become less effective when the temperature difference exceeds the departure from nucleate boiling point. This finding also is in the agreement with that presented in Section 7.5.1, that the increase of the superheated degree of the working fluid with the hot water supply temperature leads to the improvement of the electric power generation and system efficiency. But the increase range of the heat source supply temperature should be noted by considering the

working fluid and heat source, evaporator configurations and parameters, so that the evaporator instability and subsequent flow oscillation would be eliminated [274].

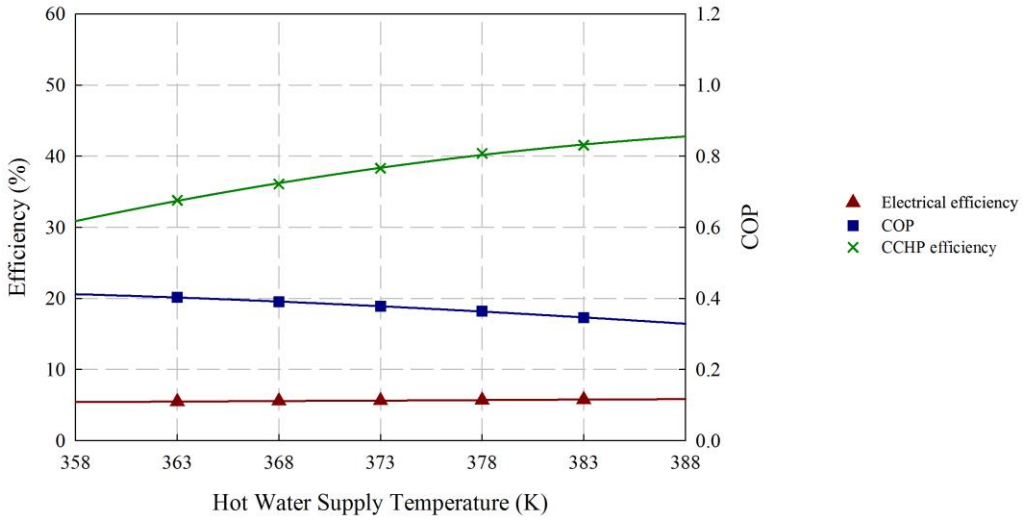


Figure 7-28 Influence of hot water supply temperature on system COP, electrical and CCHP efficiencies

7.6.2 Cold water supply temperature

On the other hand, the cold water supply temperature is another crucial operating variable for evaluation. Simulations are conducted to identify how the system performs with an increase in the cold water supply temperature from 283K to 291K and the other paratmers are constant. Figure 7-29 shows the temperature variation at the pump inlet and pressure variations at the inlet and outlet of the scroll expander. The cold water supply temperature is directly related with the working fluid temperature leaving from the condenser. It is clearly seen that the pump inlet temperature increases linearly from 287.01K to 294.96K as the cold water supply temperature rises from 283K to 291K. The evident increase in the scroll expander exhaust pressure is mainly caused by the higher condensing temperature and pressure at a higher cold water supply temperature, and therefore the scroll expander supply pressure increases so that the scroll expander runs steadily. In comparison, scroll expander exhaust pressure is more sensitive to the cold water supply temperature. For instance, as the cold supply water rises by 8K, the

scroll expander supply and exhaust pressures increase by 4.98% and 18.34% respectively.

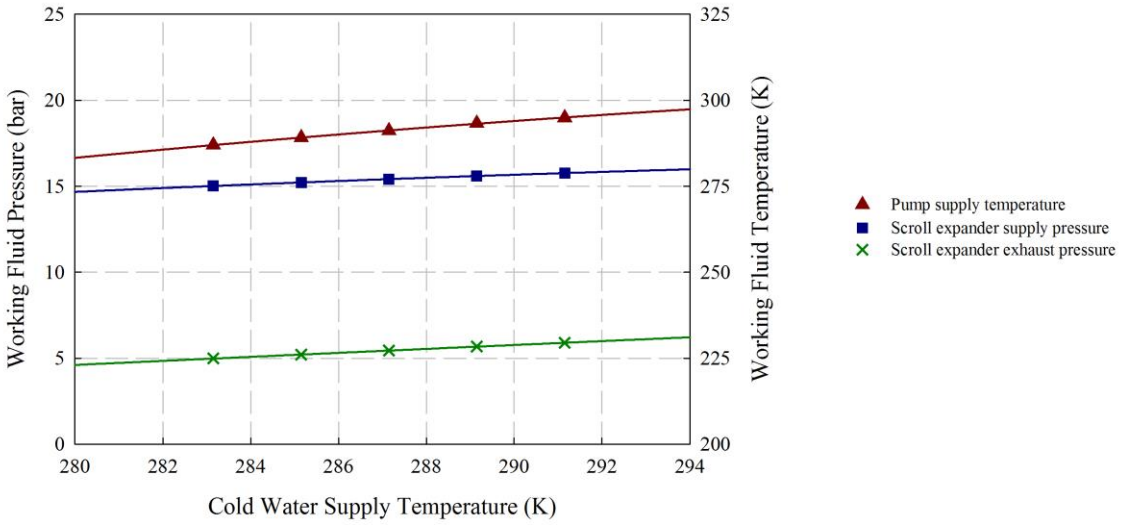


Figure 7-29 Influence of cold water supply temperature on pump supply temperature and scroll expander supply and exhaust pressures

Due to the larger increment in the exhaust pressure of the scroll expander, the scroll expander operative pressure ratio decreases in correspondence with the increasing cold water supply temperature and thus a lower isentropic efficiency is observed in Figure 7-30. The results demonstrate that at a cold water supply temperature of 283K, the scroll expander isentropic efficiency is approximately 70.91% at a pressure ratio of 3.02, while the scroll expander efficiency reduces by 5.94% and the operative pressure ratio drops to 2.68 as the cold water temperature rises by 8K.

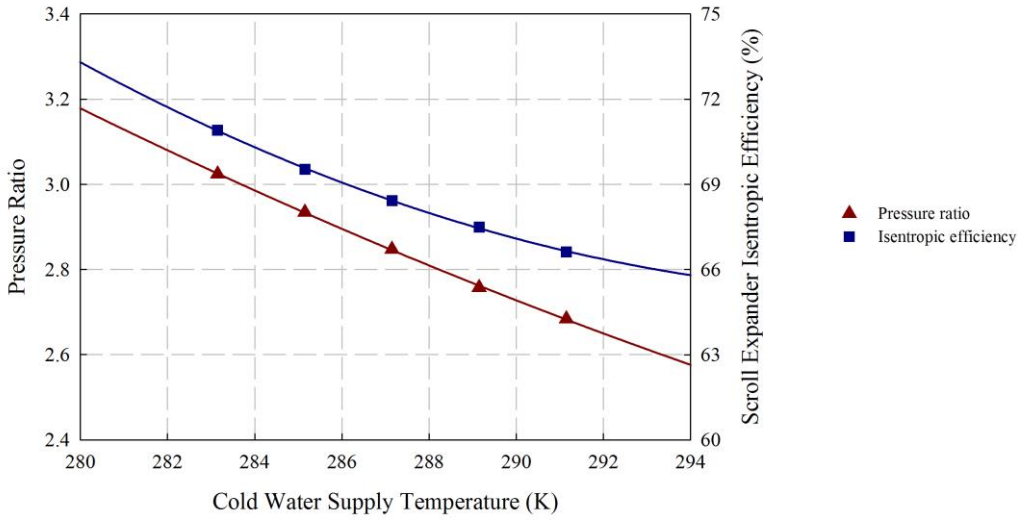


Figure 7-30 Influence of cold water supply temperature on scroll expander pressure ratio and isentropic efficiency

Additionally, it is indicated in Figure 7-31 that less heat input power is needed at a higher cold water supply temperature, which is mainly ascribed to the increasing evaporating temperature and working fluid density in the evaporator. However, the associated effect on the heat input power is not very significant. A lower scroll expander operative pressure ratio results in reduction in the power generation as well as the recovered thermal power for heating and cooling/dehumidification demands. Over the investigated temperature range of 283K to 291K, the system heat input power decreases by 1.43%, while the decreasing rates in the electric output power and total recovered thermal power are 11.84% and 9.67% respectively.

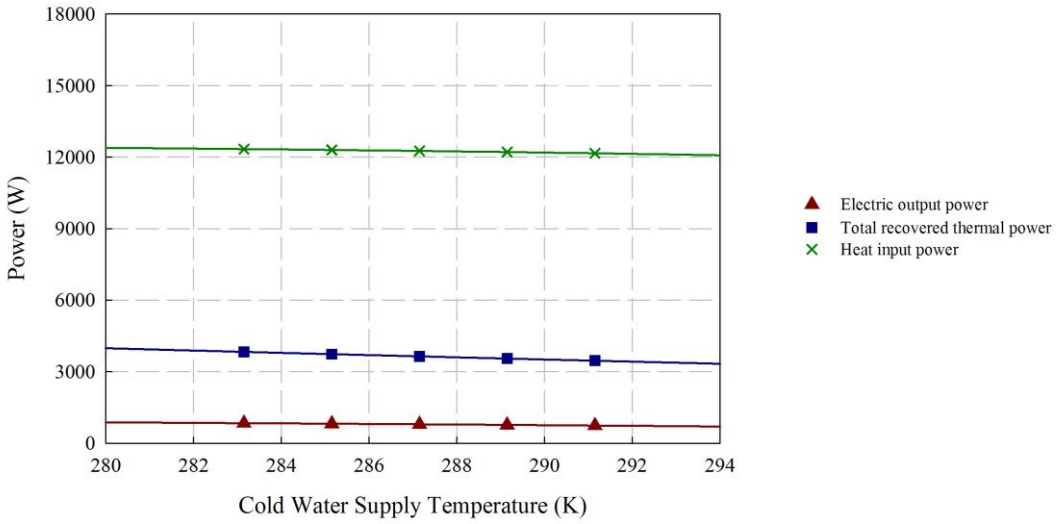


Figure 7-31 Influence of cold water supply temperature on heat input power, electric output power and total recovered thermal power

Basically, the recovered thermal power is utilised for heating the dilute solution, in other words, less heat power is added for regeneration in MLDC with the increasing cold water supply temperature. As a consequence, an improvement in the COP of MLDC is observed from Figure 7-32, because the cooling output of the MLDC changes less markedly. In contrast, more evident negative influence of a higher cold water supply water temperature on the system electrical and CCHP efficiencies are worth of noting. Over the investigated cold water supply temperature range of 283K to 291K, the CCHP efficiency and the electrical efficiency decreases by 8.91% and 6.75% respectively, while COP of MLDC increases by 3.49%. The results reveal that by considering the electrical and overall system efficiencies preferentially, cooler water should be provided to the condenser; simultaneously auxiliary measures should be implemented regarding the steady operation of the MLDC unit as previously stated in Chapter 6. Moreover, a lower cold water supply temperature causes a larger temperature difference between water and the working fluid with more heat flux obtained in the drop nucleate condensation process, and thus leads to the improvement of the electric power generation and system efficiency. Regarding the heat transfer

mechanism in the condenser, the detrimental effect of condensate sub-cooling should be concerned because less effective heat transfer in the film-wise condensation mode would take place when exceeding the critical heat flux at a higher temperature difference.

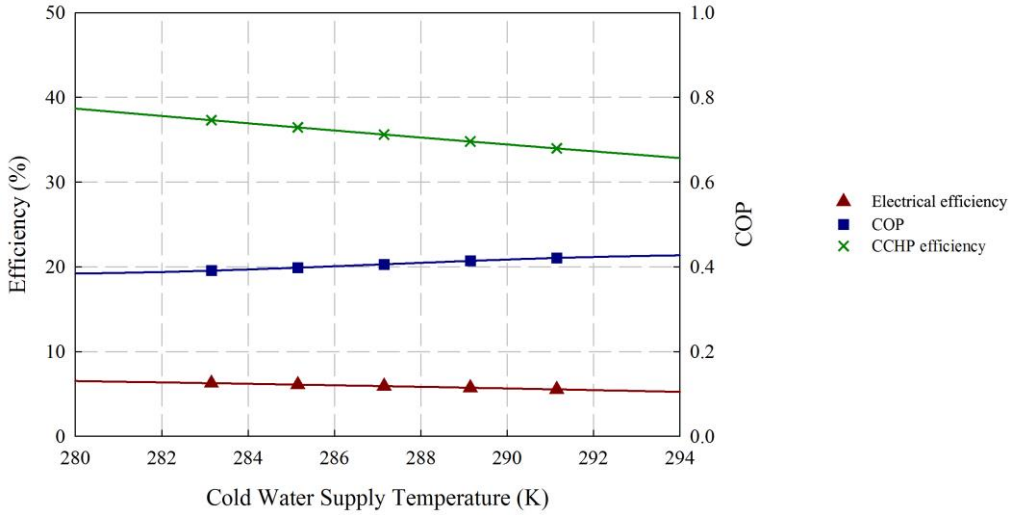


Figure 7-32 Influence of cold water supply temperature on system COP, electrical and CCHP efficiencies

7.6.3 Scroll expander rotational speed

Simulations are conducted for the micro trigeneration system operating at variable scroll expander rotational speeds. In this section, the investigated rotational speed range is from 2000rpm to 3600rpm. As discussed in Section 5.5.5 and Section 7.5.5, the higher the scroll expander rotational speed, the higher the scroll expander operating pressure ratio and isentropic efficiency can be achieved. It can be also evidently observed in Figure 7-33, the imposed pressure ratio of the scroll expander increases from 2.37 to 3.42 and the isentropic efficiency improves by 24.69% as the scroll expander rotational speed increases from 2000rpm to 3600rpm.

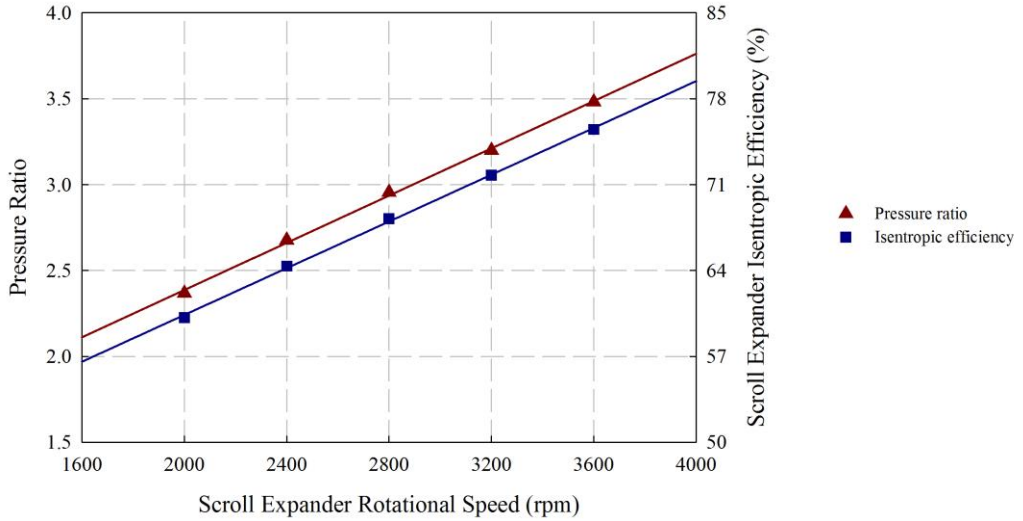


Figure 7-33 Influence of scroll expander rotational speed on scroll expander pressure ratio and isentropic efficiency

The impact of the scroll expander rotational speed on the input heat, electric output and recover thermal power is illustrated in Figure 7-34. Because of the larger pressure ratio at a higher rotational speed, more electric output power and recovered thermal energy are provided with a simultaneous increasing demand of the input heat. For instance, over the investigated rotational speed range of 2000rpm to 3600rpm, the electric output and total recovered thermal energy increase by 452.72W and 1455.81W respectively, while the heat input power increases by 39.78%.

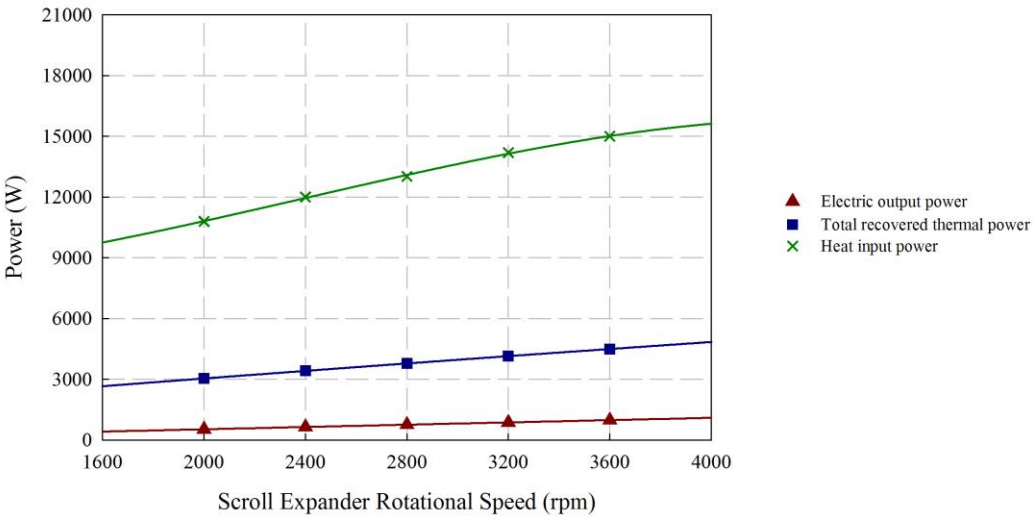


Figure 7-34 Influence of scroll expander rotational speed on heat input power, electric output power and total recovered thermal power

Figure 7-35 shows the noticeable positive impact of the scroll expander rotational speed on the system electrical and CCHP efficiencies, which are mainly attributed to the larger increase in the electric output power. The improvement in the system electrical efficiency is approximately 27.55% as the scroll expander rotational speed increases from 2000rpm to 3600rpm, while the rate of increase for the CCHP efficiency is about 10.51%. On the other hand, the COP of MLDC decreases with the rotational speed of the scroll expander, because the significant increment in the recovered exhaust heat from the scroll expander is utilised for heating the dilute solution. The results demonstrate that more electric output power would be obtained by increasing the scroll expander rotational speed and practically measures should be taken to ensure the mass balance between the membrane-based dehumidifier and regenerator for steady operation of the MLDC loop as more heat input power would be available for regeneration.

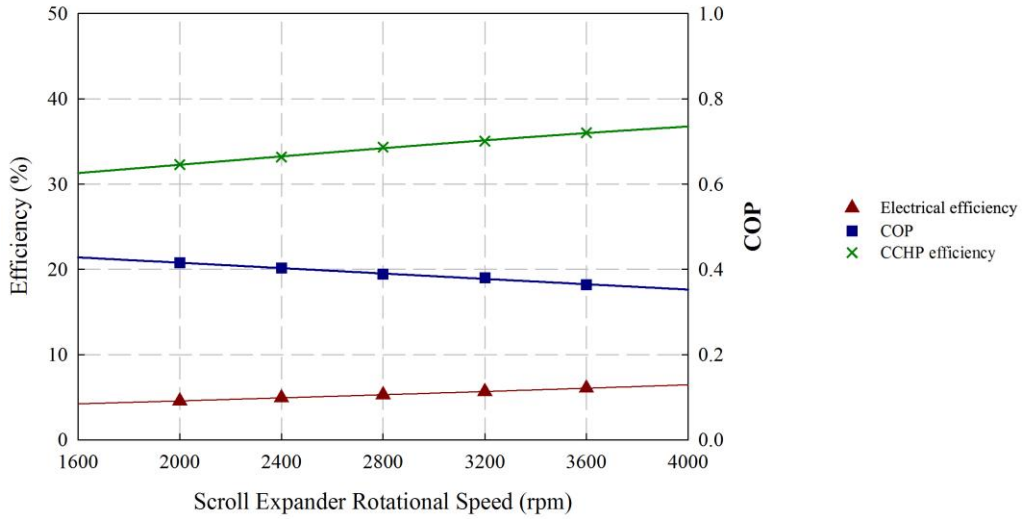


Figure 7-35 Influence of scroll expander rotational speed on system COP, electrical and CCHP efficiencies

7.6.4 Trigeneration performance summary

In this section, the effect of the hot supply temperature, cold water supply temperature and scroll expander rotational speed on the system energy performance have been investigated with the micro trigeneration system operating in CCHP mode. Based on the simulation results, following observations are summarised:

- Both the electric output power and total recovered thermal power increase in accordance with the hot water supply temperature. A higher hot water temperature leads to superheating of the working fluid and thus higher system electrical and CCHP efficiencies are attainable, whereas more heat input power is delivered into the micro trigeneration system.
- Comparatively, the system electrical efficiency is less sensitive to the hot water supply temperature compared with COP of MLDC and CCHP efficiency.
- In contrast, a higher cold water supply temperature causes worse system energy performance. Although less heat input power is consumed for heating the working fluid at a lower cold water supply temperature, more significant reduction in the electricity generation and recovered thermal power are notable. Consequently, the system electrical and CCHP efficiencies decrease in correspondence with the cold water supply temperature.
- Both higher degree of superheat and lower cold water supply temperature causes larger temperature difference between water and working fluid, however the improvement in the energy performance of the micro trigeneration system would be limited because of the heat transfer mechanism in the evaporator and condenser.
- The rotational speed of the scroll expander has evident positive impacts on the electric output power, the system electrical and CCHP efficiencies.

- COP of the MLDC is more sensitive to a variation of the recovered thermal power that is distributed for regeneration of dilute solution. To ensure better system energy performance as well as steady MLDC performance, thereupon additional measures regarding the operating variables of the MLDC should be considered.

Next, Section 7.7 summarises the chapter findings and provides implications of the micro trigeneration system operation based on the parametric studies.

7.7 Summary

In this chapter, detailed component modelling of the micro trigeneration system has been firstly described and a comprehensive model of the micro trigeneration system has been established with an integration of scroll-based ORC and MLDC. The system model has been validated with experimental data. With the validated system model, parametric studies have been conducted to investigate the impact of various operating variables on the micro trigeneration system energy performance. The simulation results have demonstrated the feasibility of the proposed micro trigeneration system and the system energy performance is influenced by operating variables in both CHP and CCHP modes. The following conclusions are drawn:

- The pairing of scroll-based ORC and MLDC is a viable option for a micro trigeneration system. The micro trigeneration system demonstrates considerable higher overall system efficiency in CHP and CCHP modes, compared to the ORC-based single power generation mode.
- Simulations of the micro trigeneration system show an overall system efficiency of 38.96% in CHP mode and 41.23% in CCHP mode. The inclusion

of MLDC contributes to an efficiency increase of approximately 35.49% compared to the ORC-based electrical generation mode.

- More precisely, a higher overall system efficiency can be realised by allowing more recovered thermal power to the MLDC unit for dealing with cooling/dehumidification demand in the micro trigeneration system.
- For the micro trigeneration operating in CHP and CCHP modes, a higher hot water supply temperature is preferred to heat up the working fluid, because of the better scroll expander performance with more electric output and recovered thermal power for heating and cooling/dehumidification demands.
- Though more heat input power from the boiler is attributed to a higher hot water supply temperature, higher superheated degree of the working fluid is reached with more remarkable improvements in the system electrical, thermal CHP and CCHP efficiencies. It is noteworthy that the heat transfer mechanism in the evaporator should be considered when magnifying the temperature difference between the working fluid and hot water.
- On the contrary, an increase of the cold water supply temperature has negative influence on the scroll expander performance as well the trigeneration system energy performance in both CHP and CCHP modes.
- The micro trigeneration system energy performance is not sensitive to the hot water or cold water mass flow rate. However, the simulation results indicate that the mass flow rates of the hot and cold water should be controlled rationally in order to provide sufficient heat input and cooling power for evaporation and condensation without any detrimental effects of evaporator instability and condensate sub-cooling. This is because that the heat transfer

mechanism in the evaporator and condenser is influenced by the temperature difference between the working fluid and water,

- When the scroll expander operates at a higher rotational speed, better micro trigeneration system energy performance can be achieved with more electric output and recovered thermal power for hot water supply and heating dilute solution.
- When the micro trigeneration system is operating in CCHP mode, the variation in the recovered thermal power distributed for the MLDC unit play a predominant role in the COP of MLDC. As a result, the operating variables of the MLDC should be adjusted correspondingly to ensure better system energy performance as well as steady operation of MLDC with mass balance between the dehumidifier and regenerator.

On the basis of the findings, following recommendations for practical operation of the micro trigeneration system can be summarised:

- The micro trigeneration system should enable operations in various modes to meet diverse energy demands, like CHP/CCP (i.e. with productions of power and heating/cooling) and CCHP (i.e. with productions of power, heating and cooling). More specifically, when the micro trigeneration system operates to provide electricity, heating and cooling demands, the amount of the recovered thermal power should be distributed appropriately to meet the heat and cooling demands respectively as well as for a higher overall system efficiency.
- Though a higher heat source supply temperature is favourable for superheating the refrigerant in the ORC, the temperature difference between the heat source and working fluid should not be provided at a too high value to eliminate less effective heat transfer and negative effect of evaporator instability.

- Cold water supply temperature is another important operating variable influencing the micro trigeneration system energy performance. Better system performance is attainable with a lower cold water supply temperature for condensation of the refrigerant in the ORC. But less thermal energy would be recovered for heating the dilute solution, therefore measures should be taken regarding to the operating variables of MLDC to ensure sufficient regeneration performance and mass balance between the dehumidifier and regenerator.
- Both hot and cold water should be supplied at adequate mass flow rates to provide sufficient heat transfer for the refrigerant in the evaporator and condenser without causing less effective heat transfer in the evaporator and condenser as well as system instabilities.
- For operation with a priority of electricity supply, the scroll expander should operate at high rotational speed but not beyond its maximum capacity.
- Renewable energy or low-grade heat sources can be integrated into the micro trigeneration system to replace the electric boiler as the primary energy source to power the scroll-based ORC.

The work presented in this chapter has demonstrated the feasibility of the micro trigeneration system combining scroll-based ORC and MLDC through semi-empirical analysis. Furthermore, this chapter has provided a contribution to knowledge of modelling and evaluating the novel ORC and MLDC-based micro trigeneration system.

Chapter 8: Conclusions and Recommendations for Future Work

8.1 Introduction

The micro trigeneration system offers significant technical, environmental and economic benefits compared to the conventional separated power generation and cogeneration systems. The main aim of this thesis has been to design, develop and evaluate a novel micro trigeneration system combining scroll-based ORC and MLDC technologies. Also the feasibility of CLFR functioning as the primary energy source for the micro trigeneration system has been investigated. In this thesis, both theoretical and experimental methods have been adopted for a rigorous and analytical piece of work. Based on the simulation and experimental results, the thesis has proved the design concept of the micro trigeneration with a pairing of scroll-based ORC and MLDC, which thereby provides an evident contribution to new knowledge in the field of the micro trigeneration technology. To produce a coherent conclusion of this thesis, this chapter is split into two sections: Section 8.2 comprehensively summarises major findings from each chapter by revisiting the thesis aim and objectives and critically examines the degree to which the objectives have been fulfilled and Section 8.3 discusses limitations of this study and provides recommendations for future work.

8.2 Major findings

The preceding seven chapters have sought to achieve the main aim of the thesis by accomplishing the thesis objectives as presented in Section 1.3. In this section, main findings of this thesis are presented and the degree to which these objectives have been completed are discussed.

(1) The first objective "*Literature review and highlight the current gap in the existing literature of the micro trigeneration system, particularly for the combination of concentrating solar collectors, ORC and liquid desiccant cooling*" has been achieved in Chapter 2. An extensive review of literature has highlighted the gap of development and a theoretical and experimental evaluation of a novel micro trigeneration system with scroll-based ORC and MLDC. A number of theoretical and experimental studies regarding the micro trigeneration system have focused on integration of mature technologies, like diesel engine, micro gas engine, absorption and adsorption chillers. In addition, the potential of utilising CLFR as the primary energy source for power generation systems has not been widely explored yet. Based on the literature review, the feasibilities of scroll-based ORC and MLDC for the trigeneration system have been already examined respectively, whereas no previous work has been reported on a micro trigeneration system incorporating with CLFR, ORC and MLDC.

(2) The second objective "*Numerical and experimental evaluation of CLFR under the local weather conditions and investigate the feasibility of integrating into the micro trigeneration system*" has been accomplished in Chapter 4 through both geometrical modelling and experimental work. The CLFR system with polar orientation is viable to effectively concentrate the sunlight onto the receivers and subsequently the absorbed heat can be utilised as the primary energy supply for power generation systems, for example power the scroll-based ORC in the proposed micro trigeneration system. Compared to the LFR and CLFR-complete systems, the CLFR-hybrid system has the highest concentration and ground utilisation ratios. The experimental results

demonstrate that for the CLFR-hybrid system with 50 pieces of flat mirror elements, a solar field width of 2100mm and a focal length of 1500mm, geometrical concentration of 15.14 and ground utilisation ratio of 0.95 are attainable. Based on the parametric study with numerical modelling, to achieve an optimum optical performance of the polar-orientated CLFR-hybrid system with flat receivers, several design parameters should be taken into account: (a) ground usage; (b) mirror arrangement with adequate proportion of mirrors in the central alternating array and common tilting array; (c) focal length and (d) horizontally orientated flat receiver. The work presented in Chapter 4 has contributed to a progress to the field of the concentrated solar power, more precisely to the knowledge of the optical design of the CLFR system with polar orientation.

(3) The third objective "*Performance evaluation based on simulation and experimental investigation of the scroll-based ORC system for an effective integration of the micro trigeneration system*" has been completed in Chapter 5. Both the simulation and experimental results demonstrate that the micro scroll-based ORC system can effectively produce electric output and under the investigated operating conditions the exhaust heat temperature typically higher than 65°C, which thus confirms the feasibility of the scroll-based ORC acting as a prime mover in the micro trigeneration system. A good agreement has been identified between the semi-empirical model of the scroll expander and experimental data. Based on the analysis of simulation results, better scroll expander performance can be achieved by increasing the working fluid supply pressure and rotational speed of the scroll expander. As only few experimental studies concerning the impact of the couple electrical resistive load to the scroll

expander-generator unit on the ORC system performance, the experimental work in Chapter 5 has clarified an evident decrease in the electric output with the resistive load when the scroll expander operates at a constant rotational speed. The negative influence of under and over-expansion operations on the scroll expander and ORC system performance have been observed both theoretically and experimentally. Results imply that an optimum scroll expander imposed pressure ratio exists which matches with the built-in volume ratio for maximum electricity production. Moreover, the optimum pressure ratio decreases significantly with the resistive load. Under the tested operating condition, the ORC system produces the maximum electric output of 564.5W at the scroll expander optimum pressure ratio of 3.6 and rotational speed of 3450rpm, with associated isentropic and volumetric efficiencies of the scroll expander are 78% and 83% respectively. The investigations in Chapter 5 have provided a contribution to the knowledge of modelling and testing of the scroll-based ORC system.

(4) The fourth objective "*Performance evaluation based on experimental data of the MLDC system for effectively integrating into the micro trigeneration system*" has been achieved in Chapter 6. The experimental results proved the feasibility of the MLDC system with $CaCl_2$ as the liquid desiccant for the hot and humid climate, which shows good dehumidification performance and sufficient cooling output without the carryover problem of liquid desiccant droplets. Under the tested operating condition with an outdoor temperature of 34°C, the MLDC system is capable of providing supply air at a temperature of 20.4°C with dehumidification effectiveness of 0.3 and system COP of 0.7. On the other hand, sufficient regeneration of $CaCl_2$ solution can be attainable with

low-grade heat sources in a supply temperature range of 55°C to 80°C, which would be also realised by the exhaust heat of the scroll expander. Thus, the MLDC system is feasible to pair with the scroll-based ORC system forming an effective integration for the micro trigeneration system. Series of experimental tests have been conducted to establish the effect of various operating variables on the dehumidification, regeneration and overall system performances of the MLDC system respectively. Based on the experimental investigations, the indicators for better MLDC system performance can be summarised as: (a) the system mass balance between the dehumidifier and regenerator should be maintained for system steady operation; (b) inlet air flow rates for the dehumidifier and regenerator should be adjusted based on the local weather condition as the inlet air condition (i.e. inlet air temperature and humidity level) significantly influences the system dehumidification and regeneration performance; (c) the solution concentration should be determined properly as the higher the concentration, the better the dehumidification performance but with less regeneration capability and potential crystallization risks; (d) the heat source supply temperature should be controlled within an appropriate range to avoid excessive thermal input power for solution regeneration and (e) the cold water supply temperature should be lower for better system performance, and desired variation in supply air temperature can be achieved by varying the cold water supply temperature of the evaporative cooler.

(5) The fifth objective "*Development of a comprehensive system model to demonstrate the feasibility of integrating scroll-based ORC and MLDC into the micro trigeneration system and to investigate effect of a wide range of operating variables on the system performance*" has been realised in Chapter

7. Through semi-empirical modelling, Chapter 7 has successfully achieved the objective of integrating scroll-based ORC and MLDC into a complete micro trigeneration system, and the system performance has been assessed on the energetic basis. The simulation results demonstrate that the pairing of scroll-based ORC and MLDC is viable for a micro trigeneration system. With the inclusion of MLDC, the improvement of 35.49% in the overall efficiency is achieved with comparison to the ORC-based separate power generation. The micro trigeneration system enables different operating modes by adjusting the amount of recovered thermal power for heating and cooling/dehumidification demands in accordance with the end-user's energy demand. An optimum distribution of the recovered thermal power facilitates effective micro trigeneration integration and operation. Based on the simulation data for the micro trigeneration system, an overall system efficiency of 38.96% is obtained in CHP mode and 41.23% in CCHP mode. Practically, the micro trigeneration system is capable of running with low-grade heat sources, but the heat source supply temperature and flow rate should be provided reasonably in order to avoid potential excessive energy. Contrarily, the higher cold water supply temperature for condensing the working fluid negatively affects both the scroll expander and overall trigeneration system energy performances in both CHP and CCHP modes. However, sufficient regeneration performance of the MLDC system should be guaranteed as less thermal energy can be recovered when cooler water is supplied to the micro trigeneration system. The work presented in Chapter 7 has provided a contribution to knowledge of modelling of the novel ORC and MLDC-based micro trigeneration system.

Overall, the thesis main aim has been successfully achieved through accomplishment of the thesis objectives and the highlighted research gap has been addressed. The micro trigeneration system appears attractive for decentralized energy supply, especially for places in the hot and humid climate, where electrical grid connection is unavailable and dehumidification and cooling are of necessity. Although the proposed design concept of the novel micro trigeneration system with effective technological pairing of scroll-based ORC and MLDC has been proved at a micro scale, the system can be scalable. Low-grade energy sources can be feasible for powering the developed system, for example industrial and automobile waste heat sources, which thereby indicates that the system applications may not be restricted only to the domestic sector. Besides integrating to the field of trigeneration, the explored technologies of CLFR, scroll-based ORC and MLDC demonstrate potential for low carbon sustainable energy conversion, energy efficient power generation and effective air conditioning respectively. Therefore it could be concluded that this thesis not only provides an evident contribution to new knowledge of the micro trigeneration system but also to the field of solar energy conversion, distributed power generation and air conditioning.

8.3 Limitations and recommendations for future work

8.3.1 Limitations of the study

Although the research aim has been reached, some limitations to this thesis have been identified. Firstly, the feasibility evaluation of the micro trigeneration system in this study has mainly focused on the system energy performance, while due to the time constraints, other aspects like exergy, economy, environment and optimisation of the micro trigeneration system have not been considered, which would be realised for examining and optimising the system comprehensively in the future. Also the system

model has been established mainly based on the semi-empirical method, which would be improved for more detailed and precise modelling of the trigeneration system. For instance, the heat exchanger modelling has been implemented using the effectiveness-NTU approach, while it may be not precise enough to simulate a two-phase heat exchanger since mass transfer in the phase change results in variable fluid properties, flow rates as well as heat transfer coefficients.

Secondly, since there are few prior studies for feasibility study of the CLFR system, only the optical performance of the CLFR system has been evaluated in this study, while an assessment of the thermodynamic behaviour has been not included. Also, regarding the MLDC system, only experimental tests have been carried out to investigate the MLDC system performance, a detailed model of the MLDC system has not been developed due to limitations in time and complexity. Hence, future work would concern the comprehensive feasibility study of a micro trigeneration system combining CLFR, scroll-based ORC and MLDC through both modelling and experimental work.

Thirdly, owing to limitations in time, finance and laboratory space, the experimental tests have been conducted for each components (i.e. CLFR, ORC and MLDC) respectively. The measuring instruments have not been calibrated rigorously depending on the measuring range used in the investigation, which could influence the accuracy of the measurement data collected from experimental work. On the other hand, for the scroll-based ORC and MLDC, only one working fluid (i.e. R134a in ORC) and one liquid desiccant (i.e. $CaCl_2$ in MLDC) have been taken into account for testing. Thus other alternatives for efficient operation of ORC and MLDC would be examined in the future. In addition, all the experimental tests were carried out in a laboratory

setting, which could not reflect the system application in the real-time situation precisely.

8.3.2 Recommendations for future work

Recommendations for the future work of the micro trigeneration system are presented as follows overcome limitations to this research.

- For a more comprehensive performance evaluation, assessments regarding perspectives of energy, exergy, economy and environment need to discuss for the system combining CLFR, scroll-based ORC and MLDC through a more detailed numerical modelling. For example, future modelling work would focus on the thermodynamic behaviour of the CLFR as the primary energy source, the detailed dynamic process of the scroll expander and the conjugate heat and mass transfers for the membrane-based dehumidifier and regenerator.
- The work presented in Chapter 6 has demonstrated the feasibility of MLDC system with $CaCl_2$ for dehumidification and cooling. Future work can be conducted for other liquid desiccants to facilitate more effective MLDC performance.
- A complete micro trigeneration system would be constructed for future work, so that more extensive tests can be conducted to further investigate the overall system performance under a wider range of operating conditions.
- The diverse end-user's energy demand requires different operating strategies for a micro trigeneration system. As a result, future work would be conducted for optimizing the micro trigeneration system based on different operating strategies through a multi-objective procedure.

- Future work would consider applying the developed micro trigeneration system to a practical operating setting, for example in a domestic home or office building which simultaneously requiring electricity, heating and dehumidification/cooling.

References

[1] O. Ibrahim, F. Fardoun, R. Younes, H. Louahlia-Gualous, and M. Ghandour, "Multi-variable optimization for future electricity-plan scenarios in Lebanon," *Energy Policy*, vol. 58, pp. 49-56, 7// 2013.

[2] B. Petroleum. (2016, 24/05). *BP Energy Outlook*. Available: https://www.bp.com/content/dam/bp/pdf/energy-economics/energy-outlook-2016/bp-energy-outlook-2016.pdf

[3] B. Petroleum. (2015, 24/05). *Statistical Review of World Energy* Available: https://www.bp.com/content/dam/bp/pdf/energy-economics/statistical-review-2015/bp-statistical-review-of-world-energy-2015-full-report.pdf

[4] H. Al Moussawi, F. Fardoun, and H. Louahlia-Gualous, "Review of tri-generation technologies: Design evaluation, optimization, decision-making, and selection approach," *Energy Conversion and Management*, vol. 120, pp. 157-196, 2016.

[5] M. Jradi and S. Riffat, "Tri-generation systems: Energy policies, prime movers, cooling technologies, configurations and operation strategies," *Renewable and Sustainable Energy Reviews*, vol. 32, pp. 396-415, 2014.

[6] DECC and DUKES. (2014). *Chapter 7:Combined heat and power*. Available: https://www.gov.uk/government/uploads/system/uploads/attachment_data/file/337711/chapter_7.pdf

[7] M. C. Ekwonu, S. Perry, and E. A. Oyedoh, "Modelling of gas engines integrated with organic Rankine cycle and Rankine cycle," *Advanced Chemical Engineering Research*, vol. 3, pp. 44-47, 2014.

[8] M. Liu, Y. Shi, and F. Fang, "Combined cooling, heating and power systems: A survey," *Renewable and Sustainable Energy Reviews,* vol. 35, pp. 1-22, 7// 2014.

[9] M. Badami, F. Camillieri, A. Portoraro, and E. Vigliani, "Energetic and economic assessment of cogeneration plants: A comparative design and experimental condition study," *Energy,* vol. 71, pp. 255-262, 2014.

[10] "Directive 2004/8/EC of the European Parliament and of the Council," *Official Journal of the European Union 2004,* vol. L52, pp. 50-60, 2004.

[11] T. Elmer, M. Worall, S. Wu, and S. Riffat, "Assessment of a novel solid oxide fuel cell tri-generation system for building applications," *Energy Conversion and Management,* vol. 124, pp. 29-41, 2016.

[12] G. Chicco and P. Mancarella, "From Cogeneration to Trigeneration: Profitable alternatives in a competitive market," *IEEE Transactions on Energy Conversion,* vol. 21, pp. 265-272, 2006.

[13] T. Kerr, "Combined heat & power and emissions trading: Options for policy makers," International Energy Agency (IEA), Paris2008.

[14] J. Hernández-Santoyo and A. Sánchez-Cifuentes, "Trigeneration: an alternative for energy savings," *Applied Energy,* vol. 76, pp. 219-227, 2003.

[15] D. Sonar, S. L. Soni, and D. Sharma, "Micro-trigeneration for energy sustainability: Technologies, tools and trends," *Applied Thermal Engineering,* vol. 71, pp. 790-796, 2014.

[16] T. Elmer, *A Novel SOFC Tri-generation System for Building Applications*: Springer International Publishing, 2016.

[17] T. von Wirth, L. Gislason, and R. Seidl, "Distributed energy systems on a neighborhood scale: Reviewing drivers of and barriers to social acceptance," *Renewable and Sustainable Energy Reviews,* 2017/10/15/ 2017.

[18] C. A. Mertler and C. M. Charles, *Introduction to educational research*. Boston, Mass.: Allyn & bacon, 2005.

[19] M. Churton, *Theory and method / Mel Churton and Anne Brown*. Basingstoke [England] ; New York: Palgrave Macmillan, 2010.

[20] D. W. Wu and R. Z. Wang, "Combined cooling, heating and power: A review," *Progress in Energy and Combustion Science,* vol. 32, pp. 459-495, 2006.

[21] E. Cardona and A. Piacentino, "A methodology for sizing a trigeneration plant in mediterranean areas," *Applied Thermal Engineering,* vol. 23, pp. 1665-1680, 2003.

[22] C. Oland, *Guide to combined heat and power systems for boiler owners and operators*. United States: Department of Energy, 2004.

[23] M. Ebrahimi and A. Keshavarz, "Climate impact on the prime mover size and design of a CCHP system for the residential building," *Energy and Buildings,* vol. 54, pp. 283-289, 2012.

[24] F. A. Al-Sulaiman, F. Hamdullahpur, and I. Dincer, "Trigeneration: A comprehensive review based on prime movers," *International Journal of Energy Research,* vol. 35, pp. 233-258, 2011.

[25] B. Yan, S. Xue, Y. Li, J. Duan, and M. Zeng, "Gas-fired combined cooling, heating and power (CCHP) in Beijing: A techno-economic analysis," *Renewable and Sustainable Energy Reviews,* vol. 63, pp. 118-131, 2016.

[26] X. Song, L. Liu, T. Zhu, T. Zhang, and Z. Wu, "Comparative analysis on operation strategies of CCHP system with cool thermal storage for a data center," *Applied Thermal Engineering*, vol. 108, pp. 680-688, 2016.

[27] R. P. Marques, D. Hacon, A. Tessarollo, and J. A. R. Parise, "Thermodynamic analysis of tri-generation systems taking into account refrigeration, heating and electricity load demands," *Energy and Buildings*, vol. 42, pp. 2323-2330, 2010.

[28] W. Liu, G. Chen, B. Yan, Z. Zhou, H. Du, and J. Zuo, "Hourly operation strategy of a CCHP system with GSHP and thermal energy storage (TES) under variable loads: A case study," *Energy and Buildings*, vol. 93, pp. 143-153, 2015.

[29] X. Zhao, L. Fu, F. Li, and H. Liu, "Design and operation of a tri-generation system for a station in China," *Energy Conversion and Management*, vol. 80, pp. 391-397, 2014.

[30] S. Hands, S. Sethuvenkatraman, M. Peristy, D. Rowe, and S. White, "Performance analysis & energy benefits of a desiccant based solar assisted trigeneration system in a building," *Renewable Energy*, vol. 85, pp. 865-879, 2016.

[31] P. Hanafizadeh, J. Eshraghi, P. Ahmadi, and A. Sattari, "Evaluation and sizing of a CCHP system for a commercial and office buildings," *Journal of Building Engineering*, vol. 5, pp. 67-78, 2016.

[32] K. F. Fong and C. K. Lee, "Performance analysis of internal-combustion-engine primed trigeneration systems for use in high-rise office buildings in Hong Kong," *Applied Energy*, vol. 160, pp. 793-801, 2015.

[33] Y. T. Ge, S. A. Tassou, I. Chaer, and N. Suguartha, "Performance evaluation of a tri-generation system with simulation and experiment," *Applied Energy*, vol. 86, pp. 2317-2326, 2009.

[34] M. Shelar and G. N. Kulkarni, "Thermodynamic and economic analysis of diesel engine based trigeneration systems for an Indian hotel," *Sustainable Energy Technologies and Assessments,* vol. 13, pp. 60-67, 2016.

[35] F. Basrawi, T. Yamada, and S. y. Obara, "Economic and environmental based operation strategies of a hybrid photovoltaic–microgas turbine trigeneration system," *Applied Energy,* vol. 121, pp. 174-183, 2014.

[36] F. Immovilli, A. Bellini, C. Bianchini, and G. Franceschini, "Solar Trigeneration for Residential Applications, a Feasible Alternative to Traditional Micro-Cogeneration and Trigeneration Plants," in *Industry Applications Society Annual Meeting, 2008. IAS '08. IEEE*, 2008, pp. 1-8.

[37] M. Ebrahimi and A. Keshavarz, "Sizing the prime mover of a residential micro-combined cooling heating and power (CCHP) system by multi-criteria sizing method for different climates," *Energy*, vol. 54, pp. 291-301, 2013.

[38] Y. Wang, Y. Huang, E. Chiremba, A. P. Roskilly, N. Hewitt, Y. Ding, *et al.*, "An investigation of a household size trigeneration running with hydrogen," *Applied Energy*, vol. 88, pp. 2176-2182, 2011.

[39] Y. Wang, Y. Shi, M. Ni, and N. Cai, "A micro tri-generation system based on direct flame fuel cells for residential applications," *International Journal of Hydrogen Energy*, vol. 39, pp. 5996-6005, 2014.

[40] M. A. Ehyaei, P. Ahmadi, F. Atabi, M. R. Heibati, and M. Khorshidvand, "Feasibility study of applying internal combustion engines in residential buildings by exergy, economic and environmental analysis," *Energy and Buildings*, vol. 55, pp. 405-413, 2012.

[41] H. Perez-Blanco and E. Vineyard, "Feasibility and operating costs of an air cycle for CCHP in a fast food restaurant," *Applied Thermal Engineering,* vol. 104, pp. 818-828, 2016.

[42] A. I. Palmero-Marrero and A. C. Oliveira, "Performance simulation of a solar-assisted micro-tri-generation system: hotel case study," *International Journal of Low-Carbon Technologies,* vol. 6, pp. 309-317, 2011.

[43] S. A. Tassou, I. Chaer, N. Sugiartha, Y. T. Ge, and D. Marriott, "Application of tri-generation systems to the food retail industry," *Energy Conversion and Management,* vol. 48, pp. 2988-2995, 2007.

[44] M. Rady, A. Amin, and M. Ahmed, "Conceptual Design of Small Scale Multi-Generation Concentrated Solar Plant for a Medical Center in Egypt," *Energy Procedia,* vol. 83, pp. 289-298, 2015.

[45] G. Ciampi, A. Rosato, M. Scorpio, and S. Sibilio, "Experimental analysis of a micro-trigeneration system composed of a micro-cogenerator coupled with an electric chiller," *Applied Thermal Engineering,* vol. 73, pp. 1309-1322, 2014.

[46] S. M. Lai and C. W. Hui, "Feasibility and flexibility for a trigeneration system," *Energy,* vol. 34, pp. 1693-1704, 2009.

[47] S. Sibilio, A. Rosato, G. Ciampi, M. Scorpio, and A. Akisawa, "Building-integrated trigeneration system: Energy, environmental and economic dynamic performance assessment for Italian residential applications," *Renewable and Sustainable Energy Reviews,* 2016.

[48] D. B. Espirito Santo, "Energy and exergy efficiency of a building internal combustion engine trigeneration system under two different operational strategies," *Energy and Buildings,* vol. 53, pp. 28-38, 2012.

[49] A. Canova, C. Cavallero, F. Freschi, L. Giaccone, M. Repetto, and M. Tartaglia, "Comparative Economical Analysis of a Small Scale Trigenerative Plant: A Case Study," in *Industry Applications Conference, 2007. 42nd IAS Annual Meeting. Conference Record of the 2007 IEEE*, 2007, pp. 1456-1459.

[50] M. Chung, H.-C. Park, and C. F. M. Coimbra, "Estimation of the building energy loads and LNG demand for a cogeneration-based community energy system: A case study in Korea," *Energy Conversion and Management*, vol. 87, pp. 1010-1026, 2014.

[51] D. Barlev, R. Vidu, and P. Stroeve, "Innovation in concentrated solar power," *Solar Energy Materials and Solar Cells*, vol. 95, pp. 2703-2725, 2011.

[52] H. Zhai, Y. J. Dai, J. Y. Wu, R. Z. Wang, and L. Y. Zhang, "Experimental investigation and analysis on a concentrating solar collector using linear Fresnel lens," *Energy Conversion and Management*, vol. 51, pp. 48-55, 2010.

[53] G. Morin, J. Dersch, W. Platzer, M. Eck, and A. Häberle, "Comparison of Linear Fresnel and Parabolic Trough Collector power plants," *Solar Energy*, vol. 86, pp. 1-12, 2012.

[54] D. A. Baharoon, H. A. Rahman, W. Z. W. Omar, and S. O. Fadhl, "Historical development of concentrating solar power technologies to generate clean electricity efficiently – A review," *Renewable and Sustainable Energy Reviews*, vol. 41, pp. 996-1027, 2015.

[55] G. Cau and D. Cocco, "Comparison of Medium-size Concentrating Solar Power Plants based on Parabolic Trough and Linear Fresnel Collectors," *Energy Procedia*, vol. 45, pp. 101-110, 2014.

[56] G. Barale, A. Heimsath, P. Nitz, and A. Toro, "Optical design of a linear Fresnel collector for Sicily," presented at the 16th SolarPACES International Symposium, Perpignan, France, 2010.

[57] A. Barbón, N. Barbón, L. Bayón, and J. A. Otero, "Theoretical elements for the design of a small scale Linear Fresnel Reflector: Frontal and lateral views," *Solar Energy*, vol. 132, pp. 188-202, 2016.

[58] V. Sharma, J. K. Nayak, and S. B. Kedare, "Effects of shading and blocking in linear Fresnel reflector field," *Solar Energy*, vol. 113, pp. 114-138, 2015.

[59] R. Abbas, M. J. Montes, M. Piera, and J. M. Martínez-Val, "Solar radiation concentration features in Linear Fresnel Reflector arrays," *Energy Conversion and Management*, vol. 54, pp. 133-144, 2012.

[60] A. Barbón, N. Barbón, L. Bayón, and J. A. Otero, "Optimization of the length and position of the absorber tube in small-scale Linear Fresnel Concentrators," *Renewable Energy*, vol. 99, pp. 986-995, 2016.

[61] V. Sharma, J. K. Nayak, and S. B. Kedare, "Comparison of line focusing solar concentrator fields considering shading and blocking," *Solar Energy*, vol. 122, pp. 924-939, 2015.

[62] V. Sharma, S. Khanna, J. K. Nayak, and S. B. Kedare, "Effects of shading and blocking in compact linear fresnel reflector field," *Energy*, vol. 94, pp. 633-653, 2016.

[63] T. C. Kandpal, S. S. Mathur, and R. N. Singh, "A fresnel-winston tandem concentrator system," *International Journal of Energy Research*, vol. 5, pp. 77-82, 1981.

[64] R. Abbas and J. M. Martínez-Val, "Analytic optical design of linear Fresnel collectors with variable widths and shifts of mirrors," *Renewable Energy,* vol. 75, pp. 81-92, 2015.

[65] Y. Qiu, Y.-L. He, M. Wu, and Z.-J. Zheng, "A comprehensive model for optical and thermal characterization of a linear Fresnel solar reflector with a trapezoidal cavity receiver," *Renewable Energy,* vol. 97, pp. 129-144, 2016.

[66] H. Mousazadeh, A. Keyhani, A. Javadi, H. Mobli, K. Abrinia, and A. Sharifi, "A review of principle and sun-tracking methods for maximizing solar systems output," *Renewable and Sustainable Energy Reviews,* vol. 13, pp. 1800-1818, 10// 2009.

[67] S. Ozcelik, H. Prakash, and R. Challoo, "Two-Axis Solar Tracker Analysis and Control for Maximum Power Generation," *Procedia Computer Science,* vol. 6, pp. 457-462, 2011.

[68] L. Barker, M. Neber, and H. Lee, "Design of a low-profile two-axis solar tracker," *Solar Energy,* vol. 97, pp. 569-576, 2013.

[69] M. J. Montes, C. Rubbia, R. Abbas, and J. M. Martínez-Val, "A comparative analysis of configurations of linear Fresnel collectors for concentrating solar power," *Energy,* vol. 73, pp. 192-203, 2014.

[70] D. R. Mills and G. L. Morrison, "Compact linear Fresnel reflector solar thermal powerplants," *Solar Energy,* vol. 68, pp. 263–283, 2000.

[71] J. Chaves and M. Collares-Pereira, "Etendue-matched two-stage concentrators with multiple receivers," *Journal Name: Solar Energy; Journal Volume: 84; Journal Issue: 2; Other Information: Elsevier Ltd. All rights reserved,* pp. Medium: X; Size: page(s) 196-207, 2010.

[72] J. He, Z. Qiu, Q. Li, and Y. Zhang, "Optical Design of Linear Fresnel Reflector Solar Concentrators," *Energy Procedia,* vol. 14, pp. 1960-1966, 2012.

[73] Q. Zhang, "Theoretical analysis and experimental study of lineat fresnel reflector solar concentrator," PhD, Engineering Thermophysics, University of Science and Technology of China, 2013.

[74] C. Sharma, A. K. Sharma, S. C. Mullick, and T. C. Kandpal, "A study of the effect of design parameters on the performance of linear solar concentrator based thermal power plants in India," *Renewable Energy,* vol. 87, pp. 666-675, 2016.

[75] G. Xu, G. Song, X. Zhu, W. Gao, H. Li, and Y. Quan, "Performance evaluation of a direct vapor generation supercritical ORC system driven by linear Fresnel reflector solar concentrator," *Applied Thermal Engineering,* vol. 80, pp. 196-204, 4/5/ 2015.

[76] Y. Qiu, Y.-L. He, Z.-D. Cheng, and K. Wang, "Study on optical and thermal performance of a linear Fresnel solar reflector using molten salt as HTF with MCRT and FVM methods," *Applied Energy,* vol. 146, pp. 162-173, 2015.

[77] G. Zhu, "Development of an analytical optical method for linear Fresnel collectors," *Solar Energy,* vol. 94, pp. 240-252, 2013.

[78] M. A. Moghimi, K. J. Craig, and J. P. Meyer, "A novel computational approach to combine the optical and thermal modelling of Linear Fresnel Collectors using the finite volume method," *Solar Energy,* vol. 116, pp. 407-427, 2015.

[79] D. Chemisana, J. Barrau, J. I. Rosell, B. Abdel-Mesih, M. Souliotis, and F. Badia, "Optical performance of solar reflective concentrators: A simple method for optical assessment," *Renewable Energy,* vol. 57, pp. 120-129, 2013.

[80] F. J. Pino, R. Caro, F. Rosa, and J. Guerra, "Experimental validation of an optical and thermal model of a linear Fresnel collector system," *Applied Thermal Engineering,* vol. 50, pp. 1463-1471, 2013.

[81] B. S. Negi, S. S. Mathur, and T. C. Kandpal, "Optical and thermal performance evaluation of a linear fresnel reflector solar concentrator," *Solar & Wind Technology,* vol. 7, pp. 379-392, 1990.

[82] S. S. Sahoo, S. M. Varghese, C. Suresh Kumar, S. P. Viswanathan, S. Singh, and R. Banerjee, "Experimental investigation and computational validation of heat losses from the cavity receiver used in linear Fresnel reflector solar thermal system," *Renewable Energy*, vol. 55, pp. 18-23, 2013.

[83] E. M. A. Mokheimer, Y. N. Dabwan, and M. A. Habib, "Performance Comparative Analysis of Three Different CSP Technologies Integrated with Gas Turbine Cogeneration Systems in Saudi Arabia," *Energy Procedia,* vol. 75, pp. 527-532, 2015.

[84] B. Aoun, "Micro combined heat and power operating on renewable energy for residential building," École Nationale Supérieure des Mines de Paris, 2008.

[85] D. Scarpete, K. Uzuneanu, and N. Badea, "Stirling Engine in Residential Systems Based on Renewable Energy," presented at the 4th WSEAS International Conference on Energy Planning, Energy Saving, Environmental Education (EPESE'10), Kantaoui, Sousse, Tunisia 2010.

[86] D. Maraver, A. Sin, J. Royo, and F. Sebastián, "Assessment of CCHP systems based on biomass combustion for small-scale applications through a review of the technology and analysis of energy efficiency parameters," *Applied Energy,* vol. 102, pp. 1303-1313, 2013.

[87] S. Murugan and B. Horák, "Tri and polygeneration systems - A review," *Renewable and Sustainable Energy Reviews*, vol. 60, pp. 1032-1051, 2016.

[88] J. L. Míguez, S. Murillo, J. Porteiro, and L. M. López, "Feasibility of a new domestic CHP trigeneration with heat pump: I. Design and development," *Applied Thermal Engineering*, vol. 24, pp. 1409-1419, 2004.

[89] K. K. Roman and J. B. Alvey, "Selection of prime mover for combined cooling, heating, and power systems based on energy savings, life cycle analysis and environmental consideration," *Energy and Buildings*, vol. 110, pp. 170-181, 2016.

[90] S. Sanaye, M. A. Meybodi, and S. Shokrollahi, "Selecting the prime movers and nominal powers in combined heat and power systems," *Applied Thermal Engineering*, vol. 28, pp. 1177-1188, 2008.

[91] E. Khorasaninejad, A. Fetanat, and H. Hajabdollahi, "Prime mover selection in thermal power plant integrated with organic Rankine cycle for waste heat recovery using a novel multi criteria decision making approach," *Applied Thermal Engineering*, vol. 102, pp. 1262-1279, 2016.

[92] U. S. E. P. Agency and C. H. a. P. Partnership, "Catalog of CHP Techonologies," 2014.

[93] R. Patrascu and E. Minciuc, "Comparative analysis of different combined heat and power generation: fuel cells, gas turbine, internal combustion engin," presented at the 4th IASME/WSEAS International Conference on Energy, Environment, Ecosystems And Sustainable Development (EEESD'08) Algarve, Portugal, 2008.

[94] Y.-Y. Jing, H. Bai, and J.-J. Wang, "A fuzzy multi-criteria decision-making model for CCHP systems driven by different energy sources," *Energy Policy*, vol. 42, pp. 286-296, 2012.

[95] F. A. Al-Sulaiman, I. Dincer, and F. Hamdullahpur, "Energy analysis of a trigeneration plant based on solid oxide fuel cell and organic Rankine cycle," *International Journal of Hydrogen Energy*, vol. 35, pp. 5104-5113, 2010.

[96] L. K. C. Tse, S. Wilkins, N. McGlashan, B. Urban, and R. Martinez-Botas, "Solid oxide fuel cell/gas turbine trigeneration system for marine applications," *Journal of Power Sources*, vol. 196, pp. 3149-3162, 2011.

[97] H. Ozcan and I. Dincer, "Thermodynamic Analysis of an Integrated SOFC, Solar ORC and Absorption Chiller for Tri-generation Applications," *Fuel Cells*, vol. 13, pp. 781-793, 2013.

[98] M. Kane, "Small hybrid solar power system," *Energy*, vol. 28, pp. 1427-1443, 2003.

[99] M. Ali Tarique, I. Dincer, and C. Zamfirescu, "Experimental investigation of a scroll expander for an organic Rankine cycle," *International Journal of Energy Research*, vol. 38, pp. 1825-1834, 2014.

[100] U. Drescher and D. Brüggemann, "Fluid selection for the Organic Rankine Cycle (ORC) in biomass power and heat plants," *Applied Thermal Engineering*, vol. 27, pp. 223-228, 2007.

[101] J. Guo, M. Xu, and L. Cheng, "Thermodynamic analysis of waste heat power generation system," *Energy*, vol. 35, pp. 2824-2835, 2010.

[102] J. Li, G. Pei, and J. Ji, "Analysis of key factors in low-temperature solar-thermal-electric power generation with organic Rankine cycle," *CIESC Journal*, vol. 60, pp. 826-832, 2009.

[103] S. Masheiti, B. Agnew, and S. Walker, "An evaluation of r134a and r245fa as the working fluid in an organic Rankine cycle energized from a low temperature geothermal energy source," *Journal of Energy and Power Engineering*, vol. 5, 2011.

[104] T.-C. Hung, "Waste heat recovery of organic Rankine cycle using dry ¯uids," *Energy Conversion and Management*, vol. 42, pp. 539-553, 2001.

[105] B.-T. Liu, K.-H. Chien, and C.-C. Wang, "Effect of working fluids on organic Rankine cycle for waste heat recovery," *Energy*, vol. 29, pp. 1207-1217, 2004.

[106] D. Wei, X. Lu, Z. Lu, and J. Gu, "Performance analysis and optimization of organic Rankine cycle (ORC) for waste heat recovery," *Energy Conversion and Management*, vol. 48, pp. 1113-1119, 2007.

[107] B. Zheng, Y. Wang, Y. Weng, and W. Gu, "Theoretical and experimental investigation of an organic Rankine cycle for a waste heat recovery system," *Proceedings of the Institution of Mechanical Engineers, Part A: Journal of Power and Energy*, vol. 223, pp. 523-533, 2009.

[108] G. Liu, Y. Zhao, L. Li, G. Bu, and P. Shu, "Simulation of scroll expander used in low-temperature waste heat recovery system," *Journal of Xi'an Jiao Tong University*, vol. 43, pp. 88-91, 2009.

[109] L. Jiang, Y. Zhu, J. Xu, and L. Yu, "Optimization study of Turbo-expander in power generation system recovering low-temperature waste heat," *Energy Conservation Technology*, vol. 30, pp. 400-404, 2012.

[110] A. M. Delgado-Torres and L. García-Rodríguez, "Preliminary assessment of solar organic Rankine cycles for driving a desalination system," *Desalination*, vol. 216, pp. 252-275, 2007.

[111] G. Kosmadakis, D. Manolakos, and G. Papadakis, "Parametric theoretical study of a two-stage solar organic Rankine cycle for RO desalination," *Renewable Energy*, vol. 35, pp. 989-996, 2010.

[112] J. Zhu and H. Huang, "Performance analysis of a cascaded solar organic Rankine cycle with superheating," *International Journal of Low-Carbon Technologies*, 2014.

[113] N. B. Desai and S. Bandyopadhyay, "Process integration of organic Rankine cycle," *Energy*, vol. 34, pp. 1674-1686, 2009.

[114] J. Bao and L. Zhao, "A review of working fluid and expander selections for organic Rankine cycle," *Renewable and Sustainable Energy Reviews*, vol. 24, pp. 325-342, 2013.

[115] S. Declaye, S. Quoilin, and V. Lemort, "Design and experimental investigation of a small scale organic Rankine cycle using a scroll expander," presented at the International Refrigeration and Air Conditioning Conference, 2010.

[116] B. F. Tchanche, G. Papadakis, G. Lambrinos, and A. Frangoudakis, "Fluid selection for a low-temperature solar organic Rankine cycle," *Applied Thermal Engineering*, vol. 29, pp. 2468-2476, 2009.

[117] P. J. Mago, L. M. Chamra, K. Srinivasan, and C. Somayaji, "An examination of regenerative organic Rankine cycles using dry fluids," *Applied Thermal Engineering*, vol. 28, pp. 998-1007, 2008.

[118] B. Saleh, G. Koglbauer, M. Wendland, and J. Fischer, "Working fluids for low-temperature organic Rankine cycles," *Energy*, vol. 32, pp. 1210-1221, 2007.

[119] R. Xu, H. Xi, and Y. He, "Experimental study on the performance of the organic Rankine cycles with and without internal heat regeneration," *Journal of Engineering Thermophysics*, vol. 34, pp. 205-210, 2013.

[120] Z. Wang, H. Ma, Y. Meng, L. Ma, and Z. Sun, "Analysis for solar power generation system of organic Rankine cycle," *Energy Conservation Technology,* vol. 32, pp. 397-403, 2014.

[121] J. Song, X. Zhang, S. Li, Q. Yao, and W. Gu, "Experimental characteristics of solar organic Rankine cycle system," *CIESC Journal,* vol. 65, pp. 4958-4964, 2014.

[122] D. Maraver, J. Royo, V. Lemort, and S. Quoilin, "Systematic optimization of subcritical and transcritical organic Rankine cycles (ORCs) constrained by technical parameters in multiple applications," *Applied Energy,* vol. 117, pp. 11-29, 2014.

[123] E. Prabhu, "Solar Trough Organic Rankine Electricity System (STORES) Stage 1: Power Plant Optimization and Economics," *NREL/SR-550-39433,* 2006.

[124] F. A. Boyaghchi and P. Heidarnejad, "Thermoeconomic assessment and multi objective optimization of a solar micro CCHP based on Organic Rankine Cycle for domestic application," *Energy Conversion and Management,* vol. 97, pp. 224-234, 2015.

[125] F. A. Al-Sulaiman, F. Hamdullahpur, and I. Dincer, "Performance comparison of three trigeneration systems using organic Rankine cycles," *Energy,* vol. 36, pp. 5741-5754, 2011.

[126] V. Lemort, S. Quoilin, C. Cuevas, and J. Lebrun, "Testing and modeling a scroll expander integrated into an Organic Rankine Cycle," *Applied Thermal Engineering,* vol. 29, pp. 3094-3102, 2009.

[127] G. Qiu, H. Liu, and S. Riffat, "Expanders for micro-CHP systems with organic Rankine cycle," *Applied Thermal Engineering,* vol. 31, pp. 3301-3307, 2011.

[128] R. B. Peterson, T. Herron, and H. Wang, "Performance of a small-scale regenerative Rankine power cycle employing a scroll expander," *Proceedings of the Institution of Mechanical Engineers, Part A: Journal of Power and Energy*, vol. 222, pp. 271-282, 2008.

[129] X. Gao, L. Li, Y. Zhao, and P. Shu, "Research on a scroll expander used for recovering work in a fuel cell," *Int. J. of Thermodynamics*, vol. 7, pp. 1-8, 2004.

[130] V. Lemort, S. Declaye, and S. Quoilin, "Experimental characterization of a hermetic scroll expander for use in a micro-scale Rankine cycle," *Proceedings of the Institution of Mechanical Engineers, Part A: Journal of Power and Energy*, vol. 226, pp. 126-136, 2011.

[131] H. Wang, R. Peterson, K. Harada, E. Miller, R. Ingram-Goble, L. Fisher, *et al.*, "Performance of a combined organic Rankine cycle and vapor compression cycle for heat activated cooling," *Energy*, vol. 36, pp. 447-458, 2011.

[132] S. Quoilin, V. Lemort, and J. Lebrun, "Experimental study and modeling of an organic Rankine cycle using scroll expander," *Applied Energy*, vol. 87, pp. 1260-1268, 2010.

[133] K. Harada, "Development of a small scale scroll expander," Master of Science, Mechanical Engineering, Oregon State University, 2010.

[134] N. Zhou, X. Wang, Z. Chen, and Z. Wang, "Experimental study on Organic Rankine Cycle for waste heat recovery from low-temperature flue gas," *Energy*, vol. 55, pp. 216-225, 2013.

[135] M. Imran, M. Usman, B.-S. Park, and D.-H. Lee, "Volumetric expanders for low grade heat and waste heat recovery applications," *Renewable and Sustainable Energy Reviews*, vol. 57, pp. 1090-1109, 2016.

[136] S. Clemente, D. Micheli, M. Reini, and R. Taccani, "Energy efficiency analysis of organic Rankine cycles with scroll expanders for cogenerative applications," *Applied Energy*, vol. 97, pp. 792-801, 2012.

[137] J. Zhu, Z. Chen, H. Huang, and Y. Yan, "Effect of resistive load on the performance of an organic Rankine cycle with a scroll expander," *Energy*, vol. 95, pp. 21-28, 2016.

[138] J.-C. Chang, T.-C. Hung, Y.-L. He, and W. Zhang, "Experimental study on low-temperature organic Rankine cycle utilizing scroll type expander," *Applied Energy*, vol. 155, pp. 150-159, 2015.

[139] J. J. Brasz and G. Holdmann, "Power Production from a Moderate-Temperature Geothermal Resource," *Geothermal Resources Council Transactions*, vol. 29, pp. 729-737, 2005.

[140] G. Liu, Y. Zhao, L. Li, and P. Shu, "Simulation and experiment research on wide ranging working process of scroll expander driven by compressed air," *Applied Thermal Engineering*, vol. 30, pp. 2073-2079, 2010.

[141] Z. Liu, G. Tian, M. Wei, P. Song, Y. Lu, G. Ashby, *et al.*, "Modellingand Optimisation on Scroll Expander for Waste Heat Recovery Organic Rankine Cycle," *Energy Procedia*, vol. 75, pp. 1603-1608, 2015.

[142] Z. Ma, H. Bao, and A. P. Roskilly, "Dynamic modelling and experimental validation of scroll expander for small scale power generation system," *Applied Energy*, 2016.

[143] J.-C. Chang, C.-W. Chang, T.-C. Hung, J.-R. Lin, and K.-C. Huang, "Experimental study and CFD approach for scroll type expander used in low-temperature organic Rankine cycle," *Applied Thermal Engineering*, vol. 73, pp. 1444-1452, 2014.

[144] D. Ziviani, A. Suman, S. Lecompte, M. De Paepe, M. van den Broek, P. R. Spina, *et al.*, "Comparison of a Single-screw and a Scroll Expander under Part-load Conditions for Low-grade Heat Recovery ORC Systems," *Energy Procedia*, vol. 61, pp. 117-120, 2014.

[145] X. Zhang, Y. Xu, J. Xu, Y. Sheng, Z. Zuo, J. Liu, *et al.*, "Study on the performance and optimization of a scroll expander driven by compressed air," *Applied Energy*, 2016.

[146] F. Ayachi, E. B. Ksayer, P. Neveu, and A. Zoughaib, "Experimental investigation and modeling of a hermetic scroll expander," *Applied Energy*, vol. 181, pp. 256-267, 2016.

[147] R. Dickes, D. Ziviani, M. De Paepe, M. van den Broek, S. Quoilin, and V. Lemort, "ORCmKit: an open-source library for organic Rankine cycle modelling and analysis," in *The 29th International Conference on Efficiency, Cost, Optimization, Simulation and Environmental impact of energy systems*, Portorož, Slovenia, 2016, pp. 1-14.

[148] A. Giuffrida, "Modelling the performance of a scroll expander for small organic Rankine cycles when changing the working fluid," *Applied Thermal Engineering*, vol. 70, pp. 1040-1049, 2014.

[149] S. Declaye, S. Quoilin, L. Guillaume, and V. Lemort, "Experimental study on an open-drive scroll expander integrated into an ORC (Organic Rankine Cycle) system with R245fa as working fluid," *Energy*, vol. 55, pp. 173-183, 2013.

[150] D. Pan, N. Gao, F. Xie, W. An, H. Wang, H. Wang, *et al.*, "Experimental research on performance of scroll expander used in organic Rankine Cycle," *Fluid Machinery*, vol. 42, pp. 10-14, 2014.

[151] Z. Wu, D. Pan, N. Gao, T. Zhu, and F. Xie, "Experimental testing and numerical simulation of scroll expander in a small scale organic Rankine cycle system," *Applied Thermal Engineering,* vol. 87, pp. 529-537, 2015.

[152] L. Tang, Y. Wang, P. Yang, and Y. Weng, "Experimental study of optimal load characteristics of low temperature heat organic Rankine cycle power generation," *Journal of Shanghai Jiao Tong University,* vol. 48, pp. 1268-1273, 2014.

[153] P. Garg, G. M. Karthik, P. Kumar, and P. Kumar, "Development of a generic tool to design scroll expanders for ORC applications," *Applied Thermal Engineering,* 2016.

[154] S. Aghahosseini and I. Dincer, "Comparative performance analysis of low-temperature Organic Rankine Cycle (ORC) using pure and zeotropic working fluids," *Applied Thermal Engineering,* vol. 54, pp. 35-42, 2013.

[155] W. W. Husband and A. Beyene, "Low-grade heat-driven Rankine cycle, a feasibility study," *International Journal of Energy Research,* vol. 32, pp. 1373-1382, 2008.

[156] W. Gu, S. Sun, Y. Weng, and Y. Wang, "Experimental study on low grade heat driven organic Rankine cycle by scroll expander," *Proceedings of the CSEE,* vol. 31, pp. 20-25, 2011.

[157] M. Jradi and S. Riffat, "Modelling and testing of a hybrid solar-biomass ORC-based micro-CHP system," *International Journal of Energy Research,* vol. 38, pp. 1039-1052, 2014.

[158] H. J. Kim, J. M. Ahn, I. Park, and P. C. Rha, "Scroll expander for power generation from a low-grade steam source," *Proceedings of the Institution of*

Mechanical Engineers, Part A: Journal of Power and Energy, vol. 221, pp. 705-711, 2007.

[159] S. Karellas and K. Braimakis, "Energy–exergy analysis and economic investigation of a cogeneration and trigeneration ORC–VCC hybrid system utilizing biomass fuel and solar power," *Energy Conversion and Management,* vol. 107, pp. 103-113, 2016.

[160] M. Jradi and S. Riffat, "Experimental investigation of a biomass-fuelled micro-scale tri-generation system with an organic Rankine cycle and liquid desiccant cooling unit," *Energy,* vol. 71, pp. 80-93, 2014.

[161] Babcock and W. Co, *Steam: Its Generation and Use*: BiblioBazaar, 2015.

[162] J. A. Orlando, R. American Society of Heating, and A.-C. Engineers, *Cogeneration Design Guide*: American Society of Heating, Refrigerating and Air-Conditioning Engineers, 1996.

[163] A. Behbahani-nia, M. Bagheri, and R. Bahrampoury, "Optimization of fire tube heat recovery steam generators for cogeneration plants through genetic algorithm," *Applied Thermal Engineering,* vol. 30, pp. 2378-2385, 2010.

[164] C. Oland, "Guide to Low-Emission Boiler and Combustion Equipment Selection," ORNL/TM-2002/19; TRN: US200316%%396 United States10.2172/814038TRN: US200316%%396Wed Dec 23 05:21:24 EST 2015ORNLEnglish, 2002.

[165] J. Deng, R. Z. Wang, and G. Y. Han, "A review of thermally activated cooling technologies for combined cooling, heating and power systems," *Progress in Energy and Combustion Science,* vol. 37, pp. 172-203, 2011.

[166] D. S. Kim and C. A. Infante Ferreira, "Solar refrigeration options – a state-of-the-art review," *International Journal of Refrigeration,* vol. 31, pp. 3-15, 1// 2008.

[167] P. Srikhirin, S. Aphornratana, and S. Chungpaibulpatana, "A review of absorption refrigeration technologies," *Renewable and Sustainable Energy Reviews,* vol. 5, pp. 343-372, 12// 2001.

[168] H.-W. D. Chiang, C.-N. Hsu, W.-B. Huang, C.-H. Lee, W.-P. Huang, and W.-T. Hong, "Design and Performance Study of a Solid Oxide Fuel Cell and Gas Turbine Hybrid System Applied in Combined Cooling, Heating, and Power System," *Journal of Energy Engineering,* vol. 138, pp. 205-214, 2012.

[169] M. Moya, J. C. Bruno, P. Eguia, E. Torres, I. Zamora, and A. Coronas, "Performance analysis of a trigeneration system based on a micro gas turbine and an air-cooled, indirect fired, ammonia–water absorption chiller," *Applied Energy,* vol. 88, pp. 4424-4440, 2011.

[170] X. Chen, G. Gong, Z. Wan, L. Luo, and J. Wan, "Performance analysis of 5 kW PEMFC-based residential micro-CCHP with absorption chiller," *International Journal of Hydrogen Energy,* vol. 40, pp. 10647-10657, 2015.

[171] J. Wang and J. Wu, "Investigation of a mixed effect absorption chiller powered by jacket water and exhaust gas waste heat of internal combustion engine," *International Journal of Refrigeration,* vol. 50, pp. 193-206, 2015.

[172] M. Clausse, F. Meunier, J. Coulié, and E. Herail, "Comparison of adsorption systems using natural gas fired fuel cell as heat source, for residential air conditioning," *International Journal of Refrigeration,* vol. 32, pp. 712-719, 6// 2009.

[173] J. Deng, R. Wang, J. Wu, G. Han, D. Wu, and S. Li, "Exergy cost analysis of a micro-trigeneration system based on the structural theory of thermoeconomics," *Energy,* vol. 33, pp. 1417-1426, 9// 2008.

[174] S. Li and J. Y. Wu, "Theoretical research of a silica gel–water adsorption chiller in a micro combined cooling, heating and power (CCHP) system," *Applied Energy*, vol. 86, pp. 958-967, 2009.

[175] X. Q. Kong, R. Z. Wang, J. Y. Wu, X. H. Huang, Y. Huangfu, D. W. Wu, *et al.*, "Experimental investigation of a micro-combined cooling, heating and power system driven by a gas engine," *International Journal of Refrigeration,* vol. 28, pp. 977-987, 2005.

[176] J. Y. Wu, J. L. Wang, S. Li, and R. Z. Wang, "Experimental and simulative investigation of a micro-CCHP (micro combined cooling, heating and power) system with thermal management controller," *Energy,* vol. 68, pp. 444-453, 4/15/ 2014.

[177] F. Xiao, G. Ge, and X. Niu, "Control performance of a dedicated outdoor air system adopting liquid desiccant dehumidification," *Applied Energy,* vol. 88, pp. 143-149, 2011.

[178] K. Daou, R. Wang, and Z. Xia, "Desiccant cooling air conditioning: a review," *Renewable and Sustainable Energy Reviews,* vol. 10, pp. 55-77, 2006.

[179] K. A. Joudi and N. S. Dhaidan, "Application of solar assisted heating and desiccant cooling systems for a domestic building," *Energy Conversion and Management,* vol. 42, pp. 995-1022, 2001.

[180] A. T. Mohammad, S. B. Mat, M. Y. Sulaiman, K. Sopian, and A. A. Al-abidi, "Historical review of liquid desiccant evaporation cooling technology," *Energy and Buildings,* vol. 67, pp. 22-33, 2013.

[181] B. S. Davanagere, S. A. Sherif, and D. Y. Goswami, "A feasibility study of a solar desiccant air-conditioning system—Part I: psychrometrics and analysis of the conditioned zone," *International Journal of Energy Research,* vol. 23, pp. 7-21, 1999.

[182] B. S. Davanagere, S. A. Sherif, and D. Y. Goswami, "A feasibility study of a solar desiccant air-conditioning system-part I: Psychrometricsand analysis of the conditioned zone," *International Journal of Energy Research,* vol. 23, pp. 7-21, 1999.

[183] M. Goldsworthy and S. White, "Optimisation of a desiccant cooling system design with indirect evaporative cooler," *International Journal of Refrigeration,* vol. 34, pp. 148-158, 2011.

[184] E. Hürdoğan, O. Büyükalaca, T. Yılmaz, A. Hepbasli, and İ. Uçkan, "Investigation of solar energy utilization in a novel desiccant based air conditioning system," *Energy and Buildings,* vol. 55, pp. 757-764, 2012.

[185] M. S. Buker and S. B. Riffat, "Recent developments in solar assisted liquid desiccant evaporative cooling technology—A review," *Energy and Buildings,* vol. 96, pp. 95-108, 2015.

[186] X. Zheng, T. S. Ge, and R. Z. Wang, "Recent progress on desiccant materials for solid desiccant cooling systems," *Energy,* vol. 74, pp. 280-294, 2014.

[187] M. Sultan, I. I. El-Sharkawy, T. Miyazaki, B. B. Saha, and S. Koyama, "An overview of solid desiccant dehumidification and air conditioning systems," *Renewable and Sustainable Energy Reviews,* vol. 46, pp. 16-29, 2015.

[188] D. La, Y. J. Dai, Y. Li, R. Z. Wang, and T. S. Ge, "Technical development of rotary desiccant dehumidification and air conditioning: A review," *Renewable and Sustainable Energy Reviews,* vol. 14, pp. 130-147, 2010.

[189] K. S. Rambhad, P. V. Walke, and D. J. Tidke, "Solid desiccant dehumidification and regeneration methods—A review," *Renewable and Sustainable Energy Reviews,* vol. 59, pp. 73-83, 2016.

[190] D. B. Jani, M. Mishra, and P. K. Sahoo, "Solid desiccant air conditioning – A state of the art review," *Renewable and Sustainable Energy Reviews,* vol. 60, pp. 1451-1469, 2016.

[191] M. Saghafifar and M. Gadalla, "Performance assessment of integrated PV/T and solid desiccant air-conditioning systems for cooling buildings using Maisotsenko cooling cycle," *Solar Energy,* vol. 127, pp. 79-95, 2016.

[192] A. Y. Petrov, A. Zaltash, E. Vineyard, S. Labinov, D. Rizy, and R. Linkous, "Baseline and IES performance of a direct-fired desiccant dehumidification unit under various environmental conditions," *Transactions-American Society Of Heating Refrigerating And Air Conditioning Engineers,* vol. 109, pp. 565-571, 2003.

[193] G. Angrisani, F. Minichiello, C. Roselli, and M. Sasso, "Experimental investigation to optimise a desiccant HVAC system coupled to a small size cogenerator," *Applied Thermal Engineering,* vol. 31, pp. 506-512, 3// 2011.

[194] X. Wang, W. Cai, J. Lu, Y. Sun, and X. Ding, "Heat and Mass Transfer Model for Desiccant Solution Regeneration Process in Liquid Desiccant Dehumidification System," *Industrial & Engineering Chemistry Research,* vol. 53, pp. 2820-2829, 2014.

[195] L. Mei and Y. J. Dai, "A technical review on use of liquid-desiccant dehumidification for air-conditioning application," *Renewable and Sustainable Energy Reviews,* vol. 12, pp. 662-689, 2008.

[196] P. Gandhidasan, "A simplified model for air dehumidification with liquid desiccant," *Solar Energy,* vol. 76, pp. 409-416, 2004.

[197] L.-Z. Zhang, "Progress on heat and moisture recovery with membranes: From fundamentals to engineering applications," *Energy Conversion and Management,* vol. 63, pp. 173-195, 2012.

[198] S. Y. Ahmed, P. Gandhidasan, and A. A. Al-Farayedhi, "Thermodynamic analysis of liquid desiccants," *Solar Energy,* vol. 62, pp. 11-18, 1998.

[199] S. Jain and P. K. Bansal, "Performance analysis of liquid desiccant dehumidification systems," *International Journal of Refrigeration,* vol. 30, pp. 861-872, 2007.

[200] M. M. Rafique, P. Gandhidasan, and H. M. S. Bahaidarah, "Liquid desiccant materials and dehumidifiers – A review," *Renewable and Sustainable Energy Reviews,* vol. 56, pp. 179-195, 2016.

[201] M. T. Zegenhagen, C. Ricart, T. Meyer, R. Kühn, and F. Ziegler, "Experimental Investigation of A Liquid Desiccant System for Air Dehumidification Working With Ionic Liquids," *Energy Procedia,* vol. 70, pp. 544-551, 2015.

[202] R. M. Lazzarin, A. Gasparella, and G. A. Longo, "Chemical dehumidification by liquid desiccants: theory and experiment," *International Journal of Refrigeration,* vol. 22, pp. 334-347, 1999.

[203] A. H. Abdel-Salam, G. Ge, and C. J. Simonson, "Performance analysis of a membrane liquid desiccant air-conditioning system," *Energy and Buildings,* vol. 62, pp. 559-569, 2013.

[204] R. Qi, L. Lu, and Y. Jiang, "Investigation on the liquid contact angle and its influence for liquid desiccant dehumidification system," *International Journal of Heat and Mass Transfer,* vol. 88, pp. 210-217, 2015.

[205] Y. Yin, J. Qian, and X. Zhang, "Recent advancements in liquid desiccant dehumidification technology," *Renewable and Sustainable Energy Reviews,* vol. 31, pp. 38-52, 2014.

[206] S.-M. Huang and L.-Z. Zhang, "Researches and trends in membrane-based liquid desiccant air dehumidification," *Renewable and Sustainable Energy Reviews,* vol. 28, pp. 425-440, 2013.

[207] Y. Luo, H. Yang, L. Lu, and R. Qi, "A review of the mathematical models for predicting the heat and mass transfer process in the liquid desiccant dehumidifier," *Renewable and Sustainable Energy Reviews,* vol. 31, pp. 587-599, 2014.

[208] S. Jain, P. L. Dhar, and S. C. Kaushik, "Experimental studies on the dehumidifier and regenerator of a liquid desiccant cooling system," *Applied Thermal Engineering,* vol. 20, pp. 253-267, 2// 2000.

[209] J. Woods, "Membrane processes for heating, ventilation, and air conditioning," *Renewable and Sustainable Energy Reviews,* vol. 33, pp. 290-304, 2014.

[210] J. Liu, T. Zhang, X. Liu, and J. Jiang, "Experimental analysis of an internally-cooled/heated liquid desiccant dehumidifier/regenerator made of thermally conductive plastic," *Energy and Buildings,* vol. 99, pp. 75-86, 2015.

[211] Y. Cerci, "A new ideal evaporative freezing cycle," *International Journal of Heat and Mass Transfer,* vol. 46, pp. 2967-2974, 2003.

[212] J. M. Wu, X. Huang, and H. Zhang, "Theoretical analysis on heat and mass transfer in a direct evaporative cooler," *Applied Thermal Engineering*, vol. 29, pp. 980-984, 4// 2009.

[213] J. Woods and E. Kozubal, "A desiccant-enhanced evaporative air conditioner: Numerical model and experiments," *Energy Conversion and Management,* vol. 65, pp. 208-220, 2013.

[214] S.-W. Ham, S.-J. Lee, and J.-W. Jeong, "Operating energy savings in a liquid desiccant and dew point evaporative cooling-assisted 100% outdoor air system," *Energy and Buildings*, vol. 116, pp. 535-552, 2016.

[215] M. R. Safizadeh, A. Morgenstern, C. Bongs, H.-M. Henning, and J. Luther, "Optimization of a heat assisted air-conditioning system comprising membrane and desiccant technologies for applications in tropical climates," *Energy,* vol. 101, pp. 52-64, 2016.

[216] M. S. Buker, B. Mempouo, and S. B. Riffat, "Experimental investigation of a building integrated photovoltaic/thermal roof collector combined with a liquid desiccant enhanced indirect evaporative cooling system," *Energy Conversion and Management,* vol. 101, pp. 239-254, 2015.

[217] H. T. El-Dessouky, H. M. Ettouney, and W. Bouhamra, "A Novel Air Conditioning System," *Chemical Engineering Research and Design,* vol. 78, pp. 999-1009, 2000.

[218] G. Ge, D. Ghadiri Moghaddam, A. H. Abdel-Salam, R. W. Besant, and C. J. Simonson, "Comparison of experimental data and a model for heat and mass transfer performance of a liquid-to-air membrane energy exchanger (LAMEE) when used for air dehumidification and salt solution regeneration," *International Journal of Heat and Mass Transfer,* vol. 68, pp. 119-131, 2014.

[219] A. H. Abdel-Salam and C. J. Simonson, "Annual evaluation of energy, environmental and economic performances of a membrane liquid desiccant air conditioning system with/without ERV," *Applied Energy*, vol. 116, pp. 134-148, 3/1/ 2014.

[220] I. P. Koronaki, R. I. Christodoulaki, V. D. Papaefthimiou, and E. D. Rogdakis, "Thermodynamic analysis of a counter flow adiabatic dehumidifier with different liquid desiccant materials," *Applied Thermal Engineering*, vol. 50, pp. 361-373, 2013.

[221] W. Y. Saman and S. Alizadeh, "An experimental study of a cross-flow type plate heat exchanger for dehumidification/cooling," *Solar Energy*, vol. 73, pp. 59-71, 2002.

[222] S. A. Abdul-Wahab, Y. H. Zurigat, and M. K. Abu-Arabi, "Predictions of moisture removal rate and dehumidification effectiveness for structured liquid desiccant air dehumidifier," *Energy*, vol. 29, pp. 19-34, 2004.

[223] A. H. Abdel-Salam, G. Ge, and C. J. Simonson, "Thermo-economic performance of a solar membrane liquid desiccant air conditioning system," *Solar Energy*, vol. 102, pp. 56-73, 4// 2014.

[224] S.-M. Huang, L.-Z. Zhang, K. Tang, and L.-X. Pei, "Fluid flow and heat mass transfer in membrane parallel-plates channels used for liquid desiccant air dehumidification," *International Journal of Heat and Mass Transfer*, vol. 55, pp. 2571-2580, 2012.

[225] T. Elmer, M. Worall, S. Wu, and S. Riffat, "An experimental study of a novel integrated desiccant air conditioning system for building applications," *Energy and Buildings*, vol. 111, pp. 434-445, 2016.

[226] L. Li, H. Mu, N. Li, and M. Li, "Analysis of the integrated performance and redundant energy of CCHP systems under different operation strategies," *Energy and Buildings,* vol. 99, pp. 231-242, 2015.

[227] V. Andiappan and D. K. S. Ng, "Synthesis of tri-generation systems: Technology selection, sizing and redundancy allocation based on operational strategy," *Computers & Chemical Engineering,* 2016.

[228] P. J. Mago, N. Fumo, and L. M. Chamra, "Performance analysis of CCHP and CHP systems operating following the thermal and electric load," *International Journal of Energy Research,* vol. 33, pp. 852-864, 2009.

[229] A. A. Jalalzadeh-Azar, "A Comparison of Electrical-and Thermal-Load-Following CHP Systems," *ASHRAE Transactions,* vol. 110, 2004.

[230] P. J. Mago and A. K. Hueffed, "Evaluation of a turbine driven CCHP system for large office buildings under different operating strategies," *Energy and Buildings,* vol. 42, pp. 1628-1636, 2010.

[231] P. J. Mago, L. M. Chamra, and J. Ramsay, "Micro-combined cooling, heating and power systems hybrid electric-thermal load following operation," *Applied Thermal Engineering,* vol. 30, pp. 800-806, 2010.

[232] A. N. Ünal, S. Ercan, and G. Kayakutlu, "Optimisation studies on tri-generation: a review," *International Journal of Energy Research,* vol. 39, pp. 1311-1334, 2015.

[233] W. Gu, Z. Wu, R. Bo, W. Liu, G. Zhou, W. Chen, *et al.*, "Modeling, planning and optimal energy management of combined cooling, heating and power microgrid: A review," *International Journal of Electrical Power & Energy Systems,* vol. 54, pp. 26-37, 2014.

[234] H. Cho, A. D. Smith, and P. Mago, "Combined cooling, heating and power: A review of performance improvement and optimization," *Applied Energy,* vol. 136, pp. 168-185, 2014.

[235] A. Hepbasli, "A key review on exergetic analysis and assessment of renewable energy resources for a sustainable future," *Renewable and Sustainable Energy Reviews,* vol. 12, pp. 593-661, 2008.

[236] A. Huicochea, W. Rivera, G. Gutiérrez-Urueta, J. C. Bruno, and A. Coronas, "Thermodynamic analysis of a trigeneration system consisting of a micro gas turbine and a double effect absorption chiller," *Applied Thermal Engineering,* vol. 31, pp. 3347-3353, 2011.

[237] M. Ebrahimi, A. Keshavarz, and A. Jamali, "Energy and exergy analyses of a micro-steam CCHP cycle for a residential building," *Energy and Buildings,* vol. 45, pp. 202-210, 2012.

[238] Y. Huangfu, J. Y. Wu, R. Z. Wang, X. Q. Kong, and B. H. Wei, "Evaluation and analysis of novel micro-scale combined cooling, heating and power (MCCHP) system," *Energy Conversion and Management,* vol. 48, pp. 1703-1709, 2007.

[239] L. Lin, Y. Wang, T. Al-Shemmeri, T. Ruxton, S. Turner, S. Zeng*, et al.,* "An experimental investigation of a household size trigeneration," *Applied Thermal Engineering,* vol. 27, pp. 576-585, 2007.

[240] G. Angrisani, A. Rosato, C. Roselli, M. Sasso, and S. Sibilio, "Experimental results of a micro-trigeneration installation," *Applied Thermal Engineering,* vol. 38, pp. 78-90, 2012.

[241] L. A. Cisternas and E. J. Lam, "An analytic correlation for the vapour pressure of aqueous and non-aqueous solutions of single and mixed electrolytes. Part II. Application and extension," *Fluid Phase Equilibria,* vol. 62, pp. 11-27, 1991.

[242] S. S. Mathur, T. C. Kandpal, and B. S. Negi, "Optical design and concentration characteristics of linear Fresnel reflector solar concentrators—I. Mirror elements of varying width," *Energy Conversion and Management,* vol. 31, pp. 205-219, // 1991.

[243] R. Foster, M. Ghassemi, and A. Cota, *Solar Energy: Renewable Energy and the Environment*. Boca Raton: CRC Press, 2010.

[244] F. Göhring, O. Bender, M. Röger, J. Nettlau, and P. Schwarzbözl, "Flux density measurement on open volumetric receivers," *Proceedings of SolarPACES,* pp. 20-23, 2011.

[245] M. L. Huber and M. O. McLinden, "Thermodynamic Properties of R134a (1, 1, 1, 2-tetrafluoroethane)," 1992.

[246] S. Bell, "Measurement Good Practice Guide No. 11 (Issue 2)," *A Beginner's Guide to Uncertainty of Measurement. National Physical Laboratory Teddington, Middlesex, United Kingdom,* 2001.

[247] N. N. Potter and J. H. Hotchkiss, "Unit Operations in Food Processing," in *Food Science: Fifth Edition*, ed Boston, MA: Springer US, 1995, pp. 69-89.

[248] T. Li, J. Zhu, W. Fu, and K. Hu, "Experimental comparison of R245fa and R245fa/R601a for organic Rankine cycle using scroll expander," *International Journal of Energy Research,* vol. 39, pp. 202-214, 2015.

[249] Z. He, Y. Zhang, S. Dong, H. Ma, X. Yu, Y. Zhang, *et al.*, "Thermodynamic analysis of a low-temperature organic Rankine cycle power plant operating at

off-design conditions," *Applied Thermal Engineering,* vol. 113, pp. 937-951, 2017.

[250] Å. Melinder, *Thermophysical Properties of Aqueous Solutions Used as Secondary Working Fluids [Elektronisk resurs]*. Stockholm: KTH, 2007.

[251] S. Liu, "A novel heat recovery/desiccant cooling system," PhD, Architecture and Built Environment, University of Nottingham, 2008.

[252] P. T. Tsilingiris, "Thermophysical and transport properties of humid air at temperature range between 0 and 100 °C," *Energy Conversion and Management,* vol. 49, pp. 1098-1110, 5// 2008.

[253] S. Bouzenada, A. N. Kaabi, L. Fraikin, and A. Léonard, "Experimental Study on dehumidification/regeneration of Liquid Desiccant: LiBr Solution," *Procedia Computer Science,* vol. 32, pp. 673-680, 2014.

[254] Z. Yang, B. Lin, K. Zhang, and Z. Lian, "Experimental study on mass transfer performances of the ultrasonic atomization liquid desiccant dehumidification system," *Energy and Buildings,* vol. 93, pp. 126-136, 2015.

[255] M. M. Hammad, R. I. El-Ghanam, R. Y. Sakr, and S. S. Ayad, "Theoretical Study for Compact Liquid Desiccant Dehumidifier/Regenerator System," in *The Al-Azhar Engineering Tenth International Conference,* Cairo, 2008, pp. 352-378.

[256] Y. Yin, S. Li, X. Zhang, and D. Peng, "Feasibility and performance analysis of a desiccant solution regenerator using hot air," *Energy and Buildings,* vol. 43, pp. 1097-1104, 2011.

[257] N. Fumo and D. Y. Goswami, "Study of an aqueous lithium chloride desiccant system: Air dehumidification and desiccant regeneration," *Solar Energy,* vol. 72, pp. 351-361, 2002.

[258] H. Liu, Y. Shao, and J. Li, "A biomass-fired micro-scale CHP system with organic Rankine cycle (ORC) e Thermodynamic modelling studies," *Biomass and Bioenergy*, vol. 35, pp. 3985-3994, 2011.

[259] L.-Z. Zhang, C.-H. Liang, and L.-X. Pei, "Conjugate heat and mass transfer in membrane-formed channels in all entry regions," *International Journal of Heat and Mass Transfer*, vol. 53, pp. 815-824, 2010.

[260] S. K. Som, *Introduction to heat transfer*. New Delhi: PHI Learning, 2008.

[261] T. L. Bergman and F. P. Incropera, *Fundamentals of heat and mass transfer*. Hoboken, NJ: Wiley, 2011.

[262] R. K. Shah and D. P. Sekulic, *Fundamentals of heat exchanger design*: John Wiley & Sons, 2003.

[263] M. Seyed-Ahmadi, B. Erb, C. J. Simonson, and R. W. Besant, "Transient behavior of run-around heat and moisture exchanger system. Part I: Model formulation and verification," *International Journal of Heat and Mass Transfer*, vol. 52, pp. 6000-6011, 2009.

[264] D. Ghadiri Moghaddam, A. Oghabi, G. Ge, R. W. Besant, and C. J. Simonson, "Numerical model of a small-scale liquid-to-air membrane energy exchanger: Parametric study of membrane resistance and air side convective heat transfer coefficient," *Applied Thermal Engineering*, vol. 61, pp. 245-258, 2013.

[265] ASHRAE, "2013 ASHRAE Handbook - Fundamentals (I-P Edition)," ed: American Society of Heating, Refrigerating and Air-Conditioning Engineers, Inc., 2013.

[266] H. J. Cho, D. J. Preston, Y. Zhu, and E. N. Wang, "Nanoengineered materials for liquid–vapour phase-change heat transfer," *Nature Reviews Materials*, vol. 2, p. 16092, 2016.

[267] E. Macchi and M. Astolfi, *Organic Rankine Cycle (ORC) Power Systems: Technologies and Applications*: Elsevier Science, 2016.

[268] A. Faghri, Y. Zhang, and J. R. Howell, *Advanced Heat and Mass Transfer*: Global Digital Press, 2010.

[269] J. P. Roy, M. K. Mishra, and A. Misra, "Performance analysis of an Organic Rankine Cycle with superheating under different heat source temperature conditions," *Applied Energy,* vol. 88, pp. 2995-3004, 2011.

[270] K. Hu, J. Zhu, W. Zhang, K. Liu, and X. Lu, "Effects of evaporator superheat on system operation stability of an organic Rankine cycle," *Applied Thermal Engineering,* vol. 111, pp. 793-801, 2017.

[271] A. Desai, D. Agrawal, S. Datta, and S. Rumde, "Selection of working fluid and exergy analysis of an organic rankine cycle," *International Journal of Advance Research In Science And Engineering* vol. 4, pp. 1063-1076, 2015.

[272] L. Pan and W. Shi, "Investigation on the pinch point position in heat exchangers," *Journal of Thermal Science,* vol. 25, pp. 258-265, 2016.

[273] V. Sukhanov, A. Bezukhov, I. Bogov, N. Dontsov, I. Volkovitsky, and V. Tolmachev, "Experimental study of condensate subcooling with the use of a model of an air-cooled condenser," *Thermal Engineering,* vol. 63, pp. 17-23, 2016.

[274] G. Ghim and J. Lee, "Condensation heat transfer of low GWP ORC working fluids in a horizontal smooth tube," *International Journal of Heat and Mass Transfer,* vol. 104, pp. 718-728, 2017.

Appendix A: Excerpt of CLFR Model Script

An excerpt from Matlab script of the CLFR model is presented in this appendix.

Function 1

```
function q=function1(p)

% CLFR input
f = 1,800;      % Focal Length
r = 35;         % Radius of Absorber
omiga_1 = 16/60;   %Subtended angle by the Sun
x0 = r;         %Position of Lower Edge of First Mirror Element

% calculation of the first mirror
a1=p(1);      % Tilt Angle of First Mirror Element
b1=p(2);      %Length from Edge Point of First Mirror Element to its Central Point

q(1)=90-2*a1-omiga_1-atand((f+b1*sind(a1)-
r*sind(2*a1+omiga_1))/(x0+r*cosd(2*a1+omiga_1)));
q(2)=tand(2*a1-omiga_1)-(x0-r*cosd(2*a1+omiga_1)+2*b1*cosd(a1))/(f-
b1*sind(a1)+r*sind(2*a1+omiga_1));

result (a_i_1, b_i_1, x_i_1) = fsolve('function1',[0.5,0.5])
```

Function 2

```
% Calculate the second mirror elements

global a_i_1 ;
global b_i_1 ;
global x_i_1;

a_i = input(1);   %Tilt Angle of Second Mirror Element
b_i = input(2);   %Length from Edge Point of Second Mirror Element to its Central Point
x_i = input(3);   %Specific Reference Location of Central Point of Second Mirror Element

output(1) = 90-2*a_i-omiga_1-atand((f+b_i*sind(a_i)-r*sind(2*a_i+omiga_1))/(x_i-
b_i*cosd(a_i)+r*cosd(2*a_i+omiga_1)));

output(2) = tand(2*a_i-omiga_1)-(x_i+b_i*cosd(a_i)-r*cosd(2*a_i+omiga_1))/(f-
b_i*sind(a_i)+r*sind(2*a_i+omiga_1));

output(3) = sind(90-2*a_i-omiga_1)*(x_i-b_i*cosd(a_i)-x0)-2*(b_i_1)*sind(180-
90+2*a_i+omiga_1-a_i_1);
```

Function 3

% calculate i^{th} mirror element

```
global a_i_1 ;
global b_i_1 ;
global x_i_1;

a_i = input(1);   %Tilt Angle of the Mirror Element
b_i = input(2);   %Length from Edge Point of the Mirror Element to its Central Point
x_i = input(3);   %Specific Reference Location of Central Point of the Mirror Element

output (1) = 90-2*a_i-omiga_1-atand((f+b_i*sind(a_i)-r*sind(2*a_i+omiga_1))/(x_i-
b_i*cosd(a_i)+r*cosd(2*a_i+omiga_1)));

output (2) = tand(2*a_i-omiga_1)-(x_i+b_i*cosd(a_i)-r*cosd(2*a_i+omiga_1))/(f-
b_i*sind(a_i)+r*sind(2*a_i+omiga_1));

output (3) = 2*(b_i_1)/sind(90-2*a_i-omiga_1)-(x_i-b_i*cosd(a_i)-
x_i_1+b_i_1*cosd(a_i_1))/sind(180-90+2*a_i+omiga_1-a_i_1);
```

Main function

```
function output = main(count)
%usage: count is the number of mirrors
%output :  a, b, x, respectively.

global a ;
global b ;
global x;
global a_i_1 ;
global b_i_1 ;
global x_i_1;

a = zeros(1,count);
b = zeros(1,count);
x = zeros(1,count);

result = fsolve('function1',[0.5,0.5],optimset('Display','off'));
a(1) = result(1);
b(1) = result(2);
x(1) = r+b(1)*cosd(a(1));

if count>=2
   result = fsolve('function2',[0.5,20,35],optimset('Display','off'));
   if function2(result)<1e-1
      a(2) = result(1);
```

```
        b(2) = result(2);
        x(2) = result(3);
    else
        function2(result)
    end
end

if count>2
    for i = 3:count
    a_i_1 = a(i-1);
    b_i_1 = b(i-1);
    x_i_1 = x(i-1);
    result = fsolve('function3',[2,20,35+i*60], optimset('Display','off'));
    if function3(result)<1e-1
        a(i) = result(1);
        b(i) = result(2);
        x(i) = result(3);
    else
        function3(result)
        i
    end
    end
end

output(1,:) = a;
output(2,:) = b;
output(3,:) = x;

end
```

Appendix B: Excerpt of Micro Trigeneration System Model Script

An excerpt from model script of the micro trigeneration system is presented in this appendix.

```
function [data] = TriModel(F_wf, F_hw, F_cw, F_hf , F_cf , P_hw_su, T_hw_su, m_hw_su, P_cw_su, T_cw_su, m_cw_su, P_hf_su,  T_amb, T_hf_su, m_hf_su, perc_heating, P_cf_su, T_cf_su, m_cf_su  N_exp, N_pp, param)

%Input parameters for ORC loop:
   F_wf = 'R134a'; %working fluid in ORC
   F_hw = 'water'; % hot source fluid in ORC
   P_hw_su = 0.78129852050448e+05; % hot source supply pressure
   T_hw_su = 373.15; % hot source supply temperature (K)
   m_hw_su = 0.133; % hot source mass flow rate
   F_cw = 'water'; % cold source fluid in ORC
   P_cw_su = 70000; % cold source supply pressure
   T_cw_su = 285.15; % cold source supply temperature (K)
   m_cw_su = 0.133; % cold source mass flow rate
   r_v =3.5 % scroll expander built-in volume ratio
   N_exp = 3600; % scroll expander rotational speed (rpm)
   V_s_exp = 1.2e-05; % scroll expander swept volume
   A_leak_exp = 2.06e-06; % scroll expander leakage area
   d_su = 0.0078 % scroll expander nozzle diameter
   T_amb = 288.15; % ambient temperature (K)
   N_pp = 3600; % pump rotational speed (rpm)
   A_leak_pp = 6.06e-09; % pump leakage area
   W_pp_loss = 15.0504; % pump mechanical loss
   K_0_loss =0.4090; % pump loss factor
   V_s_pp = 2.3e-06; % pump swept volume

%Input parameters for hot water supply loop:
   F_hf = 'water'; % heating fluid type
   P_hf_su = 70000; % heating fluid supply pressure
   T_hf_su = 293.15; % heating fluid temperature (K)
   m_hf_su = 0.53; % heating fluid mass flow rate
   perc_heating = 0.3; % percentage of exhaust heat for hot water supply

%Input parameters for MLDC loop:
   F_cf = 'water'; % cold fluid type: dilute solution
   P_cf_su = 70000; % cold fluid supply pressure
```

```
    T_cf_su = 295.15; % cold fluid temperature (K)
    m_cf_su = 0.53; % cold fluid mass flow rate
    perc_cooling = 1- perc_heating; % percentage of exhaust heat for MLDC

% Heat exchangers input parameters (i.e. evaporator, condenser and recuperator)
parameters
    param.EV.A_tot = 5.6; % evaporator total heat transfer area
    param.EV.V_h_tot = 0.05; % evaporator hot fluid volume
    param.EV.V_c_tot = 0.05; % evaporator cold fluid volume
    param.CD.A_tot = 5.6; % condenser total heat transfer area
    param.CD.V_h_tot = 0.05; % condenser hot fluid volume
    param.CD.V_c_tot = 0.05; % condenser cold fluid volume
    param.REC.A_tot = 5.6; % recuperator total heat transfer area
    param.REC.V_h_tot = 0.05; % recuperator hot fluid volume
    param.REC.V_c_tot = 0.05; % recuperator cold fluid volume
    param.HX1.A_tot = 5.6; % HX1 (hot water supply) total heat transfer area
    param.HX1.V_h_tot = 0.05; % HX1 hot fluid volume
    param.HX1.V_c_tot = 0.05; % HX1 cold fluid volume
    param.HX2.A_tot = 5.6; % HX2 (regeneration) total heat transfer area
    param.HX2.V_h_tot = 0.05; % HX2 hot fluid volume
    param.HX2.V_c_tot = 0.05; % HX2 cold fluid volume
…….
% Initial condition guess
% condenser
P_cd_ll = max (CoolProp.PropsSI('P', 'Q', 0, 'T', T_cw_su, F_wf ),
CoolProp.PropsSI('P_min', 'Q', 0, 'T', 273.15, F_wf ));
% evaporator
P_ev_ul = CoolProp.PropsSI('P', 'Q', 0, 'T', min (CoolProp.PropsSI('Tcrit', 'Q', 0, 'T', 273.15,
F_wf ), T_hw_su -1), F_wf );
orc_max = P_ev_ul/P_cd_ll;
orc_min = min (1.000, orc_max);
P_ev_ll = orc_min*P_cd_ll;
P_cd_ul = P_ev_ub/orc_min;
% initial guess
P_cd_guess0 = linspace (CoolProp.PropsSI('P', 'Q', 0, 'T', T_cw_su+10, F_wf ),
CoolProp.PropsSI('P', 'Q', 0, 'T', T_cw_su+18, F_wf ), param.init(1) );
x_orc_guess0 =  linspace (0.1, 0.8, param.init(2));
x_Q_re_guess0 = linspace (0.2, 0.5, param.init(3));
x_h_pp_su_guess0 = linspace (0.2, 0.8, param.init(4));


……..
 res(num) = guess.res;

 end
```

```
……
 % Call PPModel function
[data_PP] = PPModel(F_wf, N_pp, T_amb, param.PP, data.P_pp_su, data.h_pp_su,);
% assign outputs for TriModel inputs
data.M_pp = data_PP_M;
data.m_wf = data_PP_m;
data.W_pp = data_PP_W;
T_pr = data_PP_T_ex;
h_pr = data_PP_h_ex;
…

% Call RECModel function (cold side)
data.P_recc_su = P_pr;
data.T_recc_su = data_PP_T_ex;
data.h_recc_su = data_PP.h_ex;
h_pr = CoolProp.PropsSI('H', 'P', data.P_rec_su, 'T', T_hw_su, F_wf));
P_pr = data.P_recc_su;
T_pr = CoolProp.PropsSI('T', 'P', P_pr, 'H', h_pr, F_wf);
…

% Call EVModel function
[data_EV] = EVModel(F_hw, P_hw_su, T_hw_su, m_hw, F_wf, data.P_ev_su,
data.h_ev_su, data.m_wf , param.EV);
data.Q_ev = data_EV_Q_tot;
Q_in = data.Q_ev;
data.T_htf_ev_ex = data_EV_T_h_ex;
data.h_htf_ev_ex = data_EV_h_h_ex;
data.M_ev = data_EV.M_c;
P_pr = data.P_ev_su;
T_pre= data_EV_T_c_ex;
h_prev = data_EV_h_c_ex;
…

% Call EXPModel function
[data_EXP] = EXP(F_wf, data.P_exp_su, data.h_exp_su, N_exp, P_exp_ex, T_amb,
param.EXP);
data.m_wf = data_EXP_M;
data.W_exp = data_EXP_W;
data.WE_exp = data_EXP_W_el;
data.Q_exp = data_EXP_Q_amb;
data.is_exp = data.EXP_is;
data.vol_exp = data_EXP_vol;
T_pr = data_EXP_T_ex;
h_pr = data_EXP_h_ex;
P_pr = P_exp_ex;
…
```

```
% Call HX1Model function
[data_HX1] = HX1Model(F_wf, data.P_heating_su, data.h_heating_su, data.m_wf_heating,
fluid_hf_heating, P_hf_su_heating, T_hf_su_heating, m_hf_heating, param.HX1);
data.Q_heating = data_HX1_Q _tot;
data.T_hf_heating_ex = data_HX1_T_c_ex;
data.h_hf_heating_ex = data_HX1_h_c_ex;
…

% Call HX2Model function
[data_HX2] = HX2Model(F_wf, data.P_cooling_su, data.h_cooling_su, data.m_wf_cooling,
fluid_cf_cooling, P_cf_su_cooling, T_cf_su_cooling, m_cf_cooling, param.HX1);
data.Q_cooling = data_HX2_Q _tot;
data.T_cf_cooling_ex = data_HX2_T_c_ex;
data.h_cf_cooling_ex = data_HX2_h_c_ex;
…

% Call RECModel function (hot side)
[data_REC] = RECModel(F_wf, data.P_rech_su, data.h_rech_su, data.m _wf,
data.P_rech_su, data.h_rech_su, data.m_wf, param.REC);
data.Q_rec = out_REC.Q_tot;
…

% Call CDModel function
[data_CD] = CDModel(F_wf, data.P_cd_su, data.h_cd_su, data.m_wf, F_cw, P_cw_su,
T_cw_su, m_cw , param.CD);
data.Q _cd = data_CD_Q_tot;
data.T_cw_cd_ex = data_CD_T_c_ex;
data.h_cw_cd_ex = data_CD.h_c_ex;
…….

%overall performance
data.W _net = data.W_el - data.W _pp
data.eleff_Tri = data.W_net/data.Q_in;
data.theff _Tri = data.Q_th/ data.Q _in;
data.overalleff_Tri = (data.W_net + data.Q_th) / data.Q _in
…….

%Residuals
data.res_Tri_hsu = 1 - data.h_pp_su/h_pr;
data.res_Tri_M_dot = 1-data.m _wf/data.m_wf_rec;
data.res_Tri_Q_rec = 1 - data.Q_rec_guess/data.Q_rec;
data.res_vec  = [data.res_Tri_M_dot data.res_Tri_hsu data.res_Tri_Q_rec];
data.res  = norm(data.res_vec)

……

end
```

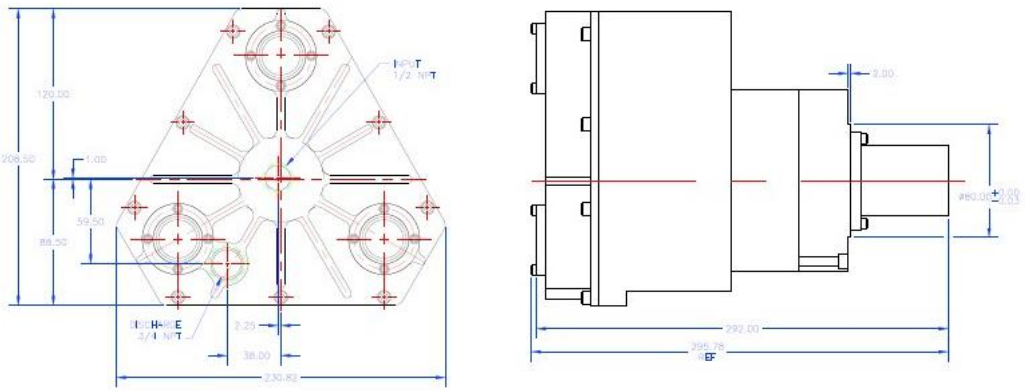
Appendix C: Experimental Instrument Manufacture Datasheets

In this appendix, manufacture datasheets of the main employed experimental and measuring instruments for the ORC and MLDC laboratory testing are presented. The listed instruments are: scroll expander (Figure A-1), electric boiler (Figure A-2), refrigerant pump (Figure A-3), heat exchanger (Figure A-4), AC axial fan (Figure A-5), magnetic liquid pump (Figure A-6), power quality analyser (Figure A-7) and humidity sensor (Figure A-8).

Scroll expander



Output	1 kW (nominal)	
Max. Pressure	200 psia	13.8 bar
Max. Flow	12 cm^3/Rev.	
Max. Speed	3600 RPM	
Max Inlet Temperature	350°F	175°C
Avg. Sound Level	55 dB(A)	
Net Weight	20 lb	9.07 kg
Working Fluid	Refrigerant	
Standard ORC Fluid	R-134a and R-245fa	
Direct Drive	DC/AC Generators, Any Rotary Equipment	
Expansion Ratio	3.5	
Model Numbers	E15H22N4.25 (Oil-free)	
	E15H22N4.25L (Lubricated)	



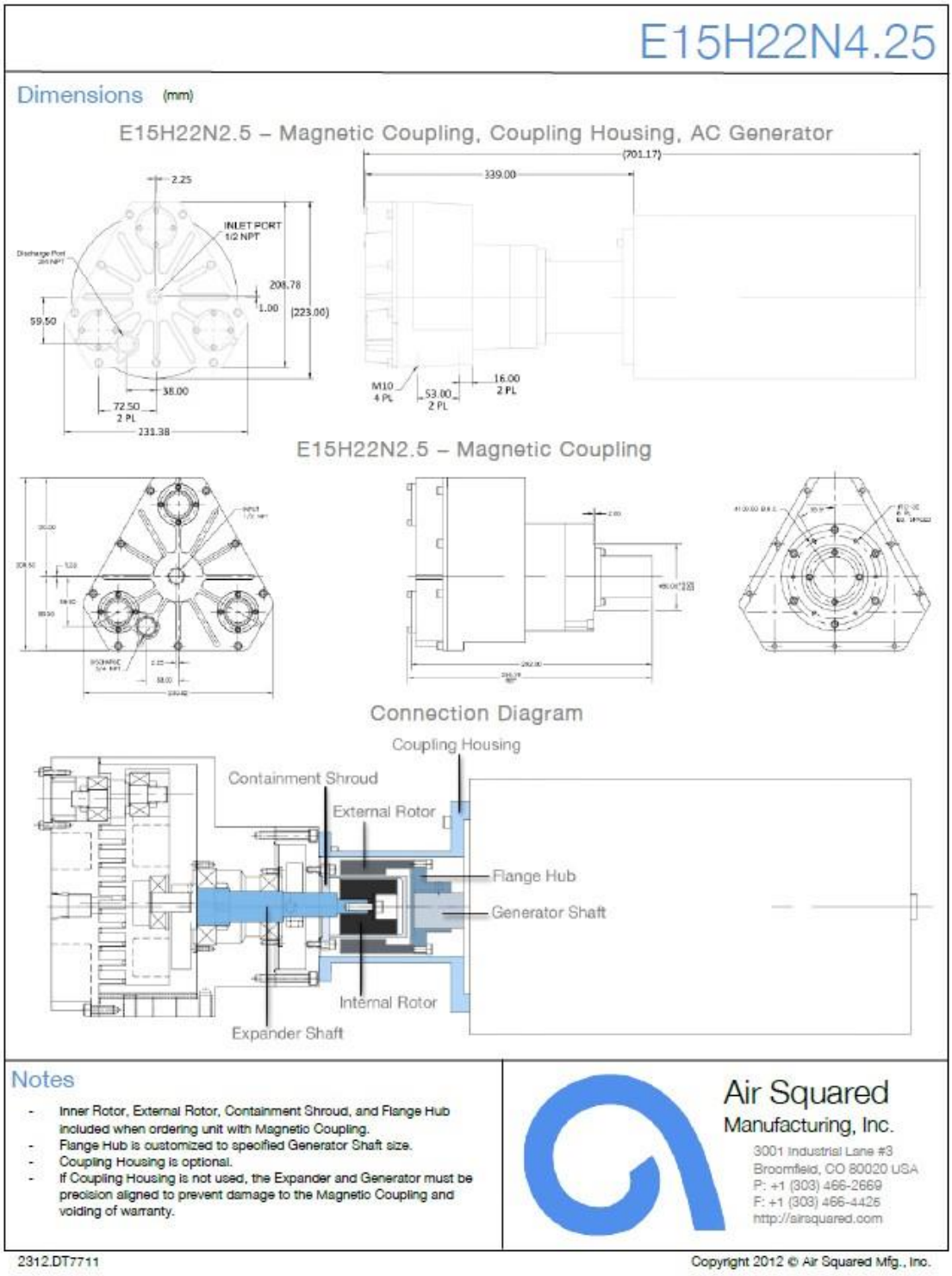


Figure A-1 Photo and manufacture datasheet of scroll expander



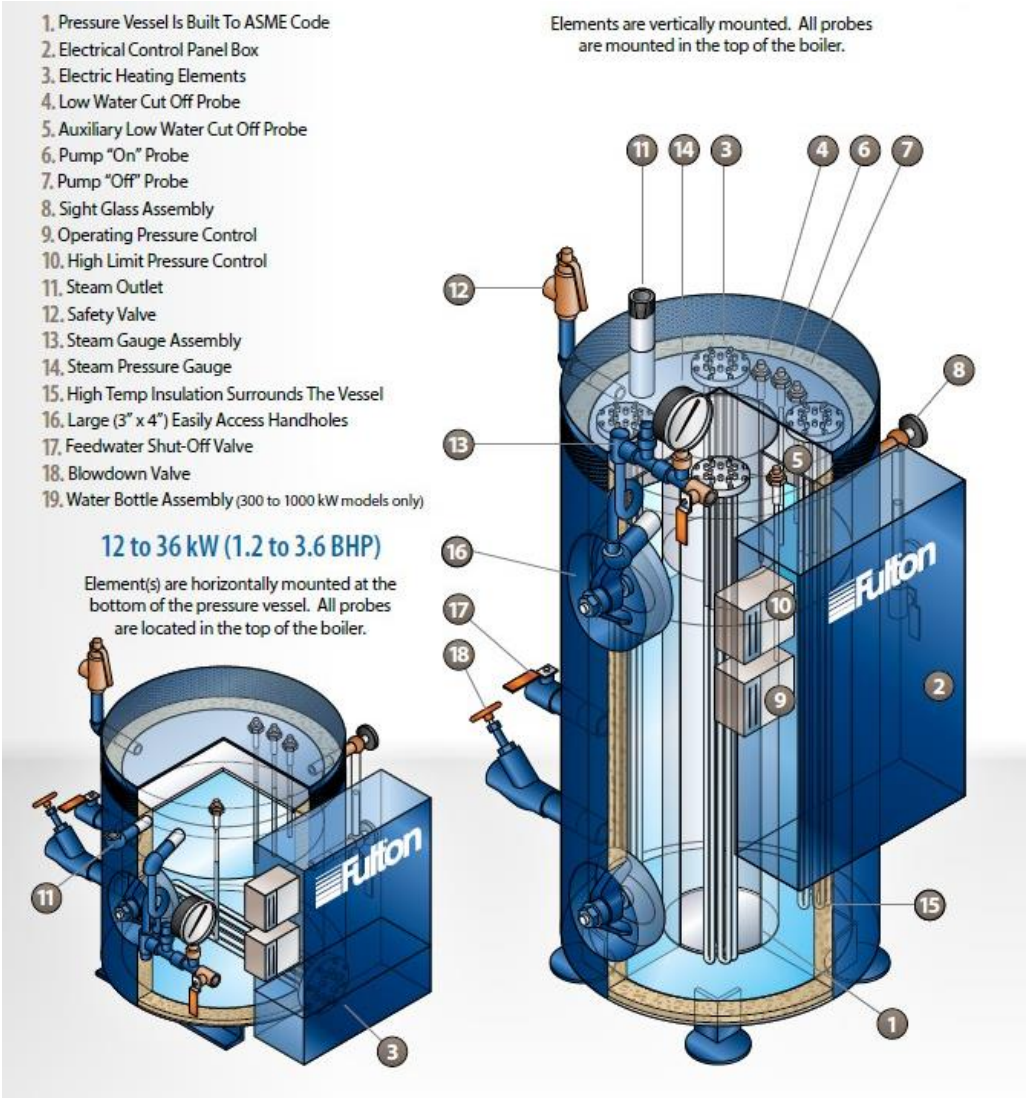


Figure A-2 Photo and manufacture datasheet of electric boiler

Tuthill

Specification Sheet
D Series Pump

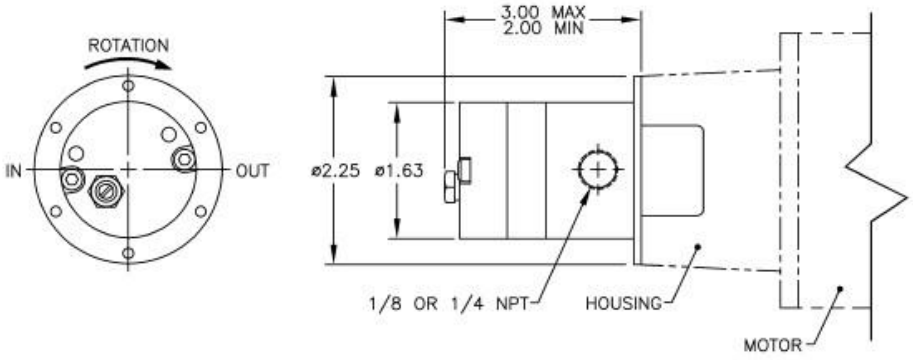
Pump Details

- Magnetic Coupled External Gear Pump
- Non-Pulsing Flow
- Positive Displacement
- Accurate
- Leak Free
- Chemical Resistant
- Long Life



Applications

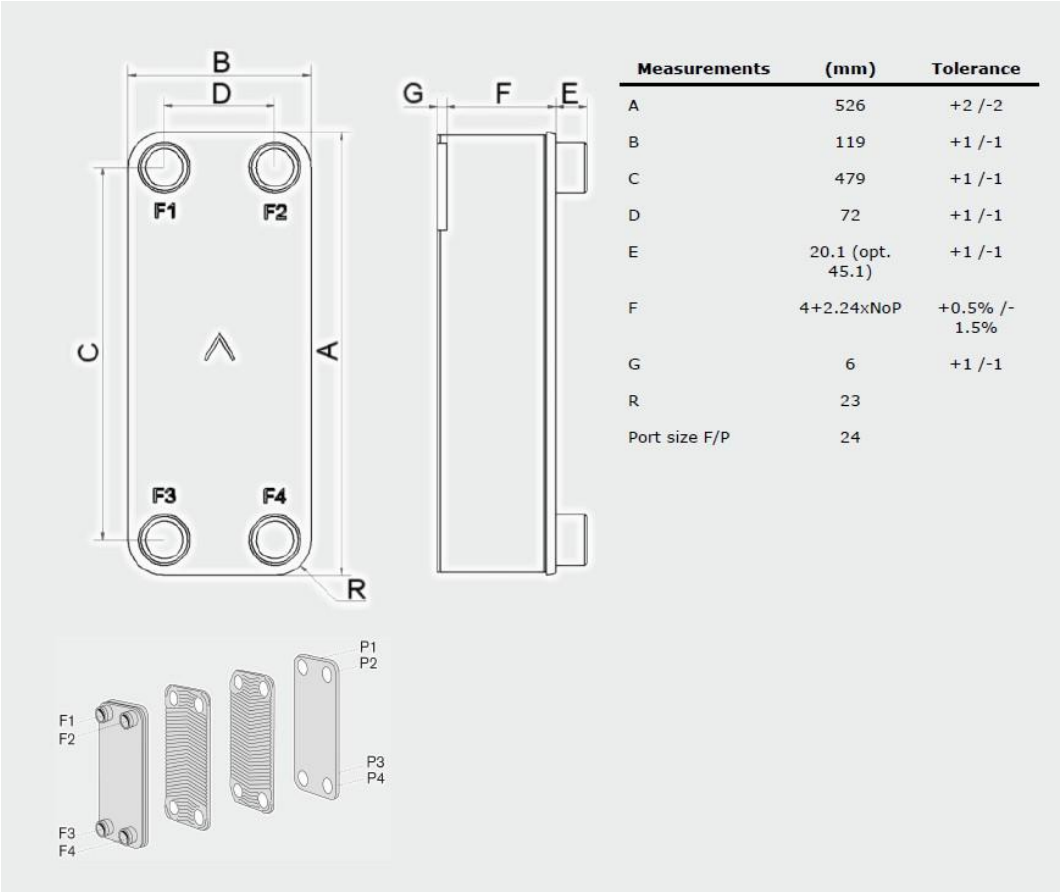
Tuthill Pump Group specializes in OEM applications. All pumps have a wide range of options. Consult factory for other options and performance requirements. Laboratory Equipment, Water Purification, Heat Transfer, Lubrication, Water Treatment, Lubrication, Fluid Transfer, Recirculation, Cooling, Chemical Metering, Fluid Sampling, Temperature Control, Additive Delivery, Proportioning, Chemical Handling, Refrigerant, Liquid Chromatography, Laser, Oil Filtration, Oil Filtration, Acids, Heat Transfer, X-Ray Equipment, etc.



General Specifications

Flow Rates	< 1 to 121 GPH (< 4 to 458 LPH)	**Metal Wetted Parts**	316 Stainless Steel, Titanium, or Hastelloy C276
Temperatures	-50 to 350°F (-46 to 176°C)	**Ports**	1/8 - 27 NPT or 1/4 - 18 NPT
Differential Pressures	250 PSI (17.2 bar)	**Speed**	5,000 RPM maximum
System Pressures	500 PSI (34.5 bar)	**Service Life**	Up to 20,000 hours + based on water
Viscosity	0.3 to 2000 cps +	**Suction Vacuum**	28.5 " Hg (724 mm Hg)
Magnet Torque	15 to 240 in-oz	**Self Priming**	Yes, wetted
Magnet Materials	Ceramic or Samarium Cobalt	**Size**	1.6" diameter pumphead

Figure A-3 Manufacture datasheet of refrigerant pump



Measurements	(mm)	Tolerance
A	526	+2 /-2
B	119	+1 /-1
C	479	+1 /-1
D	72	+1 /-1
E	20.1 (opt. 45.1)	+1 /-1
F	4+2.24xNoP	+0.5% /-1.5%
G	6	+1 /-1
R	23	
Port size F/P	24	

Technical data

Working conditions	Inner circuit	Secondary circuit
Max working pressure at155°C	31 bar	31 bar
Max working pressure at225°C	27 bar	27 bar
Test pressure	50 bar	50 bar

Min temperature: -196°C

Max temperature: 225°C

Max number of plates (NoP): 140

BPHE weight: 2.148 + NoP x 0.1775 kg

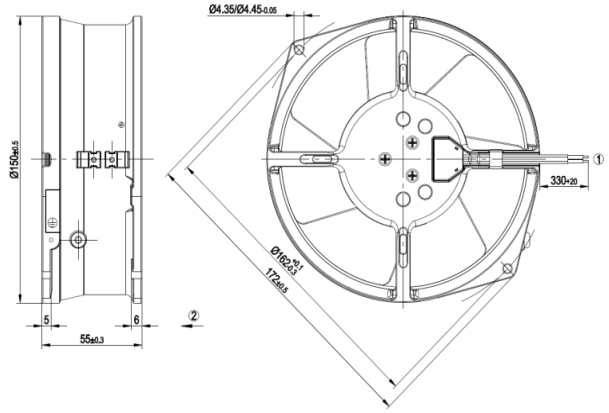
Plate material: Parts in contact with fluid: AISI 316
Parts not in contact with fluid: AISI 304

Brazing material: Pure Copper

Standard connection material: AISI 316

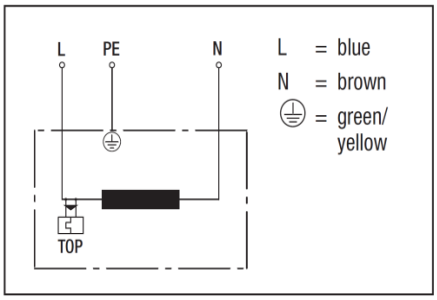
Figure A-4 Manufacture datasheet of heat exchanger

Product drawing



Type	W2S130-AA03-01		
Motor	M2S052-CA		
Phase		1~	1~
Nominal voltage	[V]	230	230
Frequency	[Hz]	50	60
Type of data definition		rfa	rfa
Valid for approval / standard		CE	CE
Speed	[min-1]	2800	3250
Power input	[W]	45	39
Current draw	[A]	0.31	0.25
Max. back pressure	[Pa]	80	120
Max. ambient temperature	[°C]	50	70

ml = max. load · me = max. efficiency · rfa = running at free air · cs = customer specs · cu = customer unit
Subject to alterations

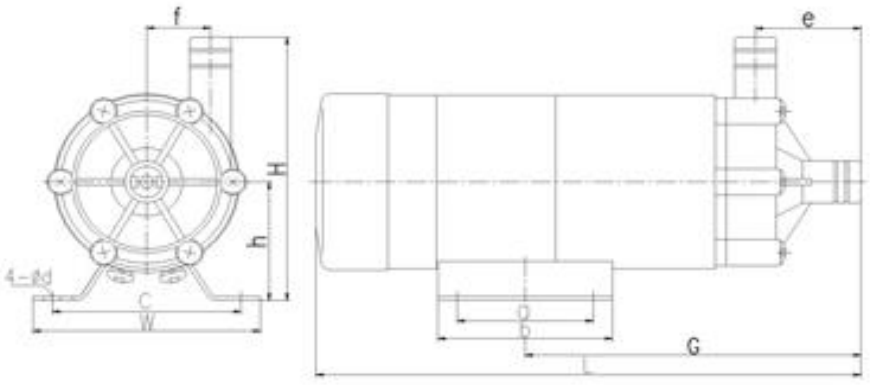


Leackage current	< 0.75 mA
Size	130 mm
Operation mode	S1
Direction of rotation	Counter-clockwise, seen on rotor
Mounting position	Any
Direction of air flow	"V"
Insulation class	"B"
Condensate discharge holes	None
Bearing motor	Ball bearing
Mass	1.1 kg
Material of impeller	Sheet steel, coated in black
Material of wall ring	Die-cast aluminium, coated in black
Motor protection	Thermal overload protector (TOP) wired internally
Product conforming to standard	CE; EN 60335-1
Surface of rotor	Rotor open, coated in black
Number of blades	7
Type of protection	IP 20
Protection class	I
Max. permissible ambient motor temp. (transp./ storage)	+ 80 °C
Min. permissible ambient motor temp. (transp./storage)	- 40 °C
Approval	CCC; CSA C22.2 Nr.113; GOST; UL 507; VDE

Figure A-5 Manufacture datasheet of AC axial fan

Model	MP-20RZ	
Tube interface	Inlet	18 mm
	Outlet	18 mm
Voltage	220 / 240 V	
Current	150 mA	
Phase	Single	
Output Power	15W	
Specific Gravity	< 1.1	
Maximum Frequency	50 Hz	60 Hz
Maximum Speed	2600rpm	3000rpm
Maximum Head	4.6 m	6.9 m
Maximum Capacity	10 L/min	11 L/min





型号 Model	a	b	c	d	e	f	G	h	H	W	L
MP-15R	49	63	68	6	38	23	121	45	100	82	196.5
MP-15RN	49	63	68	6	39.5	24.5	117.5	46	100	82	180
MP-20R	30	50	68	5.5	38.5	28.5	131.5	56	116	85	209
MP-20RZ	30	50	68	5.5	40	40	134	56	126	85	212

Figure A-6 Manufacture datasheet of magnetic liquid pump



Single-phase power quality analyser CA8230

14. FUNCTIONAL CHARACTERISTICS

14.1 Reference conditions

Quantity of influence	Reference conditions
Ambient temperature:	23°C ± 3K.
Relative humidity:	from 45 to 75%.
Atmospheric pressure:	from 860 hPa to 1 060 hPa.
phase-to-earth voltage:	from 50 V_{RMS} to 600 V_{RMS} without DC (< 0.5%).
Input voltage of the standard current circuit:	from 30 mV_{RMS} to 1 V_{RMS} without DC (< 0.5%).
Input voltage of the Rogowski current circuit:	from 11.8 mV_{RMS} to 118 mV_{RMS} without DC (< 0.5%).
Network frequency:	50 Hz ± 0.1 Hz and 60 Hz ± 0.1 Hz.
Phase shift:	0° (active power) and 90° (reactive power).
Harmonics:	< 0.1%.
Balanced three-phase connection:	3ϕ mode OFF.

14.2 Electrical characteristics

14.2.1 Characteristics of the voltage input

Range of use:	from 0 V_{RMS} to 600 V_{RMS} AC+DC phase-neutral (*). from 0 V_{RMS} to 660 V_{RMS} AC+DC phase-phase (*). *: provided that the max. with 600 V_{RMS} respect to earth is not exceeded.
Input impedance:	451 kΩ.
Allowable overload:	1.2 x V_{nom} permanent. 2 x V_{nom} for one second.

14.2.2 Characteristics of the current input

Range of operation:	from 0 V to 1 V
Input impedance:	1 MΩ.
Allowable overload:	1,7 V.

The Amp***FLEX*** configuration switches the current input to an integrating set-up ('Rogowski' chain) capable of interpreting the signals from sensors of the same name. The input impedance in this case is reduced to 12.4kΩ.

14.2.3 Pass band

Measurement channels:	256 points per period, or: ▪ At 50Hz: 6.4 kHz (256 × 50 ÷ 2). ▪ At 60Hz: 7.68 kHz (256 × 60 ÷ 2).
Analogue at -3dB:	> 10kHz.

14.2.4 Characteristics of the instrument alone

(without current sensor)

Attention: the 3ϕ mode is assumed to be deactivated (standard single-phase connection).

These data are for the case of the 'ideal current sensor' (perfect linearity and no phase shift). The characteristics in current (and derived quantities) are specified for each of the two configurations: without Amp***FLEX*** and Amp***FLEX***.

Measurement		Measurement range		Display resolution	Max. error in reference range
		Minimum	Maximum		
Frequency		40Hz	69Hz	0,01Hz	±(1pt)
TRMS voltage		6V	600V [6]	0,1V	±(0,5%+2pts)
DC voltage		6V	600V	0,1V	±(1%+5pts)
TRMS current	Without AmpFLEX	I_{nom} ÷ 1000 [A]	1,2 × I_{nom} [A]	0,1A I < 1000A	±(0,5%+2pts)
				1A I ≥ 1000A	±(0,5%+1pt)
	AmpFLEX	10A	6500A	0,1A I < 1000A	±(0,5%+1A)
				1A I ≥ 1000A	
DC current		1A	1700A[1]	0,1A I < 1000A	±(1%+1A)
				1A I ≥ 1000A	
Courant Peak	Without AmpFLEX	0A	1,7 × I_{nom} [A][2]	0,1A I < 1000A	±(1%+1A)
	AmpFLEX		9190A[3]	1A I ≥ 1000A	
Half-period TRMS current[4]	Without AmpFLEX	I_{nom} ÷ 100 [A]	1,2 × I_{nom} [A]	0,1A I < 1000A	±(1%+5pts)
				1A I ≥ 1000A	±(1%+1pt)
	AmpFLEX	100A	6500A	0,1A I < 1000A	±(1,5%+4A)
				1A I ≥ 1000A	
Peak voltage		6V	850V[4]	0,1 V	±(1%+5pts)
Half-period TRMS voltage[5]		6V	600V	0,1V	±(0,8%+5pts)
Peak factor		1	4	0,01	±(1%+2pts)
		4	9,99	0,01	±(5%+2pts)
Active power	Without AmpFLEX	0W	9999kW	4 digits	±(1%) Cos ϕ ≥ 0.8
					±(1.5%+10pts) 0.2 ≤ Cos ϕ < 0.8
	AmpFLEX	0W	9999kW	4 digits	±(1%) Cos ϕ ≥ 0,8
					±(1.5%+10pts) 0.5 ≤ Cos ϕ < 0.8
Reactive powers	Without AmpFLEX	0VAR	9999kVAR	4 digits	±(1%) Sin ϕ ≥ 0.5
					±(1.5%+10pts) 0.2 ≤ Sin ϕ < 0.5
	AmpFLEX	0VAR	9999kVAR	4 digits	±(1.5%) Sin ϕ ≥ 0.5
					±(2.5%+20 pts) 0.2 ≤ Sin ϕ < 0.5
Apparent power		0	9999kVA	4 digits	±(1%)
Power factor		-1	1	0,001	±(1.5%) Cos ϕ ≥ 0.5
					±(1.5%+10pts) 0.2 ≤ Cos ϕ < 0.5

Figure A-7 Manufacture datasheet of power quality analyser

SENSIRION
THE SENSOR COMPANY

Datasheet Evaluation Kit EK-H4

For SHT7x and SHT2x Humidity and Temperature Sensors

- Ready to use Hard and Software
- Suitable for data-logging experiments
- Programmable Interface
- Dew Point and Energy Calculation
- Multiple Multiplexer Boxes with Sensors lockable



Electrical specification:

Parameter		min	typ	max	Unit
External Supply	Input Voltage	8	9	10	V
	Input Voltage Ripple			0.5	V
	Supply Current		170	280	mA
USB Supply	Input Voltage	4.75	5	5.25	V
	Supply Current		170	280	mA
Sensor Supply Voltage	Range	2.1	3.0	3.6	V
	Resolution		0.1		V
	Accuracy		2	5	%
	Output current		40	110 [1]	mA
Temperature Resolution		11		14	Bit
Humidity Resolution		8		12	Bit
Measurement interval		1		1440	s
Communication	USB (via Virtual Com Port (VCP))				
Operating Temperature	0 – 50°C (multiplexer box) -20 – 70°C (cables, sensor)				

Default Configuration

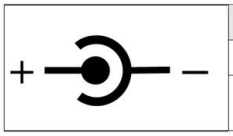
Initial configuration set for the default mode (values can be changed by using the measurement software)

Parameter		Default value
Sensor Supply Voltage		3.0 V
Temperature Resolution		12 Bit
Humidity Resolution		12 Bit
Measurement interval		1 s
Heater		off
OTP reload	SHT7x	on
	SHT2x	off

Power Supply

Used Connection	EK-H4 supplied from
DC	DC (9V)
DC and USB	DC (9V)
USB	USB (5V)

The EK-H4 may be supplied by DC Power Supply Unit at 9V or USB connection at 5V. Power supply by USB is only possible if USB driver is installed correctly.

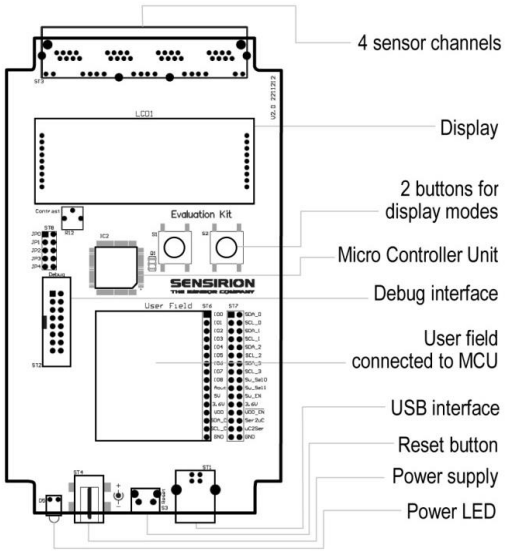


Pin	Name	Comment
-	GND	Ground
+	Positive Voltage	9V Supply

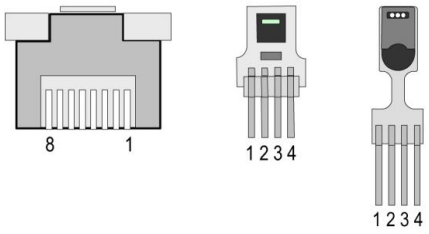
Table 1 DC Power Supply: Pin Diagram

[1] short circuit current

EK-H4 Circuit Board



EK-H4 Pin Assignment



RJ45 Pin	Sensor Pin	Name	Description
1	3	VSS	Ground
3	1	SCL	Serial clock
5	2	VDD	Supply voltage
7	4	SDA	Serial data

Table 2 Pin Assignments: Female RJ45 pin diagram on the left – SHT21 and SHT71 sensors on the right of the upper panel.

LED Functions

LED		Function
Power LED		LED off denotes low supply voltage (DC < 8V, USB < 4.75V) or not connected.
RJ45 Connector	Green LED	Sensor detected
	Orange LED	Measurement is in progress

Figure A-8 Manufacture datasheet of humidity Sensor